Extreme Mid-IR light control with SiC microstructures

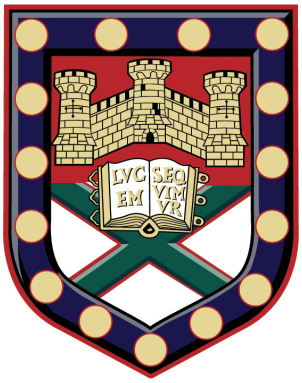

Ganga Chinna Rao Devarapu
School of Physics
University of Exeter

A thesis submitted for the degree of
Doctor of Philosophy in Physics
June 2014

Extreme mid-IR light control with SiC microstructures

Submitted by Ganga Chinna Rao Devarapu to the University of Exeter as a thesis for the degree of Doctor of Philosophy in Physics.
June 2014

I certify that all material in this thesis which is not my own work has been identified and that no material has previously submitted and approved for the award of a degree by this or any other university.

Ganga Chinna Rao Devarapu
June 2014

Abstract

In this thesis, we present our original theoretical investigations of SiC microstructures for extreme light control in the Reststrahlen band of Silicon Carbide (SiC), that occurs in the Mid-IR spectral regime. In this frequency regime, most of the light will be reflected from bulk SiC, due to the extreme permittivity response of SiC. However, we demonstrate that it is possible to control light to be absorbed or ultra refracted within the microstructures constructed from SiC in the Reststrahlen band of SiC. In particular, we show that this high reflective behaviour of SiC can be overcome via different mechanisms: by achieving a Photonic Crystal (PC) band-edge reflectionless condition in a SiC terminated one-dimensional (1D)-PC, by tailoring the effective phonon-polariton gap in SiC-based effective metamaterials, or by coupling to cavity modes in SiC structures made of rectangular-cross-section pillars. Furthermore, we demonstrate that by varying the thickness of SiC layers and filling ratio throughout SiC 1D-PC structures or by using SiC pillars of different size in a pyramid arrangement, we can achieve a broad absorption bandwidth with the SiC microstructures. This absorption control provides insight for the design of efficient thermal emitters, which can be used in thermal conversion devices. Moreover, using the concept of Bloch impedance, we find that translucent spectral regions can exist in SiC 1D-PCs. This possibility is highly desirable for constructing optical components in the Mid-IR spectrum where suitable bulk highly refractive materials are rare. In addition, we also present a complete theory of propagation in lossy 1D-PCs, by systematically extending the comprehensive theory for lossless 1D-PCs. Relying on this theory, we report superbending of light, beyond 90^0 in a judiciously designed superprism constructed with a SiC 1D-PC. Since, the findings reported in this thesis are in principle applicable to any polar material, we believe that our work will inspire the design of a variety of absorptive/emissive and ultra-refractive devices across the THz/Mid-IR spectrum.

To all my Teachers

Acknowledgements

First of all, I would like to convey my deepest gratitude to my Ph. D. supervisor Dr. Stavroula Foteinopoulou, for giving me the opportunity to work with her. I am highly indebted to her for her advice, support, patience, guidance and kindness. She has provided her timely remarks and guidance about coding, writing, presentations and research discussions. I am grateful to her for giving me such great few years in research. This thesis would not have been possible without her motivation and persistent help. Thank you Stavroula.

I would like to sincerely thank my Ph. D mentor Prof. Gyaneshwar Prasad Srivastava, for his valuable support throughout my Ph. D. He has helped me a great deal when I was struggling, and was one of the most down to earth, friendly people I have ever met. I am also grateful for his valuable career advice.

My special thanks to Prof. Misha Portnoi, for providing such a lovely atmosphere at work with his deep knowledge of science and sense of humour. I would like to thank Dr. Annette Plaut for her help in bringing access to many important journals and maintaining the Physics library books, which I have been using since my first year. I would like to thank also all other academics in the Physics department for their valuable talks, discussions and questions. My sincere thanks to Mr. Chris Forrest, Mr. David Colridge, Mr. John Meakin and other staff in the Physics Building for their kind help.

My special thanks to Ms. Liz Roberts and Mrs Denise Watts and other members in the financial office. I would like to thank staff at Wellbeing center, especially Dee Bowker, Russel Cargill and Sarah Lane for their great emotional support. I am grateful to my teachers at INTO for their invaluable help in improving my English. Many thanks to University of Exeter for providing the financial support and many great facilities during my Ph. D.

I would like to thank all my friends and colleagues in the University for their help.

My special thanks to friends in QSN group Charles Downing, Alexander Pearce, Claire Woollacott, Tom Sturges, Lachlan Marnham, Ceyda Yelgel, Celal Yelgel, Jawaher AlOtaibi and Ayman Alofi for providing such nice friendly work place. My sincere thanks to friends in EMAG group Wei Yu, Reem Alsaigh, Haidar Uday, Tom Constant, Celia Butler, Martin Gentile, Caroline Pouya, Nina Meinzer, Helen Rance, Alasdair Murray, Alastair (Ali) Humphrey and Matthew Nixon.

Many thanks to our "Indian gang" in Exeter, who has always there to cheer me up. Our meetings and celebrations are my most memorable days in Exeter. My special thanks to Prim, Kopal, Shalini, Varun, Shoyab, Suhaib, Atul, Bharani, Krupakar, Lucky, Sneha, Anusha, Madhav, Priya and Bhavana.

Many thanks to Dorothy, Ruth, Jenny and all other friends at "Globe cafe" for their great support and for introducing me to the culture of England.

I would like to thank my M. Tech supervisor Prof. Susanna Orlic, colleagues at TU Berlin and my friends in Germany.

I would like to thank all my teachers, who have shaped my career and life. Special thanks to my life time mentors Prof. Kehar Singh, Prof. M. R. Shenoy, Prof. Joby Joseph, Prof. R. Shankar, A. Rama Krishna sir, Ratnakumari, Nageswararao sir, Seshagiri sir, Kishor sir, K. Apparao, Ravi, Chinababu, Varma, Abhishek and Jagriti. I sincerely thank all my friends for their love and support throughout my life and shaping my character.

On a more personal level, I would like to thank my parents, my sister and my brother for believing in me and encouraging me for all my endeavours. Many many thanks to my grandparents for their love of education and inspiration.

Declaration

In Chapter 3 entitled *"Mid-IR near-perfect absorption with a SiC photonic crystal with angle-controlled polarization selectivity"*: Per Section 2.2 of code of practice for presentation of Theses, this chapter is presented as published in the paper: Ganga Chinna Rao Devarapu and Stavroula Foteinopoulou, "Mid-IR near-perfect absorption with a SiC photonic crystal with angle controlled polarization selectivity," Opt. Express **20**, 13040-13054 (2012) [© Optical Society of America. See `http://dx.doi.org/10.1364/OE.20.013040`]. The writing of the main text of the publication was performed by my supervisor Dr. Stavroula Foteinopoulou. The research of Section 3.5 corresponding to the derivation of the analytical formula relating energy velocity and its gradient with reflection, was performed by Dr. Stavroula Foteinopoulou.

In Chapter 5 entitled *"Compact photonic-crystal superabsorbers from strongly absorbing media"*: Per Section 2.2 of code of practice for presentation of Theses, this chapter is presented as published in the paper: Ganga Chinna Rao Devarapu and Stavroula Foteinopoulou, "Compact photonic-crystal superabsorbers from strongly absorbing media," J. Appl. Phys. **114**, 033504 (2013). [© 2013 AIP Publishing LLC. See `http://dx.doi.org/10.1063/1.4811521`]. The writing of the main text of the publication was performed by my supervisor Dr. Stavroula Foteinopoulou. The green-dashed lines in Fig. 5.9 representing the thin film calculations for SiC absorptivity for comparison purposes, was provided by Dr. Stavroula Foteinopoulou.

In Chapter 6 entitled *"Broadband Mid-IR superabsorption with aperiodic polaritonic photonic crystals"*: Per Section 2.2 of code of practice for presentation of Theses, this chapter is presented as published in the paper: Ganga Chinna Rao Devarapu and Stavroula Foteinopoulou, "Broadband Mid-IR superabsorption with aperiodic polaritonic photonic crystals," J. Euro. Opt. Soc. Rap. Pub. **9**, 14012 (2014) [© The Authors. See `10.2971/jeos.2014.14012]`. The writing of the publication was majorly performed by myself, with significant parts contributed by my supervisor Dr. Stavroula Foteinopoulou.

My supervisor Dr. Stavroula Foteinopoulou has contributed to every part of this thesis.

Contents

List of Figures

List of Tables

List of Symbols

Symbol	**Units**
1D	One-dimensional
2D	Two-dimensional
3D	Three-Dimensional
a	Lattice constant
A	Absorptance
B	Magnitude of Magnetic field
BaF_2	Barium Fluoride
BZ	Brillouin Zone
c	Speed of light
CA_{enha}	Cumulative absorptance enhancement
CAD	Computer Aided Design
D	Magnitude of electrical displacement vector
δ	Skin depth
DPR	Dissipated Power Ratio
ε_0	Vacuum Permittivity
ε_{eff}	Effective permittivity
ε_r	Relative permittivity
ε_∞	Relative permittivity at high frequencies
e	Magnitude of charge of electron
E	Magnitude of Electric field
EFC	Equi-Frequency Contours
EFS	Equi-Frequency Surfaces
EM	Electromagnetic
f_r	Filling ratio
FDTD	Finite-Difference Time-Domain
FOM	Figure of Merit
FWHM	Full Width at Half Maximum
Γ	Intrinsic damping parameter
H	Magnitude of Magnetic field strength

I	Intensity
IR	Infrared
J	Current density
k	Magnitude of wavevector
κ	Extinction coefficient
λ	Wavelength
λ_{free}	Free-space wavelength
LiF	Lithium Fluoride
LO	Longitudinal optical-phonon
LST	Lyddane-Sachs-Teller
μ_0	Permeability of vacuum
μ_r	relative permeability
m	Mass of electron
Mid-IR	Mid Infrared
n	Real part of refractive index
P	Magnitude of electric polarization
P_{loss}	Dissipated Power
$P_{loss,\mathrm{v}}$	Dissipated Power per volume
PC	Photonic Crystal
q	Magnitude of Bloch wavevector
R	Reflection
r	Reflection coefficient or amplitude
σ	Conductivity
S	Magnitude of Poynting vector
SiC	Silicon Carbide
SNOM	Scanning Near-Field Optical Microscopy
T	Transmission
TE	Transverse electric
TH	Transverse magnetic
THz	Terahertz
TMM	Transfer Matrix Method
TO	Transverse optical-phonon
t_{ratio}	Termination ratio
ω	Angular frequency
U	Energy density
v_e	Magnitude of energy velocity
v_g	Magnitude of group velocity
v_p	Magnitude of phase velocity
ω_0	Natural frequency of the oscillator

ω_L	Longitudinal-optical-phonon frequency
ω_T	Transverse-optical-phonon frequency
Z_0	Vacuum impedance
Z_{eff}	Effective impedance
Z_B	Bloch impedance
ZnSe	Zinc Selenide

1 Introduction

1.1 Background and motivation

The objective of this thesis is to achieve extreme control of light in the Mid-IR regime, which is highly desirable for applications such as biosensing [1–3], thermal emission [4–7] and detection applications [8]. Furthermore, this frequency regime is also an important atmospheric transparency window for observations of astronomical objects colder than 500 K [9, 10]. But attention to this important part of the electromagnetic (EM) spectra is missed until recently, mainly due to the lack of availability of materials that work in this frequency regime [8]. In this thesis, we aim to accomplish extreme light control within the Mid-IR frequency regime, with particular focus on near-unity absorption, i.e. near-perfect absorption [11, 12] and extreme deflection of light [13–15].

Natural materials offer limited opportunity for such extreme control of light in their bulk form [16–18]. Therefore, many research efforts focus on extraordinary light control by employing structured materials. Two large classes of structured materials that have been employed thus far for extreme light control are EM metamaterials [16–18] and photonic crystals (PCs) [19–21]. Both are periodic media, but the periodicity-size scales with respect to the wavelength of incident light are very different [22]. In particular, metamaterials are subwavelength, which allows them to behave as effective homogeneous media [16–18]. On the other hand

PCs have a periodicity of the order of the wavelength of operation and derive their light controlling properties from multiple scattering of light between their building blocks [21, 23]. These two classes of structured materials are discussed further in Chapter 2. Another strategy for extreme light control that has also been widely adopted involve exciting resonances via collective oscillations of charges in metallic-structured materials, which has given rise to the field of plasmonics [24]. Moreover, localised Mie-type of resonances in dielectric particles are also explored for extreme light enhancement and absorption [25].

As we mentioned above, one of the objectives of this thesis is absorption enhancement in the Mid-IR regime. In this frequency regime, extraordinary absorption phenomena that have been reported have been achieved mainly by two strategies. The first strategy involves an impedance-matching metallic metamaterial layer on top of an absorbing material. The metallic layer reduces reflection, thus efficiently coupling light inside the absorbing material [12, 26], resulting in near-perfect absorption. The second reported strategy involves a lossless structured material, in particular Silicon, exciting microresonances in the vicinity of an absorbing material, in particular Indium Arsenide, thus directing high electric fields and enhancing the absorption in the latter [27].

Both of these reported strategies required two kinds of material in order to achieve absorption enhancement, one of which being the relevant absorbing material, where absorption is aimed. In the first reported strategy, the metallic material is necessary for a large EM coupling [12, 26]. In the second strategy, the lossless material (Silicon) [27] is necessary for an enhanced light-matter interaction and reduced reflection achieved through the conical shape of the nano-resonators constructed from this lossless material. However, the additional metallic layer in the first strategy introduces undesired loss in the metallic layer, thus funneling less light in the relevant absorbing material. This limitation has been overcome with the second strategy by having only one kind of lossy material. However, the performance in the second strategy heavily depends on the lossless material and its structural features which may involve complex designs and pose certain limitations in the ability to conceive and realise a variety of designs.

Therefore, the objective of this thesis is to propose a new strategy for absorption control, with an operating mechanism that relies only on a single-kind of absorbing material. Specifically, we are proposing in this thesis a new PC-based absorption enhancement route by tailoring the propagation of lossy EM waves. We present these results in Chapters 3, 5 and 6. Moreover, in Chapter 4 we make a comparison of the

PC-based superabsorbers to corresponding structures that are deep-subwavelength and behave as a metamaterial. In addition, by building up on the knowledge from related structures operating in the optical regime [28], we have achieved absorption enhancement in the Mid-IR regime with micro-resonators made up only of highly reflecting absorbing material, which is not a suitable absorber in bulk form. We present these results in Chapter 7.

As mentioned earlier in this section, the second objective of this thesis is to achieve ultra-deflection of light in the Mid-IR regime, at free-space wavelengths around 10 μm, which is crucial for biosensing [1–3] and astronomical observations [9, 10]. This is very important since in this frequency regime there are very few suitable materials available for constructing optical components for beam manipulation [29], since many materials that are transparent in the visible regime become opaque in the Mid-IR regime [29]. Extreme beam manipulation has actually been studied throughout the EM spectrum [30–35]. In the optical/near-IR regime extraordinary beam deflection was reported with wedged structures constructed from negative refractive index metamaterials [30], engineered metamaterial Huygens surfaces [31], graded photonic crystals [32] and smartly designed coaxial plasmonic corner waveguides [33]. Furthermore, extreme bending of light was achieved by dispersion engineering of plasmonic waveguides based on rectangular metal blocks [34] that operate at a free-space wavelength around 1.5 mm. In the THz regime, a 30^0 bending of normally incident light with simultaneous polarisation conversion has been achieved [35] by exploiting the optical anisotropy in a carefully designed metamaterial. Now in the Mid-IR regime, although negative refraction has been reported [36] using a hyperbolic metamaterial (uniaxial material with opposite in sign permittivity for the directions parallel and perpendicular to the optical axis [22]), extreme bending of light was not demonstrated thus far. Since many materials can be lossy in the Mid-IR spectrum, it is interesting to investigate whether translucence and extreme beam bending can be achieved with structures made up of opaque materials. We present our results related to this line of research in Chapters 8 and 9.

For all the structures we consider throughout Chapters 3 to 9, we have chosen Silicon Carbide (SiC) as the key constituent material. We made this choice of SiC because of its negative permittivity values that change rapidly within the Mid-IR spectrum, in a regime spanning from 10.3 μm to 12.6 μm [37, 38]. As we mentioned before, this frequency regime is of high interest for biological [1–3] and astrophysical [9, 10] applications. These extreme values of permittivity emanate from the coupling of the incident EM field with the crystal vibrations of SiC (in particular with the transverse optical phonons), resulting in the phonon-polariton gap [39, 40], which

is also referred to as the Reststrahlen band [41, 42]. We will discuss about the Reststrahlen band in more detail in Chapter 2, where we also explain that bulk materials are nearly 100% reflective in the Reststrahlen-band frequency regime. Therefore, achieving extraordinary light control as absorption or deflection with this extremely reflective material will provide invaluable insight that can be transferred to other structures that comprise semiconductor materials around their Mid-IR absorption spectrum. Note that the permittivity of semiconductors close to their absorption edge can be described in many cases with a Lorentzian function or a summation of Lorentzian functions [27] similar to the case of SiC in the Reststrahlen band as we will see in Chapter 2. In other words, by achieving extreme light control with these SiC-based structures, we are setting example designs that are transferable to other structures with semiconductor constituents around their absorption spectrum.

Accordingly, our results presented with SiC structures here in this thesis open up exciting new research directions in the Mid-IR regime with absorbing semiconductors, beyond metallic structures. There are certain limitations for employing metallic structures for Mid-IR light control [8]. For example, due to the ohmic losses in metals [39], the light that gets absorbed by the metallic components is not useful for a carrier generation that is required for certain detection devices. Moreover, the melting point of metals is around 1000^0C [39], which limits metals for constructing thermal absorbers/emitters that operate at very high temperatures (note that emission is directly related to absorption [43]). On the other hand, SiC has a very high melting point of 2700^0C. This combined with an extraordinary mechanical stability and high thermal conductivity [44] makes SiC an excellent material to work as thermal absorber/emitter. Moreover, within the Mid-IR regime around 10 µm metals have a very small skin depth in the range of $\sim \lambda_0/300$ to $\sim \lambda_0/500$ [45] with λ_0 being the free-space wavelength. This means metals are capable of only a very small light-matter interaction path length. In contrast, within the Reststrahlen band, SiC has a larger skin depth that varies from $\sim \lambda_0$ to $\sim \lambda_0/100$ within that frequency range [38]. This suggests metals have a more limited capability for mode engineering in the Mid-IR frequency range, in comparison with SiC or other absorbing materials.

As a background, in the following, we review the properties of bulk SiC and the SiC-based microstructures studied in the photonics field thus far. SiC is a compound of Silicon and Carbon, consisting of equal number of atoms from both the elements. It was first accidentally synthesized by Edward Acheson [46, 47] in 1891, and later discovered in nature [48]. SiC exists in a large number of crystalline forms such as cubic, hexagonal, and rhombohedral [49]. Each crystalline form of SiC is characterized by a unique stacking sequence of Silicon and Carbon

layers [47, 50]. SiC possesses extraordinary material properties [44, 46, 51, 52] such as extreme hardness, high chemical-inertness, large thermal conductivity, low thermal expansion and wide bandgap. It has therefore become one of the important commercial compounds since the beginning of twentieth century, finding applications in abrasive machining [46], automobile parts [53–56], light emitting diodes [57, 58], high-power electronics [59–63], thermal detection [64–66], iron production [67–69] and in many other fields [70–72].

SiC is also interesting for photonic applications. Early applications of SiC photonics were focussed within the optical and near-IR regime. For example, SiC mirrors were employed in a large number of space telescopes due to the above mentioned extraordinary mechanical and thermal properties of SiC [73–79]. New advances of SiC applications in this frequency regime include exploiting crystal defects in SiC to generate single-photons [80–83], that operate similarly to nitrogen-vacancy centers in diamond [84]. In addition, high-photoluminescence SiC quantum dots have been used as biological labels [85–87] (SiC possesses excellent biocompatible properties [87]). Furthermore, high quality factor (high-Q) optical cavities with 2D-SiC PCs were proposed for thermally stable optical systems [88] that can operate at multiple wavelengths from IR to visible regime [89]. More recently, 2D-SiC PCs were explored for applications such as second-harmonic generation [90] and quantum information processing [91]. In addition, SiC based high-Q microdisk resonators were proposed for cavity optomechanical applications [92].

In recent years, the attention of SiC photonics research is increasingly shifting towards the Mid-IR regime, where the phonon-polariton gap of SiC exists. This increased interest in the Mid-IR regime is helped by the invention of quantum cascade lasers [93–95] that provide quality, compact and affordable light sources to work in the entire phonon-polariton gap of SiC. Furthermore, recent improvements in the fabrication of large diameter ultrahigh-quality SiC single-crystals [96, 97], availability of SiC wafers on insulating material [98, 99] and direct wafer bonding of SiC wafers [100] inspire to realise high quality, complex SiC microstructures that operate in the Mid-IR regime.

In the earlier years of SiC Mid-IR photonics research, SiC microstructures were explored for thermal emission applications. In particular, SiC surface relief gratings were considered for coherent thermal emission by exciting the surface phonon-polaritons [4, 5]. Thereafter, many research directions have emerged around SiC structures in the Mid-IR regime. For example, SiC surfaces and micro-particles are studied for Scanning Near-field Optical Microscopy applications

(SNOM) by taking advantage of the phonon-enhanced near-field coupling [101, 102]. Furthermore, a Mid-IR superlensing effect, i.e a lens with subwavelength resolution, was demonstrated using a thin SiC layer [103]. This SiC superlens operates in a narrow spectral bandwidth within the Reststrahlen regime by exciting the surface phonon-polariton modes at the interfaces of the SiC layer, in an analogous manner to Pendry's silver superlens [105]. Operation of such a superlens at a wider spectral range was extended in Ref. [104], by adding thin film lenses made of other polaritonic materials.

Other interesting phenomena with SiC microstructures that have been reported include extraordinary optical transmission (EOT) using SiC slabs with hole arrays in the Reststrahlen band of SiC [37, 106, 107]. This was achieved by exciting propagating modes inside the subwavelength holes and surface resonances on the SiC layer interfaces [37]. In addition, an effective magnetic response was realised with SiC microparticle media [108–110] by exciting the magnetic-mode Mie resonances on the particles [111, 112]. Moreover, sub-diffraction light confinement was demonstrated with SiC nanopillar antennas by exciting localized surface phonon-polariton modes [113]. In addition, in Ref. [114] a similar principle was used to guide and concentrate high EM energy with SiC microstructures that has led to optical force enhancement.

As mentioned above, absorption enhancement within the Mid-IR regime was reported before with SiC surface relief gratings [4, 5]. Recent advances for absorption/emission with SiC microstructures include SiC antenna structures [115, 116]. However, in all these works [4, 5, 115, 116] only a narrow band absorption/emission is reported. In Ref. [117] a larger absorption bandwidth was achieved with a low reflecting SiC metasurface. However the absorption is moderate and peaks at a wavelength of about $\sim 11.8\,\mu\text{m}$ with an absorption value of about 50%. Although, emission at multiple wavelengths was reported with microstructures consisting of SiC photonic crystals [118], these structures are complicated designs involving five different materials. So far, near-perfect absorption or a high absorption exceeding 80% over a broad range of wavelengths with designs relying on structuring a single kind of material has not been achieved.

To recap, the main findings of this thesis with respect to extra-ordinary absorption control in the Mid-IR regime involve uncovering a new PC-based absorption mechanism, in a PC comprising absorbing and highly reflective SiC. Furthermore, broadband cavity-mode-based absorption enhancement reported in the optical regime [28] is extended to the Mid-IR regime with a SiC micropyramid design. This design not only yields a broadband absorption of more than 80%, but also

rests on an insulator, which suggests a potential for realisation of more power efficient thermal sources, in comparison to the surface relief grating structures in Refs. [4] and [5]. Moreover, we have extended the theoretical studies of 1D-lossy PCs and developed a complete theoretical framework for propagation analysis for such lossy structures. Based on this framework, we have designed a superprism with SiC 1D-PC that can deflect light beyond 90^0. In the following, we present the organisation of the thesis, where we discuss these results in individual Chapters.

1.2 Outline of Thesis

For completeness we present in Chapter 2, the key background on both concepts and methodology that this thesis relies on. We start by discussing the EM wave propagation in natural polaritonic materials. In particular, we describe the lossy, dispersive nature of natural polaritonic media, through their permittivity response and define their phonon-polaritonic gap. Then we describe the energy propagation in such lossy material through Poynting's theorem, from which we derive the expression for the power dissipation rate and energy density in these lossy materials. These properties are crucial to understand and optimise the absorption in the SiC microstructures, that we will study in the following chapters.

Furthermore, we discuss the limitations of natural materials to control light in the Mid-IR regime and explain the necessity of artificial structures. We briefly review the two broad categories of artificial structures: photonic crystals and effective metamaterials, that we will be investigating in this thesis. In addition, we describe the propagation theory in lossless 1D-PCs, which will form the basis to understand later the propagation theory in lossy 1D-PCs in Chapter 8. Finally, we describe the methodologies, namely the Transfer Matrix Method (TMM) [119–122], the wavevector diagram formalism [14, 15, 123–125] and the Finite-Difference Time-Domain (FDTD) method [126–128] that we employ in this thesis to investigate the optical properties of the SiC microstructures under study.

In Chapter 3, we demonstrate a near-perfect Mid-IR absorption with a 1D-SiC PC structure within the Reststrahlen band of SiC. The design of this structure was based on a theoretically derived condition for zero reflection at the interface of the 1D-SiC PCs. Furthermore, we demonstrate in this Chapter, that this near-perfect absorptive property can be tuned with the incident light angle, to be polarization insensitive or polarization selective.

The previous chapter dealt with the absorption enhancement in a PC-based system. However, it is interesting to see how the absorption performance of the SiC multilayer structures will change in the limit, where the spacing between the building blocks is extremely subwavelength, so that the structure would behave as an effective medium. Therefore, in Chapter 4, we investigate SiC multilayer stacks with a deep-subwavelength lattice spacing that behave as effective homogeneous materials, with effective permittivity. We find that near-perfect absorption can also be achieved with these effective metamaterial structures within the phonon-polariton gap of the SiC material. This is because the effective phonon-polaritonic gap of these metamaterials shifts, yielding a near-zero reflection peak towards the middle of the Reststrahlen band of SiC, which normally appears outside of latter. However, these effective metamaterials require many thin SiC layers to achieve such superabsorption, compared to the large lattice constant SiC 1D-PCs in the previous Chapter that require few SiC layers. Since, fabrication of several SiC layers may be challenging, we will explore only PC-based absorber designs in the rest of the thesis.

The total thickness of the PC based absorber in Chapter 3 is roughly of the order of twenty-free-space-wavelengths, which makes it quite bulky. Therefore, in Chapter 5, we optimise this SiC 1D-PC design relying on the reflectionless conditions we derived in Chapter 3. In particular, we propose a compact three layer SiC-BaF_2-SiC structure that absorbs more than 90% light in the top SiC layer of thickness $\lambda/1000$, and is practically realisable.

Although, the SiC-BaF_2-SiC absorber design in Chapter 5 is compact, its operation bandwidth is narrow. To overcome this, we investigate aperiodic SiC 1D-PC systems in Chapter 6, inspired by the broadband capabilities observed in chirped gratings. We demonstrate that near-perfect absorption over a broad wavelength regime covering the entire Reststrahlen band of SiC can be achieved with aperiodic SiC PCs consisting of large number of building blocks of linearly varying widths. Furthermore, we find that if we compromise on the near-perfect absorptance, then we can obtain broadband absorption with a compact aperiodic PC design. We also investigate the influence of the order of the building blocks on the absorption bandwidth of aperiodic PCs.

Relying on the insights gained in 1D-PC superabsorber designs in Chapters 3, 4 and 6, and inspired by the subwavelength structures in the eyes of the Moth insects, we propose a new SiC micropyramid absorber paradigm in Chapter 7. With the total thickness of just one-third of the operating wavelength, this

micropyramid system absorbs more than 80% of light over a broad wavelength regime within the Reststrahlen band of SiC. Moreover, we find that absorptivity of these micropyramid structures is asymmetric and polarization dependent. Since the emissivity is directly related to absorption [43], these structures are promising for highly directional polarization-selective emitters.

From Chapter 3 to Chapter 7, we discuss only the absorption properties of SiC microstructures. In Chapter 8, we investigate an opposite effect where the SiC 1D-PCs are nearly translucent, yet can bend light beyond the capabilities of natural prisms. For this purpose, we explore the concept of effective Bloch impedance and find that SiC 1D-PCs have smoother transmission spectra in the Reststrahlen band of SiC. This translucent effect of lossy PCs is attractive for Mid-IR optical components, where suitable materials for constructing such components are rare. Furthermore, in this Chapter, we systematically extend the propagation theory of lossless 1D-PCs that we discussed in Chapter 2, to include the lossy constituents. Based on this propagation theory of lossy PCs, we demonstrate both theoretically and numerically that although backward-type modes exist for lossy 1D-PCs, they do not guarantee negative refraction inside these PCs.

We follow up the theoretical analysis in Chapter 8, and demonstrate extreme bending of light beyond 90^0 with a carefully designed superprism constructed from a SiC-BaF_2 1D-PC in Chapter 9.

Finally, we present our conclusions and suggestions for further study in Chapter 10.

Bibliography

[1] R. W. Waynant, I. K. Ilev and I. Gannot, "Mid-infrared laser applications in medicine and biology," Phil. Trans. R. Soc. Lond. A., **359**, 635-644 (2001).

[2] B. Mizaikoff, "Waveguide-enhanced mid-infrared chem/bio sensors," Chem. Soc. Rev., **42**, 8683-8699 (2013).

[3] J. M. Bakker, L. M. Aleese, G. Meijer, and G. von Helden, "Fingerprint IR spectroscopy to probe amino acid conformations in the gas phase," Phys. Rev. Lett., **91**, 203003 (2003).

[4] J. Le Gall, M. Olivier, and J.-J. Greffet, "Experimental and theoretical study of reflection and coherent thermal emissionby a SiC grating supporting a surface-phonon polariton," Phys. Rev. B **55**, 10105–10114 (1997).

[5] J. J. Greffet, R. Carminati, K. Joulain, J.-P. Mulet, S. Mainguy, and Y. Chen, "Coherent emission of light by thermal sources," Nature **416**, 61–64 (2002).

[6] W. Wang, C. Fu, and W. Tan, "Thermal Radiative Properties of a SiC Grating on a Photonic Crystal," J. Heat Transfer **135**, 091504 (2013).

[7] W. Wang, C. Fu, and W. Tan, "Thermal radiative properties of a photonic crystal structure sandwiched by SiC gratings," J. Quant. Spectrosc. Radiat. Transf. **132**, 36-42 (2014).

[8] L. Stephanie, V. Podolskiy, and D. Wasserman. "Towards nano-scale photonics with micro-scale photons: the opportunities and challenges of mid-infrared plasmonics," Nanophotonics **2** 103-130, (2013).

[9] R. Assendorp, P. R. Wesselius, T. Prusti, and D. C. B. Whittet, "A study of the Chamaeleon I dark cloud and T-association. II-High-resolution IRAS maps around HD 97048 and 97300," Mon. Not. R. Astron. Soc. **247**, 624–631 (1990).

[10] H. U. Käufl, "Ground-based astronomy in the 10 and 20 mum atmospheric windows at ESO-scientific potential at present and in the future," The Messenger **73**, 8–12 (1993).

[11] N. Landy, S. Sajuyigbe, J. Mock, D. Smith, and W. Padilla, "Perfect Metamaterial Absorber," Phys. Rev. Lett. **100**, 207402 (2008).

[12] C. M. Watts, X. Liu, and W. J. Padilla, "Metamaterial electromagnetic wave absorbers," Adv. Mater. **24**, 98120, (2012).

[13] D. R. Smith, W. J. Padilla, D. C. Vier, S. C. Nemat-Nasser, and S. Schultz, "Composite medium with simultaneously negative permeability and permittivity," Phys. Rev. Lett. **84**, 4184-4187 (2000).

[14] M. Notomi, "Theory of light propagation in strongly modulated photonic crystals: Refractionlike behavior in the vicinity of the photonic band gap," Phys. Rev. B **62**, 10696 (2000).

[15] S. Foteinopoulou and C. M. Soukoulis, "Electromagnetic wave propagation in two-dimensional photonic crystals: A study of anomalous refractive effects," Phys. Rev. B **72**, 165112 (2005).

[16] J. B. Pendry, D. Schurig, and D. R. Smith, "Controlling electromagnetic fields," Science. **312**, 1780-1782 (2006).

[17] D. R. Smith, W. J. Padilla, D. C. Vier, S. C. Nemat-Nasser, and S. Schultz, "Composite medium with simultaneously negative permeability and permittivity," Phys. Rev. Lett. **84**, 4184 (2000).

[18] W. Cai and V. M. Shalaev, Optical Metamaterials (Springer, 2010).

[19] E. Yablonovitch, "Inhibited spontaneous emission in solid-state physics and electronics," Phys. Rev. Lett. **58**, 2059-2062 (1987).

[20] S. John, "Strong Localization of Photons in Certain Disordered Dielectric Superlattices," Phys. Rev. Lett. **58**, 2486-2489 (1987).

[21] J. D. Joannopoulos, S. G. Johnson, J. N. Winn and R. D. Mead, *Photonic Crystals: Molding the Flow of light* (Princeton University Press, Princeton, 2008).

[22] S. Foteinopoulou, "Photonic crystals as metamaterials," Phys. B Condens. Matter **407**, 4056-4061 (2012) and references therein.

[23] S. John in Photonic Band Gap Materials, Vol 315 of NATO Advanced Studies Institute, Series E: Applied sciences, edited by C. M. Soukoulis (Kluwer, Dordrecht, 1996). p. 563.

[24] W. A. Murray and W. L. Barnes, "Plasmonic Materials," Adv. Mater. **19**, 3771-3782 (2007) and references therein.

[25] J. A. Schuller and M. L. Brongersma, "General properties of dielectric optical antennas," Opt. Express **17**, 2408424095 (2009).

[26] X. Liu, T. Starr, A. F. Starr, and W. J. Padilla, "Infrared spatial and frequency selective metamaterial with near-unity absorbance," Phys. Rev. Lett **104**, 207403 (2010).

[27] W. Dai, D. Yap, and G. Chen, "Wideband enhancement of infrared absorption in a direct band-gap semiconductor by using nonabsorptive pyramids," Opt. Express **20**, A519 (2012).

[28] K. X. Wang, Z. Yu, V. Liu, Y. Cui, and S. Fan, "Absorption enhancement in ultrathin crystalline silicon solar cells with antireflection and light-trapping nanocone gratings," Nano Lett. **12**, 16169 (2012).

[29] R. A. Paquin, *Materials for Optical Systems* in *Handbook of Optomechanical Engineering*, edited by A. Ahmad, (CRC Press 1996), p.69.

[30] N. H. Shen, Th. Koschny, M. Kafesaki, and C. M. Soukoulis, "Robust wedge demonstration to optical negative index metamaterials," Appl. Phys. Lett **102**, 241915 (2013).

[31] C. Pfeiffer, N. K. Emani, A. M. Shaltout, A. Boltasseva, V. M. Shalaev and A. Grbic "Efficient Light Bending with Isotropic Metamaterial Huygen's Surfaces," Nano Lett, **15**, 2491-2497 (2014).

[32] E. Centeno, D. Cassagne, and J. P. Albert, "Mirage and superbending effect in two-dimensional graded photonic crystals," Phys. Rev. Lett. **112**, 068103 (2006).

[33] W. Shin, W. Cai, P. B. Catrysse, G. Veronis, M. L. Brongersma, and S. Fan "Broadband Sharp 90-degree Bends and T-Splitters in Plasmonic Coaxial Waveguides," Nano Lett. **13**, 4753-4758 (2013).

[34] D. Martin-Cano, M. L. Nesterov, A. I. Fernandez-Dominguez, F. J. Garcia-Vidal, L. Martin-Moreno, and Esteban Moreno "Domino plasmons for subwavelength terahertz circuitry," Opt. Express. **18**, 754-764, (2010).

[35] N. K. Grady, J. E. Heyes, D. R. Chowdhury, Y. Zeng, M. T. Reiten, A. K. Azad, A. J. Taylor, D. A. R. Dalvit, H. T. Chen, "Terahertz Metamaterials for Linear Polarization Conversion and Anomalous Refraction," Science, **340**, 1304-1307 (2014).

[36] A. J. Hoffman, L. Alekseyev, S. S. Howard, K. J. Franz, D. Wasserman, V. A. Podolskiy, E. E. Narimanov, D. L. Sivco and C. Gmachl, "Negative refraction in semiconductor metamaterials," Nat. Mat. **6**, 946-950 (2007).

[37] P. B. Catrysse and S. Fan, "Near-complete transmission through subwavelength hole arrays in phonon-polaritonic thin films," Phys. Rev. B **75**, 075422 (2007).

[38] E. D. Palik, *Handbook of Optical Constants of Solids* (Academic Press, 1985).

[39] C. Kittel, *Introduction to Solid State Physics* (John Wiley and Sons, Hoboken, 2005).

[40] K. Huang, P. Bienstman, J. Joannopoulos, K. Nelson, and S. Fan, "Phonon-polariton excitations in photonic crystals," Phys. Rev. B **68**, 075209 (2003).

[41] H. Rubens and E. F. Nichols, "Über Wärmestrahlen von grosser Wellenlänge," Naturwissenschaftliche Rundschau **11**, 545–549 (1896).

[42] E. D. Palik, "History of far-infrared research. I. The Rubens era," JOSA **67**, 857–865 (1977).

[43] M. Born and E. Wolf, *Principles of Optics : Electromagnetic Theory of Propagation, Interference, and Diffraction of Light*, (University Press, Cambridge, 2006).

[44] G. L. Harris, *Properties of Silicon Carbide* (London, INSPEC 1995).

[45] M. A. Ordal, L. L. Long, R. J. Bell, S. E. Bell, R. R. Bell, R. W. Alexander, Jr., and C. A. Ward, "Optical properties of the metals Al, Co, Cu, Au, Fe, Pb, Ni, Pd, Pt, Ag, Ti, and W in the infrared and far infrared," Appl. Opt. **22**, 1099-1119 (1983).

[46] E. G. Acheson, "Carborundum: Its history, manufacture and uses," J. Franklin Inst. **136**, 194–203 (1893); *ibid* **136**, 279–289 (1893).

[47] N. G. Wright and A. B. Horsfall, "Silicon carbide: The return of an old friend," Mater. Matters **4**, 1–5, (2009).

[48] H. Moissan "Nouvelles recherches sur la météorité de Cañon Diablo". Comptes rendus **139**, 773–786 (1904).

[49] P. T. B. Shaffer, "A review of the structure of silicon carbide," Acta Crystallogr. Sect. B Struct. Crystallogr. Cryst. Chem. **25**, 477–488 (1969).

[50] D. Pandey and P. Krishna, "The origin of polytype structures," Prog. Cryst. growth Charact. **7**, 213–258 (1983).

[51] Y. Goldberg, M. Levinshtein, S. Rumyantsev, Silicon carbide (SiC), "Properties of Advanced Semiconductor Materials: GaN, AIN, InN, BN, SiC, SiGe," edited by M. Shur, M.Levinshtein, S. Rumyantsev (JohnWiley and Sons, New York, 2001), 93–147.

[52] `http://www.ioffe.ru/SVA/NSM/Semicond/SiC/` and references therein.

[53] W. Krenkel and F. Berndt, "C/C–SiC composites for space applications and advanced friction systems," Mater. Sci. Eng. A **412**, 177–181 (2005).

[54] W. Krenkel, B. Heidenreich, and R. Renz, "C/C-SiC Composites for Advanced Friction Systems," Adv. Eng. Mater. **4**, 427–436 (2002).

[55] S. Fan, L. Zhang, L. Cheng, J. Zhang, S. Yang, and H. Liu, "Wear mechanisms of the C/SiC brake materials," Tribol. Int. **44**, 25–28 (2011).

[56] D. O'Sullivan, M. J. Pomeroy, S. Hampshire, and M. J. Murtagh, "Degradation resistance of silicon carbide diesel particulate filters to diesel fuel ash deposits," J. Mater. Res. **19**, 2913–2921 (2004).

[57] H. J. Round, "A note on carborundum," Electri. World **49**, 309 (1907).

[58] O. V. Losev, "CII. Luminous carborundum detector and detection effect and oscillations with crystals," Philos. Mag. Ser. **76**, 1024–1044 (1928).

[59] D. H. C. Henry, "Wireless telegraph system (silicon carbide detector)," U.S. Patent **837**, 616 (1906).

[60] J. A. Cooper Jr and A. Agarwal, "SiC power-switching devices-the second electronics revolution?," Proc. IEEE **90**, 956–968 (2002).

[61] L. M. Porter and R. F. Davis, "A critical review of ohmic and rectifying contacts for silicon carbide," Mater. Sci. Eng. B **34**, 83–105 (1995).

[62] J. B. Casady and R. W. Johnson, "Status of silicon carbide (SiC) as a wide-bandgap semiconductor for high-temperature applications: a review," Solid. State. Electron. **39**, 1409–1422 (1996).

[63] J. Rabkowski, D. Peftitsis, and H.-P. Nee, "Silicon carbide power transistors: A new era in power electronics is initiated," Ind. Electron. Mag. IEEE **6**, 17–26 (2012).

[64] F. Nava, G. Bertuccio, A. Cavallini, and E. Vittone, "Silicon carbide and its use as a radiation detector material," Meas. Sci. Technol. **19**, 102001 (2008).

[65] F. H. Ruddy, A. R. Dulloo, J. G. Seidel, S. Seshadri, and L. B. Rowland, "Development of a silicon carbide radiation detector," Nucl. Sci. IEEE Trans. **45**, 536–541 (1998).

[66] T. J. Fawcett, J. T. Wolan, A. L. Spetz, M. Reyes, and S. E. Saddow, "Thermal detection mechanism of SiC based hydrogen resistive gas sensors," Appl. Phys. Lett. **89**, 182102 (2006).

[67] A. Vařko, "Influence of SiC additive on microstructure and mechanical properties of nodular cast iron," Mater. Sci. **14**, 311 (2008).

[68] K. Edalati, F. Akhlaghi, and M. Nili-Ahmadabadi, "Influence of SiC and FeSi addition on the characteristics of gray cast iron melts poured at different temperatures," J. Mater. Process. Technol. **160**, 183–187 (2005).

[69] T. Benecke, A. T. Ta, G. Kahr, W.-D. Schubert, and B. Lux, "Dissolution Behavior and Pre-Inoculating Effect of SiC in Molten Cast Iron," Giesserei **74**, 301–306 (1987).

[70] S. K. Singh, K. M. Parida, B. C. Mohanty, and S. B. Rao, "High surface area silicon carbide from rice husk: a support material for catalysts," React. Kinet. Catal. Lett. **54**, 29–34 (1995).

[71] M. Flinders, D. Ray, A. Anderson, and R. A. Cutler, "High-Toughness Silicon Carbide as Armor," J. Am. Ceram. Soc. **88**, 2217–2226 (2005).

[72] D. I. Godfrey-Smith, "Applicability of moissanite, a monocrystalline form of silicon carbide,to retrospective and forensic dosimetry," Radiat. Meas. **41**, 976–981 (2006).

[73] J. S. Johnson, K. D. Grobsky, and D. Bray, "Rapid fabrication of lightweight silicon-carbide mirrors," in International Symposium on Optical Science and Technology (International Society for Optics and Photonics, 2002), 243–253.

[74] N. Ebizuka, Y. Dai, H. Eto, W. Lin, T. Ebisuzaki, H. Omori, T. Handa, H. Takami, and Y. Takahashi, "Development of SiC ultra light mirror for large

space telescope and for extremely huge ground-based telescope," in Astronomical Telescopes and Instrumentation (International Society for Optics and Photonics, 2003), 329–334.

[75] M. A. Ealey and G. Q. Weaver, "Developmental history and trends for reaction-bonded silicon carbide mirrors," in SPIEs 1996 International Symposium on Optical Science, Engineering, and Instrumentation (International Society for Optics and Photonics, 1996), 66–72.

[76] J. S. Goela, M. A. Pickering, R. L. Taylor, B. W. Murray, and A. Lompado, "Properties of chemical-vapor-deposited silicon carbide for optics applications in severe environments," Appl. Opt. **30**, 3166–3175 (1991).

[77] J. Robichaud, J. Schwartz, D. Landry, W. Glenn, B. Rider, and M. Chung, "Recent advances in reaction bonded silicon carbide optics and optical systems," in Optics & Photonics 2005 (International Society for Optics and Photonics, 2005), p. 586802.

[78] C. E. Mueller, U. Papenburg, W. A. Goodman, and M. T. Jacoby, "C/SiC high-precision lightweight components for optomechanical applications," Proc. SPIE **4198**, 249–259 (2001).

[79] U. Papenburg, W. Pfrang, G. S. Kutter, C. Mueller, B. Kunkel, M. Deyerler, and S. Bauereisen, "Optical and optomechanical ultra-light weight C/SiC components," in Proc. of SPIE, **3782**, 141–156 (1999).

[80] W. F. Koehl, B. B. Buckley, F. J. Heremans, G. Calusine, and D. D. Awschalom, "Room temperature coherent control of defect spin qubits in silicon carbide," Nature **479**, 84–87 (2011).

[81] S. Castelletto, B. C. Johnson, V. Ivády, N. Stavrias, T. Umeda, A. Gali, and T. Ohshima, "A silicon carbide room-temperature single-photon source," Nat. Mater. **12**, 1–6 (2013).

[82] A. L. Falk, B. B. Buckley, G. Calusine, W. F. Koehl, V. V Dobrovitski, A. Politi, C. a Zorman, P. X.-L. Feng, and D. D. Awschalom, "Polytype control of spin qubits in silicon carbide," Nat. Commun. **4**, 1819 (2013).

[83] P. G. Baranov, A. P. Bundakova, A. a. Soltamova, S. B. Orlinskii, I. V. Borovykh, R. Zondervan, R. Verberk, and J. Schmidt, "Silicon vacancy in SiC as a promising quantum system for single-defect and single-photon spectroscopy," Phys. Rev. B **83**, 125203 (2011).

[84] F. Jelezko and J. Wrachtrup, "Single defect centres in diamond: A review," Phys. status solidi **203**, 3207-3225 (2006).

[85] A. P. Magyar, I. Aharonovich, M. Baram, and E. L. Hu, "Photoluminescent SiC tetrapods," Nano Lett. **13**, 1210 (2013).

[86] D. Beke, Z. Szekrènyes, D. Pàlfi, G. Ròna, I. Balogh, P. A. Maàk, G. Katona, Z. Czigàny, K. Kamars, B. Ràzsa, L. Buday, B. Vèrtessy, and A. Gali, "Silicon carbide quantum dots for bioimaging," J. Mater. Res. **28**, 205–209 (2013).

[87] J. Fan, H. Li, J. Jiang, L. K. Y. So, Y. W. Lam, and P. K. Chu, "3C-SiC nanocrystals as fluorescent biological labels," Small **4**, 1058–62 (2008).

[88] B.-S. Song, S. Yamada, T. Asano, and S. Noda, "Demonstration of two-dimensional photonic crystals based on silicon carbide," Opt. Express **19**, 11084 (2011).

[89] S. Yamada, B.-S. Song, T. Asano, and S. Noda, "Silicon carbide-based photonic crystal nanocavities for ultra-broadband operation from infrared to visible wavelengths," Appl. Phys. Lett. **99**, 201102 (2011).

[90] S. Yamada, B.-S. Song, S. Jeon, J. Upham, Y. Tanaka, T. Asano, and S. Noda, "Second-harmonic generation in a silicon-carbide-based photonic crystal nanocavity," Opt. Lett. **39**, 1768–1771 (2014).

[91] M. Radulaski, T. M. Babinec, S. Buckley, A. Rundquist, J. Provine, K. Alassaad, G. Ferro, and J. Vučković, "Photonic crystal cavities in cubic (3C) polytype silicon carbide films," Opt. Express **21**, 32623–32629 (2013).

[92] X. Lu, J. Y. Lee, P. X.-L. Feng, and Q. Lin, "Silicon carbide microdisk resonator," Opt. Lett. **38**, 1304 (2013).

[93] J. Faist, F. Capasso, D. L. Sivco, C. Sirtori, A. L. Hutchinson, and A. Y. Cho, "Quantum Cascade Laser," Science **264** , 553–556 (1994).

[94] Y. Bai, S. Slivken, S. Kuboya, S. R. Darvish, and M. Razeghi, "Quantum cascade lasers that emit more light than heat," Nat Phot. **4**, 99–102 (2010).

[95] P. Q. Liu, A. J. Hoffman, M. D. Escarra, K. J. Franz, J. B. Khurgin, Y. Dikmelik, X. Wang, J.-Y. Fan, and C. F. Gmachl, "Highly power-efficient quantum cascade lasers," Nat Phot. **4**, 95–98 (2010).

[96] D. Nakamura, I. Gunjishima, S. Yamaguchi, T. Ito, A. Okamoto, H. Kondo, S. Onda, and K. Takatori, "Ultrahigh-quality silicon carbide single crystals," Nature **430**, 1009–1012 (2004).

[97] G. Ferro, T. Chassagne, A. Leycuras, F. Cauwet, and Y. Monteil, "Strain Tailoring in 3C-SiC Heteroepitaxial Layers Grown on Si (100)," Chem. Vap. Depos. **12**, 483–488 (2006).

[98] L. Di Cioccio, Y. Le Tiec, F. Letertre, C. Jaussaud, and M. Bruel, "Silicon carbide on insulator formation using the Smart Cut process," Electron. Lett. **32**, 1144–1145 (1996).

[99] J.-H. Lee, I. Bargatin, J. Park, K. M. Milaninia, L. S. Theogarajan, R. Sinclair, and R. T. Howe, "Smart-cut layer transfer of single-crystal SiC using spin-on-glass," J. Vac. Sci. Technol. B **30**, 42001 (2012).

[100] G. N. Yushin, A. V. Kvit, R. Collazo, and Z. Sitar, "SiC to SiC wafer bonding," MRS Proceedings **742**, (2002).

[101] R. Hillenbrand, T. Taubner, and F. Keilmann, "Phonon-enhanced light-matter interaction at the nanometre scale," Nature **418**, 159–162 (2002).

[102] M. S. Anderson, "Enhanced infrared absorption with dielectric nanoparticles," Appl. Phys. Lett. **83**, 2964 (2003).

[103] T. Taubner, D. Korobkin, Y. Urzhumov, G. Shvets, and R. Hillenbrand, "Near-field microscopy through a SiC superlens," Science **313**, 1595 (2006).

[104] P. Li and T. Taubner, "Multi-wavelength superlensing with layered phonon-resonant dielectrics," Opt. Express **20**, 11787–11795 (2012).

[105] J. B. Pendry, "Negative refraction makes a perfect lens," Phys. Rev. Lett. **85**, 3966 (2000).

[106] Y. A. Urzhumov, D. Korobkin, B. Neuner III, C. Zorman, and G. Shvets, "Optical properties of sub-wavelength hole arrays in SiC membranes," J. Opt. A Pure Appl. Opt. **9**, S322–S333 (2007).

[107] F. Marquier, K. Joulain, and J. J. Greffet, "Resonant infrared transmission through SiC films," Opt. Lett. **29**, 2178–2180 (2004).

[108] J. A. Schuller, R. Zia, T. Taubner, and M. L. Brongersma, "Dielectric metamaterials based on electric and magnetic resonances of silicon carbide particles," Phys. Rev. Lett. **99**, 107401 (2007).

[109] M. Wheeler, J. Aitchison, J. Chen, G. Ozin, and M. Mojahedi, "Infrared magnetic response in a random silicon carbide micropowder," Phys. Rev. B **79**, 073103 (2009).

[110] X. Li, C. Yang, D. Jia, Z. Cao, Q. Mu, L. Hu, Z. Peng, Y. Liu, L. Yao, and L. Xuan, "Isotropic magnetic response of silicon carbide microspheres at mid-infrared wavelength," Opt. Laser Tech. **54**, 284–287 (2013).

[111] S. O. Brien and J. B. Pendry, "Photonic band-gap effects and magnetic activity in dielectric composites," J. Phys. Condens. Matter **14**, 40354044 (2012).

[112] M. Wheeler, J. Aitchison, and M. Mojahedi, "Three-dimensional array of dielectric spheres with an isotropic negative permeability at infrared frequencies," Phys. Rev. B **72**, 193103 (2005).

[113] J. D. Caldwell, O. J. Glembocki, Y. Francescato, N. Sharac, V. Giannini, F. J. Bezares, J. P. Long, C. Owrutsky, I. Vurgaftman, J. G. Tischler, V. D. Wheeler, N. D. Bassim, L. M. Shirey, R. Kasica, and S. A. Maier, "Low-Loss, Extreme Subdiffraction Photon Confinement via Silicon Carbide Localized Surface Phonon Polariton Resonators," Nano Lett. **13**, 3690-3697 (2013).

[114] D. Li, N. M. Lawandy, and R. Zia, "Surface phonon-polariton enhanced optical forces in silicon carbide nanostructures," Opt. Express **21**, 20900–20910 (2013).

[115] M. Ameen, A. Garcia-Etxarri, M. Schnell, R. Hillenbrand, and J. Aizpurua, "Infrared phononic nanoantennas: Localized surface phonon polaritons in SiC disks," Chine. Sci. Bull. **55**, 2625–2628 (2010).

[116] J. A. Schuller, T. Taubner, and M. L. Brongersma, "Optical antenna thermal emitters," Nat. Photonics **3**, 658–661 (2009).

[117] B. Neuner III, C. Wu, G. T. Eyck, M. Sinclair, I. Brener, and G. Shvets, "Efficient infrared thermal emitters based on low-albedo polaritonic meta-surfaces," Appl. Phys. Lett. **102**, 211111 (2013).

[118] E. Rephaeli, A. Raman, and S. Fan, "Ultrabroadband photonic structures to achieve high-performance daytime radiative cooling," Nano Lett. **13**, 1457-1461 (2013).

[119] A. Yariv and P. Yeh, *Optical Waves in Crystals: Propagation and Control of Laser Radiation* (Wiley-Interscience, Hoboken 1984).

[120] P. Yeh, *Optical waves in layered media* (Wiley-Interscience, Hoboken 2005).

[121] P. Yeh, A. Yariv, and C. S. Hong, "Electromagnetic propagation in periodic stratified media. I. General theory*," J. Opt. Soc. Am. **67**, 423-438 (1977).

[122] A. Yariv and P. Yeh, "Electromagnetic propagation in periodic stratified media. II. Birefringence, phase matching, and x-ray lasers," J. Opt. Soc. Am. **67**, 438-447 (1977).

[123] P. St. J. Russell, T. A. Birks, and F.DominicLloyd-Lucas, in Confined Electrons and Photons, New Physics and Applications, Vol. **340** of NATO Advanced Studies Institute, Series B: Physics, edited by E. Burstein and C. Weisbuch (Plenum, New York, 1995), p. 585.

[124] S. Foteinopoulou and C. M. Soukoulis, "Negative refraction and left-handed behavior in two-dimensional photonic crystals," Phys. Rev. B **67**, 235107 (2003).

[125] S. Foteinopoulou, M. Kafesaki, E. N. Economou, and C. M. Soukoulis,"Backward surface waves at photonic crystals," Phys. Rev. B **75**, 245116 (2007).

[126] A. Taflove, "Application of the finite-difference time-domain method to sinusoidal steady state electromagnetic penetration problems," IEEE Trans. Electroma. Compatibility **22**, 191202 (1980).

[127] A. Taflove, *Computational ElectrodynamicsThe Finite Difference Time-Domain Method* (Artech House, Boston, 1995).

[128] Lumerical Solutions, Inc. `http://www.lumerical.com/tcad-products/fdtd/`

2

Background concepts, principles and methods

2.1 Electromagnetic (EM) properties of natural materials

2.1.1 EM wave propagation and extinction in natural materials: dielectrics vs. polar materials

The crucial material parameters that determine the electromagnetic wave propagation in most materials are the relative permittivity, ε_r, and the relative permeability, μ_r. The relative permittivity relates the electric field $\mathbf{E}$ with the electrical displacement vector, $\mathbf{D}$. Conversely, the relative permeability, μ_r relates the magnetic field strength $\mathbf{H}$ with the magnetic field $\mathbf{B}$. In simple systems, these relations are given by the following constitutive equations [1] [1]:

$$\mathbf{D} = \varepsilon_0 \varepsilon_r \mathbf{E}, \tag{2.1}$$

where

$$\mathbf{D} = \varepsilon_0 \mathbf{E} + \mathbf{P}, \tag{2.2}$$

[1] Throughout the thesis for representation of all EM wave equations S.I units are used.

and

$$\mathbf{H} = \frac{\mathbf{B}}{\mu_0 \mu_r}. \tag{2.3}$$

In Eq. 2.2, $\mathbf{P}$ denotes the electric polarization of the material. Throughout the thesis we will deal only with non-magnetic media, thus from now on we consider $\mu_r = 1$. Also, we will deal only with isotropic linear materials, where the above constitutive relations are valid. However, in general the constitutive relations can take more complex form for anisotropic materials [2–6], non-linear [7, 8] and chiral materials [9–13]. If Eq. 2.1 and 2.3 are valid, and we assume that an EM wave with an angular frequency ω is propagating inside the material, then the electric and magnetic fields $\mathbf{E}$, and $\mathbf{H}$ at any time, t and position, $\mathbf{r}$ inside that material can be expressed through the following expressions [1]:

$$\mathbf{E}(\mathbf{r}, t) = \mathbf{E}_0 e^{i(\mathbf{k}\cdot\mathbf{r} - \omega t)}, \tag{2.4}$$

and

$$\mathbf{H}(\mathbf{r}, t) = \mathbf{H}_0 e^{i(\mathbf{k}\cdot\mathbf{r} - \omega t)}, \tag{2.5}$$

where $\mathbf{E_0}$ and $\mathbf{H_0}$ represent the electric and magnetic field amplitudes. In Eq. 2.4 and Eq. 2.5, $\mathbf{k}$ represents the wavevector inside the material, with its magnitude, k given by [1]:

$$k = |\mathbf{k}| = \sqrt{\varepsilon_r}\frac{\omega}{c} = \sqrt{\varepsilon_r}\frac{2\pi}{\lambda_{free}} = \frac{2\pi}{\lambda_m} \qquad \text{where} \qquad \lambda_m = \frac{\lambda_{free}}{\sqrt{\varepsilon_r}}. \tag{2.6}$$

In Eq. 2.6, c designates the speed of light in vacuum, λ_{free} represents the wavelength of the EM wave in free space and λ_m represents the wavelength of the EM wave in the material. The wavevector determines the phase of the EM wave propagation inside the material.

Lossless dielectrics would have a real and positive relative permittivity, ε_r. There are materials with a negative real part for the relative permittivity, ε_r, such as metals [14–39], but the permittivity is complex in such case. At this stage, for simplicity lets ignore the imaginary part in the permittivity in metals, in order to make a brief comparison of the dramatic difference in wave behaviour inside a material with a positive permittivity and a material with a negative permittivity. In particular, in Fig. 2.1, we qualitatively illustrate the consequences of the sign of the permittivity on the EM wave propagation inside a material. We assume an EM wave is incident normally on the material slab (the yellow shaded regime in Fig. 2.1) from free space (at the left side of the material slab in Fig. 2.1). In particular, in Fig. 2.1(a) [2.1(b)], we show the real part of the electric field amplitude of an EM wave for the case

of a material slab with positive (negative) permittivity. As expected the EM wave continues to propagate inside the dielectric ($\varepsilon_r > 0$), but its wavelength inside the material, λ_m is shortened, as predicted by Eq. 2.6, implying that the dielectric is an optically denser medium in comparison to vacuum.

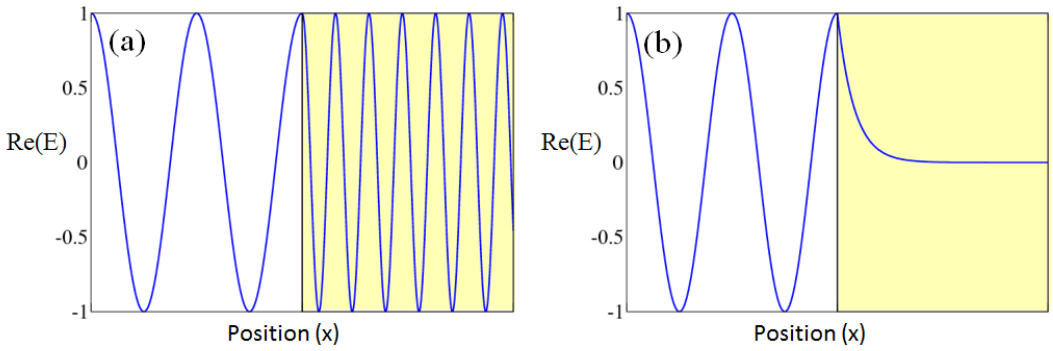

Figure 2.1: (a) Real part of the electric field amplitude of an EM wave incident normally on a material slab with a positive permittivity. (b) same as in (a), but in a material with a negative permittivity.

However for the case of the metal depicted in Fig. 2.1(b), we observe that the field is not propagating, but it is rapidly decaying inside. This is because, for negative values of the relative permittivity, the magnitude of the wavevector, k in Eq. 2.6 will become imaginary for the ideal but fictitious case of a purely real and negative permittivity, yielding the exponential decay.

Now realistic materials, even dielectrics in certain frequency regions, but most certainly metals and polaritonic materials, which will be the subject matter of this thesis, have complex permittivity values. i.e:

$$\varepsilon_r(\omega) = \varepsilon_r'(\omega) + i\varepsilon_r''(\omega), \tag{2.7}$$

where $\varepsilon_r'(\omega)$ and $\varepsilon_r''(\omega)$ are the real and imaginary parts of the complex permittivity. For example, metals have a complex permittivity in the optical regime with a negative real part, $\varepsilon_r'(\omega)$, and a positive imaginary part, $\varepsilon_r''(\omega)$ [14–39]. As a result, EM waves in such materials will be attenuated similar to what we have seen in the idealised case of Fig. 2.1(b). This phenomenon can be exploited to drive collective oscillation of electrons at the surface of metals [14–39], which in turn can lead to huge electric field enhancement in structures with subwavelength geometry [14–16, 34, 35, 40]. This has led to many revolutionary applications in the optical regime such as photovoltaics [17, 18], EM superabsorbers [19–21], chemical sensors [23–26], high resolution microscopy [27–30], imaging applications [31–33]

and nanoscale optical circuit elements [34–38]. However, these plasmon-based phenomena in metals are not transferable to the Mid-IR/THz regime, because of the small metal skin depth in this spectral region, that limits the interaction between the incoming field and the plasmon oscillations [41–43].

There is another class of materials known as polaritonic media that also have a negative permittivity within a particular spectral regime, which is also referred to as Reststrahlen-band regime, which can fall in the IR/THz spectrum. Therefore, the interesting applications that are possible with the metals in the visible regime can be extended to the THz/Mid-IR regime with these polaritonic media [44]. This is especially important since there is no abundance of materials for EM wave control in the THz/Mid-IR spectrum. The possibility to use such phonon-polariton excitations to control the EM waves has opened up the exciting new field of polaritonics [4, 44–50].

The electrons in the metals are free, but in polaritonic media the electrons are bound to the nucleus of atoms. When an EM wave is incident on such material, these bound electrons behave as damped harmonic oscillators. The Newton's equation of motion of such electrons can be expressed as [5, 51, 52]:

$$m\frac{\partial^2 \mathbf{x}}{\partial t^2} + m\Gamma\frac{\partial \mathbf{x}}{\partial t} + k_e\mathbf{x} = -e\mathbf{E_0}e^{-i\omega t}, \tag{2.8}$$

where m and $-e$ designate the mass and charge of an electron, $\mathbf{x}$ denotes the displacement vector of the electron, Γ denotes the intrinsic damping parameter and $k_e = m{\omega_0}^2$ denotes the restoring force constant. Here, ω_0 designates the natural frequency of the oscillator. In the above equation, the first term, i.e. $m\frac{\partial^2 \mathbf{x}}{\partial t^2}$ represents the total force experienced by the bound electron, the second term, i.e. $m\Gamma\frac{\partial \mathbf{x}}{\partial t}$ represents the damping force, the third term $k_e\mathbf{x}$ represents the restoring force from the ion core, and $q\mathbf{E_0}e^{-i\omega t}$ represents the driving force due to the electric field of the incident EM wave. The damping in the oscillations results from the scattering at crystal defects [53].

The solution for the above differential equation can be obtained as [51]:

$$x(t) = x_e e^{-i\omega t}, \qquad \text{where} \qquad x_e = \frac{-e}{m}\frac{1}{(\omega_0^2 - \omega^2 - i\omega\Gamma)}E_0. \tag{2.9}$$

The dipole moment of the individual electron will be $p = -ex$ [1, 5]. The magnitude of the electric polarization, P of a material is defined as the dipole moment per unit volume [1], i.e.

$$P(\omega) = n_e p = -n_e e x, \tag{2.10}$$

where n_e is the number of electrons per unit volume. With the use of Eq. 2.9, the above equation yields for the electric polarization, P:

$$P(\omega) = \frac{n_e e^2 E_0}{m} \frac{e^{-i\omega t}}{(\omega_0^2 - \omega^2 - i\omega\Gamma)}. \tag{2.11}$$

Thus by using Eq. 2.1, we obtain for the relative permittivity of the polaritonic material, $\varepsilon_r(\omega)$:

$$\varepsilon_r(\omega) = \frac{D}{E} = 1 + \frac{P}{\varepsilon_0 E} = 1 + \frac{n_e e^2 E_0}{m} \frac{e^{-i\omega t}}{(\omega_0^2 - \omega^2 - i\omega\Gamma)} = 1 + \frac{\omega_p^2}{\omega_0^2 - \omega^2 - i\omega\Gamma}, \tag{2.12}$$

where $\omega_p = \dfrac{n_e e^2}{m\varepsilon_0}$. In a more realistic picture the contribution of the ion cores in the polarizability should be included [51], which implies:

$$\varepsilon_r(\omega) = \varepsilon_\infty + \frac{\omega_p^2}{\omega_0^2 - \omega^2 - i\omega\Gamma}, \tag{2.13}$$

where ε_∞ is the relative permittivity response of the material at high frequencies. In Eq. 2.13, in the absence of the electronic contributions of the ion cores to the polarizability, ε_∞ becomes one as was the case of Eq. 2.12. In the above equation, the frequency at which $\varepsilon_r(\omega)$ becomes zero (in the absence of absorption, $\Gamma = 0$) is referred to as the longitudinal optical phonon frequency, ω_L i.e. $\varepsilon_r(\omega_L) = 0$, where $\Gamma = 0$ [51, 54–57]. Similarly, the frequency at which $\varepsilon_r(\omega)$ becomes ∞ (in the absence of absorption, $\Gamma = 0$) is referred to as the transverse optical phonon frequency, ω_T i.e. $\varepsilon_r(\omega_T) = \infty$, at $\Gamma = 0$ [51, 54–57]. Therefore, by using the ω_L and ω_T frequency values, we obtain:

$$\varepsilon_r(\omega) = \varepsilon_\infty \left(1 + \frac{\omega_L^2 - \omega_T^2}{\omega_T^2 - \omega^2 - i\omega\Gamma}\right). \tag{2.14}$$

We can identify that the above equation has the Lorentzian functional form. Moreover, the above equation essentially represents the phonon-polariton dispersion that emanates from the coupling of the transverse optical phonon with the incident transverse EM waves [51]. Note that although the frequency of the longitudinal optical phonon, ω_L, appears in Eq. 2.14, there is no physical origin [51] for its appearance other than designating the zero crossing of the permittivity as discussed above. Note that longitudinal optical phonons do not couple to the EM field. This is because EM waves are transverse in free space and thus do not couple with the longitudinal phonon modes [51].

From Eq. 2.14, we can obtain the real and imaginary parts of $\varepsilon_r(\omega)$ as:

$$\varepsilon_r'(\omega) = \varepsilon_\infty \left(1 + \frac{({\omega_L}^2 - \omega_T^2)(\omega_T^2 - \omega^2)}{(\omega_T^2 - \omega^2)^2 + (\omega\Gamma)^2}\right), \tag{2.15}$$

and

$$\varepsilon_r''(\omega) = \varepsilon_\infty \left(\frac{({\omega_L}^2 - \omega_T^2)\omega\Gamma}{(\omega_T^2 - \omega^2)^2 + (\omega\Gamma)^2}\right). \tag{2.16}$$

We can observe from Eq. 2.15, that $\varepsilon_r'(\omega)$ becomes negative in the frequency regime between ω_T and ω_L. Therefore, the propagation of light is prohibited in this region, implying a very high reflection from these polar materials. This frequency regime between ω_T and ω_L is referred to as phonon-polaritonic gap [57] or Reststrahlen-band [58, 59]. Most of the semiconductors and ionic crystals have their Reststrahlen-band in the THz/Mid-IR region [4, 51, 59].

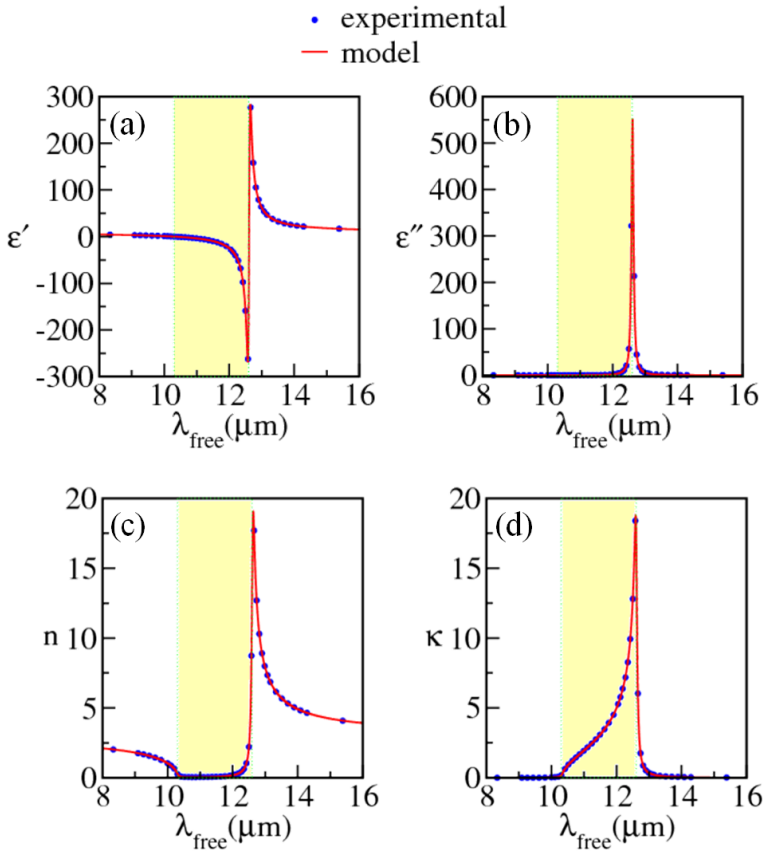

Figure 2.2: (a) and (b): The spectral response of the real and imaginary parts of the permittivity of SiC. (c) and (d): The spectral response of the real and imaginary parts of the refractive index of SiC. The blue circles represent the experimental optical data of Palik [60], while the red lines represent the modelled data from Eqs. 2.15, 2.16, 2.19a(a) and 2.19a(b) with use of the fitting parameters from Ref. [49]. The shaded region in each panel indicates the phonon-polariton gap of SiC.

In this thesis, we will explore the perfect absorption and extraordinary deflection

of light using SiC. We have particularly chosen SiC because the Reststrahlen band of the SiC is around 10 μm, where many pathogens and bio-molecules have their fingerprints [61–63]. Moreover this frequency regime is also an important atmospheric transparency window [64–66]. We model the permittivity response of SiC with Eq. 2.15 by using the parameters ε_∞=6.7, ω_T =2π×23.79 THz, ω_L =2π×29.07 THz and Γ =2π×0.1428 THz, which we have taken from Ref. [49]. In Fig. 2.2(a) and (b), we plot the spectral response of the real and imaginary parts of the permittivities, ε_r' and ε_r'' respectively, of the Lorentzian model with red lines and the experimental optical Palik data [60, 67] with blue circles. We can observe an excellent agreement between the model and the experimental data. We notice from Fig. 2.2 that the Reststrahlen band of SiC spans from 10.3 μm to 12.6 μm, which we highlighted with the yellow shading.

Now, the refractive index of the material is the square root of its relative permittivity:

$$n + i\,\kappa = \sqrt{\varepsilon_r' + i\,\varepsilon_r''}, \tag{2.17}$$

where n and κ represent the real and imaginary parts of the refractive index respectively. The imaginary part of the refractive index, κ is known as the extinction coefficient of the material. From Eq. 2.17, we have that:

$$\varepsilon_r' = n^2 - \kappa^2, \tag{2.18a}$$

$$\varepsilon_r'' = 2n\kappa. \tag{2.18b}$$

That implies [68]:

$$n = \sqrt{\frac{\sqrt{\varepsilon_r'^2 + \varepsilon_r''^2} + \varepsilon_r'}{2}}, \tag{2.19a}$$

$$\kappa = \sqrt{\frac{\sqrt{\varepsilon_r'^2 + \varepsilon_r''^2} - \varepsilon_r'}{2}}. \tag{2.19b}$$

In Fig. 2.2 (c) and (d), we show the real and imaginary parts for the refractive index, n and κ of SiC. Note for complex-refractive-index-materials, the wavevector will also become complex as:

$$k = |\mathbf{k}| = \sqrt{\varepsilon_r}\frac{\omega}{c} = (n + i\,\kappa)\frac{\omega}{c}. \tag{2.20}$$

From the above equation for the wavevector, k, and Eq. 2.4, it becomes evident that the wave decays inside materials with a complex permittivity. In metals and polar materials or more general materials with complex permittivity [4, 14–39, 45–50], where fields decay inside the material, it is useful to have a measure of the

penetration depth of the EM fields. For this purpose, the skin depth, δ, is introduced to represent such measure of the field penetration depth. It is defined as the distance inside the material where the amplitude of the EM field decays by a factor of $1/e$ from the surface [1]. That means:

$$\frac{|E_0|}{e} = |E_0 e^{ik\delta}| = |E_0 e^{i(n+i\kappa)\frac{\omega}{c}\delta}| = |E_0 e^{in\delta\frac{\omega}{c}} e^{-\frac{\omega}{c}\kappa\delta}| = |E_0| e^{-\frac{\omega}{c}\kappa\delta}. \tag{2.21}$$

That implies:

$$\frac{1}{e} = e^{-\frac{\omega}{c}\kappa\delta}. \tag{2.22}$$

From the above equation, we obtain the expression for the skin depth, δ as:

$$\delta = c/\omega\kappa. \tag{2.23}$$

in terms of the EM wave frequency, ω and material extinction coefficient, κ. From the above equation, it is obvious that fields will be quickly attenuated inside materials that have a large extinction coefficient, κ.

2.1.2 Poynting vector

The EM waves carry energy while they propagate through materials or free space. The Poynting vector, $\mathbf{S}$ represents the directional flow of this EM energy, which is given by [1, 69]:

$$\mathbf{S} = \mathbf{E}^{\mathbf{R}} \times \mathbf{H}^{\mathbf{R}}. \tag{2.24}$$

Note that in the above equation, the superscript R designates that the real valued fields are used. The time averaged Poynting vector $\overline{\mathbf{S}}$ is given by:

$$\overline{\mathbf{S}} = \frac{1}{2}\mathrm{Re}(\mathbf{E} \times \mathbf{H}^*). \tag{2.25}$$

Now, if we consider a TE-polarized EM wave propagating inside a material along the x-direction, then with the use of Eqs. 2.4 and 2.6, we can obtain the electric and magnetic fields inside the material as:

$$\mathbf{E} = E_y(x,t)\hat{\mathbf{y}} = E_0 e^{i(k_x x - \omega t)}\hat{\mathbf{y}}, \tag{2.26}$$

and

$$\mathbf{H} = H_z(x,t)\hat{\mathbf{z}} = H_0 e^{i(kx - \omega t)}\hat{\mathbf{z}}, \tag{2.27}$$

where E_y represents the y-component of the electric field, H_z represents the z component of the magnetic field, and k_x represents the x-component of the wavevector inside the material. From Maxwell's equations in a non-magnetic medium, we get:

$$H_z(x,t) = \frac{k_x}{\omega\mu_0} E_0 e^{i(k_x x - \omega t)}. \tag{2.28}$$

With the use of Eqs. 2.26 and 2.28, Eq. 2.25 yields the time-averaged Poynting's vector along the propagation direction:

$$\overline{S_x} = \frac{|E_0|^2}{2\omega\mu_0} \mathrm{Re}(k_x^*). \tag{2.29}$$

The above equation determines the energy carried by the EM waves inside the material along the propagation direction, i.e. the x-direction. From Eq. 2.29, we can infer that purely evanescent waves, which have a purely imaginary part of the wavevector, carry absolutely no energy, while highly lossy waves would carry some energy.

2.1.3 Poynting's Theorem

By using the divergence theorem [1], we can express Eq. 2.24 as:

$$\oint_A (\mathbf{S}\cdot\mathbf{n})\, dA = \int_V \left(\nabla\cdot(\mathbf{E^R}\times\mathbf{H^R})\right)\, dV, \tag{2.30}$$

where A is a closed surface surrounding the volume V. That implies:

$$\oint_A (\mathbf{S}\cdot\mathbf{n})\, dA = \int_V \left(\nabla\times\mathbf{E^R}\cdot\mathbf{H^R} - \nabla\times\mathbf{H^R}\cdot\mathbf{E^R}\right)\, dV. \tag{2.31}$$

With the use of Maxwell's equations, the above equation yields:

$$\oint_A (\mathbf{S}\cdot\mathbf{n})\, dA = \int_V \left(-\frac{\partial\mathbf{B^R}}{\partial t}\cdot\mathbf{H^R} - (\mathbf{J_f^R} + \frac{\partial\mathbf{D^R}}{\partial t})\cdot\mathbf{E^R}\right)\, dV, \tag{2.32}$$

where $\mathbf{J_f}$ is the current density due to the free electrons in the medium. With the use of constitutive relation Eq. 2.2, Eq. 2.32 can be written as:

$$\oint_A (\mathbf{S}\cdot\mathbf{n})\, dA = -\int_V \left(\frac{\partial\mathbf{B^R}}{\partial t}\cdot\mathbf{H^R}\right)\, dV - \varepsilon_0\int_V \left(\frac{\partial\mathbf{E^R}}{\partial t}\right)\cdot\mathbf{E^R}\, dV - \int_V \left(\frac{\partial\mathbf{P^R}}{\partial t}\right)\cdot\mathbf{E^R}\, dV - \int_V \left(\mathbf{J_f^R}\cdot\mathbf{E^R}\right)\, dV. \tag{2.33}$$

In the above equation, the left-hand side expression represents the energy flow through the surrounding surface, A. On the right-hand-side expression, terms that can be expressed as a perfect time-differential represent the rate of decrease of the energy stored within the volume, V and the rest of the terms represent the rate of energy loss due to dissipation within the volume, V [52]. The above equation is referred to as Poynting's theorem, which is essentially a statement of conservation

of energy [1, 5, 52, 70].

As we mentioned before, one of the main objectives of this thesis is to evaluate the absorptance of the microstructures constructed from polaritonic media. Therefore, evaluating the energy dissipation rate from the above Poynting's theorem for the particular case of polaritonic material will allow us to calculate where exactly the light gets absorbed within these media. This is key information for designing our proposed superabsorbing structures in Chapters 4, 5, 6 and 7. Therefore, in the following we proceed in expressing Poynting's theorem for the particular case of phonon-polaritonic media.

2.1.4 Poynting's Theorem for polaritonic media

In the case of polaritonic media, $\mathbf{J_f} = 0$ since there are no free electrons. Therefore, Eq. 2.33 will become:

$$\oint_A (\mathbf{S}\cdot\mathbf{n})\, dA = -\int_V \left(\frac{\partial \mathbf{B^R}}{\partial t}\cdot \mathbf{H^R}\right) dV - \varepsilon_0 \int_V \left(\frac{\partial \mathbf{E^R}}{\partial t}\right)\cdot \mathbf{E^R}\, dV - \int_V \left(\frac{\partial \mathbf{P^R}}{\partial t}\right)\cdot \mathbf{E^R}\, dV. \tag{2.34}$$

In the following, we will derive an expression for $\left(\frac{\partial \mathbf{P^R}}{\partial t}\right)\cdot \mathbf{E^R}$ in Eq. 2.34 that will be appropriate for the polaritonic materials. From Eqs. 2.8 and 2.11, we can write [70]:

$$\frac{m}{n_e e}\frac{\partial^2 \mathbf{P^R}}{\partial t^2} + \frac{m\Gamma}{n_e e}\frac{\partial \mathbf{P^R}}{\partial t} + \frac{m\omega_0^2}{n_e e}\mathbf{P^R} = e\mathbf{E}. \tag{2.35}$$

With the use of $\omega_p = \dfrac{n_e e^2}{m\varepsilon_0}$, Eq. 2.35 can be simplified as:

$$\frac{\partial^2 \mathbf{P^R}}{\partial t^2} + \Gamma\frac{\partial \mathbf{P^R}}{\partial t} + \omega_0^2 \mathbf{P^R} = \varepsilon_0 \omega_p^2 \mathbf{E^R}, \tag{2.36}$$

By multiplying $\left(\frac{\partial \mathbf{P^R}}{\partial t}\right)$ on each hand side of Eq. 2.36, we obtain:

$$\frac{\partial \mathbf{P^R}}{\partial t}\cdot \mathbf{E^R} = \frac{1}{\varepsilon_0\omega_p^2}\frac{\partial \mathbf{P^R}}{\partial t}\cdot\left(\frac{\partial^2 \mathbf{P^R}}{\partial t^2} + \Gamma\frac{\partial \mathbf{P^R}}{\partial t} + \omega_0^2\mathbf{P^R}\right). \tag{2.37}$$

$$\implies \frac{\partial \mathbf{P^R}}{\partial t}\cdot \mathbf{E^R} = \frac{1}{2\varepsilon_0\omega_p^2}\frac{\partial}{\partial t}\left[\left(\frac{\partial P^R}{\partial t}\right)^2 + \omega_0^2 (P^R)^2\right] + \frac{\Gamma}{\varepsilon_0\omega_p^2}\left(\frac{\partial P^R}{\partial t}\right)^2. \tag{2.38}$$

With the use of Eq. 2.38, Eq. 2.34 yields:

$$\oint_A (\mathbf{S}\cdot\mathbf{n})\,dA = -\int_V \left(\frac{\partial \mathbf{B^R}}{\partial t}\cdot\mathbf{H^R}\right)\,dV - \varepsilon_0\int_V \left(\frac{\partial \mathbf{E^R}}{\partial t}\right)\cdot\mathbf{E^R}\,dV$$
$$-\frac{1}{2\varepsilon_0\omega_p^2}\int_V \frac{\partial}{\partial t}\left[\left(\frac{\partial P^R}{\partial t}\right)^2 + \omega_0^2 (P^R)^2\right]\,dV - \frac{\Gamma}{\varepsilon_0\omega_p^2}\int_V \left(\frac{\partial P^R}{\partial t}\right)^2 dV. \quad (2.39)$$

Using the assumption of non-magnetic medium, which is our case, we obtain:

$$\oint_A (\mathbf{S}\cdot\mathbf{n})dA = -\frac{\mu_0}{2}\int_V \left(\frac{\partial (H^R)^2}{\partial t}\right)dV - \frac{\varepsilon_0}{2}\int_V \left(\frac{\partial (E^R)^2}{\partial t}\right)dV$$
$$-\frac{1}{2\varepsilon_0\omega_p^2}\int_V \frac{\partial}{\partial t}\left[\left(\frac{\partial P^R}{\partial t}\right)^2 + \omega_0^2 (P^R)^2\right]\,dV - \frac{\Gamma}{\varepsilon_0\omega_p^2}\int_V \left(\frac{\partial P^R}{\partial t}\right)^2 dV. \quad (2.40)$$

The above equation is a representation of Poynting's theorem for the particular case of the polaritonic medium. Since in Eq. 2.40, $\mathbf{S}$ represents the Poynting vector, the left-hand-side integral represents the EM energy flow through the surface A. Now this energy flow will cause a change in the stored energy within the volume enclosed by that surface A. However to account for that energy change, we should also consider the decrease of the EM energy stored within the volume V, that is caused by dissipation and would be converted to some other form of energy, such as heat for the case of polaritonic media. In order to be able to better identify the contribution of each term, we rearrange some terms and also express in the form of a perfect differential with respect to time the terms for which this is possible. After doing this, we get:

$$\oint_A (\mathbf{S}\cdot\mathbf{n})\,dA + \frac{\Gamma}{\varepsilon_0\omega_p^2}\int_V \left(\frac{\partial P^R}{\partial t}\right)^2 dV =$$
$$-\frac{\partial}{\partial t}\int_V \left\{\frac{\varepsilon_0}{2}(E^R)^2 + \frac{\mu_0}{2}(H^R)^2 + \frac{1}{2\varepsilon_0\omega_p^2}\left[\left(\frac{\partial P^R}{\partial t}\right)^2 + \omega_0^2 (P^R)^2\right]\right\}\,dV. \quad (2.41)$$

Notice that in the above equation, the term on the right-hand side is a perfect time-differential, therefore it represents the rate of decrease of the energy stored within the volume, V of the material [52]. As we explained above, this decrease of energy can only be caused by energy escaping through surface A (given by the first term in the left-hand side) and the dissipation due to the damping mechanism [52]. Therefore the second term in the left-hand side represents the energy dissipated due to the damping mechanism.

2.1.5 Power dissipation in a polaritonic material slab

Now we proceed in relating the rate of energy dissipation per volume, i.e. power dissipation per volume, with the intrinsic material parameters of the polaritonic material. From Eq. 2.41, we can express the power dissipation per volume, $P_{loss,\mathrm{v}}$ as:

$$P_{loss,\mathrm{v}} = \frac{\Gamma}{\varepsilon_0 \omega_p^2} \left(\frac{\partial P^R}{\partial t} \right)^2 . \tag{2.42}$$

Since, in the above equation P^R is the real valued electric polarization, it will be $P^R = P_0 \cos(\omega t)$. Therefore, Eq. 2.42 yields:

$$P_{loss,\mathrm{v}} = \frac{\Gamma}{\varepsilon_0 \omega_p^2} \left(\omega P_0 \sin(\omega t) \right)^2 . \tag{2.43}$$

By using the time averaged real electric polarization $\overline{(P^R)^2} = \frac{1}{2} P P^*$ [52], the time-averaged power dissipation, $\overline{P_{loss,\mathrm{v}}}$ can be obtained as:

$$\overline{P_{loss,\mathrm{v}}} = \frac{\Gamma \omega^2}{\varepsilon_0 \omega_p^2} P_0^2 \overline{\sin^2(\omega t)} = \frac{\Gamma \omega^2}{2\varepsilon_0 \omega_p^2} P_0^2 = \frac{\Gamma \omega^2}{2\varepsilon_0 \omega_p^2} |P|^2, \tag{2.44}$$

since ${P_0}^2 = P P^*$. Now with the use of Eq. 2.11, Eq. 2.44 yields:

$$\overline{P_{loss,\mathrm{v}}} = \frac{\Gamma \omega^2 \varepsilon_0 \omega_p^2}{2((\omega_T^2 - \omega^2)^2 + (\omega\Gamma)^2)} |E|^2. \tag{2.45}$$

Finally, from Eqs. 2.16 and 2.45, we can obtain the expression for $\overline{P_{loss,\mathrm{v}}}$ as:

$$\overline{P_{loss,\mathrm{v}}} = \frac{\omega \varepsilon_0 \varepsilon_r''}{2} |E|^2. \tag{2.46}$$

From the above equation, it is obvious that materials with larger ε_r'' imply a large EM power dissipation, provided that the light enters inside them.

In this thesis, most of the cases we study are 1D-PCs. In such cases, we will require to calculate how much power is absorbed within the slabs of the 1D-PCs. Therefore, we consider a slab of a material, with thickness, d in the x direction, and infinitely extending in y-and z-directions (see the schematics in Fig. 2.3). However, the same principles would apply for more complicated geometries such as micropyramid structures that we present in Appendix B.The EM power dissipation within a volume Ad of such material can be obtained from Eq. 2.46 as:

$$\overline{P_{loss}} = \frac{A \omega \varepsilon_0 \varepsilon_r''}{2} \int_0^d |E(x)|^2 \, dx, \tag{2.47}$$

where A represents the area on the face of the slab in the yz plane and d represents

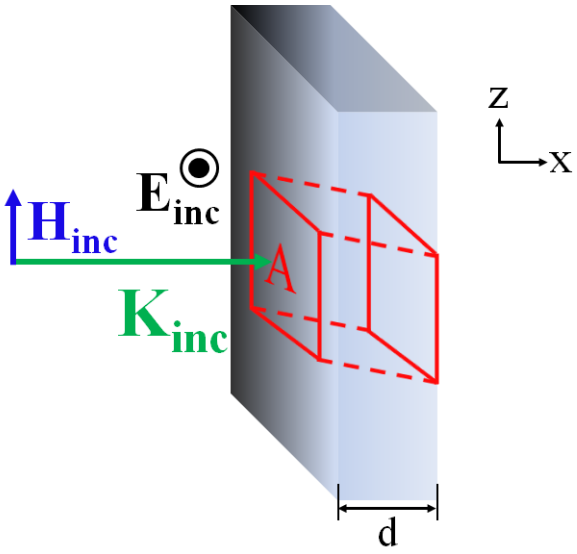

Figure 2.3: Schematic diagram to illustrate the power dissipation of an EM wave within a volume equal to Ad of a material slab. Here A represents the selected area (red-line rectangle) on the face of the material slab and d indicates the thickness of the material slab. The wavevector, $\mathbf{k_{inc}}$, electric field, $\mathbf{E_{inc}}$ and the magnetic field, $\mathbf{H_{inc}}$ of the incident EM wave are also indicated.

the thickness of the material slab, along the x axis. Furthermore, in Chapters, 4, 5, 6 and 7, we will require the ratio of dissipated to incident power, P_{ratio} within the absorbing material slabs, which is defined as:

$$\overline{P_{ratio}} = \frac{\overline{P_{loss}}}{\overline{P_{inc}}}, \tag{2.48}$$

where $\overline{P_{inc}}$ is the time-averaged power of the incident EM wave. Note:

$$P_{inc} = |\mathbf{S}_{inc}|A = |\mathbf{E^R_{inc}} \times \mathbf{H^R_{inc}}| = \left|\mathbf{E^R_{inc}} \times \frac{(\mathbf{k_{inc}} \times \mathbf{E^R_{inc}})}{\omega\mu_0}\right|, \tag{2.49}$$

where $\mathbf{E^R_{inc}}$, $\mathbf{H^R_{inc}}$ and $\mathbf{k_{inc}}$ denote the electric field, magnetic field and wavevector of the incident EM wave (see the schematics in Fig. 2.3).
That implies:

$$P_{inc} = \frac{A}{\omega\mu_0}\left(k_{inc}E^{R\ 2}_{inc}\right). \tag{2.50}$$

From the above equation, the time-averaged incident power, $\overline{P_{inc}}$ can be obtained as:

$$\overline{P_{inc}} = \frac{A}{2c\mu_0}|E_{inc}|^2. \tag{2.51}$$

From Eqs. 2.47, 2.48 and 2.51, we can obtain $\overline{P_{ratio}}$ as:

$$\overline{P_{ratio}} = \frac{\omega\varepsilon_r''}{c|E_{inc}|^2}\int_0^d |E(x)|^2\,dx = \frac{\omega\varepsilon_r''}{c}\int_0^d |E_{enha}(x)|^2\,dx, \tag{2.52}$$

where $E_{enha}(x) = \dfrac{E(x)}{E_{inc}}$ represents the enhanced electric field. We use Eq. 2.52 in Chapters 4, 5, 6 to calculate the power dissipation in a particular slab within the 1D-PCs.

2.1.6 Energy density expression for phonon-polaritonic material

The EM energy density, U is a measure of the energy stored in the electric and magnetic fields. In normal dielectrics, the time-averaged EM wave energy density is defined as:

$$\overline{U} = \frac{1}{4}\left(\varepsilon_r\varepsilon_0|E|^2 + \mu_0|H|^2\right). \tag{2.53}$$

However, for highly dispersive materials such as polaritonic media, the above expression for energy density is not applicable. This is because, in the Reststrahlen band of polaritonic media, ε_r is negative. Thus according to Eq. 2.53, polaritonic media would have a negative energy density, which is unphysical. We note for the interested reader, the above expression for the energy density is also inappropriate for metals, since they also have a negative permittivity. We will not discuss the energy density of metals further as these materials are out of the scope of this thesis.

To deal with such highly dispersive materials, Ruppin [70], following Loudon's work [52], has derived the general expression for the energy density considering materials with a dispersive nature for both their permittivity and permeability. However, in this thesis we only deal with non-magnetic media, therefore in the following, we present the derivation for the appropriate energy density for media with polaritonic permittivity. For this purpose, we start from the energy density, U expression contained in Eq. 2.41, which we write again below [52, 70]:

$$U = \frac{\varepsilon_0}{2}(E^R)^2 + \frac{\mu_0}{2}(H^R)^2 + \frac{1}{2\varepsilon_0\omega_p^2}\left[\left(\frac{\partial P^R}{\partial t}\right)^2 + \omega_0^2(P^R)^2\right]. \tag{2.54}$$

Since, in the above equation P^R is the real valued electric polarization, it will be $P^R = P_0\cos(\omega t)$. Therefore, Eq. 2.54 can be written as:

$$U = \frac{\varepsilon_0}{2}(E^R)^2 + \frac{\mu_0}{2}(H^R)^2 + \frac{1}{2\varepsilon_0\omega_p^2}\left[(\omega P_0\sin(\omega t))^2 + \omega_0^2(P^R)^2\right]. \tag{2.55}$$

With the use of the time-averaged values of the electric polarization, $\overline{(P^R)^2} = \frac{1}{2}PP^*$, electric field, $\overline{(E^R)^2} = \frac{1}{2}EE^*$, and the magnetic field, $\overline{(H^R)^2} = \frac{1}{2}HH^*$, we can obtain the the time-averaged energy density $\overline{U}$ as:

$$\overline{U} = \frac{\varepsilon_0}{4}|E|^2 + \frac{\mu_0}{4}|H|^2 + \frac{1}{4\varepsilon_0\omega_p^2}\left(\omega^2 + \omega_0^2\right)|P|^2, \tag{2.56}$$

Further, with the use of Eq. 2.11, Eq. 2.55 can be written as:

$$\overline{U} = \frac{\varepsilon_0}{4}|E|^2 + \frac{\mu_0}{4}|H|^2 + \frac{(\omega^2 + \omega_0^2)\varepsilon_0\omega_p^2}{4((\omega_T^2 - \omega^2)^2 + (\omega\Gamma)^2)}|E|^2. \tag{2.57}$$

Finally, with the use of Eqs. 2.15 and 2.16, Eq. 2.57 yields for the time-averaged energy density, $\overline{U}$:

$$\overline{U} = \frac{\varepsilon_0}{4}\left(\varepsilon_r' + \frac{2\omega\varepsilon_r''}{\Gamma_e}\right)|E|^2 + \frac{\mu_0}{4}|H|^2. \tag{2.58}$$

In the above equation, the first and second terms on the right-hand side represent the time-averaged values of the energy stored in the electric field and magnetic field respectively. The energy density given in Eq. 2.58 must always be a positive quantity. That implies that in the Reststrahlen band regime, where ε_r' becomes negative, ε_r'' should have a non-zero value, meaning that the negative permittivity ε_r' regime always coexists with loss. Clearly, in general, lossless material with a negative permittivity do not exist. Therefore, we always find that metals and polaritonic materials are lossy materials. In this thesis it is this loss in polaritonic materials we try to exploit to manage superabsorption beyond the capabilities of bulk materials.

2.1.7 Phase velocity, group velocity and energy velocity

Phase velocity

The phase velocity, $\mathbf{v_p}$ is defined as the velocity of the constant phase, $\mathbf{k}\cdot\mathbf{x}$ of an EM wave travelling in the x direction with the wavevector, $\mathbf{k}$, for a single frequency component, ω [1, 71]. Then $\mathbf{v_p}$ can be defined as [71]:

$$\mathbf{v_p} = \frac{dx}{dt}\hat{x} = \frac{\omega}{k}\hat{x}. \tag{2.59}$$

The phase velocity is a useful quantity to find the angle of refraction when crossing an interface between two homogeneous media, i.e. in Snell's law. The phase velocity does not contain any information about the speed the signal travels.

Group velocity

The group velocity, $\mathbf{v_g}$ is defined as the velocity at which the envelope of a wave packet of many frequencies propagate through space [1, 71]. If we assume the propagation of an EM wave is along the x-direction, then $\mathbf{v_g}$ is defined as:

$$\mathbf{v_g} = \frac{d\omega}{dk}\hat{x}. \tag{2.60}$$

The group velocity is a useful quantity, when the group delay has to be calculated for a signal passing through a certain structure. Group velocity is not useful when the medium is highly frequency dispersive [1]. This is because the dispersion will distort the shape of the pulse significantly, so it is not possible to clearly identify the maximum amplitude of the pulse coming in and the maximum amplitude of the pulse going out to be able to find the group delay.

Energy velocity

The energy velocity for general cases (including lossy dispersive mediums) is defined as [52, 70, 72]:

$$\mathbf{v_e} = \frac{\overline{\mathbf{S}}}{\overline{U}}. \tag{2.61}$$

where $\overline{\mathbf{S}}$ and $\overline{U}$ are the time-averaged Poynting vector and energy density respectively. The energy velocity represents the velocity of the energy transport of the EM waves in a material. As mentioned above, the group delay does not always captures the time taken for an EM pulsed signal to go through a certain structure. To calculate this time, the energy velocity should be used instead as defined from Eq. 2.61. The energy velocity equals to the group velocity in many cases, but this is not always true [70].

Comparison of energy and group velocity

In the case of lossless materials group velocity is exactly equal to the energy velocity [72–74]. However, when an EM wave travels in a lossy strongly-dispersive material such as polaritonic media, the pulse shape of the wave distorts significantly [1] and the group velocity loses its meaning. It can become negative and superluminal and different from the actual energy velocity for the propagation of light [1, 52]. It was analytically proven by Ruppin [70], that $\mathbf{v_g}$ is very different from $\mathbf{v_e}$ for lossy strongly dispersive materials. To make it evident, in the following, we will compare the two velocities for SiC within the phonon-polariton gap.

For this purpose, we assume that the EM wave is propagating in the x direction.

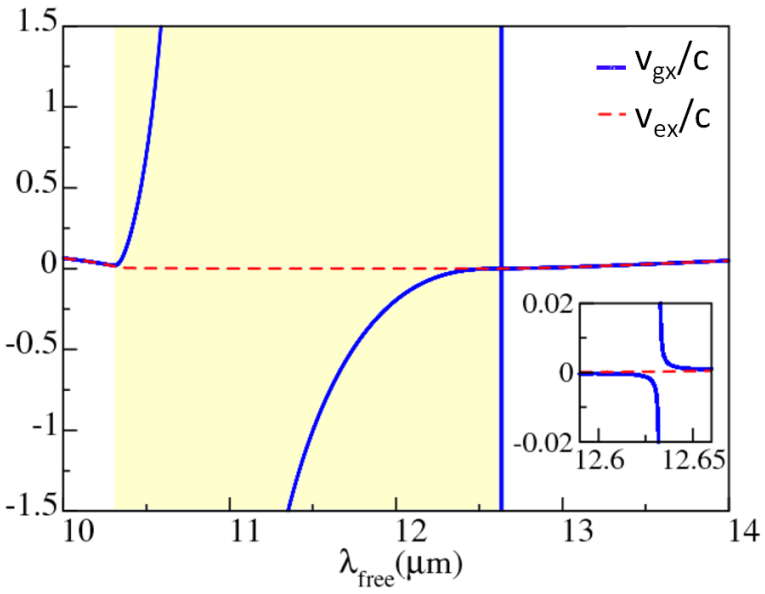

Figure 2.4: Spectral response of the group velocity v_{gx} (blue-solid line), and the energy v_{ex} (red-dashed line) in SiC. Note, both v_{gx} and v_{ex} are expressed in terms of the speed of light in vacuum c. The yellow shading indicates the Reststrahlen band regime of SiC.

Then the x-component of the group velocity is:

$$v_{gx} = \frac{d\omega}{dRe(k_x)}. \tag{2.62}$$

where k_x is the x-component of the wavevector inside SiC. Conversely, the x-component of the energy velocity is:

$$v_{ex} = \frac{\overline{S_x}}{\overline{U}}. \tag{2.63}$$

where $\overline{S_x}$ is the x-component of the time-averaged Poynting's vector. We plot the spectral response of v_{gx} in Fig. 2.4 with a blue line. In the same figure, we also plot the energy velocity, v_{ex} with a red dashed line. We notice that the group velocity matches exactly with the energy velocity in the frequency region outside the Reststrahlen band. However, it diverges from the energy velocity within the entire Reststrahlen-band frequency region (the yellow shaded region in Fig. 2.4). In particular, the maximum discrepancy occurs at 10.8 μm and close to the peak of the Lorentzian function of the SiC permittivity (see the inset in Fig. 2.4). Moreover, it is obvious from Fig. 2.4 that the group velocity exceeds the speed of light in vacuum in the Reststrahlen band frequency regime, which is unphysical. Therefore, we can conclude that the group velocity is not a meaningful quantity in highly lossy dispersive materials. On the other hand, we can see from Fig. 2.4 that the energy velocity is always less than speed of light throughout the spectrum and almost zero

within the Reststrahlen band regime. This is because the decaying EM waves in the Reststrahlen band regime carry almost negligible energy, as we can infer from Eq. 2.29.

2.1.8 Transmission, reflection, and refraction properties of EM waves at a plane boundary

When an EM plane wave is incident on a boundary of a medium with an incident angle θ_i, part of it reflects into the incident medium and part of it transmits through the boundary as shown in Fig. 2.5. In the following, we will present the transmission and reflection results for the two polarization cases depending on the orientation of the electric field with respect to the plane of incidence. The plane of incidence is defined by the incident wavevector and normal to the interface boundary. Therefore, in Fig. 2.5, the plane of the paper is the plane of incidence.

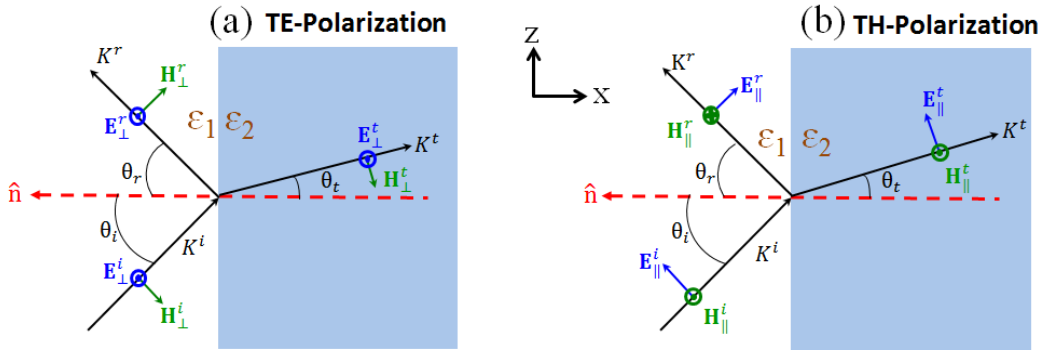

Figure 2.5: (a) Schematic diagram of transmission and reflection of a transverse electric (TE) polarized light at a boundary separating two mediums. (b) same as (a), but for the transverse magnetic (TH) polarized light. The electric field is indicated with a blue arrow or arrow trace and the magnetic field is indicated with a green arrow or arrow trace in both cases.

Transverse Electric polarization (TE) case:

In the TE polarization case, the electric field is oriented perpendicular to the plane of incidence and the magnetic field is parallel to the plane of incidence (see the schematics in Fig. 2.5(a)). After solving the electric and magnetic fields on either sides of the boundary by applying the EM continuity conditions (i.e. tangential component of electric field and tangential component of magnetic field are continuous across a boundary) [1, 5], the transmission amplitude t, and reflection amplitude r, at the boundary can be obtained as [75]:

$$t = \frac{E_{\perp}^{r}}{E_{\perp}^{i}} = \frac{2Z_2 \cos\theta_i}{Z_2 \cos\theta_i + Z_1 \cos\theta_t}, \tag{2.64}$$

and

$$r = \frac{E_{\perp}^{r}}{E_{\perp}^{i}} = \frac{Z_2 \cos\theta_i - Z_1 \cos\theta_t}{Z_2 \cos\theta_i + Z_1 \cos\theta_t}, \tag{2.65}$$

where $Z_1 = \sqrt{\frac{1}{\varepsilon_1}}$ and $Z_2 = \sqrt{\frac{1}{\varepsilon_2}}$ are the relative impedances of the first and the second medium respectively. In Eqs. 2.64 and 2.65, ε_1 and ε_2 denote the relative permittivities of the first and the second medium respectively and θ_t represents the angle of the transmitted beam.

Transverse magnetic polarization (TH) case:

In this case, the electric field is oriented parallel to the plane of incidence and the magnetic field is perpendicular to the plane of incidence (see the schematics in Fig. 2.5(b)). For this case, the transmission amplitude t, and reflection amplitude r, at the boundary are obtained [75] by following the same procedure as done for the TE case:

$$t = \frac{E_{||}^{r}}{E_{||}^{i}} = \frac{2Z_2 \cos\theta_i}{Z_1 \cos\theta_i + Z_2 \cos\theta_t}, \tag{2.66}$$

and

$$r = \frac{E_{||}^{r}}{E_{||}^{i}} = \frac{Z_2 \cos\theta_t - Z_1 \cos\theta_i}{Z_2 \cos\theta_t + Z_1 \cos\theta_i}, \tag{2.67}$$

where Z_1, Z_2, θ_i and θ_t have the same meaning as in the TE polarization case.

Now with the use of these transmission and reflection amplitudes, we can obtain the transmission and reflection for both polarizations at a boundary [75, 76]:

$$T = \frac{Z_1 \cos\theta_t}{Z_2 \cos\theta_i} |t|^2, \tag{2.68}$$

and

$$R = |r|^2. \tag{2.69}$$

In the absence of losses, the energy conservation yields $R+T = 1$. For lossy mediums, from the energy conservation we get:

$$R + T + A = 1. \tag{2.70}$$

where A is the absorption. Since $T = 0$ for semi-infinite media, we have:

$$R + A = 1. \tag{2.71}$$

Snell's law of refraction

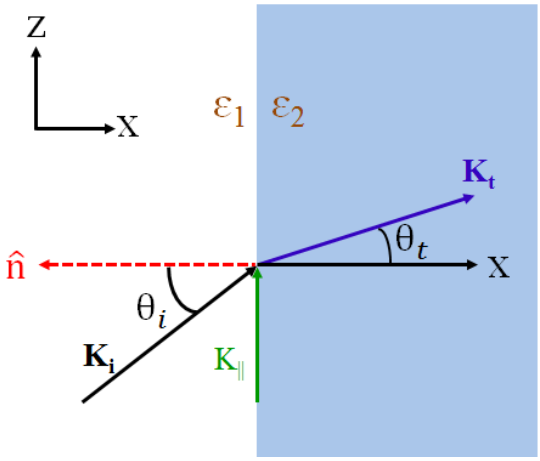

Figure 2.6: (a) The refraction of EM waves at a boundary separating two mediums is depicted schematically. We denote the angle of incidence θ_i, and angle of refraction, θ_t. We indicate the incident wavevector (black arrow), $\mathbf{K_t}$, refracted wavevector (blue arrow), $\mathbf{K_t}$ and the parallel wavevector (green arrow), $\mathbf{K}_{||}$.

In the above, we discussed that when an EM wave incident from medium 1 on medium 2, part of the EM wave will be transmitted through the medium 2. The angle of refraction, θ_t (see the schematics in Fig. 2.6) of this transmitted EM wave is determined by using Snell's law [1, 75]:

$$\frac{\sin\theta_i}{\sin\theta_t} = \sqrt{\frac{\varepsilon_2}{\varepsilon_1}}. \tag{2.72}$$

Note that the Snell's law is another manifestation of the conservation of the wavevector parallel to interface, $\mathbf{K}_{||}$ (the green arrow in Fig. 2.6) [76–78].

So far, we briefly reviewed the EM propagation in natural materials. In the following, we will explain the limitations of natural materials for extraordinary control of light and how we can overcome them with the artificial materials.

2.2 Necessity of artificial materials

From Eqs. 2.65 and 2.67, it can be understood that if the relative impedances of both the media are equal i.e. $Z_1 = Z_2$, then the reflection coefficients become zero for normal incidence. Therefore, the equality of the two impedances is frequently referred to as the impedance matching condition. Many applications such as superlensing [79–83], superabsorption [84–87] and superprism [78, 88–91] effect of light benefit by operating in the near-reflectionless regime. However,

natural materials offer little possibility to achieve such reflectionless condition, especially in our frequency regime of interest, i.e. the mid-IR/THz spectrum. For example, polaritonic materials could be attractive for absorbers because of the large imaginary part of the permittivity, ε'' in their Reststrahlen band spectral regime. However, these materials are also highly reflective in bulk form. Thus natural materials have limited possibilities as absorbers in their bulk form. In addition, they offer very little possibilities for extraordinary deflection of the refracted beam, since the angle of refraction inside these natural materials is only controlled by Snell's law. Therefore, in this thesis, we will go beyond these natural materials and explore man-made structured materials for superabsorption and extraordinary deflection of light.

The man-made structured materials fall in general into two categories: photonic crystals and metamaterials.

2.2.1 Photonic crystals

Photonic crystals are periodically arranged structures of material building blocks in space which can control the flow of photons like semiconductor crystals control the flow of electrons [92]. The periodicity of building blocks in the PCs is comparable with the wavelength of operation. The Photonic Crystals (PCs) have allowed and forbidden frequency bands. EM waves of frequencies within the allowed bands can propagate through the PCs, but propagation of EM waves with frequencies within the forbidden band cannot occur [77, 92]. These band gaps in PCs arise from the interplay between two synergic mechanisms: Mie resonance in the microscopic level, and coherent Bragg scattering in the macroscopic level [93]. These PCs exist as one-dimensional (1D), two dimensional (2D) and three dimensional (3D), periodic arrangements. We show schematically examples of 1D and 2D-PCs in Fig. 2.7(a) and (b) respectively.

Historically, 1D-PCs were the first man-made periodic structures known to us to mold light; hence they are the precursors of the modern more complex three-dimensional photonic crystals where propagation of light can be controlled in all three directions to achieve a full bandgap [94, 95]. 1D-multilayers were studied as early as in 1887 by Lord Rayleigh [96, 97]. Even before Rayleigh, Floquet had developed a theory of propagation of classical waves in 1D-periodic structures [98]. Since 1948, Abelès had investigated EM wave propagation in one-dimensional stratified media [99]. Although, we will not use his formalism, for historical reasons and to correlate our effective impedance formalism, with other reported impedance

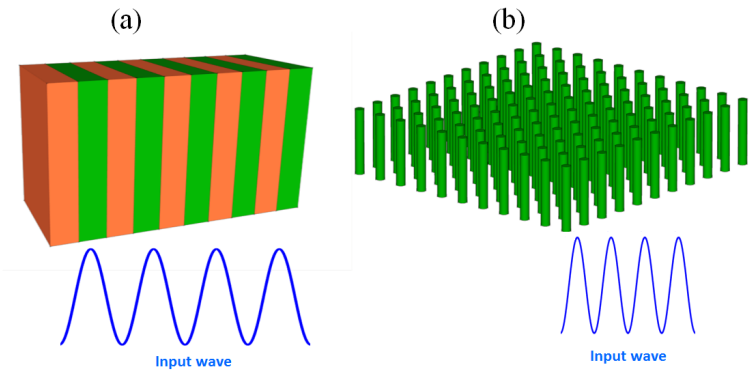

Figure 2.7: Two varieties of Photonic Crystals 1D (a) and 2D (b) are depicted schematically. In each case, the wavelength of the impinging EM wave is indicatively shown. The lattice constant, a, is smaller than but roughly of the order of the free space wavelength, λ_{free}.

formalism adopted thus far in the literature based on the Abelès technique, we have briefly recapped this method in Appendix A.

During the 1970s, EM wave propagation in 1D-multilayers have been thoroughly explored by Yeh, Yariv [73, 100, 101]. However, the term "photonic crystals" was coined by Yablonovitch [102] only in 1989. Despite three-dimensional periodicity being thought as necessary to give a full bandgap, light control by 1D-PCs is still attractive for many applications. Traditionally, 1D-PCs have been employed in distributed feedback lasers [100] and optical filters [103, 104]. However, in recent years many other interesting applications have emerged using 1D-PC structures such as omnidirectional mirrors [105–107], thermophotovoltaic devices [108–110], high quality factor optical cavities [111–113], Bragg colour sensors [114, 115] and chirped gratings [116–118]. With the exploration of a variety of materials, beyond the standard dielectrics, including negative index materials [119], these simple lamellar structures offer interface effects [120, 121], periodicity insensitive bandgap [122, 123] and complete bandgap [124, 125]. Moreover, it is easy to manufacture 1D-PCs in comparison to 2D and 3D PCs. Therefore, in this thesis, we will explore extreme light control such as superabsorption and superprism effect in the Mid-IR spectrum with the use of 1D-PCs based on SiC. It is very interesting from the physics point of view to see if we can get extreme light propagation phenomena from a material that in bulk form does not give any interesting effects other than reflection.

2.2.2 Metamaterials

Photonic metamaterials are artificial structures with effective EM properties not available in nature or in the frequency range of interest [126–128]. Metamaterials

have effective constitutive parameters. In other words, these metamaterials behave as effective homogeneous media, obeying the constitutive relations of Eqs. 2.1 and 2.3 with an effective permittivity, ε_{eff} and an effective permeability, μ_{eff} [127, 129–131] (in the absence of magnetoelectric coupling). Their feature sizes or the periodicity of the unit cells should be deep sub-wavelength in such structures, roughly ten times smaller than the wavelength of operation (see the schematics in Fig. 2.8) [132]. So the incident radiation "sees" such medium as effectively homogeneous and ignores the fine details in its structure. Some of the extra-ordinary constitutive parameters that were made possible with these metamaterials are negative refractive index [133–138] and optical magnetism [131, 139–143], which are achieved by structuring the meta-atom to respond resonantly to the incoming EM wave.

However, there are other kinds of metamaterials that do not rely on the resonances of meta-atoms, such as hyperbolic metamaterials, [4, 144–148]. These metamaterials, mainly consists of simple multilayer structures with the principal elements of their effective permittivity tensors having opposite signs, that results in hyperbolic dispersion [4, 144–147]. These can demonstrate exotic light controlling effects such as polarization conversion [4], superlensing [149–151] and converting evanescent waves to propagating waves [152].

In this thesis, we will study a case falling within this second type of the non-resonant metamaterial, relying on the effective permittivity response of the material. For this purpose, we will use in Chapter 4 a polaritonic multilayer structure with a deep sub-wavelength spacing, that acts as an effective homogeneous material with effective permittivity, ε_{eff}. Our aim is to tailor on-demand the phonon-polaritonic gap region of the effective metamaterial. Therefore, in the following, we will derive an expression for the effective permittivity, ε_{eff}, of a multilayer structure with deep sub-wavelength building blocks.

Effective medium response of deep sub-wavelength multilayers in the quasi-static limit

We consider a 1D-PC comprising of alternate layers of two materials designated with 1 and 2 in Fig. 2.8, and with thicknesses d_1 and d_2 respectively. The respective dielectric functions of the two materials are represented as ε_1 and ε_2. We denote the lattice constant of the PC as $a = d_1 + d_2$ and the filling ratio as $f_r = d_1/a$. If a TE-polarized monochromatic plane EM wave is incident on this PC and its wavelength is much larger than the thickness of layers d_1 and d_2 in the PC, then we can consider

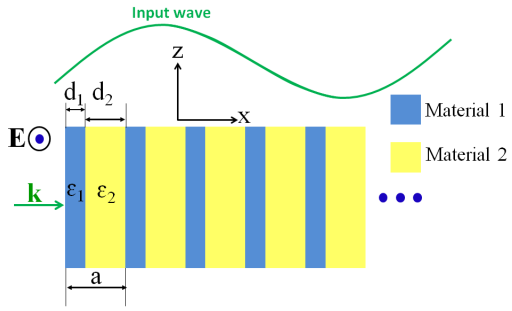

Figure 2.8: Schematic diagram of a deep-subwavelength lattice constant 1D-PC structure with the geometric and material parameters indicated. Notice that the lattice constant, a, is much smaller, about an order of magnitude in comparison to the impinging EM wave's (green curve) wavelength, λ_{free}.

the EM field to be uniform across the PC. Since the tangential component of the electric field **E** must be continuous across the boundaries of the two materials in the PC, its value will be the same inside both the material layers. Therefore, the respective electric displacements $\mathbf{D}_1$ and $\mathbf{D}_2$ inside these two material layers can be expressed as:

$$\mathbf{D_1} = \varepsilon_1 \mathbf{E}, \qquad \text{and} \qquad \mathbf{D_2} = \varepsilon_2 \mathbf{E}. \tag{2.73}$$

From the above equation, we can evaluate the mean electric displacement averaged over the total volume of the PC:

$$\mathbf{D} = \frac{\int_0^{d_1} \mathbf{D_1}\, d\mathrm{x} + \int_{d_1}^{\mathrm{a}} \mathbf{D_2}\, d\mathrm{x}}{\int_0^{\mathrm{a}} d\mathrm{x}} = \frac{\varepsilon_1 \mathbf{E} \mathrm{d}_1 + \varepsilon_2 \mathbf{E} \mathrm{d}_2}{\mathrm{a}} = (\varepsilon_1 f_r + \varepsilon_2 (1 - f_r))\mathbf{E}. \tag{2.74}$$

Finally, the effective dielectric constant ε_{eff} of the PC can be expressed as [4, 153–159]:

$$\varepsilon_{eff} = |\mathbf{D}|/|\mathbf{E}| = \varepsilon_1 f_r + \varepsilon_2 (1 - f_r). \tag{2.75}$$

With this effective dielectric constant, we can describe the macroscopic optical properties of the 1D-PCs in the effective medium range. We use this expression of effective permittivity, ε_{eff} in Chapter 4 to study metamaterial 1D-PC structures for tailoring the spectral regime of the effective phonon-polaritonic gap. With these effective polaritonic media, we are able to control the spectral occurrence of the near-perfect absorption that was not previously possible with the bulk material at such frequency. Note that Eq. 2.75 is an approximation derived under the assumption that the electric field varies quasi-statically within the constituents of the multilayer stack. For this to hold, the building blocks in the multilayer stack should be really much smaller in size in comparison to the wavelength of the incident

light. In Chapter 4, we confirm that this approximation holds true for a multilayer with a building block size of $\sim \lambda_0/10$, where λ_0 is the free space wavelength. We do this by comparison of the reflection/absorption spectra predicted from this effective medium picture with exact calculations.

So far we discussed natural materials and their limitations. Furthermore, we briefly discussed the artificial materials that we are going to investigate in this thesis to overcome these limitations. In the following, we will describe the methodologies that we employ to study these artificial materials, such as Transfer Matrix Method (TMM), the wavevector formalism and the Finite-Difference Time-Domain (FDTD) method. We start from the TMM method, presented in the following section.

2.3 The TMM method

The TMM method is one of the prominent methods used to study the properties of 1D-PCs. This method was developed by Yariv and Yeh's [73, 100, 101, 160]. We employed this to calculate all pertinent properties of 1D-PCs such as band structure, transmission, reflection and absorption of EM fields.

2.3.1 Determination of dynamical matrices

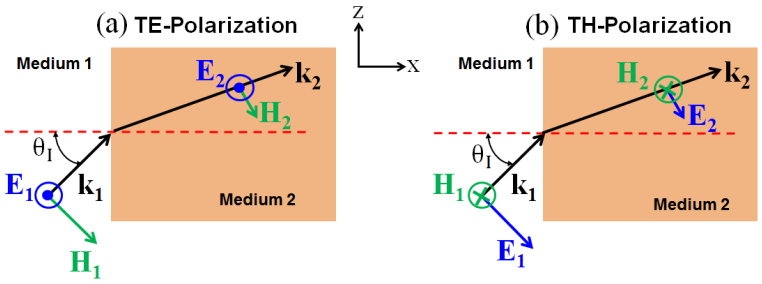

Figure 2.9: (a) Schematic diagram of an EM wave incident from medium 1 to medium 2 for the TE polarization case. (b) Same as in (a) but for the TH-polarization case.

To start with the TMM analysis, we consider a plane EM wave with frequency, ω incident from medium 1 on a medium 2 at an angle, θ_I as schematically depicted in Fig. 2.9. We take both the media to be non-magnetic, which will be the case throughout this thesis. The plane of incidence is the plane of the paper, i.e. the xz plane. In the following discussion, we will derive the results only for the TE-polarization case and just present similar results for the TH-polarization case. For the TE-polarization case depicted in Fig. 2.9(a), we can express the EM field in both

medium 1 and medium 2 in the form:

$$\mathbf{E}(\mathbf{r},t) = \hat{y}E_y(x)e^{i(k_z z-\omega t)}. \tag{2.76}$$

Here, k_z is the z-component of the wavevector in the medium parallel to the interface. In Eq. 2.76, $E_y(x)$ can be written as a combination of a forward going wave part and a backward going wave part:

$$E_{yj}(x) = E_{yj}^{+}e^{ik_{jx}x} + E_{yj}^{-}e^{-ik_{jx}x}, \tag{2.77}$$

where E_{yj}^{+} and E_{yj}^{-} are the respective forward and backward going electric field amplitudes in medium j, with j=1, 2 for medium 1 and medium 2 respectively. Then, the EM boundary conditions state that the tangential components of the electric and magnetic fields at the interface, where $x = 0$ should be conserved respectively. The continuity of the electric field at the interface gives:

$$E_{1y}^{+}e^{ik_{1x}x}\big|_{x=0} + E_{1y}^{-}e^{-ik_{1x}x}\big|_{x=0} = E_{2y}^{+}e^{ik_{2x}x}\big|_{x=0} + E_{2y}^{-}e^{-ik_{2x}x}\big|_{x=0}, \tag{2.78}$$

where k_{1x} and k_{2x} are the x components of the wavevector inside medium 1 and medium 2 respectively, given by:

$$k_{1x} = \sqrt{\varepsilon_1 - \sin^2\theta_I}\,\frac{\omega}{c} \quad \text{and} \quad k_{2x} = \sqrt{\varepsilon_2 - \sin^2\theta_I}\,\frac{\omega}{c}. \tag{2.79}$$

From Maxwell's equations for propagation in non-magnetic media, we have:

$$\nabla \times \mathbf{E} = -\frac{\partial \mathbf{B}}{\partial t} \Rightarrow \nabla \times \mathbf{E} = -\mu_0 \frac{\partial \mathbf{H}}{\partial t}, \tag{2.80}$$

with μ_0 representing the permeability of the vacuum. That implies:

$$H_z(x) = \frac{1}{i\omega\mu_0}\frac{\partial E_y(x)}{\partial x}. \tag{2.81}$$

From now on, we will ignore the subscripts y and z for the electric and magnetic field amplitudes. Then from Eqs. 2.77 and 2.81, we can obtain the magnetic fields for $x < 0$:

$$\frac{k_{1x}}{\mu_0\omega}(E_1^{+}e^{ik_{1x}x} - E_1^{-}e^{-ik_{1x}x}), \tag{2.82}$$

and for $x > 0$:

$$\frac{k_{2x}}{\mu_0\omega}(E_2^{+}e^{ik_{2x}x} - E_2^{-}e^{-ik_{2x}x}). \tag{2.83}$$

The magnetic field at $x = 0$, from both expressions in Eqs. 2.82 and 2.83, should be the same because of the continuity of the tangential magnetic field. So:

$$\frac{k_{1x}}{\mu_0\omega}(E_1^+ - E_1^-) = \frac{k_{2x}}{\mu_0\omega}(E_2^+ - E_2^-). \tag{2.84}$$

We can express Eqs. 2.78 and 2.84 together in a matrix form as:

$$\begin{bmatrix} 1 & 1 \\ -k_{1x} & k_{1x} \end{bmatrix} \begin{bmatrix} E_1^+ \\ E_1^- \end{bmatrix} = \begin{bmatrix} 1 & 1 \\ -k_{2x} & k_{2x} \end{bmatrix} \begin{bmatrix} E_2^+ \\ E_2^- \end{bmatrix}, \tag{2.85}$$

which leads to:

$$\begin{bmatrix} E_1^+ \\ E_1^- \end{bmatrix} = \frac{1}{2} \begin{bmatrix} 1 + \frac{k_{2x}}{k_{1x}} & 1 - \frac{k_{2x}}{k_{1x}} \\ 1 - \frac{k_{2x}}{k_{1x}} & 1 + \frac{k_{2x}}{k_{1x}} \end{bmatrix} \begin{bmatrix} E_2^+ \\ E_2^- \end{bmatrix}. \tag{2.86}$$

The above equation can be written simply:

$$\begin{bmatrix} E_1^+ \\ E_1^- \end{bmatrix} = M^{12} \begin{bmatrix} E_2^+ \\ E_2^- \end{bmatrix}, \tag{2.87}$$

where

$$M^{12} = \frac{1}{2} \begin{bmatrix} 1 + \chi_E^{12} & 1 - \chi_E^{12} \\ 1 - \chi_E^{12} & 1 + \chi_E^{12} \end{bmatrix}, \tag{2.88}$$

with $\chi_E^{12} = \frac{k_{2x}}{k_{1x}}$. M^{12} is typically referred to as the dynamical matrix [73, 160] that relates the amplitude of the electric fields, when TE-polarised EM is going from medium 1 to medium 2. Similarly, we can obtain the dynamical matrix M^{21} that relates the amplitude of the electric fields, when a TE-polarised EM wave is going from medium 2 to medium 1 as:

$$M^{21} = \frac{1}{2} \begin{bmatrix} 1 + \chi_E^{21} & 1 - \chi_E^{21} \\ 1 - \chi_E^{21} & 1 + \chi_E^{21} \end{bmatrix}, \qquad \text{where} \qquad \chi_E^{21} = \frac{k_{1x}}{k_{2x}}. \tag{2.89}$$

Note that, $M^{12}M^{21} = 1$, which implies $M^{12} = (M^{21})^{-1}$ (see Appendix C).

Following similar procedure, the dynamical matrices M^{12} and M^{21} for the case of TH polarization will be:

$$M^{12} = \frac{1}{2} \begin{bmatrix} 1 + \chi_M^{12} & 1 - \chi_M^{12} \\ 1 - \chi_M^{12} & 1 + \chi_M^{12} \end{bmatrix}, \text{and } M^{21} = \frac{1}{2} \begin{bmatrix} 1 + \chi_M^{21} & 1 - \chi_M^{21} \\ 1 - \chi_M^{21} & 1 + \chi_M^{21}, \end{bmatrix} \tag{2.90}$$

with $\chi_M^{12} = \frac{\frac{k_{2x}}{\varepsilon_2}}{\frac{k_{1x}}{\varepsilon_1}}$, and $\chi_M^{21} = \frac{\frac{k_{1x}}{\varepsilon_1}}{\frac{k_{2x}}{\varepsilon_2}}$.

Determination of the propagation matrices

Now let us assume that an EM wave travels a distance, d within the medium 1, between two points A, and B. If E^{A+}, and E^{A-} represent the respective amplitudes of the forward and backward going electric field parts at point A, then after travelling a distance d, these amplitudes acquire a phase of $e^{ik_{1x}d}$ and $e^{-ik_{1x}d}$ respectively. Therefore, the amplitudes of the forward and backward going parts of the electric field at point B, E^{B+}, and E^{B-} can be obtained as:

$$E^{B+} = E^{A+}e^{ik_{1x}d} \text{ and } E^{B-} = E^{A-}e^{-ik_{1x}d}. \tag{2.91}$$

We can write the above equations in a matrix form as:

$$\begin{bmatrix} E^{A+} \\ E^{A-} \end{bmatrix} = P^1 \begin{bmatrix} E^{B+} \\ E^{B-} \end{bmatrix}, \tag{2.92}$$

where

$$P^1(d) = \begin{bmatrix} e^{-ik_{1x}d} & 0 \\ 0 & e^{ik_{1x}d} \end{bmatrix}. \tag{2.93}$$

$P^1(d)$ is the propagation matrix for a distance d in medium 1. Similarly, the propagation matrix for a distance d in medium 2, $P^2(d)$ is:

$$P^2(d) = \begin{bmatrix} e^{-ik_{2x}d} & 0 \\ 0 & e^{ik_{2x}d} \end{bmatrix}. \tag{2.94}$$

In the following, we will analyse the EM wave propagation in a 1D-PC structure consisting of medium 1 and medium 2, by using the dynamical and the propagation matrices that we just determined for these two media.

2.3.2 Bandstructure and modal field distributions in 1D-PCs

Bandstructure for 1D-PCs: determination and properties

The band structure or the dispersion relation gives the relation between the wavevector, q inside the periodic structure and the frequency of the impinging EM wave, ω. In the TMM technique, we input the frequency, ω and find the wavevector, q. This has the advantage of being able to easily treat dispersive systems, in comparison to other methods such as the plane wave expansion method, in which the frequency is found out for a given wavevector [161]. The TMM bandstructure method is a modal method, meaning that it determines which modes will survive

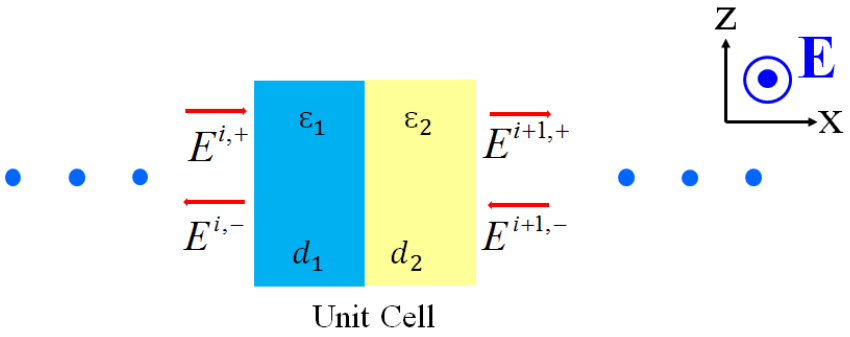

Figure 2.10: Schematic diagram of a unit cell in an infinitely periodic 1D-PC consisting of two materials. The electric fields that enter and leave the unit cell are indicated.

inside the PC system. However it does not give any insight of the coupling details for a specific mode, for which the exact finite extent of the 1D PC structure must be considered. In this section, we will consider only the building block extending infinitely and we will determine the properties of the modes that exist in such systems.

In particular, we consider an infinitely extending 1D-PC consisting of medium 1 and medium 2 as schematically depicted in Fig. 2.10. We will represent the electric field at a certain location inside the PC, as a column matrix, where the top and bottom elements denote the forward and backward going parts of the electric fields. Now, if an EM wave crosses a boundary between the two media within the PC, then the electric fields on either side of the boundary will be related by the dynamical matrices: M^{12} if we go from medium 1 to medium 2 and M^{21} if we go from medium 2 to medium 1 (see Eqs. 2.88 and 2.89). Conversely, if an EM wave travels a distance between two points within the same constituent layers of the PC, then the electric fields at these two points will be related by the propagation matrices: P^1 for medium 1 and P^2 for medium 2 (see Eqs. 2.93 and 2.94). With this information, now we will proceed in deriving the dispersion relation for 1D-PCs.

If we select the i^{th} unit cell, then fields entering $\begin{bmatrix} E^{i,+} \\ E^{i,-} \end{bmatrix}$ and leaving $\begin{bmatrix} E^{i+1,+} \\ E^{i+1,-} \end{bmatrix}$ that unit cell can be correlated as:

$$\begin{bmatrix} E^{i,+} \\ E^{i,-} \end{bmatrix} = M^{21}P^1(d_1)M^{12}P^2(d_2) \begin{bmatrix} E^{i+1,+} \\ E^{i+1,-} \end{bmatrix}, \tag{2.95}$$

where $M^{21}P^1(d_1)M^{12}P^2(d_2) = M^u$ is the transfer matrix of the unit cell. Let the

eigenvalues of M^u be $\Lambda_{1,2}$:

$$\begin{bmatrix} E^{i,+} \\ E^{i,-} \end{bmatrix} = \Lambda_{1,2} \begin{bmatrix} E^{i+1,+} \\ E^{i+1,-} \end{bmatrix}. \tag{2.96}$$

We can obtain these eigenvalues of M^u as:

$$\Lambda_{1,2} = \frac{1}{2}\left[(M^u_{11} + M^u_{22}) \pm \sqrt{(M^u_{11} + M^u_{22})^2 - 4\mathrm{det[M^u]}}\right], \tag{2.97}$$

where

$$\det[M^u] = M^u_{11}M^u_{22} - M^u_{12}M^u_{21}. \tag{2.98}$$

In Appendix D, we have shown that $\det[M^u] = 1$ for a general case, including lossy PCs, since we did not make any assumptions for the material properties of the constituent media. Therefore, the above equation becomes:

$$\Lambda_{1,2} = \frac{1}{2}\left[(M^u_{11} + M^u_{22}) \pm \sqrt{(M^u_{11} + M^u_{22})^2 - 4}\right]. \tag{2.99}$$

Since the multilayer system is periodic in nature, the modes should obey the Bloch condition [162], which implies:

$$\begin{bmatrix} E^{i,+} \\ E^{i,-} \end{bmatrix} = e^{-i\mathrm{qa}} \begin{bmatrix} E^{i+1,+} \\ E^{i+1,-} \end{bmatrix}. \tag{2.100}$$

From Eqs. 2.99 and 2.100, we can write:

$$\Lambda_{1,2} = e^{-i\mathrm{qa}} = \frac{1}{2}\left[(M^u_{11} + M^u_{22}) \pm \sqrt{(M^u_{11} + M^u_{22})^2 - 4}\right]. \tag{2.101}$$

Since the elements in the above equation implicitly depend on the frequency of the impinging EM wave, this equation directly establishes the relation between the wavevector, q and frequency, ω of the mode or in other words gives the band structure of the multilayer stack. Throughout the thesis, we use this dispersion relation to compute the bandstructure of both lossy and lossless 1D-PCs. Eq. 2.101 can be written in an elegant form, using the fact that both the eigenvalues, $e^{-i\mathrm{qa}}$ and $e^{i\mathrm{qa}}$ are possible for a given frequency, ω. That implies:

$$e^{+i\mathrm{qa}} + e^{-i\mathrm{qa}} = (M^u_{11} + M^u_{22}). \tag{2.102}$$

With the use of the matrix elements M_{11}^{u} and M_{22}^{u}, the above equation yields:

$$\cos(\mathrm{qa}) = \cos(k_{1x}d_1)\cos(k_{2x}d_2) - \frac{1}{2}(\chi_E^{12} + \chi_E^{21})\sin(k_{1x}d_1)\sin(k_{2x}d_1). \tag{2.103}$$

Similarly, for the TM case the above relation can be expressed as:

$$\cos(\mathrm{qa}) = \cos(k_{1x}d_1)\cos(k_{2x}d_2) - \frac{1}{2}(\chi_M^{12} + \chi_M^{21})\sin(k_{1x}d_1)\sin(k_{2x}d_1). \tag{2.104}$$

Note that for lossless PCs, where q is purely real, Eq. 2.103 is more suitable to calculate the bandstructure in the region of allowed propagation. However, for lossy PCs, it is easy to use Eq. 2.101 to compute the bandstructure. Eq. 2.101 gives two roots for q, but only one is permissible, as only one satisfies the passivity condition. We will explain this in detail in Chapter 8. This information of choosing the correct root for q has been missed in the majority of prior works [157, 163–165].

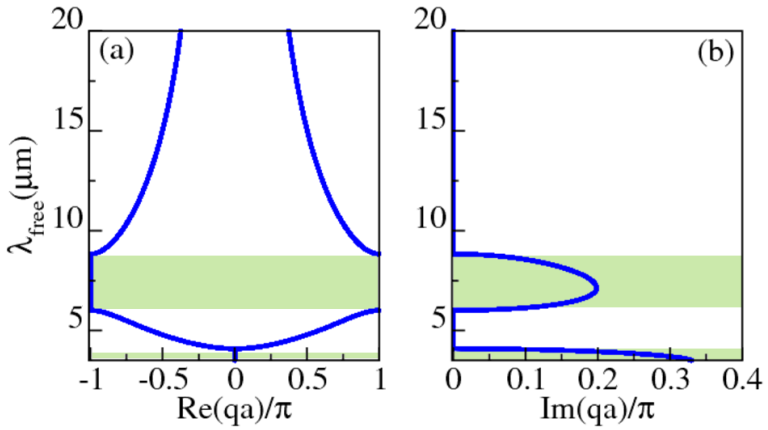

Figure 2.11: Bandstructure (free space wavelength λ_{free}, versus Bloch wave vector, q) of a purely dielectric-air 1D-PC with a lattice constant, a= 3 μm and filling ratio 0.05. The permittivity of the dielectric layer is 11.56. The shaded regions indicate the bandgap regimes of the PC. An impinging EM wave along the $+x$ direction is assumed, hence the positive Im(q) value is taken to assure decaying waves within the PC in the bandgap.

As an example, we show the bandstructure for a dielectric-air 1D-PC with a lattice constant, a = 3 μm and filling ratio, $f_r = 0.05$. The permittivity of the dielectric layer is 11.56, which is close to the realistic value of Si in the THz/Mid-IR regime [60]. We show the bandstructure of this PC in Fig. 2.11. We plot the free space wavelength λ_{free} versus the real and imaginary parts of the Bloch wavevector, q in Fig. 2.11(a) and (b) respectively. In both panels we highlight the PC bandgaps. From Fig. 2.11(a), we notice that the bandstructure is symmetric, in the band regions, where Im(q)=0. Since, we assume an impinging wave along the $+x$

direction, we take only positive values for Im(q) in Fig. 2.11(b) to ensure decaying waves inside the photonic crystal (growing wave solutions are unphysical) in the bandgap region. Notice also that in the band gap regime Re(q) is either equal to zero or $\mp\pi/a$, which means the Bloch envelope from the real part of the wavevector, q is just ∓ 1.

Modal EM fields in 1D-PCs

In Chapter 3, we will require the EM fields in infinitely extending 1D-PCs to calculate the energy velocity averaged within the SiC layers using Eq. 2.61. The latter will be useful to design 1D-PCs with superabsorption properties. For this purpose, in the following, we will describe the TMM method to evaluate these EM fields in infinitely extending 1D-PCs.

To start with, we dissolve the matrices in Eqs. 2.95 and 2.100 into the following set of equations:

$$E^{i,+} = M^u_{11} E^{i+1,+} + M^u_{12} E^{i+1,-}, \tag{2.105a}$$
$$E^{i,-} = M^u_{21} E^{i+1,+} + M^u_{22} E^{i+1,-}, \tag{2.105b}$$
$$E^{i,+} = e^{-iqa} E^{i+1,+}, \tag{2.105c}$$
$$E^{i,-} = e^{-iqa} E^{i+1,-}. \tag{2.105d}$$

By rearranging the above equations, we have:

$$E^{i,+} = M^u_{11} e^{iqa} E^{i,+} + M^u_{12} e^{iqa} E^{i,-} \tag{2.106a}$$
$$E^{i,-} = M^u_{21} e^{iqa} E^{i,+} + M^u_{22} e^{iqa} E^{i,-}. \tag{2.106b}$$

That implies:

$$E^{i,+}(1 - M^u_{11} e^{iqa}) = M^u_{12} e^{iqa} E^{i,-}, \tag{2.107a}$$
$$E^{i,-}(1 - M^u_{22} e^{iqa}) = M^u_{21} e^{iqa} E^{i,+}. \tag{2.107b}$$

This process is equivalent to finding the eigenvectors as was performed in Ref. [73, 100]. From Eqs. 2.107(a) and 2.107(b), the ratio between the fields $E^{i,-}$ and $E^{i,+}$

can be expressed as:

$$\frac{E^{i,-}}{E^{i,+}} = \frac{(1 - M^u_{11}e^{i\mathrm{qa}})}{M^u_{12}e^{i\mathrm{qa}}} = \eta_1, \tag{2.108a}$$

$$\frac{E^{i,-}}{E^{i,+}} = \frac{M^u_{21}e^{i\mathrm{qa}}}{(1 - M^u_{22}e^{i\mathrm{qa}})} = \eta_2. \tag{2.108b}$$

This means $\eta = \eta_1 = \eta_2$ and assuming $E^{i,+}$ to be equal to one, Eq. 2.108 implies $E^{i,-}$ will be η, in other words we would have the eigenvector:

$$\begin{bmatrix} E^{i,+} \\ E^{i,-} \end{bmatrix} = \begin{bmatrix} 1 \\ \eta \end{bmatrix} = \begin{bmatrix} 1 \\ \frac{(1-M^u_{11}e^{i\mathrm{qa}})}{M^u_{12}e^{i\mathrm{qa}}} \end{bmatrix}. \tag{2.109}$$

Now with the use of this eigenvector, we can evaluate the electric field at any point inside the unit cell of the PC, as we will explain below. The total electric field at any point x between 0 and d_1 in the medium 1 in Fig. 2.10 can be expressed:

$$E_1(x) = E_1^{i,+}(x) + E_1^{i,-}(x). \tag{2.110}$$

In the above equation, the forward and backward going electric field parts, $E_1^{i,+}$ and $E_1^{i,-}$ are related to the eigenvector as (Fig. 2.10):

$$\begin{bmatrix} 1 \\ \eta \end{bmatrix} = M^{12}P^2(x) \begin{bmatrix} E_1^{i,+}(x) \\ E_1^{i,-}(x) \end{bmatrix}, \tag{2.111}$$

which implies:

$$\begin{bmatrix} E_1^{i,+}(x) \\ E_1^{i,-}(x) \end{bmatrix} = [M^{12}P^2(x)]^{-1} \begin{bmatrix} 1 \\ \eta \end{bmatrix}. \tag{2.112}$$

Similarly, the electric field within the medium 2 in Fig. 2.10 can be obtained by:

$$E_2(x) = E_2^{i,+}(x) + E_2^{i,-}(x), \tag{2.113}$$

with

$$\begin{bmatrix} E_2^{i,+}(x) \\ E_2^{i,-}(x) \end{bmatrix} = [M^{12}P^2M^{21}P^1(x)]^{-1} \begin{bmatrix} 1 \\ \eta \end{bmatrix}. \tag{2.114}$$

In this manner, electric fields are calculated within the entire unit cell. Furthermore, to calculate the time-averaged Poynting vector $\overline{\mathbf{S}}$ in Eq. 2.25 and the time-averaged energy density, $\overline{U}$ in Eq. 2.58, we also require magnetic fields of the infinitely extended PCs. These magnetic field components can be calculated from the above calculated electric fields by using Faraday's law. In particular, we get for medium

1:

$$H_{1z}(x) = \frac{k_{1x}}{\mu_0\omega}(E_1^+(x) - E_1^-(x)), \tag{2.115a}$$

$$H_{1x}(x) = \frac{-k_{1z}}{\mu_0\omega}(E_1^+(x) + E_1^-(x)); \tag{2.115b}$$

and for medium 2:

$$H_{2z}(x) = \frac{k_{2x}}{\mu_0\omega}(E_2^+(x) - E_2^-(x)), \tag{2.116a}$$

$$H_{2x}(x) = \frac{-k_{2z}}{\mu_0\omega}(E_2^+(x) + E_2^-(x)). \tag{2.116b}$$

2.3.3 Transmission, Reflection and Absorption of 1D-PCs

As we mentioned before, superabsorption with lossy PCs is one of the main objectives of this thesis. To evaluate the absorption performance of the 1D-PCs, we require spectral information on their absorptance A. We can calculate A with the Transfer Matrix Method (TMM) as $A = 1 - T - R$, where T and R represent the transmittance and reflectance of the 1D-PC respectively. Therefore, in the following, we will describe the TMM Method to obtain T and R of a 1D-PC.

General formulation

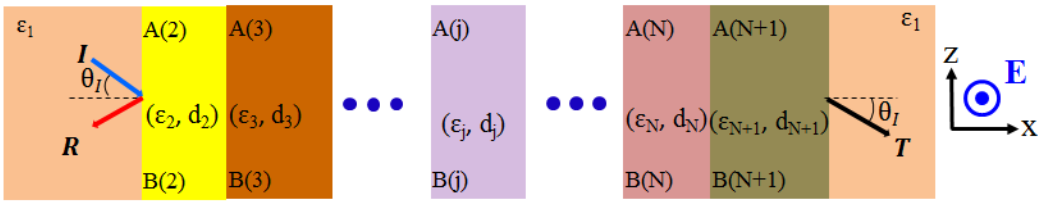

Figure 2.12: A finite sized 1D-PC consisting of N slabs of different materials is shown schematically. Notice that the incident medium and the outgoing medium are the same, which we designate with medium 1 (salmon region). Therefore, the incident angle, θ_I and the transmitted angle, θ_I are also same. In each material slab, we denote its relative permittivity and thickness. Furthermore, we designate the forward going EM wave part and the backward going EM wave part in each layer, j, as $A(j)$ and $B(j)$. We indicate the incident (blue arrow), reflected (red arrow) and transmitted (black arrow) EM waves. The polarization direction of the electric field is also indicated.

In this thesis, we study periodic and terminated PCs in Chapters 3, 4, 5 and 8 and aperiodic 1D-PCs in Chapter 6. Therefore, we will try to present the TMM method

for calculating transmission properties for a general case that encompasses all the cases that will be studied in this thesis. For this purpose, we consider a 1D-PC constructed from N slabs that could be of different materials and thicknesses as schematically shown in Fig. 2.12. We take the incident medium and exit medium to be same and a purely dielectric medium and designate this medium as medium 1. Therefore, if a plane EM wave is incident on the stack, in the positive x direction, at an angle, θ_I, it will exit the stack with the same angle, θ_I as shown in Fig. 2.12.

Now the column elements representing the forward going and backward going parts of the electric field at the entrance of the stack is $\begin{bmatrix} E^I \\ E^R \end{bmatrix}$. Similarly, the column elements representing the forward going and backward going parts of the electric field at the exit of the stack is $\begin{bmatrix} E^T \\ 0 \end{bmatrix}$. Note that the backward going electric field part at the exit of the stack is zero, since there will be no EM waves coming from + infinity towards the stack in the opposite direction of the incident EM wave. These electric field parts at the two ends of the PC can be related by a total transfer matrix M^{total} as:

$$\begin{bmatrix} E^I \\ E^R \end{bmatrix} = M^{total} \begin{bmatrix} E^T \\ 0 \end{bmatrix} = \begin{bmatrix} M_{11}^{total} & M_{12}^{total} \\ M_{21}^{total} & M_{22}^{total} \end{bmatrix} \begin{bmatrix} E^T \\ 0 \end{bmatrix}. \tag{2.117}$$

By applying the TMM method, M^{total} can be expressed as a combination of the dynamical matrices and propagation matrices corresponding to the different materials of the stack and the incident and exit media as:

$$M^{total} = \left(\prod_{j=1}^{N} M^{j,j+1} P^{j+1}(d_{j+1}) \right) M^{N+1,1}, \tag{2.118}$$

where $M^{j,j+1}$ represents the dynamical matrix that relates the amplitude of the electric fields, when an EM wave is going from medium j to medium $j+1$, while P^{j+1} designates the propagation matrix of medium $j+1$, with a thickness of d_{j+1}. After knowing the transfer matrix from Eq. 2.118, we can obtain the transmission amplitude, t and reflection amplitude, r of the multilayer stack as (see Appendix E)[73, 100]:

$$t = \frac{E^T}{E^I} = \frac{1}{M_{11}^{total}}, \tag{2.119a}$$

$$r = \frac{E^R}{E^I} = \frac{M_{21}^{total}}{M_{11}^{total}}. \tag{2.119b}$$

Now, if we assume that the incident and exit media are the same and are a purely

dielectric medium, then the transmittance T, and reflectance R of the entire stack can be determined as (see Appendix E):

$$T = |t|^2, \tag{2.120a}$$

$$R = |r|^2. \tag{2.120b}$$

In the above, we considered that the EM wave is incident on the stack from the left side. However, if we assume that the EM wave is incident on the stack from the right-hand side, then we can obtain the transmission amplitude, t', and reflection amplitude, r', of the multilayer stack as (see Appendix E) [73, 100]:

$$t' = \frac{1}{M_{11}^{total}}, \tag{2.121a}$$

$$r' = -\frac{M_{12}^{total}}{M_{11}^{total}}. \tag{2.121b}$$

Then the transmittance, T', and reflectance, R', of the stack can be determined as:

$$T' = |t'|^2, \tag{2.122a}$$

$$R' = |r'|^2, \tag{2.122b}$$

if the incident and exit media are the same material that is a lossless dielectric.

Because $\det[M^{total}]$ will be equal to 1 (see Appendix F) [73], since the incident and exit media are the same, $T = T'$ in such cases, meaning that the transmittance of a multilayer stack does not change, whether light is incident on the left side of the stack or light is incident on the right-hand side of the stack. Note that this is true for both lossy and lossless lamellar structures. Therefore, transmittance is symmetric in both lossy and lossless layered structures. However, from Eqs. 2.119(b) and 2.121(b), it is obvious that for general cases $r \neq r'$. Therefore, we expect that the reflectance to be different in lossy multilayer stacks when light incident from the left side and when light incident from the right side. In the following, we will present an example for the asymmetric behaviour for the reflection of lossy multilayer stacks.

Lossy multilayer stacks and asymmetric reflection

In the above, we discussed that transmittance is symmetric for both lossy and lossless media, but reflectance can be different, depending on the incident EM wave's direction. To make it evident, we consider two multilayer stacks that are embedded in air, and each of these stacks consists of three layers as shown schematically in the bottom of Fig. 2.13. We take the thicknesses of the first,

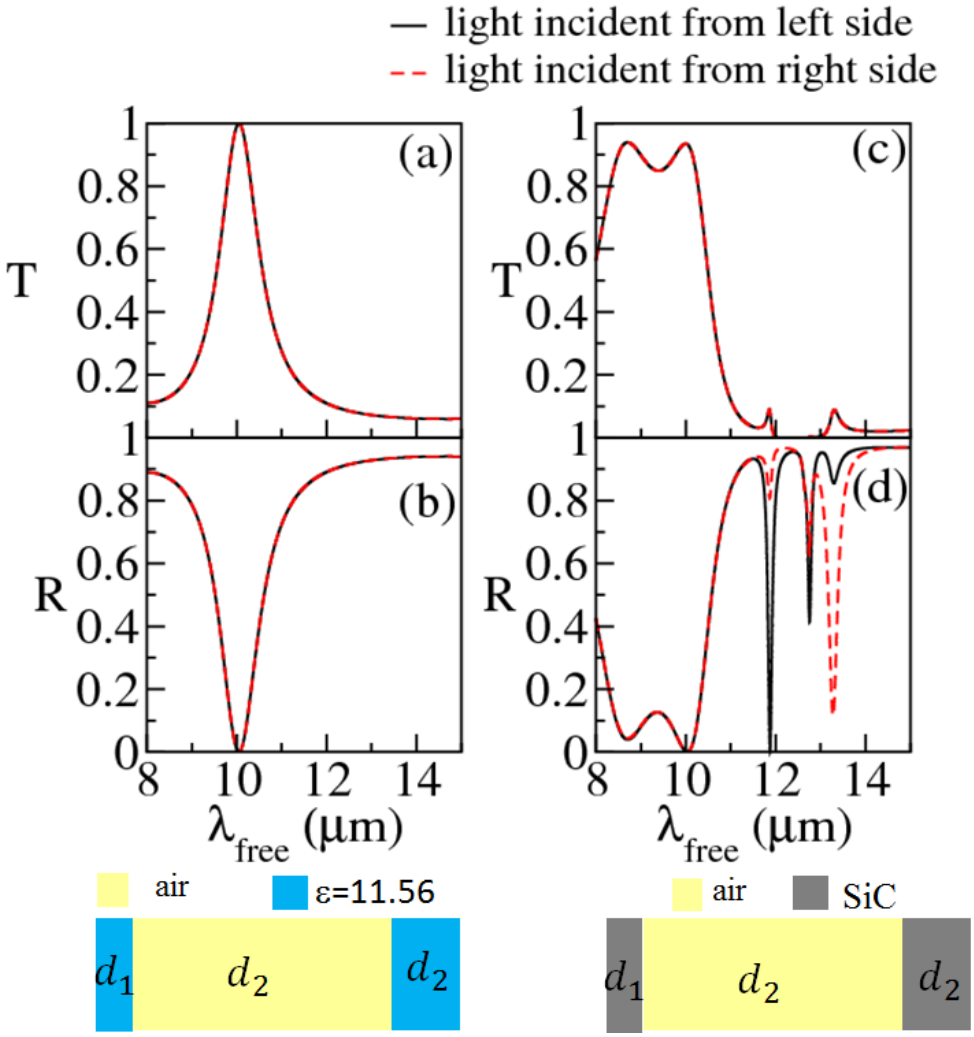

Figure 2.13: (a) and (b): The spectral response of the transmittance, T and reflectance, R of a three layer purely dielectric lamellar structure. The first and third layer are constructed from a material with permittivity, $\varepsilon = 11.56$, while the second layer is air, as shown in the left-hand-side schematics. (c) and (d): same as (a) and (b), but for the lossy multilayer stack, with the first and the third layers constructed from SiC. The second layer is air, as shown in the right-hand-side schematics. In both the lossless and lossy stacks, the thicknesses of the layers are taken to be $d_1 = 0.5\mu$m, $d_2 = 5\mu$m and $d_3 = 1.0\mu$m.

second and third layers in each of the multilayer structures to be $d_1 = 0.5\mu$m, $d_2 = 5\mu$m and $d_3 = 1.0\mu$m respectively.

Now in the first type of the multilayer, we consider the first and the third slabs to be made of a lossless material with a relative permittivity of $\varepsilon = 11.56$ and the second layer to be air (see the schematics on the left-hand side in Fig. 2.13). Therefore, this is a purely dielectric structure. We show the spectral response of the transmittance and the reflectance of this structure in Fig. 2.13(a) and (b) respectively. In each panel, the black-solid line (red-dashed line) indicates the case when the light incident on the stack from the left side (right side).

We notice that both the transmittance and the reflectance of this purely dielectric layered structure is the same for both the incident cases considered. We stress that this comes as result of $M_{12}^{total} = M_{21}^{total*}$ for lossless PCs (see Appendix E).

On the other hand, we consider that in the second type of multilayer, the first and the third layers are made up of SiC, which is a lossy material as we discussed before (see Fig. 2.2). We consider the second layer to be air, as in the previous case (see the schematics on the right-hand side in Fig. 2.13). The permittivity of the SiC, is modelled by using the Lorentzian function given by Eq. 2.14 with the fitting parameters taken from Ref. [49]. We plot the transmittance and reflectance versus free space wavelength, for this lossy structure in Fig. 2.13(c) and (d) respectively. Here also we notice that the transmittance is the same whether the EM wave is incident from the left side or from the right side, as we expected from the analysis in Appendix E. However, we can see that the reflectance is not the same for the two incident directions considered. This is because M_{12}^{total} here is not equal to M_{21}^{total*}, and thus leads to $R \neq R'$.

We have exploited this asymmetric property of reflectance in Chapter 3, to achieve a reflectionless condition in lossy 1D-PCs for one of the incident cases. In particular, we will terminate the input interface of a SiC-air 1D-PC to achieve a near-zero reflectance, thereby achieving a near-perfect absorptance. Furthermore we also used this asymmetric property of reflectance in Chapter 6, to obtain the absorptance of more than 90% covering almost the entire phonon-polariton gap of SiC with a SiC-air aperiodic 1D-PCs. In particular, we will find the crucial importance of the building block arrangement in an increasing order of thickness in these aperiodic PCs.

So far, we discussed the transmission properties of a special case of multilayer stack that consists of different material slabs with different sizes. In the following, we will describe the transmission properties of multilayer stacks that consists of just two types of material slabs, which are periodically repeated in space to form 1D-PCs.

Transmission properties of finite sized 1D-periodic structures

In this special case, the 1D-PC consists of medium 1 and medium 2 (see the schematics in Fig.2.14) with the respective relative permittivities, ε_1 and ε_2 and embedded in medium 2 with relative permittivity ε_2. We take the thicknesses of the constituent layers to be d_1 and d_2. We consider a total N number of building blocks, each consisting of medium1 and medium 2. The total transfer matrix of this stack, M^{total}

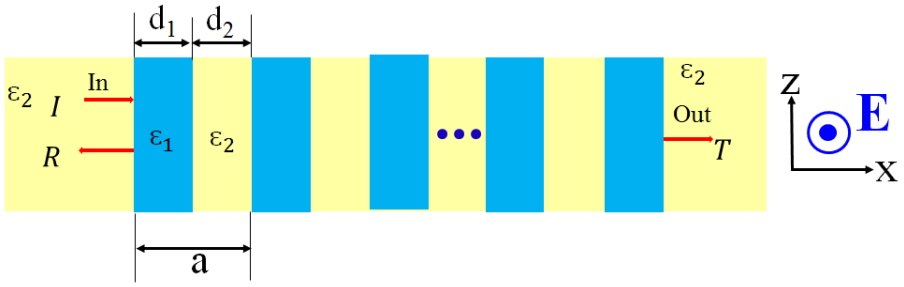

Figure 2.14: Schematics of a finite sized 1D-PC consisting of two materials, medium 1 and medium 2. The material and geometrical parameters of the PC are designated. The forward going and backward going electric field parts are denoted, at the entrance, and at the exit of the stack.

can be obtained from Eq. 2.118 as:

$$M^{total} = [M^{21}P^{1}M^{12}P^{2}]^{N} = [M^{u}]^{N}, \tag{2.123}$$

where $M^u = M^{21}P^1M^{12}P^2$ is the transfer matrix of the unit cell. In Appendix D, we have shown that M^u is a unimodular matrix. Therefore, we can express $[M^u]^N$ in terms of the elements of M^u using the Chebyshev identity [73, 76, 100, 159] as:

$$M^{total} = \begin{bmatrix} M^u_{11} & M^u_{12} \\ M^u_{21} & M^u_{22} \end{bmatrix}^N = \begin{bmatrix} M^u_{11}U_{N-1} - U_{N-2} & M^u_{12}U_{N-1} \\ M^u_{21}U_{N-1} & M^u_{22}U_{N-1} - U_{N-2} \end{bmatrix}, \tag{2.124}$$

where

$$U_N = \frac{\sin((N+1)\mathrm{qa})}{\sin(\mathrm{qa})}, \tag{2.125}$$

with q and a= $d_1 + d_2$ representing the Bloch wavevector and lattice constant of the PC respectively. Furthermore, q is related to the elements of the transfer matrix of the unit cell in the PC as:

$$\cos(\mathrm{qa}) = \frac{1}{2}(M^u_{11} + M^u_{22}). \tag{2.126}$$

Now from Eqs. 2.119(b) and 2.124, we can obtain the reflection amplitude of a 1D-PC with N unit cells, $r(N)$ as:

$$r(N) = \frac{M^u_{21}U_{N-1}}{M^u_{11}U_{N-1} - U_{N-2}}. \tag{2.127}$$

With the use of Eq. 2.125, we can rewrite Eq. 2.127 as:

$$r(N) = \frac{M^u_{21}}{M^u_{11} - \frac{\sin((N-1)\mathrm{qa})}{\sin(N\mathrm{qa})}}. \tag{2.128}$$

After mathematical simplification, we get:

$$r(N) = \frac{M_{21}^u}{M_{11}^u - \cos(\mathrm{qa}) + \frac{\sin(\mathrm{qa})}{\tan(N\mathrm{qa})}}. \tag{2.129}$$

We use the above equation later in this Chapter to show that the reflectance within the bandgap regime of a lossless 1D-PC is unity. In addition, we use this equation in Chapter 8, to obtain the effective impedance of a lossy 1D-PC.

EM fields in actual finite sized 1D-PCs

In the previous section, we described the TMM method for calculating the EM fields in infinitely extending PC systems. However, EM field distributions in the actual finite sized systems is not expected to be the same as the field distributions in infinitely extending systems. This is because of back and forth reflections at the interfaces of the finite systems. These calculations are very important to evaluate finite size effects on the energy velocity of the EM waves in lossy PCs as we will see in Chapters 3, 4, 5 and 6. Also they will be crucial to understand where EM power gets absorbed inside lossy PCs. Therefore, in the following, we present the methodology to obtain the EM fields in finite-sized PC system.

For this purpose, we consider the same finite sized 1D-PC we studied in the previous section. i.e. the case shown in Fig. 2.12. As we can see from the schematics of Fig. 2.12, the total electrical field at any point x inside a material j can be expressed:

$$E_j(x) = [A(j)e^{ik_{jx}(x-l_j)} + B(j)e^{-ik_{jx}(x-l_j))}], \tag{2.130}$$

where $A(j)$ and $B(j)$ designate the forward and backward going electric field parts in medium j (see schematics in Fig. 2.12), and k_{jx} represents the x-component of the wavevector in medium j. In Eq. 2.130, $l_j = \sum_{i=2}^{j-1} d_i$ for j ≥ 3 and $l_j = 0$ for $j = 2$. In order to find out the forward and backward going electric field parts $A(j)$ and $B(j)$ in Eq. 2.130, first we will calculate the forward and backward going electric field parts in the last material slab $N + 1$ as:

$$\begin{bmatrix} A(N+1) \\ B(N+1) \end{bmatrix} = P^{N+1} M^{N+1,1} \begin{bmatrix} E^T \\ 0 \end{bmatrix}. \tag{2.131}$$

After finding $A(N+1)$ and $B(N+1)$ in the last layer, the electric field parts in any preceding layer j can be determined by the following recursive relation:

$$\begin{bmatrix} A(j) \\ B(j) \end{bmatrix} = P^j M^{j,j+1} \begin{bmatrix} A(j+1) \\ B(j+1) \end{bmatrix}, \tag{2.132}$$

with $2 \leq \mathrm{j} < \mathrm{N} + 1$.

As mentioned before, along with these electric fields, we will also require the magnetic field components within each layer of the lamellar stack for evaluating the time-averaged values of the energy density and Poynting vector respectively. Therefore, by using the above calculated electric fields, we will now calculate the corresponding magnetic field components for the TE-polarization case by using Faraday's law. The magnetic components inside a layer j can be obtained as:

$$H_{jz}(x) = \frac{k_{jx}}{\mu_0 \omega}[A(j)e^{ik_{jx}(x-l_j)} - B(j)e^{-ik_{jx}(x-l_j)}], \tag{2.133a}$$

$$H_{jx}(x) = \frac{-k_{jz}}{\mu_0 \omega}[A(j)e^{ik_{jx}(x-l_j)} + B(j)e^{-ik_{jx}(x-l_j)}], \tag{2.133b}$$

$$\tag{2.133c}$$

where k_{jx}, k_{jz} are the x- and z-components of the wavevector within a j^{th} layer of the lamellar structure.

Similarly, to obtain the EM fields for the TH-polarization case, we start from the expression for the total magnetic field at a location x inside the j^{th} layer:

$$H_j(x) = [A(j)e^{ik_{jx}(x-l_j)} + B(j)e^{-ik_{jx}(x-l_j))}], \tag{2.134}$$

where $A(j)$ and $B(j)$ are the forward and backward going magnetic field parts in material slab j of the multilayer stack. In a similar manner like for the TE-polarization case, we will first obtain the magnetic fields in the last material slab $N+1$ as:

$$\begin{bmatrix} A(N+1) \\ B(N+1) \end{bmatrix} = P^{N+1} M^{N+1,1} \begin{bmatrix} E^T \\ 0 \end{bmatrix}. \tag{2.135}$$

Note, here $M^{N+1,1}$ is the dynamical matrix for the TH-polarization, when going from medium $(N+1)$ to medium 1 given by Eq. 2.90. Now we can determine $A(j)$ and $B(j)$ in any preceding layer j using the following recursive relation:

$$\begin{bmatrix} A(j) \\ B(j) \end{bmatrix} = P^{j} M^{j,j+1} \begin{bmatrix} A(j+1) \\ B(j+1) \end{bmatrix}, \tag{2.136}$$

where similarly $M^{j,j+1}$ is the TH-polarization dynamical matrix when going from medium (j) to medium $(j+1)$. With the use of these magnetic fields we will evaluate

the electric fields in the j^{th} layer, by using the Ampère's law as:

$$E_{jz}(x) = \frac{k_{jx}}{\varepsilon_0 \varepsilon_j \omega}[A(j)e^{ik_{jx}(x-l_j)} - B(j)e^{-ik_{jx}(x-l_j)}], \tag{2.137a}$$

$$E_{jx}(x) = \frac{-k_{jz}}{\varepsilon_0 \varepsilon_j \omega}[A(j)e^{ik_{jx}(x-l_j)} + B(j)e^{-ik_{jx}(x-l_j)}], \tag{2.137b}$$

where ε_j is the relative permittivity of the j^{th} layer in the stack.

In Chapters 8 and 9, we will investigate lossy 1D-PCs for ultra-refraction and extreme bending of EM waves. In order to understand these propagation properties in such lossy structures, we will first require to understand the propagation properties in lossless PCs. For this purpose, in the following section, we will present the EM wave propagation theory in lossless 1D-PCs.

2.4 Propagation properties in lossless 1D-PCs

2.4.1 Propagation properties in Photonic bandgaps

In the above, we discussed that in the bandgap regime of a lossless PC, the Bloch wavevector, q is imaginary. Now we proceed in showing that the EM waves falling in this frequency regime will be completely reflected from the 1D-PC. For this purpose, we will consider q= ip, where p is real. So we can express Eq. 2.129 as:

$$r(N) = \frac{M_{21}^u}{M_{11}^u - \cos(i\text{pa}) + \frac{\sin(i\text{pa})}{\tan(iN\text{pa})}}. \tag{2.138}$$

Since $\tan(iN\text{pa})$ can be expanded as:

$$\tan(iN\text{pa}) = \frac{e^{-N\text{pa}} - e^{N\text{pa}}}{i\left(e^{-N\text{pa}} + e^{N\text{pa}}\right)}. \tag{2.139}$$

For a semi-infinite PC, $N \to \infty$, and we have $e^{-N\text{pa}} \to 0$. That means, we can approximate $\tan(iN\text{pa})$ as:

$$\tan(N\text{ipa}) \approx \frac{-e^{N\text{pa}}}{i\left(e^{N\text{pa}}\right)} = i. \tag{2.140}$$

Therefore, the amplitude of the reflection of a semi-infinite PC, r_{semi} can be determined from Eq. 2.138 as:

$$r_{semi} \approx \frac{M_{21}^u}{M_{11}^u - e^{\text{-pa}}}. \tag{2.141}$$

From the above equation, the reflectance, R of a semi-infinite 1D-PC can be obtained as:

$$R_{semi} = r_{semi} r^*_{semi} = \left[\frac{M^u_{21}}{M^u_{11} - e^{-\mathrm{pa}}}\right]\left[\frac{M^{u*}_{21}}{M^{u*}_{11} - e^{-\mathrm{pa}}}\right]. \tag{2.142}$$

That implies:

$$R_{semi} = \left[\frac{|M^u_{21}|^2}{|M^u_{11}|^2 - e^{-\mathrm{pa}}(M^u_{11} + M^{u*}_{11}) + e^{-2\mathrm{pa}}}\right]. \tag{2.143}$$

Now from the trace of the transfer matrix M^u in Eq. 2.126, we can write:

$$(M^u_{11} + M^u_{22}) = 2\cos(i\mathrm{pa}) \Longrightarrow (M^u_{11} + M^{u*}_{11}) = e^{\mathrm{pa}} + e^{-\mathrm{pa}}, \tag{2.144}$$

since we have shown in Appendix E that $M^u_{22} = M^{u*}_{11}$ for lossless lamellar structures. From Eq. 2.143 and Eq. 2.144, we get:

$$R_{semi} = \left[\frac{|M^u_{21}|^2}{|M^u_{11}|^2 - e^{-\mathrm{pa}}(e^{\mathrm{pa}} + e^{-\mathrm{pa}}) + e^{-2\mathrm{pa}}}\right]. \tag{2.145}$$

After some mathematical simplification, we have:

$$R_{semi} = \left[\frac{|M^u_{21}|^2}{|M^u_{11}|^2 - 1}\right]. \tag{2.146}$$

Since $|M^{total}_{21}|^2 + 1 = |M^{total}_{11}|^2$ for lossless multilayer stacks (see Eq. E.13 in Appendix E), the above equation yields:

$$R_{semi} = 1. \tag{2.147}$$

From the above equation, it is obvious that EM waves with frequencies that fall within the bandgaps, will be completely reflected from the PC. In the following, we will proceed in understanding the propagation properties in the allowed band regions of lossless 1D-PCs.

2.4.2 Propagation properties in Photonic bands: Forward and backward waves

First we will analyse the important implications of the sign of the real part of the Bloch wavevector, Re(q) in the band regime, on the type of wave propagation. We consider the reference direction of the wave propagation inside the PC as the energy propagation direction, which should be along the $+x$ direction (since energy cannot propagate towards the source due to causality [77, 78, 166]) for an impinging wave along the $+x$ direction. Then if Re(q) is positive, the mode is referred to as a forward Bloch wave since the phase velocity, $\mathbf{v_p}$ will be also in the the $+x$ direction, which means that the energy velocity, $\mathbf{v_e}$ and phase velocity, $\mathbf{v_p}$ are parallel [78, 167–

170]. On the other hand, if Re(q) is negative, then it is referred to as a backward Bloch wave, since the phase velocity, $\mathbf{v_p}$ will be in the the $-x$ direction, which means that the energy velocity, $\mathbf{v_e}$ and phase velocity, $\mathbf{v_p}$ are anti-parallel [78, 167–170]. However, just by solving Eq. 2.101, we cannot immediately know the sign of Re(q), since we cannot exclude any root from the two roots obtained from Eq. 2.101. Therefore, we plot both the branches in Fig. 2.15, for the first two bands of the dielectric lossless PC of Fig. 2.11. To choose the appropriate root, we should study more carefully the PC's band properties.

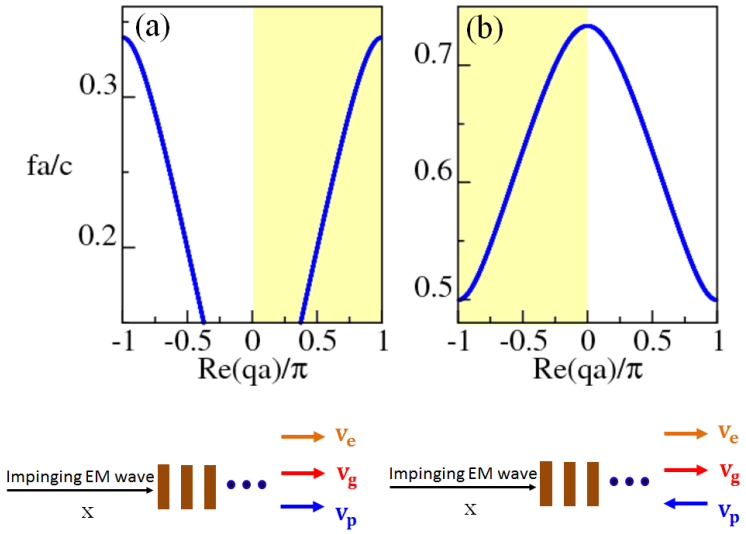

Figure 2.15: (a) First band of the bandstructure (dimensionless frequency fa/c, versus Bloch wave vector, q) of the PC of Fig. 2.11. (b) same as (a), but for the second band. The direction of the impinging EM wave, the energy velocity, $\mathbf{v_e}$, the group velocity, $\mathbf{v_g}$ and the phase velocity, $\mathbf{v_p}$ of the wave that has coupled into the 1D-PC are indicated for the corresponding bands. The part of the dispersion band that is relevant is highlighted for each case.

If we assume an impinging EM wave along the $+x$ direction, then the energy velocity will be always in the $+x$ direction. The group velocity, $\mathbf{v_g}$ is always equal to the energy velocity, $\mathbf{v_e}$ in any 1D-lossless PC [74]. This means that the direction of the group velocity would also be fixed along the $+x$ direction. In a 1D-PC system, with impinging wave along the $+x$ direction, the group velocity, $\mathbf{v_g}$ can be expressed in the band region as:

$$\mathbf{v_g} = \frac{\partial \omega}{\partial \mathrm{q}} \hat{x}, \tag{2.148}$$

with $\frac{\partial \omega}{\partial \mathrm{q}}$ being the band slope, and q being real. From the above equation, we can infer that $\frac{\partial \omega}{\partial \mathrm{q}}$ will be always positive for an an impinging wave along the $+x$ direction,

to satisfy the causality. Further, the phase velocity of the wave will be:

$$\mathbf{v_p} = \frac{\omega}{\mathrm{q}}\hat{x}. \tag{2.149}$$

Note, it is the sign of $\mathbf{v_p}\cdot\mathbf{v_g}$ that determines whether the Bloch wave inside the PC is forward type or backward type [78, 168–170]. For an impinging wave along the $+x$ direction, we can express $\mathbf{v_p}\cdot\mathbf{v_g}$ as:

$$\mathbf{v_p}\cdot\mathbf{v_g} = \frac{\omega}{\mathrm{q}}\frac{\partial\omega}{\partial\mathrm{q}} \tag{2.150}$$

It becomes evident from the above equation that $\frac{\omega}{\mathrm{q}}\frac{\partial\omega}{\partial\mathrm{q}}$ should be positive for a forward-type wave, and should be negative for a backward-type wave. Therefore, q must be positive for a forward-type wave and negative for a backward-type, since $\frac{\partial\omega}{\partial\mathrm{q}}$ will be always positive for an an impinging wave along the $+x$ direction, to satisfy the causality as discussed above. By causality here we mean that the EM wave that couples inside the medium must have its energy propagation pointing away from the source [166].

To explain this further, we look at the first two bands in the bandstructure of the dielectric PC shown in Fig. 2.15. Note that we plot the dimensionless frequency, $f\mathrm{a}/c$ versus q in Fig. 2.15 to make it easy for determining the sign of the band slope. It is evident from Fig. 2.15(a) that $\frac{\omega}{\mathrm{q}}\frac{\partial\omega}{\partial\mathrm{q}}$ is positive, thus q must be positive. Thus the coupled Bloch wave in this band is forward type. Accordingly, we highlight the positive branch in Fig. 2.15(a) with the yellow shaded region.

On the other hand, we can see from Fig. 2.15 (b) that $\frac{\omega}{\mathrm{q}}\frac{\partial\omega}{\partial\mathrm{q}}$ is negative, thus q must be negative, from the above analysis. Thus the Bloch wave emanating from this band is backward type. Hence we highlight the negative branch in Fig. 2.15(b) with the yellow shaded region. Below each panel of Fig. 2.15, we also indicate the corresponding direction of the energy velocity, $\mathbf{v_e}$, the group velocity, $\mathbf{v_g}$ and the phase velocity, $\mathbf{v_p}$.

So far, we understand how to determine the rightness of the Bloch wave inside the PC for normal incidence. The term "rightness" here is used in analogy with Veselago's definition [119] in negative index media. The purpose of the use of this term in photonic crystals [168] is to describe an averaged EM wave behaviour within the PC unit cell with a Poynting vector and Bloch phase that are antiparallel [119, 168]. The understanding of the "rightness" property of the PC at a certain frequency will be crucial to determine the angle of propagation inside PCs when an

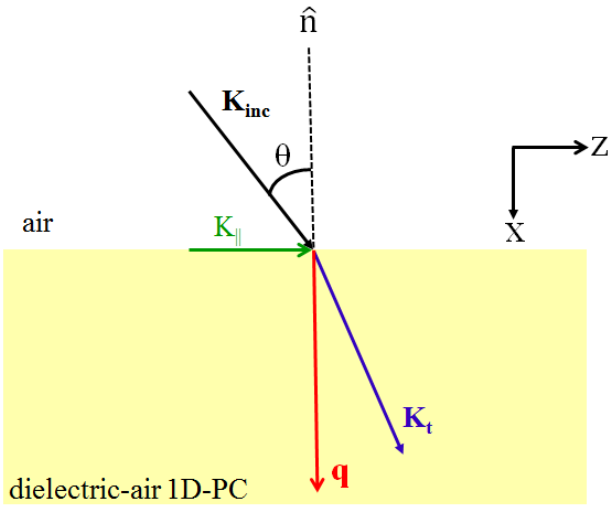

Figure 2.16: Oblique incidence of light at an angle θ at the dielectric-air PC interface. The incident wavevector, $\mathbf{k_{inc}}$, transmitted wavevectors, $\mathbf{k_t}$, Bloch wavevector, $\mathbf{q}$ and the parallel component of the incident wavevector, $\mathbf{k}_{||} = \omega/c \sin\theta\hat{z}$ are indicated.

EM wave incident on the PC at a certain angle. Note that, in the case of oblique incidence (see schematics of Fig. 2.16), the wave is referred to as forward type if the angle between the transmitted wavevector, $\mathbf{k_t}$ and the group velocity, $\mathbf{v_g}$ is acute. On the other hand, if the angle between them is obtuse, we refer to that Bloch wave as backward type [78, 168]. For general incidence at the interface of 1D-PCs, $\mathbf{k_t} = \mathbf{k}_{||}\hat{z}+\mathbf{q}$, where $\mathbf{k}_{||} = \omega/c \sin\theta\hat{z}$ is the parallel component of the wavevector, that is conserved across the 1D-PC interface. We will see how the information on the type of wave (forward or backward) is crucial in determining the refracted angle in the following section.

2.5 Refraction at the interface of lossless 1D-PCs: Wavevector diagram formalism

Here we will present the methodology on how to determine the refraction angle at the interface of a lossless 1D-PC. For this purpose, we will apply the wavevector diagram formalism [77, 78, 89, 104, 168, 169]. The important part of this formalism is the equifrequency surfaces (EFSs). EFSs are the graphical representation of the set of all the propagating modes within the first Brillouin zone (BZ), at a particular frequency, ω. Since, we have translation symmetry in the y-direction for our PC and have chosen the xz to be the plane of incidence (see schematic of Fig. 2.16), we represent these EFSs in the xz plane only. Thus EFSs are essentially equifrequency

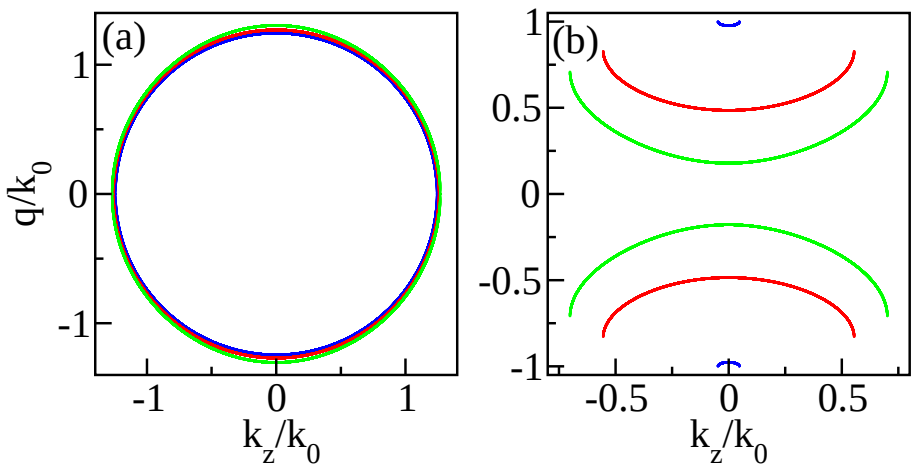

Figure 2.17: (a) Equi-frequency contours (EFC) for the case of Fig. 2.15(a), at dimensionless frequencies fa$/c$ equal to 0.15 (blue curves), 0.25 (red curves) and 0.3 (green curves) respectively. (b) Same as (a), but for the case of Fig. 2.15(b) at dimensionless frequencies fa$/c$ equal to 0.5 (blue curves), 0.6 (red curves) and 0.7 (green curves) respectively.

contours in the 2D plane that we will denote as EFCs from hereon.

We obtain the EFC of the PC, by solving the dispersion relation given in Eq. 2.101 for q, for different k_z ($k_z = k_{||}$ conserved) components by employing the TMM method [73, 100, 101, 160]. In Fig. 2.17, we show the EFCs of our dielectric-air PC of Fig. 2.11. Note that both q and k_z are expressed in terms of the vacuum wavevector, $\mathrm{k}_0 = \omega/c$. In particular, in Fig. 2.17(a) we show three EFCs at dimensionless frequencies, fa$/c$ equal to 0.15, 0.25 and 0.3 respectively. These frequencies are in the band of Fig. 2.15(a), that corresponds to forward-type Bloch wave. We notice that the shape of all these EFCs is elliptical-like and almost isotropic (i.e. circle). On the other hand, in Fig. 2.17(a), we show the three EFCs at dimensionless frequencies, fa$/c$ equal to 0.5, 0.6 and 0.7 respectively, that are in the band of Fig. 2.15(b). As we discussed above, this band corresponds to the backward-type Bloch wave. We notice that the shape of these EFCs are concave, from the BZ center with q=0.

The sign of the band slope and shape of the EFCs are crucial in determining the correct refraction angle. This is because, the gradient $\nabla_{\mathbf{k}}\omega$, of an EFC at a point in the $\mathbf{k}$ space, gives the group velocity $\mathbf{v_g}$. From the mathematical properties of the gradient, the direction of $\mathbf{v_g}$ will be in the direction of the normal to the EFC at that point pointing towards increasing values of frequency.

To proceed with the wavevector formalism, we consider a plane EM wave of frequency ω incident from air onto the PC at an angle θ. First, we represent the EFC of the

incoming medium i.e. air. The dispersion relation for the air medium at the xz plane, which is the plane of incidence is given as:

$$k_x{}^2 + k_z{}^2 = \frac{\omega^2}{c^2}, \tag{2.151}$$

which is an equation of a circle, with radius equal to ω/c. Next, we indicate the EFC of the PC at the frequency of the incident wave. To determine the increasing frequency direction, we should also plot the EFC of the PC at a higher frequency than the operating frequency. Then we draw a line parallel to the normal of the PC interface at a distance equal to the k_z, from the origin of the wavevector space. This k_z represents the conservation of the parallel component of the incident wavevector, $k_{||} = \omega/c\,\sin\theta$ at the PC interface. We refer to this line as the construction line in accordance with Ref. [104].

The intersection of the construction line with the EFC of the air medium with a positive k_x component equal to $\omega/c\,\cos\theta$, represents the incident wavevector, $\mathbf{k_{inc}}$. Similarly, the intersection of this line with the EFC of the PC, gives all the possible refracted wavevectors $\mathbf{k_{ref}}$. Furthermore, from the gradient of the EFC, we obtain the direction of $\mathbf{v_g}$, which is identical to direction of the energy velocity, $\mathbf{v_e}$. Depending on the $\mathbf{v_g}$ direction, we select the refracted wave that has $\mathbf{v_g}$ pointing away from the source, to satisfy the causality condition. In the following we will apply this formalism to our dielectric-PC of Fig. 2.15(a) to determine the direction of the refracted wave inside the PC for such case.

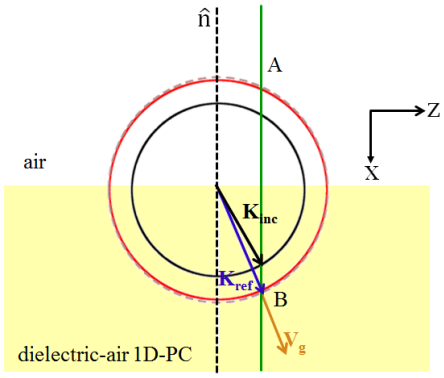

Figure 2.18: Wavevector diagram for the PC of Fig. 2.15(a). The red curve represents the EFC at dimensionless frequency $fa/c = 0.25$. The black circle represents the EFC of the air. The normal to the PC interface and the construction line are indicated with a black-dashed line and a green-solid line respectively. The incident and refracted wavevectors are designated with $\mathbf{k_{inc}}$ and $\mathbf{k_{ref}}$ respectively. The energy propagation direction of the wave given by $\mathbf{v_g}$ is indicated with the orange arrow, drawn normally to point B and pointing outwards in the direction of increasing frequency.

For this purpose, we show the wavevector diagram of the PC in Fig. 2.18 at a dimensionless frequency, fa/c equal to 0.25. We consider an angle of incidence of 30^0. We represent the EFC of the PC and the air at this frequency with a red-curve and a black curve respectively. To determine the increasing frequency direction, we also plot the EFC of the PC at a dimensionless frequency, fa/c equal to 0.3 and represent it with a brown dashed curve. We represent the construction line with a green vertical line, that intersects the z-axis of $\mathbf{k}$-space at $k_z = \omega/c \sin 30^0$, which is the parallel component of the wavevector that must be conserved. We indicate the incident wavevector, $\mathbf{k_{inc}}$ with a black arrow at the intersection of the construction line with the EFC of air. We notice that the construction line intersects with the EFC of the PC at two points A and B. This suggests that there are two possible directions for the refracted wavevector $\mathbf{k_{ref}}$.

Since the EFC of the PC corresponds to a frequency in the forward-type band (see Fig. 2.15(a)), the group velocity, $\mathbf{v_g}$ which is given by the normal to the EFC at the intersection, must point towards the increasing frequency direction and away from the source. From Fig. 2.18, it is evident that the point A, has $\mathbf{v_g}$ pointing towards the source, while the point B, has $\mathbf{v_g}$ pointing away from the source. This means only point B, gives the propagating wave inside the PC, while the other possibility is non-causal. We indicate this propagating wave with an orange arrow in Fig. 2.18. It is clearly seen that the Bloch wave gets positively refracted at the PC interface.

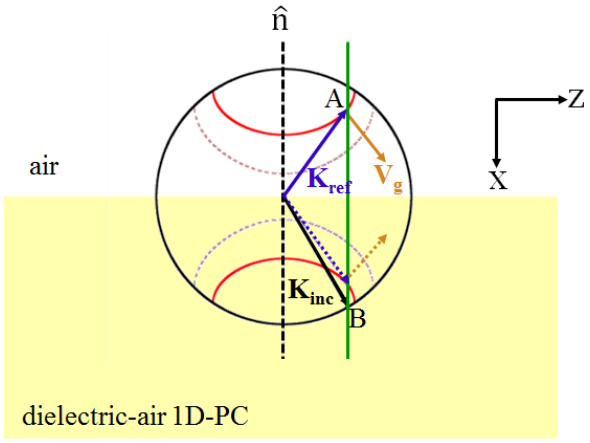

Figure 2.19: Same as Fig. 2.18, but for the dimensionless frequency $fa/c = 0.6$, that corresponds to a backward wave band. The non-causal possibilities for refracted wavevector and group velocity that were rejected are shown with the dotted blue and orange arrows.

In the above, we discussed the propagation of the refracted beam for a frequency that corresponds to a forward-type wave. In the following, we analyse the case where the operating frequency corresponds to a backward-type wave. For this

purpose, we show the wavevector diagram of the PC in Fig. 2.19 at a dimensionless frequency, $f\mathrm{a}/c$ equal to 0.6. From Fig. 2.15, we know that this frequency corresponds to a backward-type wave. To determine the increasing frequency direction, we also plotted the EFC of the PC at a dimensionless frequency, $f\mathrm{a}/c$ equal to 0.7 and represent this with the brown dashed curve. We consider the same 30^0 angle of incidence as in the case of Fig. 2.18, thus the construction line intersects the z axis in the $\mathbf{k}$-space at $k_z = \omega/c \sin 30^0$.

We notice from Fig. 2.19 that this construction line intersects with the EFC of the PC at two points, A and B. We indicate the two possible refracted wavevectors $\mathbf{k_{ref}}$ with solid and dotted blue arrows respectively. We also indicate the direction of the corresponding $\mathbf{v_g}$ with solid and dotted arrows, chosen to be normal to the EFC at the intersection with the construction line towards the point and pointing towards increasing frequency values. It is evident from Fig. 2.19, the point B has the $\mathbf{v_g}$ propagating towards the source, while the point A has the $\mathbf{v_g}$ propagating away from source. Thus only the latter represents the actual refracted beam direction inside the PC, as the other possibility is non-causal. It is clear from Fig. 2.19, that this EM wave is also positively refracted, even though propagation inside the PC is backward-type.

From the above analysis, we can understand that backward propagation in PCs does not immediately imply negative refraction. One would need isotropic and backward type of modes to have negative refraction. This is not typically possible with 1D-PCs. However, we will see the important implications of having backward-type Bloch waves for 1D-PCs in a wedged type structure in Chapter 9. In particular, we will be able to design a system where the incident light will undergo a 90^0 angle of bending, based on the existence of backward Bloch waves within a 1D-PC.

From section 2.4 and section 2.5, we have presented the theory of propagation for lossless 1D-PCs. However, the theory of propagation for lossy PCs is not systematically presented in the literature. Therefore, in Chapter 8, we will expand this propagation theory of lossless 1D-PCs appropriately to include 1D-PCs with lossy constituents.

In Chapter 7, we will study the superabsorption in a pyramid shaped 2D-PC design. In Chapters 8 and 9, we will explore the ultra-refraction properties of the finite sized lossy 1D-PCs such as superprisms. These higher dimensionality structures cannot be modelled with the TMM formulation of 1D PCs. Therefore, we have used a commercial-grade simulator based on the Finite-Difference Time-Domain (FDTD)

method [171] to simulate these structures. In the following, we will briefly review the basic principles of the FDTD method as well as different kinds of set-ups that must be implemented in such solver to investigate the desirable properties for the system under study.

2.6 The Finite-Difference Time-Domain (FDTD) method

The Finite-Difference Time-Domain (FDTD) method has been a very useful technique in electrodynamics, since the time evolution of electric and magnetic field maps can be obtained for realistic structures as the EM wave propagates through these structures. In addition, transmission, reflection and absorption properties of realistic structures can be studied with the FDTD method. For the FDTD calculations described throughout the thesis, we have used a commercial-grade simulator based on the Finite-Difference Time-Domain (FDTD) method [171]. In the following, we will briefly review the basic principles of the FDTD method as well as different kinds of set-ups that must be implemented in such solver to investigate the desirable properties for the system under study. We employed the Lumerical solutions [171] FDTD method, in Chapter 7, to study the superabsorption in a 2D pyramid design. We employed the FDTD method in Chapters 8 and 9 to study refraction and extreme bending in structures made from 1D-SiC PCs.

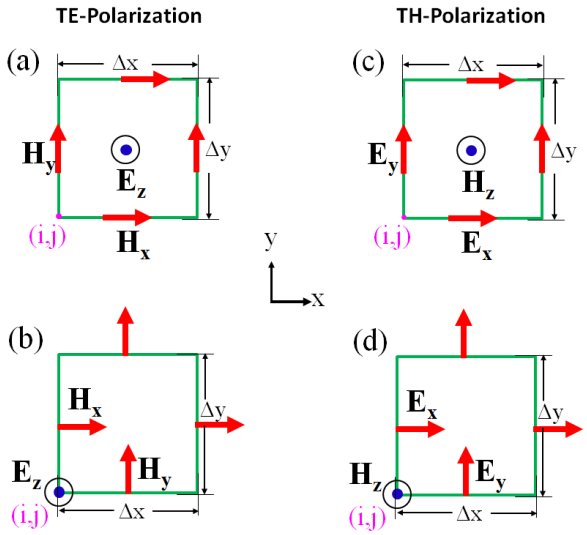

Figure 2.20: (a) and (b): Schematics of two possible field locations in the staggered grid approach for the TE-polarization case. (c) and (d): same as (a) and (b), respectively but for the TH-polarization case. The green square represents the basic elements of the mesh sizes Δx and Δy in the x and y directions respectively.

2.6.1 Overview of the FDTD method

The FDTD method is a grid based numerical technique that solves the time-dependent Maxwell's equations. In this method, Maxwell's equations are discretised both in time and space by using the central-difference formulation [172, 173]. These differential equations are solved by using Yee's staggered grid approach (see schematics in Fig. 2.20) that preserves the divergence-free nature of the EM fields in free space [174]. These staggered grids are shown for cases of translational symmetry in one direction, i.e. for so called 2D EM problems in Fig. 2.20. For these 2D problems, Maxwell's equations decouple into two sets of equations. We studied such 2D type problems in Chapters 7-9, with the FDTD method for non-magnetic media. Therefore, we present below Maxwell's equations for 2D problems with non-magnetic media.

i) When electric field is parallel to the direction of translational symmetry: TE polarization case (see Fig. 2.20(a) or (b))

$$\frac{\partial H_x}{\partial t} = \frac{1}{\mu_0}\left[-\frac{\partial E_z}{\partial y}\right], \tag{2.152}$$

$$\frac{\partial H_y}{\partial t} = \frac{1}{\mu_0}\left[\frac{\partial E_z}{\partial x}\right], \tag{2.153}$$

$$\frac{\partial E_z}{\partial t} = \frac{1}{\varepsilon_0\varepsilon_r}\left[\frac{\partial H_y}{\partial x} - \frac{\partial H_x}{\partial y} - (J_{ES_z} + \sigma E_z)\right], \tag{2.154}$$

ii) When magnetic field is parallel to the direction of translational symmetry: TH polarization case (see Fig. 2.20(c) or (d))

$$\frac{\partial E_x}{\partial t} = \frac{1}{\varepsilon_0\varepsilon_r}\left[-\frac{\partial H_z}{\partial y} - \sigma E_x\right], \tag{2.155}$$

$$\frac{\partial E_y}{\partial t} = \frac{1}{\varepsilon_0\varepsilon_r}\left[\frac{\partial H_z}{\partial x} - \sigma E_y\right], \tag{2.156}$$

$$\frac{\partial H_z}{\partial t} = \frac{1}{\mu_0}\left[\frac{\partial E_x}{\partial y} - \frac{\partial E_y}{\partial x} - J_{MS_z}\right], \tag{2.157}$$

In the above equations J_{ES} and J_{MS} are the sources used for the TE and TH polarisation cases respectively. Also, ε_0 is the permittivity of vacuum and μ_0 is the permeability of vacuum. Moreover, σ and ε_r are the electric conductivity and the relative permittivity of the medium at a certain location of the structure to be simulated. The imaginary part of permittivity, ε_r'', and the conductivity σ of a

material are related by [1]:

$$\sigma = \varepsilon_0 \varepsilon_r'' \omega. \tag{2.158}$$

According to Yee's scheme, by using the electric fields at a given time between two adjacent positions in the x and y directions, Δx and Δy apart, the magnetic fields are obtained in the next instant in time. Subsequently, in the next time instant the electric fields are calculated from the just obtained magnetic fields. This cycle continues until the steady-state solutions to the Maxwell's equation are obtained. Note, that time progresses in a discrete manner with a step Δt. This time step value should be carefully chosen with respect to the spatial discretisation, otherwise the algorithm is not stable [173]. This is determined by the Courant condition [173, 175] given from:

$$\Delta t < \frac{1}{c\sqrt{\left(\frac{1}{\Delta x}\right)^2 + \left(\frac{1}{\Delta y}\right)^2}}, \tag{2.159}$$

where c represents the speed of light in vacuum. i.e.

$$\Delta t = \frac{f_{stab}}{c\sqrt{\left(\frac{1}{\Delta x}\right)^2 + \left(\frac{1}{\Delta y}\right)^2}}, \tag{2.160}$$

where f_{stab} is the Courant stability factor.

2.6.2 Principles and implementation set-up in Lumerical FDTD software for calculation of electric and magnetic fields in periodic systems for EM waves at normal incidence

In Chapter 7, we will investigate the absorption performance of SiC pyramid-shaped 2D-PCs. To gain more insight into the absorption performance in these PC systems, we will require the electric and magnetic field maps of these PCs. In Fig. 2.21, we show the appropriate simulation set-up to obtain the field plots in 2D periodic structures, that extend infinitely in one direction. We assume that this periodic direction is along the x-direction and that the structure has also translational symmetry in the z-direction as shown in Fig. 2.21. The blue rectangle in Fig. 2.21 represents a building block of arbitrary shape that repeats periodically along the x-direction.

In order to simulate this periodic structure, we specify a 2D-FDTD spatial region in the xy-plane, with its length in the x direction equal to the lattice constant of the PC, thus it represents one unit cell of the PC. We apply periodic conditions in the

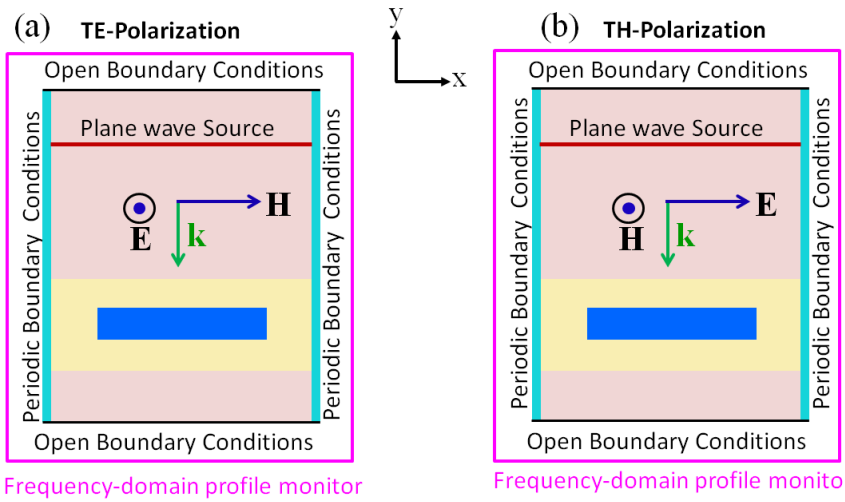

Figure 2.21: (a) Schematics of the simulation set-up in the FDTD simulator to calculate electric and magnetic fields of periodic systems for the TE-polarization case. The boundary conditions in each direction are indicated. The spatial profile of the plane wave EM source is indicated with the brown line in the figure. The polarization of the incident EM wave is also indicated. The frequency domain monitor encompasses the region bounded with the magenta box. The blue block represents the structural element that is repeated periodically in the x-direction. For simplicity we show one block, but more complicated structures can be considered. The yellow shaded region represents the regime where a user defined mesh was used. The brown region represent the region where the default Lumerical simulator [176] mesh has been used. (b) same as (a) but for the TH-polarization case.

x-direction (the aqua lines in the figure) in the software, which effectively simulates an infinitely extending PC along the x-direction. On the other hand, we apply open boundary conditions in the y-direction (the black lines in the figure). These open boundary conditions allow the propagation of fields without reflection at the boundary. We use a plane wave spatial profile for the source. The source is an electric current source (see Eq. 2.154) designated by the brown line in Fig. 2.21(a) for the TE-polarization case. Conversely, we use a magnetic current source (see Eq. 2.157) designated by the brown line in Fig. 2.21(b) for the TH-polarization case.

Within the specified FDTD simulation region, we build the rectangular block (see the blue-block in Fig. 2.21) with the desired structural parameters using the Computer Aided Design (CAD) tool provided with the commercial software [177]. Further, we assign the desired material properties to this rectangular block by representing its permittivity in the material base interface of the software, where a user defined Lorentzian [51] can be introduced for SiC with the precise parameters used in Eq. 2.14 of Section 2.1.

Now we use a user defined mesh that encompasses the structural elements (yellow

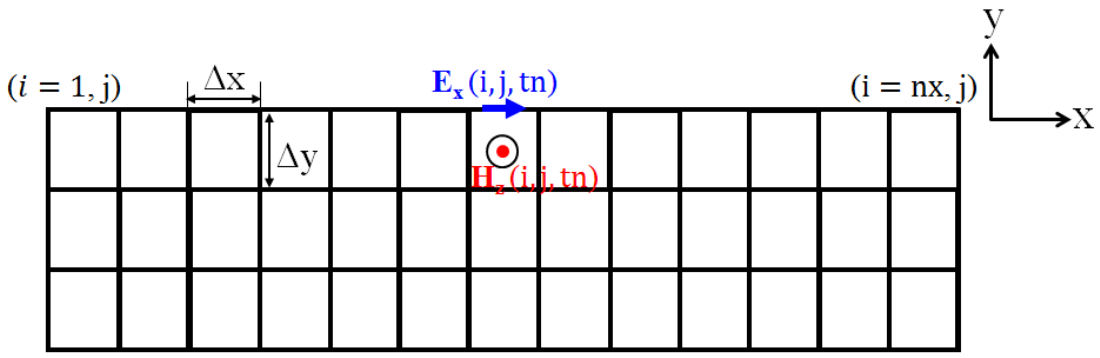

Figure 2.22: Schematic diagram of the part of the frequency-domain profile monitor to show the computation of the electric and magnetic fields in the FDTD method (TH-polarisation case). Δx and Δy designate the discretisation in space, that define the numerical mesh.

region in Fig. 2.21). This allows us to manually control the grid size within the structure to ensure that we use a sufficiently small grid. The grid should be smaller than the wavelength of the EM wave within the structure, and also much smaller than the smallest structural element [4]. Outside this user defined mesh region, we use the software's default mesh which produces a non-uniform mesh. The mesh size gradually increases as we move away from the structural elements but is at least of the order of $\lambda_{\text{free}}/30$ [176], which is adequate for vacuum. Furthermore, we set the Δt stability factor, f_{stab}, to be 0.9, to ensure that the stability condition in Eq. 2.159 is satisfied. Then, we place an EM plane wave source above the PC that injects energy into the simulation region along the y-direction. Such plane wave source, can be set-up with a Gaussian frequency profile, centred around ω_0 [77, 172] as:

$$J_z(t) = Ae^{-(t-t_d)^2/2\sigma_t^2}\cos(\omega_0(t-t_d)), \tag{2.161}$$

where A, t_d, σ_t represent the amplitude, centre of the time profile, and temporal width of the source respectively. The current, $J_z(t)$ in Eq. 2.161, (the electric or the magnetic type depending on polarization) is generated in each mesh point along the brown line in Fig. 2.21. Note, that a larger σ_t in Eq. 2.161 results in smaller spectral width of around ω_0, and vice versa. The simulator typically considers a fast pulse with a spectral interval that contains information for a high number of frequencies. The parameters in Eq. 2.161 are controlled by a special input window of the FDTD Lumerical software. The pulse signal increases and goes to zero, while interacting with the structural elements in the simulation region. The simulation time should be sufficiently large, so that the signal completely passes through the structural elements. This means the fields should be near zero at the end of the simulation in the entire simulation domain. Therefore, we run the simulation until

most of the energy in the simulation region is decayed.

Now, in order to record the field values throughout the simulation region, we use a two-dimensional frequency domain monitor (the magenta box in Fig. 2.21), with its size larger than the simulation region. In this monitor, using a designated input window of the software we can specify the desired frequency/frequencies at which we are interested to plot the fields of the structure. One should avoid choosing frequencies outside the Full Width Half Maximum (FWHM) range of the pulsed signal of Eq. 2.161.

Below we explain further the process of computing these fields during the simulation. In Fig. 2.22, we show the part of the frequency domain monitor schematically. i, j represent the co-ordinates of a grid point in the simulation region. The electric-field values will be updated in each grid point (i, j) of the monitor, at every time step, n and stored by the software. At the end of the simulation, the software performs a Fast Fourier Transform [178] at each grid and stores the result for the frequencies specified in the input frequency domain monitor. By using a special script in the Lumerical software, we retrieve the electric or magnetic fields at each grid point for these initially specified frequency/frequencies [179]. After that we plot the 2D-landscape of these fields at each frequency by using standard visualisation software (MATLAB) [180].

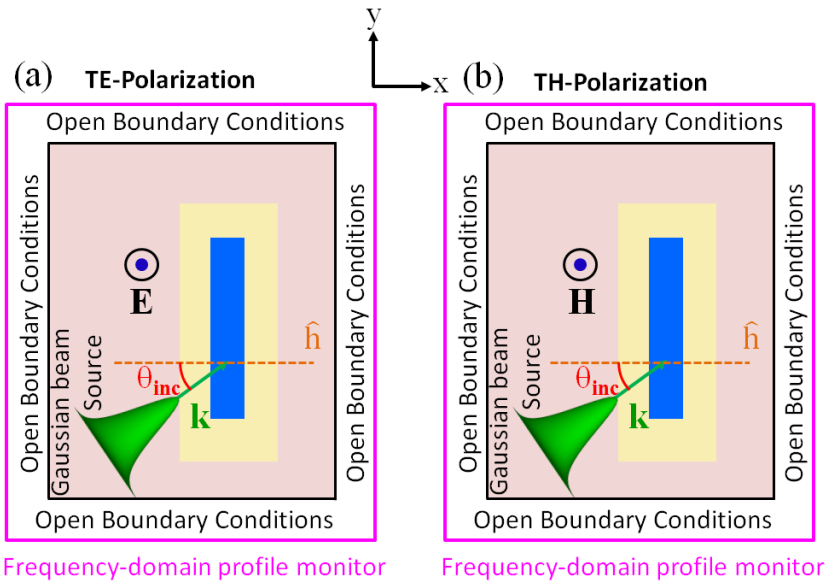

Figure 2.23: Same as Fig. 2.21, but the simulation set-up for systems of finite extent. The main differences from the periodic systems set-up in Fig. 2.21 are the open boundary conditions in both x- and y-directions and the source that has Gaussian spatial profile. The incident angle, θ_{inc} is also indicated.

2.6.3 Implementation set-up in Lumerical FDTD software for calculation of electric and magnetic fields in systems with a finite extent

In Chapters 8 and 9, to understand the EM wave propagation in lossy 1D-PCs, we will investigate PC structures that are finite in extent in both directions. For this purpose, we will require the electric-field maps in these finite-sized PC structures. Therefore, we discuss below the appropriate set-up for simulating such structures in the FDTD Lumerical software [171]. These finite-sized simulation set-ups are useful, since they closely resemble the actual experimental set-ups. For example, with this finite system FDTD simulation set-ups, it is possible to simulate realistic experimental fieldmaps such as a fieldmap from a microwave PC superlens obtained from a raster-scan with a monopole antenna [83] or a fieldmap obtained from a PC cavity from Scanning Near-Field Optical Microscopy (SNOM) experiments on PC cavities [181].

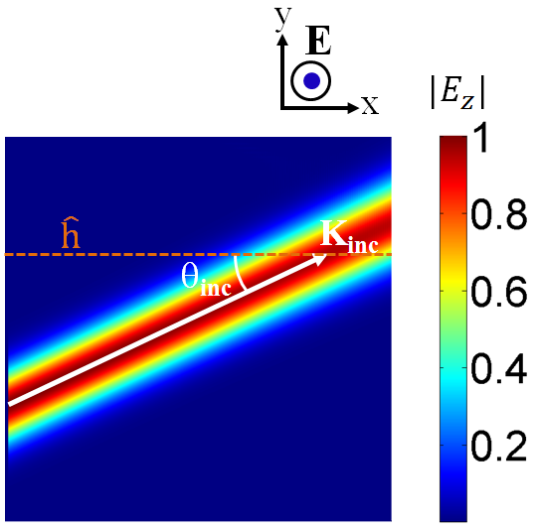

Figure 2.24: The fieldmap of the z-component of the electric field, E_z obtained for a Gaussian beam propagating in free space, at an angle $\theta_{inc} = 45^0$ with the x-axis. The direction of the beam can be clearly seen and has been designated with the incident wavevector, $\mathbf{K_{inc}}$ (white arrow).

In Fig. 2.23, we show the simulation set-up for a finite in extent system. We notice that this simulation set-up is similar to the above discussed periodic systems set-up, expect for the two important settings: the boundary conditions and the EM wave source. Since, the finite-sized systems are not infinitely periodic, we use the open boundary conditions in both x- and y-directions. Furthermore, to simulate realistic type of light sources used in experiments, we set-up a source with a Gaussian spatial

profile. The control parameters to inject a fully vectorial Gaussian beam source are specified through an artificial thin-lens set-up in the software's beam options interface [182, 183]. To launch a highly collimated Gaussian beam, we select the distance from the focus of this artificial lens to be zero. Further, we specify the width of the Gaussian beam by adjusting the numerical aperture and diameter of the lens and the source width size [182, 183]. We show an example of such source incident at 45^0 for a TE-polarised wave in Fig. 2.24.

2.6.4 Principles and implementation set-up in the Lumerical FDTD software for calculation of transmission properties of EM waves at normal incidence on periodic structures

As mentioned before, in Chapter 7, we will study the absorption performance of the SiC pyramid-shaped 2D-PCs. For this purpose, we will require the transmittance, T and reflectance, R calculations of these periodic structures. In the following, we will describe the appropriate simulation set-up in the software for such calculations.

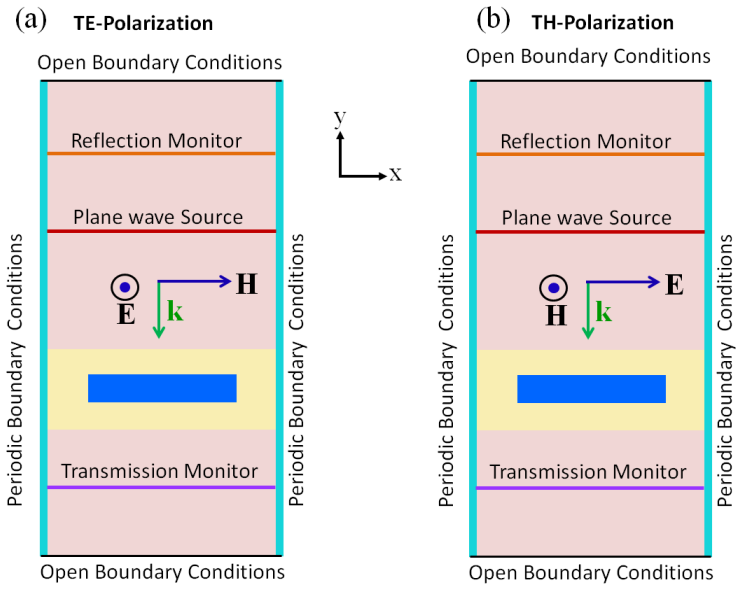

Figure 2.25: Same as Fig. 2.21, but here the simulation set-up aims to calculate the transmittance and reflectance of the structure. The transmission and reflection monitors are designated with the violet lines and the orange lines respectively.

In Fig. 2.25, we show the simulation set-up to calculate the transmission properties of a periodic system. We can see that this set-up is the same as the periodic system

set-up shown in Fig. 2.21 for calculation of the fieldmaps, but now we have two frequency-domain power monitors (violet lines and orange lines in Fig. 2.21) [184] instead of a frequency-domain profile monitor that we used in Fig. 2.21 [184]. These frequency-domain power monitors record the Poynting vector data, through which we can calculate the transmittance and reflectance of the structure as we explain below.

For this purpose, in Fig. 2.26, we show schematically the process of evaluating the Poynting vector, at the transmission power detector positioned at the $j = j_{dt}$ line in the 2D simulation region. Notice the grid area highlighted with a green-dashed-line box in Fig. 2.26 which is positioned at co-ordinate $(i, j = j_{dt})$ of the simulation region. The electric and magnetic fields are obtained as real values during the simulation, and the time series corresponding to these are stored [2]. Subsequently, a Fast Fourier Transformation [178] is performed by the simulator to obtain the complex field values as, $E_x(i, j = j_{dt}, \nu)$ and $H_z(i, j = j_{dt}, \nu)$ respectively, where ν represents the frequency. By using these complex fields, we can evaluate the y-component of the Poynting vector, $S_y(i, j = j_{dt}, \nu)$ as:

$$S_y(i, j = j_{dt}, \nu) = Re(E_x(i, j = j_{dt}, \nu)H_z^*(i, j = j_{dt}, \nu)) \tag{2.162}$$

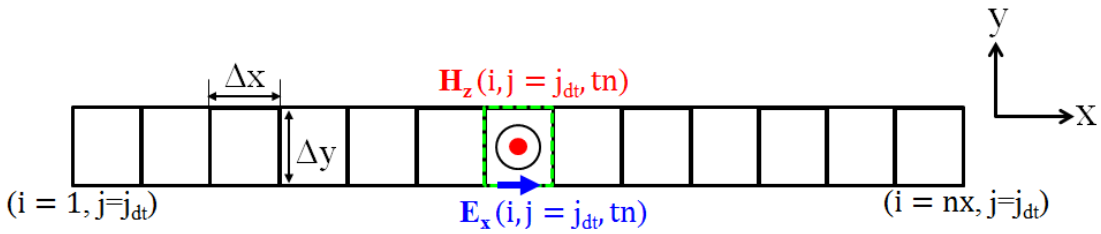

Figure 2.26: Schematic diagram of the frequency-domain power monitor to show the computation of the Poynting vector in the FDTD method, for the TH-polarization case. Δx and Δy designate the discretisation in space. (see also footnote).

Then transmittance, T [185] is evaluated from:

$$T(\nu) = \frac{\frac{1}{2}\int Re(\mathbf{S}(\nu)^{\mathrm{mt}}) \cdot L\mathbf{dl}}{\mathrm{sourcepower}}, \tag{2.163}$$

where $\mathbf{S}(\nu)^{\mathrm{mt}}$ is the Poynting vector at the monitor plane at $j = j_{dt}$, L is an out-of-

[2]Because of the Yee updating cycle there is half a time step apart between the electric field and magnetic field values [174]

plane length unit and **dl** is a length element normal to the monitor line. We can observe from Fig. 2.25, that **dl** will be along the y direction. In Eq. 2.163, the source power designates the amount of the power injected into the simulation region [186], which would be given by:

$$\text{sourcepower}(\nu) = \frac{1}{2}\int Re(\mathbf{S}(\nu)^{\text{sc}}) \cdot L\mathbf{dl}, \tag{2.164}$$

where $\mathbf{S}(\nu)^{\text{sc}}$ designates the Poynting vector at the source line (brown line in Fig. 2.21). Note that out-of-plane length unit, L is in place to preserve units in Eqs. 2.162 and 2.164, but its value is of no consequence in the calculation of the expressions in both the equations. Note that the integrals in Eqs. 2.162 and 2.164 would essentially be a summation of the individual Poynting vector values evaluated at each of the grid points given by Eq. 2.162, along the detector source lines. Therefore, we obtain $T(\nu)$ as:

$$T(\nu) = \frac{\frac{1}{2}\sum_{i=1}^{i=nx} S_y(i, j_{dt}, \nu)}{\frac{1}{2}\sum_{i=1}^{i=nx} S_y(i, j_s, \nu)}, \tag{2.165}$$

where j_s is the y-axis position of the source line. In similar manner we obtain the reflectance $R(\nu)$ as:

$$R(\nu) = \frac{\frac{1}{2}\sum_{i=1}^{i=nx} S_y(i, j_{dr}, \nu)}{\frac{1}{2}\sum_{i=1}^{i=nx} S_y(i, j_s, \nu)}, \tag{2.166}$$

where j_{dr} is the y-axis position of the reflection monitor.

Finally, by using the transmittance and reflectance, we can evaluate the absorptance, $A(\nu)$ of the 2D-PC in this FDTD simulation set-up as:

$$A(\nu) = 1 - T(\nu) - R(\nu). \tag{2.167}$$

Bibliography

[1] J. D. Jackson, *Classial Electrodynamics*, (Wiley, Third edition, 1999)

[2] Q. Cheng, W. X. Jiang, and T. J. Cui, "Spatial Power Combination for Omnidirectional Radiation via Anisotropic Metamaterials," Phys. Rev. Lett. **112**, 068103, (2012).

[3] Y. Cui, K. H. Fung, J. Xu, H. Ma, Y. Jin, S. He, and N. X. Fang, "Ultrabroadband Light Absorption by a Sawtooth Anisotropic Metamaterial Slab," Nano Lett., **12** 14431447, (2012).

[4] S. Foteinopoulou, M. Kafesaki, E. N. Economou, and C. M. Soukoulis, "Two-dimensional polaritonic photonic crystals as terahertz uniaxial metamaterials," Phys. Rev. B **84**, 035128 (2011).

[5] D. J. Griffiths, *Introduction to electrodynamics* (Third edition, Pearson international, 2008).

[6] J. A. Fleck, Jr. and M. D. Feit, "Beam propagation in uniaxial anisotropic media," J. Opt. Soc. Ame. **73**, 920-926 (1983)

[7] P. N. Butcher and T. P. McLean, "The Non-linear Constitutive Relation in Solids at Optical Frequencies," Proc. Phys. Soc. **81**, 219, (1963)

[8] P. D. Maker and R. W. Terhune "Study of Optical Effects Due to an Induced Polarization Third Order in the Electric Field Strength," Phys. Rev. **137** , A801 (1965).

[9] E. U. Condon, Theories of optical rotatory power, Rev. Mod. Phys. **9**, 432457 (1937).

[10] M. P. Silverman, "Reflection and refraction at the surface of a chiral medium: comparison of gyrotropic constitutive relations invariant or noninvariant under a duality transformation," J. Opt. Soc. A. A, **3**, 830-837 (1986).

[11] W. S. Weiglhofer, and A. Lakhtakia,"The correct constitutive relations of chiroplasmas and chiroferrites," Microwave Opt. Tech. Lett. **17**, 405408, (1998).

[12] R. Zhao, Th. Koschny, E. N. Economou, and C. M. Soukoulis "Comparison of chiral metamaterial designs for repulsive Casimir force," Phys. Rev. B **81**, 235126 (2010).

[13] E. Plum, J. Zhou, J. Dong, V. A. Fedotov, T. Koschny, C. M. Soukoulis, and N. I. Zheludev "Metamaterial with negative index due to chirality," Phys. Rev. B **79**, 035407 (2009).

[14] H. Duan, A. I. Fernndez-Domnguez, M. Bosman, S. A. Maier, and J. K. Yang, "Nanoplasmonics: classical down to the nanometer scale," Nano Lett. **12**, 16831689 (2012).

[15] W. L. Barnes, "Metallic metamaterials and plasmonics," Phil. Trans. R. Soc. A **369** 3431-3433 (2011).

[16] V. G. Kravets, G. Zoriniants, C. P. Burrows, F. Schedin, C. Casiraghi, P. Klar, A. K Geim, W. L. Barnes, A. N. Grigorenko, "Cascaded optical field enhancement in composite plasmonic nanostructures," Phys. Rev. Lett. **112**, 068103, (2010).

[17] H. A. Atwater and A. Polman, "Plasmonics for improved photovoltaic devices," Nat. Mat. **9**, 205-213 (2010).

[18] X. Dang, J. Qi, M. T. Klug, Po-Yen Chen, D. Soo Yun, N. X. Fang, P. T. Hammond, and Angela M. Belcher "Tunable Localized Surface Plasmon-Enabled Broadband Light-Harvesting Enhancement for High-Efficiency Panchromatic Dye-Sensitized Solar Cells," Nano Lett. **13**, 637642 (2013,)

[19] K. Aydin, V. E. Ferry, R. M. Briggs, and H. A. Atwater, "Broadband polarization-indepedent resonant light absorption using ultrathin plasmonic super absorbers," Nat. Commun. **2**, 517 (2011)

[20] C. Wu, , I. I. I. Burton Neuner, G. Shvets, J. John, A. Milder, B. Zollars, and S. Savoy, "Large-area wide-angle spectrally selective plasmonic absorber," Physical Review B, **84**, 075102 (2011).

[21] MK Hedayati, F Faupel, M Elbahri, "Review of Plasmonic Nanocomposite Metamaterial Absorber," Materials **7**, 1221-1248 (2014).

[22] V. Voisina, J. Pilateb, P. Dammanb, P. Mgreta, C. Caucheteura, "Highly sensitive detection of molecular interactions with plasmonic optical fiber grating sensors," Biosen. Bioelect. **51**, 249254 (2014).

[23] M. Xiao, R. Jiang, F. Wang, C. Fang, J. Wang and J. C. Yub "Plasmon-enhanced chemical reactions." J. Mat. Chem. A **1**, 5790-5805 (2013).

[24] B. Luk'yanchuk, N. I. Zheludev, S. A. Maier, N. J. Halas, P. Nordlander, H. Giessen and C. T. Chong, "The Fano resonance in plasmonic nanostructures and metamaterials," Nat. Mat. **9**, 707715, (2010).

[25] F. Shafiei, F. Monticone, K. Q. Le, X. X. Liu, T. Hartsfield, A. Al and X. Li, "A subwavelength plasmonic metamolecule exhibiting magnetic-based optical Fano resonance," Nat. Nanotech. **8**, 9599, (2013).

[26] V. G. Kravets, F. Schedin, R. Jalil, L. Britnell, R. V. Gorbachev, D. Ansell, B. Thackray, K. S. Novoselov, A. K. Geim, A. V. Kabashin and A. N. Grigorenko, "Singular phase nano-optics in plasmonic metamaterials for label-free single-molecule detection," Nat. Mat. **12**, 304309 (2013).

[27] J. A. Schuller, E. S. Barnard, W. Cai, Y. C. Jun, J. S. White and M. L. Brongersma, "Plasmonics for extreme light concentration and manipulation," Nat. Mat. **9**, 193204, (2010).

[28] O. L. Muskens, V. Giannini, J. A. Snchez-Gil,and J. Gmez Rivas, "Strong enhancement of the radiative decay rate of emitters by single plasmonic nanoantennas," Nano Lett. **9**, 28712875 (2007).

[29] O. Sqalli, M.-P. Bernal, P. Hoffmann and F. Marquis-Weible,"Improved tip performance for scanning near-field optical microscopy by the attachment of a single gold nanoparticle," Appl. Phys. Lett. **76**, 2134 (2000).

[30] J. R. Krenn, A. Dereux, J. C. Weeber, E. Bourillot, Y. Lacroute, J. P. Goudonnet, G. Schider, W. Gotschy, A. Leitner, F. R. Aussenegg, and C. Girard "Squeezing the Optical Near-Field Zone by Plasmon Coupling of Metallic Nanoparticles," Phys. Rev. Lett. **82**, 2590, (1999).

[31] S. Yokogawa, S. P Burgos, H. A Atwater "Plasmonic color filters for CMOS image sensor applications," Nano lett. **12**, 4349-4354, (2012).

[32] L. Tang, S. Latif, and D. A. B. Miller, "Plasmonic device in silicon CMOS," Electr. lett. **45**, 706-708 (2009)

[33] J. T. Kim, "CMOS-compatible hybrid plasmonic waveguide for subwavelength light confinement and on-chip integration," Phot. Tech. Lett., IEEE, **23**, 206-208 (2011).

[34] M. S. Tame, K. R. McEnery, . K. zdemir, J. Lee, S. A. Maier and M. S. Kim,"Quantum plasmonics," Nat. Phys. **9**, 329340 (2013).

[35] S. A. Maier, M. D. Friedman, P. E. Barclay, and O. Painter, "Experimental demonstration of fiber-accessible metal nanoparticle plasmon waveguides for planar energy guiding and sensing," Appl. Phys. Lett. **86**, 071103, (2005).

[36] E. Ozbay, "Plasmonics: Merging photonics and electronics at nanoscale dimensions," Science **311**, 189193 (2006).

[37] N. P. De Leon, M. D. Lukin, and H. Park, "Quantum plasmonic circuits," IEEE Sel. Top. Quant. Elec. **18**, 17811791 (2012).

[38] D. E. Chang, A. S Srensen, E. A. Demler, and M. D. Lukin, "A single-photon transistor using nanoscale surface plasmons," Nature Phys. **3**, 807812 (2007).

[39] S. A Maier, M. L Brongersma, P. G Kik, S. Meltzer, A. A. G Requicha, H. A Atwater, "Plasmonicsa route to nanoscale optical devices," Adv. Mat. **13** , 1501-1505 (2001).

[40] S. Foteinopoulou, J. P. Vigneron, C. Vandenbem, "Optical near-field excitations on plasmonic nanoparticle-based structures," Opt. Express. **15**, 4253-4267 (2003).

[41] John H. Booske, "Plasma physics and related challenges of millimeter-wave-to-terahertz and high power microwave generation," Phys. Plasmas **15**, 055502 (2008).

[42] L. Stephanie, V. Podolskiy, and D. Wasserman. "Towards nano-scale photonics with micro-scale photons: the opportunities and challenges of mid-infrared plasmonics." Nanophotonics **2** 103-130, (2013).

[43] M. A. Ordal, L. L. Long, R. J. Bell, S. E. Bell, R. R. Bell, R. W. Alexander, Jr., and C. A. Ward, "Optical properties of the metals Al, Co, Cu, Au, Fe, Pb, Ni, Pd, Pt, Ag, Ti, and W in the infrared and far infrared", Appl. Opt. **22**, 1099-1119 (1983).

[44] W. Streyer, S. Law, A. Rosenberg, C. Roberts, V. A. Podolskiy, A. J. Hoffman and D. Wasserman "Engineering absorption and blackbody radiation in the far-infrared with surface phonon polaritons on gallium phosphide," Appl. Phys. Lett. **104**, 131105 (2014)

[45] T. Feurer, N. S. Stoyanov, D. W. Ward, J. C. Vaughan, E. R. Statz, and K. A. Nelson "Terahertz Polaritonics," Annu. Rev. Mater. Res. **37**, 317-350 (2007).

[46] W. Dai, D. Yap, and G. Chen, "Wideband enhancement of infrared absorption in a direct band-gap semiconductor by using nonabsorptive pyramids", Opt. Express, **20**, A519 (2012).

[47] T. Tanabe, K. Suto, J. Nishizawa, K. Saito and Tomoyuki Kimura, "Frequency-tunable terahertz wave generation via excitation of phonon-polaritons in GaP," J. Phys. D: Appl. Phys. **36**, 953, (2003).

[48] N. S. Stoyanov, D. W. Ward, T. Feurer and K. A. Nelson, "Terahertz polariton propagation in patterned materials," Nature Materials **1**, 95 - 98 (2002).

[49] P. B. Catrysse and S. Fan, "Near-complete transmission through subwavelength hole arrays in phonon-polaritonic thin films," Phys. Rev. B, **75**, 075422 (2007).

[50] Jon A. Schuller, R. Zia, T. Taubner, and M. L. Brongersma, "Dielectric Metamaterials Based on Electric and Magnetic Resonances of Silicon Carbide Particles," Phys. Rev. Lett. **99**, 107401 (2007).

[51] C. Kittel, *Introduction to Solid State Physics* (John Wiley and Sons, Hoboken, 2005).

[52] R. Loudon, "The propagation of electromagnetic energy through an absorbing dielectric," J. Phys. A **3**, 233245 (1970).

[53] U. T. Schwarz and M. Maier, "Damping mechanisms of phonon polaritons, exploited by stimulated Raman gain measurements," Phys. Rev. B **58**, 766 (1998).

[54] D. W. Berreman and F. C. Unterwald, "Adjusting Poles and Zeros of Dielectric Dispersion to Fit Reststrahlen of $PrCl_3$ and $LaCl_3$," Phys. Rev. **174**, 791 (1968).

[55] U. Fano, "Atomic theory of electromagnetic interactions in dense materials," Phys. Rev. **103**, 1202 (1956).

[56] U. Fano and J. W. Cooper, "Spectral distribution of atomic oscillator strengths," Rev. Mod. Phys. **40**, 441 (1968).

[57] J. J. Hopfield, "Theory of the contribution of excitons to the complex dielectric constant of crystals," Phys. Rev. **112**, 1555 (1958).

[58] H. Rubens and E. F. Nichols, "ber Wrmestrahlen von grosser Wellenlnge, in Naturwissenschaftliche Rundschau," 11 545549 (1896).

[59] E. D. Palik, "History of far-infrared research. I. The Rubens era," JOSA **67**, 857865 (1977).

[60] E. D. Palik, *Handbook of Optical Constants of Solids* (Academic Press, 1985).

[61] R. W. Waynant, I. K. Ilev and I. Gannot, "Mid-infrared laser applications in medicine and biology," Phil. Trans. R. Soc. Lond. A., **359**, 635-644 (2001).

[62] B. Mizaikoff, "Waveguide-enhanced mid-infrared chem/bio sensors," Chem. Soc. Rev., **42**, 8683-8699 (2013).

[63] J. M. Bakker, L. M. Aleese, G. Meijer, and G. von Helden, "Finger-print IR spectroscopy to probe amino acid conformations in the gas phase," Phys. Rev. Lett., **91**, 203003 (2003).

[64] R. Assendorp, P. R. Wesselius, D. C. B. Whittet, and T. Prusti, "A study of the Chamaeleon I Dark Cloud and T-association II: High resolution IRAS maps around HD97048 and HD97300,,"Mon. Not. R. Astro. Soc., **247**, 624-631 (1990).

[65] H. L. Johnson and W. W. Morgan, "Fundamental stellar photometry for standards of spectral type on the revised system of the Yerkes spectral atlas," Astrophysical Journal, **117**, 313-352 (1953).

[66] H.U. Kufl, "Ground-based astronomy in the 10 and 20 μm atmospheric windows at ESO scientific potential at present and in the future," The Messenger, **73**, 8-12 (1993).

[67] `http://ftp.esrf.eu/pub/scisoft/xop2.3/DabaxFiles/nk_Palik.dat`

[68] F. Wooten, *Optical properties of Solids*, (Academic press, Newyork, 1972).

[69] J. H. Poynting, "On the Transfer of Energy in the Electromagnetic Field". Philo. Trans. Roy. Soc. London **175** 343361, (1884).

[70] R. Ruppin, "Electromagnetic energy density in a dispersive and absorptive material," Phys. Lett. A **299**, 309312 (2002).

[71] S. Anantha Ramakrishna and T.M. Grzegorczyk, *Physics and Applications of Negative Refractive Index Materials* (CRC Press and SPIE Press, 2008).

[72] L. Brillouin, *Wave Propagation in Periodic Structures: Electric Filters and Crystal Lattices* (Courier Dover Publications, 1953).

[73] P. Yeh, *Optical waves in layered media* (Wiley-Interscience, Hoboken 2005).

[74] P. Yeh, "Electromagnetic propagation in birefringent layered media," J. Opt. Soc. Am. A **69**, 742756 (1979).

[75] C. A. Balanis, *Advanced engineering electromagnetics*, (Wiley, Canada, 1968)

[76] P. Markos and C. M. Soukoulis, *Wave Propagation: From Electrons to Photonic Crystals and Left-Handed Materials* (Princeton University Press, 2008).

[77] S. Foteinopoulou, "Electromagnetic wave propagation in two-dimensional photonic crystals," Ph.D thesis, Iowa State University (2003).

[78] S. Foteinopoulou and C. M. Soukoulis, "Electromagnetic wave propagation in two-dimensional photonic crystals: A study of anomalous refractive effects," Phys. Rev. B **72**, 165112 (2005).

[79] J. B. Pendry, "Negative refraction makes a perfect lens," Phys. Rev. Lett. **85**, 3966 (2000).

[80] N. Fang, H. Lee, C. Sun, and X. Zhang, "Subdiffraction-limited optical imaging with a silver superlens," Science **308**, 534537 (2005).

[81] T. Taubner, D. Korobkin, Y. Urzhumov, G. Shvets, and R. Hillenbrand, "Near-field microscopy through a SiC superlens.," Science **313**, 1595 (2006).

[82] P. Chaturvedi, W. Wu, V. J. Logeeswaran, Z. Yu, M. S. Islam, S. Y. Wang, R. S. Williams, and N. X. Fang, "A smooth optical superlens," Appl. Phys. Lett. **96**, 43102 (2010).

[83] E. Cubukcu, K. Aydin, and E. Ozbay, S. Foteinopoulou, and C. M. Soukoulis, "Subwavelength Resolution in a Two-Dimensional Photonic-Crystal-Based Superlens," Phys. Rev.Lett. **91**, 207401 (2003).

[84] N. Landy, S. Sajuyigbe, J. Mock, D. Smith, and W. Padilla, "Perfect Metamaterial Absorber," Phys. Rev. Lett. **100**, 207402 (2008).

[85] H. Tao, N. I. Landy, C. M. Bingham, X. Zhang, R. D. Averitt, and W. J. Padilla, "A metamaterial absorber for the terahertz regime: Design, fabrication and characterization," Opt. Express **16**, 71817188 (2008).

[86] J. Hendrickson, J. Guo, B. Zhang, W. Buchwald, and R. Soref, "Wideband perfect light absorber at midwave infrared using multiplexed metal structures," Opt. Lett. **37**, 371373 (2012).

[87] L. Meng, D. Zhao, Q. Li, and M. Qiu, "Polarization-sensitive perfect absorbers at near-infrared wavelengths," Opt. Express **21**, A111A122 (2013).

[88] H. Kosaka, T. Kawashima, A. Tomita, M. Notomi, T. Tamamura, T. Sato, and S. Kawakami, "Superprism phenomena in photonic crystals," Phys. Rev. B**58**, R10096 (1998).

[89] M. Notomi, "Theory of light propagation in strongly modulated photonic crystals: Refractionlike behavior in the vicinity of the photonic band gap," Phys. Rev. B **62**, 10696 (2000).

[90] M.-P. Bernal, J. Amet, J. Safioui, F. Devaux, M. Chauvet, J. Salvi, and F. I. Baida, "Pyroelectric control of the superprism effect in a lithium niobate photonic crystal in slow light configuration," Appl. Phys. Lett. **98**, 71101 (2011).

[91] N. K. Grady, J. E. Heyes, D. R. Chowdhury, Y. Zeng, M. T. Reiten, A. K. Azad, A. J. Taylor, D. A. R. Dalvit, and H.-T. Chen, "Terahertz metamaterials for linear polarization conversion and anomalous refraction," Science (80-.). 340, 13041307 (2013).

[92] J. D. Joannopoulos, S. G. Johnson, J. N. Winn and R. D. Mead, *Photonic Crystals: Molding the Flow of light* (Princeton University Press, Princeton, 2008)

[93] S. John in Photonic Band Gap Materials, Vol 315 of NATO Advanced Studies Institute, Series E: Applied sciences, edited by C. M. Soukoulis (Kluwer, Dordrecht, 1996). p. 563.

[94] E. Yablonovitch, "Inhibited spontaneous emission in solid-state physics and electronics," Phys. Rev. Lett. **58**, 2059-2062 (1987).

[95] S. John, "Strong Localization of Photons in Certain Disordered Dielectric Superlattices," Phys. Rev. Lett. **58**, 24862489 (1987).

[96] Lord Rayleigh, "On the Maintenance of Vibrations by Forces of Double Frequency, and on the Propagation of Waves Through a Medium Endowed with a Periodic Structure," Phil. Mag. S.5, **24**, 145-159 (1887).

[97] Lord Rayleigh, "On the Remarkable Phenomenon of Crystalline Reflexion described by Professor Stokes," Phil. Mag. S.5, **26**, 256-265 (1888).

[98] G. Floquet, "Sur les equations differentielles lineaires," Ann. ENS **12**, 4788 (1883).

[99] F. Abeles, "* Sur la propagation des ondes electromagnetiques dans les milieux stratifies," Anna. Phys. **3** 504-520 (1948).

[100] P. Yeh, A. Yariv, and C. S. Hong, "Electromagnetic propagation in periodic stratified media. I. General theory*," J. Opt. Soc. Am., **67**, 423-438 (1977).

[101] A. Yariv and P. Yeh, "Electromagnetic propagation in periodic stratified media. II. Birefringence, phase matching, and x-ray lasers," J. Opt. Soc. Am., **67**, 438-447 (1977).

[102] E. Yablonovitch and T. J. Gmitter, "Photonic band structure: The face-centered-cubic case," Phys. Rev. Lett. **63**, 1950 (1989).

[103] C. Elachi, "Waves in active and passive periodic structures: A review," Proc. IEEE **64**, 16661698 (1976).

[104] P. St. J. Russell, T. A. Birks, and F.DominicLloyd-Lucas, in Confined Electrons and Photons, New Physics and Applications, Vol. **340** of NATO Advanced Studies Institute, Series B: Physics, edited by E. Burstein and C. Weisbuch (Plenum, New York, 1995), p. 585.

[105] J. Manzanares-Martinez, R. Archuleta-Garcia, P. Castro-Garay, D. Moctezuma-Enriquez, and E. Urrutia-Banuelos, "One-dimensional photonic heterostructure with broadband omnidirectional reflection," Prog. Electromagn. Res. **111**, 105117 (2011).

[106] Y. Fink, J. N. Winn, S. Fan, C. Chen, J. Michel, J. D. Joannopoulos, and E. L. Thomas, "A dielectric omnidirectional reflector," Science, **282**, 16791682 (1998).

[107] J. N. Winn, Y. Fink, S. Fan, and J. D. Joannopoulos, "Omnidirectional reflection from a one-dimensional photonic crystal," Opt. Lett. **23**, 15731575 (1998).

[108] B. J. Lee, C. J. Fu, and Z. M. Zhang, "Coherent thermal emission from one-dimensional photonic crystals," Appl. Phys. Lett. **87**, 71904 (2005).

[109] N. P. Sergeant, O. Pincon, M. Agrawal, and P. Peumans, "Design of wide-angle solar-selective absorbers using aperiodic metal-dielectric stacks," Opt. Express **17**, 2280022812 (2009).

[110] F. O'Sullivan, I. Celanovic, N. Jovanovic, J. Kassakian, S. Akiyama, and K. Wada, "Optical characteristics of one-dimensional SiSiO2 photonic crystals for thermophotovoltaic applications," J. Appl. Phys. **97**, 033529 (2005).

[111] H. Jiang, H. Chen, H. Li, Y. Zhang, and S. Zhu, "Compact high-Q filters based on one-dimensional photonic crystals containing single-negative materials," J. Appl. Phys. **98**, 013101 (2005).

[112] E. Kuramochi, H. Taniyama, T. Tanabe, K. Kawasaki, Y.-G. Roh, and M. Notomi, "Ultrahigh-Q one-dimensional photonic crystal nanocavities with modulated mode-gap barriers on SiO2 claddings and on air claddings," Opt. Express **18**, 1585915869 (2010).

[113] B. Maes, J. Petrek, S. Burger, P. Kwiecien, J. Luksch, and I. Richter, "Simulations of high-Q optical nanocavities with a gradual 1D bandgap," Opt. Express **21**, 67946806 (2013).

[114] S. Y. Choi, M. Mamak, G. von Freymann, N. Chopra, and G. A. Ozin, "Mesoporous Bragg Stack Color Tunable Sensors," Nano Lett. 6, 24562461 (2006).

[115] S. Colodrero, M. Ocaa, and H. Mguez, "Nanoparticle-Based One-Dimensional Photonic Crystals," Langmuir 24, 44304434 (2008).

[116] A. Katzir, A. C. Livanos, J. Shellan, and A. Yariv, "Chirped gratings in integrated optics," Quantum Electron. IEEE J. **13**, 296304 (1977).

[117] A. Mouldi and M. Kanzari, "Design of an omnidirectional mirror using one dimensional photonic crystal with graded geometric layers thicknesses," Opt. J. Light Electron Opt. **123**, 125131 (2012).

[118] A. Mouldi and M. Kanzari, "Broad multilayer antireflection coating by apodized and chirped photonic crystal," Opt. Commun. **284**, 41244128 (2011).

[119] V. G. Veselago, "THE ELECTRODYNAMICS OF SUBSTANCES WITH SIMULTANEOUSLY NEGATIVE VALUES OF ε, μ" Physics-Uspekhi **10**, 509514 (1968).

[120] T.-B. Wang, C.-P. Yin, W.-Y. Liang, J.-W. Dong, and H.-Z. Wang, "Electromagnetic surface modes in one-dimensional photonic crystals with dispersive metamaterials," J. Opt. Soc. Am. B **26**, 16351640 (2009).

[121] C. Vandenbem, "Electromagnetic surface waves of multilayer stacks: coupling between guided modes and Bloch modes," Opt. Lett. **33**, 22602262 (2008).

[122] J. Li, L. Zhou, C. T. Chan, and P. Sheng, "Photonic band gap from a stack of positive and negative index materials," Phys. Rev. Lett. **90**, 83901 (2003).

[123] H. Daninthe, S. Foteinopoulou, and C. M. Soukoulis, "Omni-reflectance and enhanced resonant tunneling from multilayers containing left-handed materials," Phot. Nanostru. Fund. Appl. **4**, 123131 (2006).

[124] I. V Shadrivov, A. A. Sukhorukov, and Y. S. Kivshar, "Complete band gaps in one-dimensional left-handed periodic structures," Phys. Rev. Lett. **95**, 193903 (2005).

[125] Y. Cao and J. Li, "Complete band gaps in one-dimensional photonic crystals with negative refraction arising from strong chirality," Phys. Rev. B **89**, 115420 (2014).

[126] J. B. Pendry, D. Schurig, and D. R. Smith, "Controlling electromagnetic fields," Science. **312**, 17801782 (2006).

[127] W. Cai and V. M. Shalaev, Optical Metamaterials (Springer, 2010)

[128] C. M. Soukoulis and M. Wegener, "Past achievements and future challenges in the development of three-dimensional photonic metamaterials," Nat. Photonics **5**, 523530 (2011).

[129] D. R. Smith, W. J. Padilla, D. C. Vier, S. C. Nemat-Nasser, and S. Schultz, "Composite medium with simultaneously negative permeability and permittivity," Phys. Rev. Lett. **84**, 4184 (2000).

[130] J. B. Pendry, A. J. Holden, W. J. Stewart, and I. Youngs, "Extremely low frequency plasmons in metallic mesostructures," Phys. Rev. Lett. **76**, 4773 (1996).

[131] J. B. Pendry, A. J. Holden, D. J. Robbins, and W. J. Stewart, "Magnetism from conductors and enhanced nonlinear phenomena," Microw. Theory Tech. IEEE Trans. **47**, 20752084 (1999).

[132] S. Foteinopoulou, "Photonic crystals as metamaterials," Phys. B Condens. Matter **407**, 40564061 (2012).

[133] R. A. Shelby, D. R. Smith, and S. Schultz, "Experimental verification of a negative index of refraction," Science **292**, 7779 (2001).

[134] C. Parazzoli, R. Greegor, K. Li, B. Koltenbah, and M. Tanielian, "Experimental Verification and Simulation of Negative Index of Refraction Using Snells Law," Phys. Rev. Lett. **90**, 107401 (2003).

[135] D. R. Smith and D. Schurig, "Electromagnetic wave propagation in media with indefinite permittivity and permeability tensors," Phys. Rev. Lett. **90**, 77405 (2003).

[136] C. Garca-Meca, J. Hurtado, J. Mart, A. Martnez, W. Dickson, and A. V Zayats, "Low-loss multilayered metamaterial exhibiting a negative index of refraction at visible wavelengths," Phys. Rev. Lett. **106**, 67402 (2011).

[137] D. R. Smith, J. B. Pendry, and M. C. K. Wiltshire, "Metamaterials and negative refractive index," Science **305**, 788792 (2004).

[138] Z. Li, M. Mutlu, and E. Ozbay, "Chiral metamaterials: from optical activity and negative refractive index to asymmetric transmission," J. Opt. **15**, 23001 (2013).

[139] S. N. Sheikholeslami, H. Alaeian, A. L. Koh, and J. A. Dionne, "A metafluid exhibiting strong optical magnetism," Nano Lett. **13**, 41374141 (2013).

[140] A. Al and N. Engheta, "Dynamical theory of artificial optical magnetism produced by rings of plasmonic nanoparticles," Phys. Rev. B **78**, 85112 (2008).

[141] Y. A. Urzhumov and G. Shvets, "Optical magnetism and negative refraction in plasmonic metamaterials," Solid State Commun. **146**, 208220 (2008).

[142] J. C. Ginn, I. Brener, D. W. Peters, J. R. Wendt, J. O. Stevens, P. F. Hines, L. I. Basilio, L. K. Warne, J. F. Ihlefeld, and P. G. Clem, "Realizing optical magnetism from dielectric metamaterials," Phys. Rev. Lett. **108**, 97402 (2012).

[143] A. N. Grigorenko, A. K. Geim, H. F. Gleeson, Y. Zhang, A. A. Firsov, I. Y. Khrushchev, and J. Petrovic, "Nanofabricated media with negative permeability at visible frequencies," Nat Phot. **438**, 335338 (2005).

[144] C. L. Cortes, W. Newman, S. Molesky, and Z. Jacob, "Quantum nanophotonics using hyperbolic metamaterials," J. Opt. 14, 63001 (2012).

[145] A. Poddubny, I. Iorsh, P. Belov, and Y. Kivshar, "Hyperbolic metamaterials," Nat Phot. 7, 948957 (2013).

[146] A. Fang, T. Koschny, and C. M. Soukoulis, "Optical anisotropic metamaterials: Negative refraction and focusing," Phys. Rev. B 79, 245127 (2009).

[147] C. L. Cortes, W. Newman, S. Molesky, and Z. Jacob, "Quantum nanophotonics using hyperbolic metamaterials," J. Opt. 14, 63001 (2012).

[148] A. J. Hoffman, L. Alekseyev, S. S. Howard, K. J. Franz, D. Wasserman, V. a Podolskiy, E. E. Narimanov, D. L. Sivco, and C. Gmachl, "Negative refraction in semiconductor metamaterials.," Nat. Mater. 6, 94650 (2007).

[149] H. Lee, Z. Liu, Y. Xiong, C. Sun, and X. Zhang, "Development of optical hyperlens for imaging below the diffraction limit," Opt. Express 15, 1588615891 (2007).

[150] Z. Jacob, L. V Alekseyev, and E. Narimanov, "Optical hyperlens: far-field imaging beyond the diffraction limit," Opt. Express 14, 82478256 (2006).

[151] Z. Liu, H. Lee, Y. Xiong, C. Sun, and X. Zhang, "Far-field optical hyperlens magnifying sub-diffraction-limited objects," Science. 315, 1686 (2007).

[152] A. Salandrino and N. Engheta, "Far-field subdiffraction optical microscopy using metamaterial crystals: Theory and simulations," Phys. Rev. B 74, 75103 (2006).

[153] D. E. Aspnes, "Local-field effects and effective-medium theory: A microscopic perspective ," Am. J. Phys. **50**, 704-709 (1982).

[154] D. A. G. Bruggeman, "Berechnung verschiedener physikalischer Konstanten von heterogenen Substanzen. I. Dielektrizitaetskonstanten und Leitfaehigkeiten der Mischkoerper aus isotropen Substanzen," Ann. Phys. (Leipzig), **24**, 636-664 (1935).

[155] J. C. M. Garnett, "Colours in Metal Glasses and in Metallic Films," Philos. Trans. R. Soc. London A, **203**, 385-420 (1904).

[156] J. C. M. Garnett, "Colours in Metal Glasses, in Metallic Films, and in Metallic Solutions. II," Philos. Trans. R. Soc. London A, **205**, 237-288 (1906).

[157] A. Kirchner, K. Busch and C. M. Soukoulis, "Transport properties of random arrays of dielectric cylinders," Phys. Rev. B, **57**, 277 (1998).

[158] V. M. Shalaev, W. Cai, U. K. Chettiar, H.-K. Yuan, A. K. Sarychev, V. P. Drachev, and A. V Kildishev, "Negative index of refraction in optical metamaterials," Opt. Lett. **30**, 33563358 (2005).

[159] M. Born and E. Wolf, *Principles of Optics : Electromagnetic Theory of Propagation, Interference, and Diffraction of Light*, (University Press, Cambridge, 2006).

[160] A. Yariv and P. Yeh, *Optical Waves in Crystals: Propagation and Control of Laser Radiation* (Wiley-Interscience, Hoboken 1984).

[161] K. M. Ho, C. T. Chan, and C. M. Soukoulis, "Existence of a photonic gap in periodic dielectric structures," Phys. Rev. Lett. **65**, 3152 (1990).

[162] F. Bloch "ber die Quantenmechanik der Elektronen in Kristallgittern," Z. Physik **52** 555600 (1928).

[163] B. Jiang, Y. Zhang, Y. Wang, and W. Zheng, "Band structure of photonic crystal with dispersive and lossy materials using Dirichlet-to-Neumann wave vector eigen equation method," J. App. Phys. **112**, 033112 (2012).

[164] T. W. Chang, J .J. Wu, and C. J. Wu, " Complex photonic band structures in a photonic crystal containing lossy semiconductor InSb," Prog. in Electromagn. Research **131**, 153-167, (2012).

[165] M. Bergmair, M. Huber, and K. Hingerl, "Band structure, Wiener bounds, and coupled surface plasmons in one dimensional photonic crystals," Appl. Phys. Lett. **89**, 081907 (2006).

[166] S. Foteinopoulou, E. N. Economou, and C. M. Soukoulis, "Refraction in Media with a Negative Refractive Index," Phys. Rev. Lett. **90**, 107402 (2003).

[167] I. V. Lindell, S. A. Tretyakov, K. I. Nikoskinen, S. Ilvonen, "BW media-media with negative parameters, capable of supporting backward waves," Microwave Opt. Tech. Lett. **31**, 163-165 (20ra01).

[168] S. Foteinopoulou and C. M. Soukoulis, "Negative refraction and left-handed behavior in two-dimensional photonic crystals," Phys. Rev. B **67**, 235107 (2003).

[169] S. Foteinopoulou, M. Kafesaki, E. N. Economou, and C. M. Soukoulis,"Backward surface waves at photonic crystals," Phys. Rev. B **75**, 245116 (2007).

[170] S. Foteinopoulou, G. Kenanakis, N. Katsarakis, I. Tsiapa, M. Kafesaki, E. N. Economou and C. M. Soukoulis, "Experimental verification of backward wave propagation at photonic crystal surfaces," Appl. Phys. Lett. **91**, 214102 (2007).

[171] Lumerical Solutions, Inc. `http://www.lumerical.com/tcad-products/fdtd/`

[172] A. Taflove, "Application of the finite-difference time-domain method to sinusoidal steady state electromagnetic penetration problems," IEEE Trans. Electroma. Compatibility **22** 191202 (1980).

[173] A. Taflove, *Computational ElectrodynamicsThe Finite Difference Time-Domain Method* (Artech House, Boston, 1995)

[174] K. Yee, "Numerical solution of initial boundary value problems involving Maxwell's equations in isotropic media," IEEE Trans. Ante. Prop. **14** 302307 (1966).

[175] R. Courant, K. O. Friedrichs, and H. Lewy "ber die partiellen Differenzengleichungen der mathematischen Physik". Mathematische Annalen **100** : 3274, (1928).

[176] Lumerical Solutions, Inc. `http://docs.lumerical.com/en/fdtd/ref_sim_obj_mesh_settings_tab.html`

[177] Lumerical Solutions, Inc. `http://docs.lumerical.com/en/fdtd/get_started_fdtd_gui.html`

[178] P. Duhamel and M. Vetterli, "Fast Fourier transforms: A tutorial review and a state of the art," Sign. Proc. **19**, 259299, (1990).

[179] Lumerical Solutions, Inc. `http://docs.lumerical.com/en/fdtd/ref_scripts_pinch.html`

[180] `http://www.mathworks.co.uk/`

[181] S. Mujumdar, A. Koenderink, T. Snner, B. Buchler, M. Kamp, A. Forchel, and V. Sandoghdar, "Near-field imaging and frequency tuning of a high-Q photonic crystal membrane microcavity," Opt. Express **15**, 17214-17220 (2007).

[182] Lumerical Solutions, Inc. `http://docs.lumerical.com/en/fdtd/ref_sim_obj_beam_options_tab.html`

[183] Lumerical Solutions, Inc. `http://docs.lumerical.com/en/fdtd/ref_sim_obj_radiation_sources.html`

[184] Lumerical Solutions, Inc. `http://docs.lumerical.com/en/fdtd/ref_sim_obj_measurement_monitors.html`

[185] Lumerical Solutions, Inc. `http://docs.lumerical.com/en/fdtd/ref_scripts_transmission.html`

[186] Lumerical Solutions, Inc. `http://docs.lumerical.com/en/fdtd/ref_scripts_sourcepower.html`

3

Mid-IR near-perfect absorption with a SiC photonic crystal with angle-controlled polarization selectivity

3.1 Chapter overview

In this Chapter[1,2], we present our first theoretical investigations of absorption enhancement with SiC microstructures. In particular, we demonstrate a near-perfect absorption with a SiC 1D-PC in the phonon-polariton mid-gap of SiC. As we explained in the previous Chapter, in this frequency region most of the light will be reflected from bulk SiC. However, we show that high absorption can be obtained in this highly reflecting spectrum, by carefully tailoring the energy velocity of the EM wave at the input interface to satisfy the theoretically derived reflectionless conditions, that we present in Section 3.5 of this chapter. We demonstrate that

[1]Per Section 2.2 of code of practice for presentation of Theses, this chapter is presented as published in the paper: Ganga Chinna Rao Devarapu and Stavroula Foteinopoulou, "Mid-IR near-perfect absorption with a SiC photonic crystal with angle controlled polarization selectivity," Opt. Express **20**, 13040-13054 (2012) [© Optical Society of America. See `http://dx.doi.org/10.1364/OE.20.013040`].

[2]This paper was published in Optics Express and is made available as an electronic reprint with the permission of OSA. The paper can be found at the following URL on the OSA website: `http://dx.doi.org/10.1364/OE.20.013040`. Systematic or multiple reproduction or distribution to multiple locations via electronic or other means is prohibited and is subject to penalties under law.

such high control of energy velocity can be achieved by appropriately terminating the SiC layer at the entrance of the PC. In addition, we will also explore the angular and polarization dependency of the near-perfect absorptive property in these SiC 1D-PCs. Although the thickness of the PC absorber presented in this Chapter is larger than the operating wavelength by a factor of 20, we will show in Chapter 5 that the insights gained by the investigations in this chapter will lead to a compact absorber with a total thickness of just one-third of the impinging wavelength.

Before proceeding to our results and analysis we briefly recap the methods employed in this chapter. The results in this chapter have been calculated with computer programs that have been developed based on Yariv and Yeh's Transfer Matrix Method (TMM) [1, 2] that we have presented in Chapter 2, adapted to the specific parameters of the structures studied here.

Abstract

We theoretically investigate mid-IR absorption enhancement with a SiC one-dimensional photonic crystal (PC) microstructure at the frequency regime of the phonon-polariton band gap, where efficient absorption is unattainable in the bulk material. Our study reveals an intricate relationship between absorption efficiency and the energy velocity of light propagation, that is far more complex than hitherto believed. In particular, our findings suggest that absorption peaks away from the photonic-crystal band edge where energy velocity is minimum. While efficient absorption is still associated with a slow-light mode, the latter is faster by at least an order of magnitude in comparison to the bulk material. Moreover, our calculations suggest that absorption becomes optimal when light gradually slows down as it enters the PC. Relying on this insight, we achieved near-perfect absorption around the phonon-polariton mid-gap frequency with a PC with a suitably terminated end face. We further demonstrate that the near-perfect absorptive property can be tuned with the incident light angle, to be polarization insensitive or polarization selective. We believe our proposed non-metallic paradigm opens up a new route for harnessing infrared absorption with semiconductor and ionic-crystal materials.

3.2 Introduction

Harnessing absorption at visible frequencies with nanostructured materials has been a subject of numerous current research efforts [3–11] driven by the strong

interest to enhance the performance of photovoltaic devices. The design principles employed by these works to optimize the photon absorption involve enhancement of the near-field by excitation of surface or waveguide electromagnetic (EM) modes [5, 7, 8, 10], engineering lossy material surfaces with ultra-low reflectivity [4, 6, 11], or directing the EM energy into slow waveguide modes that would imply a large interaction time between light and matter [9]. However, manipulating photonic absorption at mid-IR frequencies is also an extremely desirable functionality pertinent to biosensing and medical diagnostic applications. Typical pathogens have their absorption fingerprint around 10 μm [12]. Also, infrared imaging systems [13, 14] have been recently proposed for cancer diagnosis at early stages [13, 15]. Thus far, mainly metallic microstructures have been employed to achieve absorption enhancement at mid-IR frequencies. The pioneering proposal of S. Y. Lin [16] et al. reported an absorptance as high as 50% with a tungsten (W) three-dimensional layer-by-layer PC. The latter was attributed to a large photon-matter interaction time emanating from a slow Bloch mode [17], occurring at the PC band edge, and a long material path within the PC.

Metallic PCs are typically highly reflective at mid-IR frequencies, and accordingly have significant limitations with respect to absorption enhancement. In particular, at this frequency range bulk metals are near-perfect reflectors, with a skin depth of the order of $\lambda_0/300$, with λ_0 being the free space wavelength, and essentially a 100% reflectivity. Only very recently, J. A. Mason et al. [18] achieved a 100% absorption with an Au-SOG (spin-on glass)-Au periodic strip structure, and demonstrated its potential as a bio-sensing platform [19]. The latter perfect absorbing system relied on the excitation of the composite waveguide modes, and exploited absorption in both the Au and SOG layers [18]. Given the immense need for mid-IR absorption manipulation, it is of utmost interest to explore alternate schemes that can yield a near-perfect absorption in this frequency range.

Here we report for the first time a non-metallic route to near-perfect mid-IR absorption by employing a semiconductor-based PC. We will analyze carefully the design principles that lead to such a near-perfect absorption in a one-dimensional PC structure. Semiconductor materials have their phonon-polariton gap in the infrared spectrum [20] and have a high loss-tangent within this frequency region. The bulk structures are still highly reflective, but considerably better impedance matched with vacuum than metals are. Also their respective skin depth in the mid-IR spectrum is at least an order of magnitude higher, which means they can offer a larger effective light-matter interaction path in comparison to their metallic counterparts.

In particular, we present the periodic SiC PC system under study in Section 3.3 and briefly discuss the theoretical method employed in our calculations. We present the results obtained for the absorptance in Section 3.4, and discuss their correlation to intensity enhancement in the SiC layers. In Section 3.5 we analyze the intricate role of the energy velocity of the in-coupled electromagnetic (EM) wave in association to absorptance. Based on the insight gained by this analysis, we propose in Section 3.6 a suitable PC with a terminated end face that exhibits a near-perfect mid-IR absorption. This result essentially represents a dramatic absorption enhancement, about 30 times larger in comparison to the bulk SiC structure. We further explore the capability of this paradigm to demonstrate polarization insensitive as well as polarization selective near-perfect absorption in Section 3.7. Finally, we discuss our conclusions in Section 3.8.

3.3 The one-dimensional SiC photonic crystal system modeled with TMM

We choose SiC (Silicon Carbide) for the semiconductor constituent, because its phonon-polariton mid-gap is around 11μm, where the absorption fingerprint of many biological substances lies [12, 21]. The periodic one-dimensional (1D) PC comprises of alternating SiC and air slabs, of widths d_1 and d_2 respectively and has a unit cell size $a = d_1 + d_2$. The ratio $f = d_1/a$ represents the SiC filling ratio [22]. In all of the following, we consider a structural unit cell with a=10.3μm. In Fig. 3.1(a), the first two unit cells of the structure are depicted. As seen in the figure, we consider normal incidence along the x-direction, which is also the stacking direction, with the electric field $\mathbf{E}$ polarized along the y-direction. To model the optical response of the SiC layer we consider a suitable Lorentzian fit to the experimental optical data, as reported in Ref. [23]. So, we take the permittivity ε_1 of the SiC layer to be:

$$\varepsilon_1(\omega) = \varepsilon_\infty \left(1 + \frac{\omega_L^2 - \omega_T^2}{\omega_T^2 - \omega^2 - i\omega\Gamma}\right) \tag{3.1}$$

with ε_∞=6.7, ω_T =2$\pi\times$23.79 THz, ω_L =2$\pi\times$29.07 THz and Γ =2$\pi\times$0.1428 THz and ω representing the cyclic frequency of the incoming EM wave. The spectral region between ω_T and ω_L is generally known as the phonon-polariton gap [20], where propagation within the bulk material is prohibited. So, SiC has a phonon-polariton gap region that extends roughly from 10.3 to 12.6 μm (free space wavelength). We note that the form of permittivity dispersion given in Eq. 3.1 corre-

sponds to EM waves varying in time as $e^{-i\omega t}$ [24, 25]. We take ε_2=1 for the air slabs.

The absorptance, A, will be calculated with the Transfer Matrix Method (TMM) of Yeh, Yariv and Hong [1, 2], as A=1-R-T with R and T being the reflectance and transmittance respectively. We will see in the following, that to interpret and understand the absorptance behavior, the calculation and analysis of additional PC properties will be needed. We will also calculate the electric and magnetic field across the actual 1D PC of finite thickness with the TMM method. The band structure of the 1D PC, representing the dispersion relation for the propagating EM modes will be calculated with TMM by considering Bloch boundary conditions across the structural unit cell[1], thus modeling an infinitely extending 1D PC. Note, we will refer to the associated electric and magnetic field distributions for the infinite extending PC as modal fields.

3.4 Results and discussion on absorptance enhancement with the periodic SiC 1D PC

We consider the absorptance, A, through a 20 cell-thick PC for different filling ratios, f. We show the results versus free space wavelength, λ_{free}, in Fig. 3.1(b) as red dashed lines for f=0.07, green dot-dashed lines for f=0.15 and blue dotted lines for f=0.30. The magenta vertical lines represent the spectral limits of the SiC phonon-polariton gap. The black solid line corresponds to the absorptance through a SiC block with thickness of 14.42 μm, which is equal to the total SiC thickness of the PC with f=0.07. Note, the latter represents a saturated absorptance value for bulk SiC in the phonon-polariton gap region, i.e. a thicker SiC slab won't yield a higher absorptance.

For the cases of Fig. 3.1(b) we show the corresponding reflectance in Fig. 3.1(c). It is clear that reflectance is the major limiting factor of absorption. Our results suggest that parting a SiC block into thin slices can reduce the reflectance and in this manner enhance the absorption[3]. We observe that the thinner these slices are the larger the absorption enhancement is, which also peaks more towards the center of the phonon-polariton gap. The higher filling ratio PC (f=0.30),

[3]SiC is highly reflective in bulk form. However, 1D-PCs constructed from thin SiC layers, i.e. "SiC slices", will have a low reflectance as we can see in Fig. 3.1(c). Due to this low reflectance, light will enter inside these PCs and get absorbed in the SiC layers if the total PC structure is thick enough. We explore the limits of how small we can make the thickness of the PC structure in Chapter 5.

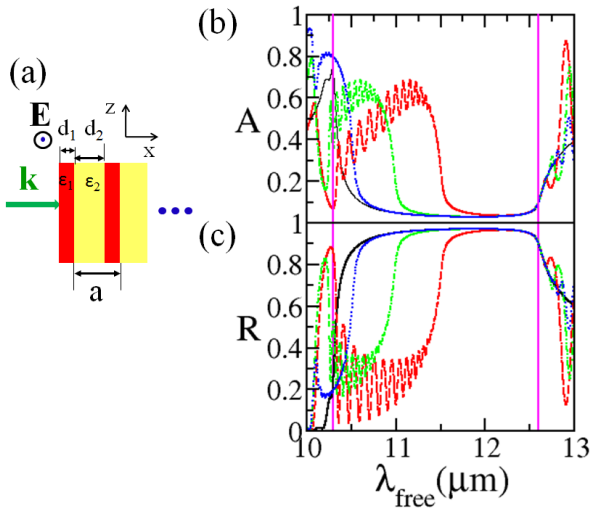

Figure 3.1: (a) Normal incidence at the 1D SiC-air PC structure (first two unit cells are shown). The geometric and material parameters of the PC system are indicated. (b) Absorptance versus free space wavelength, λ_{free}, for a 20-unit-cell SiC-air PC with filling ratio 0.07 (red dashed lines), 0.15 (green dotted-dashed lines) and 0.30 (blue dotted lines) (a=10.3 μm). The absorptance of a bulk SiC block of thickness equal to 14.42 μm is shown for reference as a black solid line. The magenta vertical lines encompass the SiC phonon-polariton spectral gap region. (c) Same as in (b), but for reflectance versus the free space wavelength.

is very little different from the bulk SiC structure. In other words, lower filling ratio polaritonic PCs are better absorbers in the frequency regime of the phonon-polariton gap. Our findings are consistent with observations on visible spectrum absorption with a plasmonic nanowire PC in the work of Ref. [6]. Accordingly, in the following we focus only in the lower filling ratio structure of f=0.07.

The work of S. Y. Lin et al. [16] suggests that in PCs with lossy material constituents, absorption would be expected to peak around the PC band edge, were propagating modes are ultra-slow allowing for a larger interaction time between light and matter. We show the band structure for the SiC PC in Fig. 3.2(a). We plot the free space wavelength, λ_{free}, with the photonic crystal (Bloch) wavevector q in dimensionless units [real part is shown in left panel and imaginary part is shown in the right panel]. The PC band edge in polaritonic PCs is actually not as sharply defined as for the case of lossless PCs. We will identify as the band-gap region the regime where the real part of the wavevector is in the vicinity of the Brillouin zone boundary (i.e. close to π/a), with a correspondingly large imaginary part. Accordingly, the result in Fig. 3.2(a) suggest an allowed band within SiC the phonon-polariton gap up until 11.5 μm, which we designate with the yellow shaded region. Notice the band edge is in agreement with the onset of a large reflectivity as we see in Fig. 3.1(c).

It is very interesting to note that, absorptance actually peaks at about 10.9 μm, which is around the middle of the allowed propagation band, well away from the PC band edge. The absorptance at the peak wavelength is about 60%, representing an enhancement factor around 15 with respect to bulk SiC.

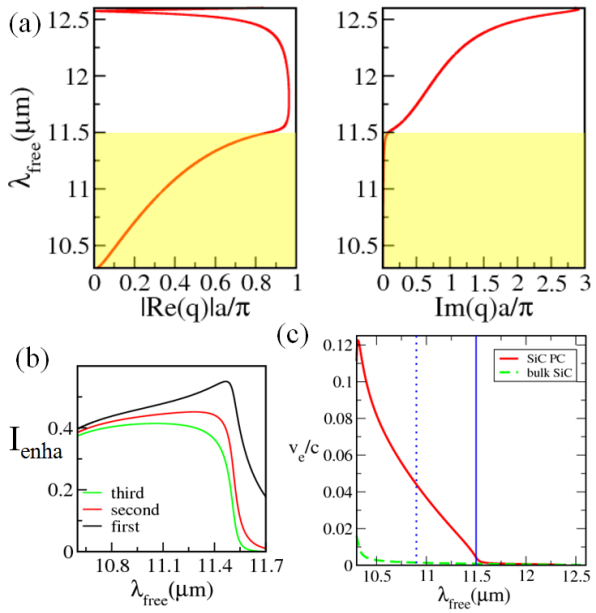

Figure 3.2: (a) Band structure of the SiC PC with a filling ratio 0.07 within the SiC phonon-polariton gap spectrum. The left (right) panel depicts the modal free space wavelength λ_{free}, with respect to the real (imaginary) part of the Bloch wavevector q (dimensionless units). We find an allowed propagation band for the SiC PC, with spectral limits designated with the shaded region in the figure. (b) Corresponding spectral response of the averaged normalized intensity at the first (black line), second (red line) and third (green line) SiC layer for the semi-infinite SiC-air PC. (c) Energy velocity in the infinite PC structure averaged within the SiC layer (red solid line). Energy velocity within bulk SiC is shown for comparison (green dashed line). The blue solid vertical line designates the PC band-gap edge, while the vertical blue dotted line designates the free space wavelength where absorptance peaks [see Fig. 3.1(b)].

In the following, we attempt to understand better the factors underpinning the occurrence of the absorptance peak away from the band edge. In plasmonic-based nanostructures intensity enhancement within the metal has been quoted as a criterion to optimize asborptance [5, 7, 8, 10]. Therefore, we calculate here also the spectral behavior of the normalized electric-field intensity within the SiC layers in the PC. In order to do that we consider a long –two-hundred-cell– PC structure that emulates a semi-infinite PC [17]. We consider the averaged intensity within the first, second and third SiC layer (counting from the interface) and normalize it with the intensity I_0 of the incoming EM wave. Thus, the normalized averaged intensity enhancement I_{enha} is given by:

$$\mathrm{I_{enha}} = \frac{1}{\mathrm{I_0}} \frac{1}{\mathrm{d_1}} \int_0^{\mathrm{d_1}} |E_y(x)|^2 dx, \tag{3.2}$$

where x=0 in Eq. 3.2 is taken at the front SiC face of the first, second and third PC cell in each case. $E_y(x)$ represents the electric field distribution that is calculated with TMM for the two-hundred-cell-thick PC system.

We plot the results in Fig. 3.2(b), with black, red and green solid line for the normalized intensity average within the first, second and third SiC layer respectively. Interestingly, throughout the allowed band the normalized intensity enhancement seems to peak toward the band edge in the first cell, while its response gets relatively flat at the third unit cell. The results in Fig. 3.2(b) imply that the absorptance peak does not coincide spectrally with the intensity enhancement peak. Note, the latter is less than one implying that throughout the allowed band the normalized averaged intensity in the SiC layer is less than the incident light intensity. The intensity in the air layers is about 3 times larger but with similar spectral response as in the SiC layers.

We proceed now to shed light into the relationship between the energy velocity of the propagating mode and absorption. Frequently, the group velocity is used to characterize the energy velocity of the propagating mode. However, the energy and group velocities are equal only in the case of lossless constituents [17, 26]. Actually, these can be quite different when constituents with anomalous dispersion are considered, such as polaritonic media [27]. Also, the group velocity captures the average energy velocity within the unit cell [17, 28]. However, the energy-velocity definition allows for spatial resolution within the individual SiC and air layers [28], which is crucial to obtain a measure of the light-matter interaction time within the SiC layer. We will consider in the following the energy velocity averaged within the SiC layer of an infinitely extending PC structure. This will be given by [27, 29]:

$$\mathrm{v_e} = \frac{<\bar{\mathrm{S}}_\mathrm{x}>}{<\bar{\mathrm{U}}>} = \frac{\frac{1}{2}\int_0^{\mathrm{d_1}} \mathrm{Re}[E_y(x)H_z^*(x)]dx}{\frac{1}{4}\int_0^{\mathrm{d_1}} [\varepsilon_0(\varepsilon_1{}' + \frac{2\omega\varepsilon_1''}{\Gamma})|E_y(x)|^2 + \mu_0|H_z(x)|^2]dx}, \tag{3.3}$$

where the bar on $\mathrm{S_x}$ and U indicates the time-averaged quantities of the Poynting vector and energy density respectively while the brackets <> denote the spatial average within the SiC layer. $E_y(x)$, and $H_z(x)$ are the modal electric and magnetic field distributions, that we obtain with the TMM for the infinitely extending PC (unit cell with Bloch boundary conditions). Also, ε_0 and μ_0 are the vacuum permittivity and permeability, ε_1', ε_1'' and Γ are the real part, imaginary part and dissipation parameter of the SiC permittivity given in Eq. 3.1. Note, that the

proper form for the EM energy density is used here for the polaritonic SiC medium [27] that is consistent with Loudon [29].

The energy velocity result from Eq. 3.3 is plotted versus free space wavelength, λ_{free}, as a solid red line in Fig. 3.2(c). The result is shown in units of the speed of light, c. We see that the energy velocity drops to almost zero from the band edge at about 11.5 μm – designated with the blue solid vertical line in the figure. However, as also discussed above the absorptance peak– designated with the blue dotted vertical line–is well away spectrally from this point. This result is contrary to the observations in Ref. [16], where absorptance maxima and energy velocity minima overlap spectrally at the PC band edge. We observe that in our polaritonic PC system the PC band edge ceases to be sharply defined [30]. As a result, the energy velocity does not also sharply reduce to zero, but there is rather an extended region with a low v_e. For the periodic PC, absorptance is peaking within the latter frequency regime but away from the point where v_e almost drops to zero. We stress that the propagation mode at the absorptance peak wavelength is much faster in the SiC layer of the SiC-air PC, by at least an order of magnitude, in comparison to the one in bulk SiC. The energy velocity of the latter is shown with the green dashed line in Fig. 3.2(c).

We argue that the role played by the energy velocity in absorption is bi-fold. In particular, we assert that while slow light is conducive to absorption, due to a longer light-matter interaction time, at the same time it is an adverse factor causing an elevated reflectance. Accordingly, a slower mode with a larger interaction time does not necessarily imply also a greater absorption enhancement. We investigate further this aspect in the following section.

3.5 Energy velocity and reflectance

We attempt in this paragraph to develop a relationship between the energy velocity of light inside the SiC layers of the 1D PC and reflectance on the air-PC interface. We will consider again the semi-infinite PC medium. Note that, while in a PC with lossless constituents the energy velocity does not vary spatially within the individual constituent layers [28] this is not the case for lossy constituents. Inside the lossy SiC layers the energy velocity, v_e has a spatial variation. We depict the spatial variation of v_e in Fig. 3.3(a) within the first SiC PC layer, of the effectively semi-infinite PC for a free space wavelength of 10.9 μm. This represents a wavelength falling close to the absorptance peak in Fig. 3.1(b) for the twenty-cell

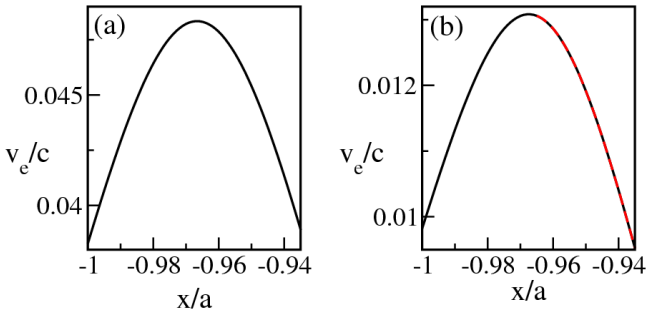

Figure 3.3: (a) Energy velocity at the interfacial SiC layer as a function of position, x, for the periodic PC at 10.9 μm free space wavelength. (b) The same but for a terminated PC, with a half-sized SiC end face at 11.4 μm free space wavelength (red dashed line). The black solid line represents the corresponding periodic PC case. Note, in all cases x=0 was taken at the front face of the second PC cell.

PC [Note as we approach the semi-infinite limit the absorptance peak shown in Fig. 3.1(b) is inhomogeneously broadened]. We find that this spatial variation of $\mathrm{v_e}$ within SiC remains exactly the same for layers inside the semi-infinite PC. Also we find that throughout the allowed PC band region [shaded region in Fig. 3.2(a)], the $\mathrm{v_e}$ within the SiC layers retains this characteristic increasing-decreasing $\mathrm{v_e}$ profile shape.

In the following we attempt to get a relation between the energy velocity, $\mathrm{v_e}$, at the interface of the semi-infinite PC and reflectance, R. Let α and β represent the electric field contributions just after the air-PC interface, propagating along the $+x$ and $-x$ directions respectively [where the axis system has been defined in Fig. 3.1(a)]. It can be easily shown with TMM that:

$$\alpha = \frac{1}{2}[(1+\chi)+(1-\chi)r], \tag{3.4}$$

and

$$\beta = \frac{1}{2}[(1-\chi)+(1+\chi)r], \tag{3.5}$$

with r being the reflection coefficient (i.e. reflectance, $R = |r|^2$) and $\chi = k_2/k_1$ with k_1, k_2 being the wavevectors inside SiC and air respectively. Then with the use of Maxwell's equations and the $\mathrm{v_e}$ expression [see Eq. 3.3 without the spatial average], after some math manipulations we obtain for the energy velocity at the air-PC interface:

$$\mathrm{v_{e,\,int}} = \frac{2c(1-\mathrm{R})}{(\varepsilon_{\mathrm{fac}}+1)(1+\mathrm{R})+2\mathrm{Re}(r)(\varepsilon_{\mathrm{fac}}-1)}, \tag{3.6}$$

with c being the velocity of light,

$$\varepsilon_{\text{fac}} = \varepsilon_1{}' + \frac{2\omega\varepsilon_1''}{\Gamma}, \tag{3.7}$$

and the parameters $\varepsilon_1{}'$, ε_1'', Γ have the same meaning as defined below Eq. 3.3.

Equation 3.6 implies that when $\mathrm{v_e} = 0$ then R=1. In other words, zero energy velocity signifies the photonic band gap. Now if we require zero reflection, the energy velocity from Eq. 3.6 becomes:

$$\mathrm{v_{e,\ int}}(R = 0) = \frac{2c}{\varepsilon_{\text{fac}} + 1}. \tag{3.8}$$

If a reflectionless mode couples into the PC, then effectively all energy can get absorbed for a sufficiently thick structure. Such a mode would need to be slow at the interface, as implied by Eq. 3.8 (ε_{fac} ranges between roughly 50 and 175 within the allowed PC band regime). However, a comparison of $\mathrm{v_{e,\ int}}$ from Eq. 3.8 and the energy velocity in the bulk SiC [27] yields that the PC medium would need to actually speed-up the light propagation inside the SiC material, in order to absorb the incoming light efficiently. We found that depending on the free space wavelength within the SiC polariton-gap regime, this speed-up factor ranges between 5 and 15.

Since we observe a rather smooth spatial variation of $\mathrm{v_e}$ within the SiC layer, it is a fair assumption that the value of $\mathrm{v_e}$ at the interface is close to the value averaged within the entire layer. Then, based on the expectation for the energy velocity of the reflectionless PC, and the spectral response of $\mathrm{v_e}$ shown in Fig. 3.2(c), one would predict a near-perfect absorption around 11.35 μm. We however have not observed such near-perfect absorption for the periodic PC. This leads us to understand that there may be also a correlation between the type of energy velocity spatial profile at the interface (growing or decaying) and the reflectance R. We thus explore the existence of such correlation. The electric field expressions from the TMM method within the SiC interface layer, after some extensive math manipulations, yield the following expression for the energy velocity slope at the interface:

$$\left(\frac{d\mathrm{v_e}}{dx}\right)_{\text{int}} = \mathrm{v_{e,\ int}}\frac{\varepsilon_1''\omega}{c}\left[-\frac{1+\mathrm{R}+2\mathrm{Re(r)}}{1-\mathrm{R}} + 2\frac{1-\mathrm{R}-4\frac{\omega}{\Gamma}\mathrm{Im(r)}}{(\varepsilon_{\text{fac}}+1)(1+\mathrm{R})+2\mathrm{Re(r)}(\varepsilon_{\text{fac}}-1)}\right]. \tag{3.9}$$

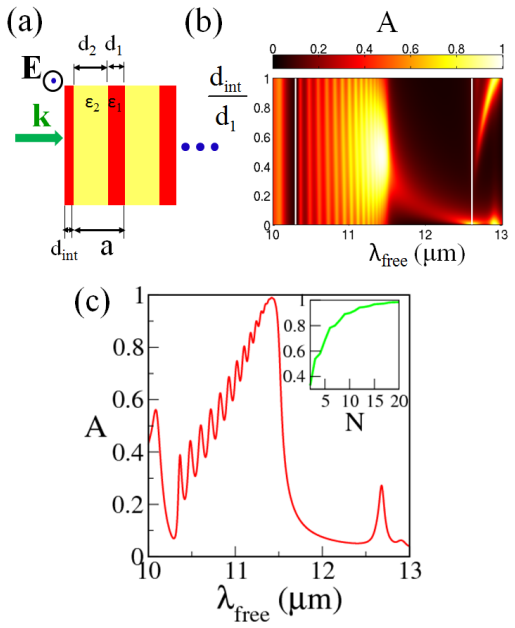

Figure 3.4: (a) Normal incidence at the 1D SiC-air PC, with the first SiC layer truncated. The geometric parameters of the PC system, and truncated layer, are indicated. (b) Absorptance versus free space wavelength, λ_{free}, and termination ratio, $t_{\text{ratio}} = \text{d}_{\text{int}}/\text{d}_1$, for a twenty-cell SiC-air PC with a filling ratio 0.07. The two vertical white lines designate the phonon-polariton gap region. (c) Same as in (b) plotted for the case with t_{ratio}=0.5. The inset shows the absorptance versus the number of total cells, N, for the peak wavelength of 11.4 μm.

Now from Eq. 3.9 at the reflectionless condition, we obtain the following value for the energy velocity slope at the PC interface:

$$\left(\frac{d\text{v}_\text{e}}{dx}\right)_{\text{int}}(R=0) = \text{v}_{\text{e, int}}\frac{\varepsilon_1''\omega}{c}\left[-1+\frac{2}{\varepsilon_{\text{fac}}+1}\right] < 0, \tag{3.10}$$

since $\varepsilon_{\text{fac}} > 1$. Equation 3.10 suggests that for the reflectionless PC light should gradually slow down when entering the SiC-air PC. We note that this observation is not specific to SiC, but is general and applies to any air-layered-structure interface, comprised of any absorbing material including metals.

However, as we observe in Fig. 3.3(a) light initially speeds up and then slows down while coupling into the SiC-air PC. As we find this increasing-decreasing spatial profile for v_e throughout the allowed PC-band region, this seems to pose a substantial limiting factor to the reflection minimization and accordingly to the optimization of absorptance. We therefore subsequently focus on investigating the possibility to manipulate the spatial v_e profile at the PC-structure entry. For this reason we explore a PC design, where the first face is truncated. We note, that truncation of end faces has been considered before in lossless PCs as a route of transmission con-

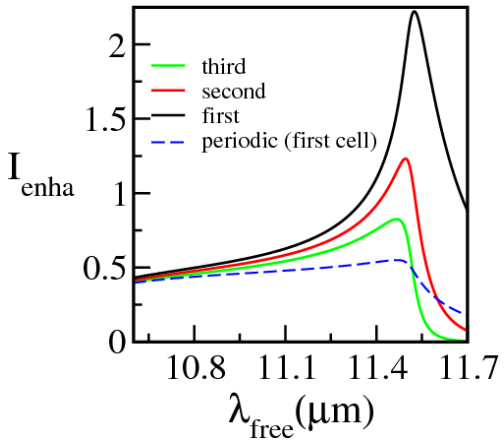

Figure 3.5: Spectral response of the averaged normalized intensity, I_{enha} at the first (black line), second (red line) and third (green line) SiC layer for the semi-infinite truncated SiC PC with $t_{ratio} = 0.5$. The result for the first layer of the corresponding full periodic PC is also shown as dashed blue lines.

trol [31, 32]. Our TMM based calculations for v_e in the semi-infinite PC shows that the truncation leaves the energy velocity intact for layers well inside the PC medium.

Then, at the interface SiC layer, the v_e spatial profile follows exactly the same functional form as in the overlapping periodic PC. As an example we show such v_e profile for a truncated PC at 11.4 μm free space wavelength in Fig. 3.3(b) for a PC structure with a total of 20 cells. The SiC end face has half the width of a SiC layer within the bulk PC structure. We clearly observe a decaying v_e profile from the interface, shown as a red dashed line in the figure. For comparison, the corresponding v_e profile for the periodic semi-infinite PC is also shown as a black solid line. Note that in the figures we have taken x =0 at the front face of the second cell, that is the same for both periodic and truncated PC. The latter result essentially affirms that truncating the PC end face provides a route to manipulate $\left(\frac{dv_e}{dx}\right)$ at the interface. Equation (9) implies that this translates into manipulating the reflectance, R, and thus the absorptance of the PC structure. We explore such truncation based optimization route in the section that follows.

3.6 Near-perfect mid-IR absorption in the truncated PC design

We truncate the first layer to a thickness d_{int}, while the remaining PC remains intact, as we depict in Fig. 3.4(a). We plot the absorptance, A, versus the free space wavelength, λ_{free}, and the termination ratio $t_{ratio} = d_{int}/d_1$ in Fig. 3.4(b). The latter

represents the thickness ratio of the truncated SiC layer and the SiC layers in the remaining periodic PC. The results suggest that the optimum absorptance occurs at a termination ratio close to 0.5 yielding essentially a near-perfect absorption. We depict the absorptance versus free space wavelength for the latter case separately in Fig. 3.4(c), where we can see clearly the near-perfect absorption at $\lambda_{\text{free}} \sim 11.4\ \mu$m.

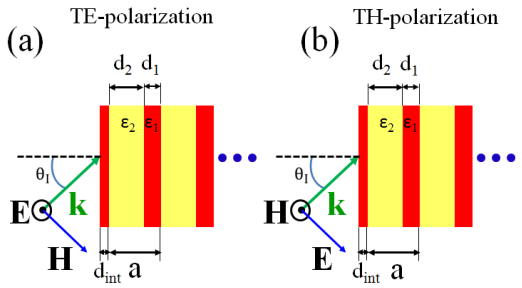

Figure 3.6: (a) TE-polarization incidence on the truncated PC design (b) TH-polarization incidence on the truncated PC design

This results represents essentially an absorptance enhancement factor of 30, i.e. an increase of $\sim 2900\%$, in reference to the bulk SiC structure. For the peak wavelength we show also in the inset the absorptance versus the total number of photonic crystal cells. We see that with just three cells, corresponding to a total SiC thickness of $\sim 0.15\lambda_{\text{free}}$, we can obtain absorptance exceeding 50%. Thus, our paradigm structure achieves essentially the same IR absorption as a metallic PC [16], with a photon-matter interaction path that is more than an order of magnitude smaller. This is because the effective interaction path in metallic PCs is much smaller than the material thickness that is crossed by the EM wave, due to the ultra-small metallic skin depth at IR frequencies.
Thus, the truncation of the PC end face introduces a propagation mode where light gradually slows down as it enters which seems to facilitate the efficient in-coupling of slow light of $v_{e,\,\text{int}} \sim 0.0115c$, in this manner optimizing absorptance. We note that while the absorptance peak red-shifts towards the band edge for the truncated PC, it still remains spectrally away from it [4].

Also, still the absorptance peak does not coincide spectrally with the intensity enhancement maximum, as we show in Fig. 3.5. The calculation was again performed with TMM for the semi-infinite truncated PC with $t_{\text{ratio}} = 0.5$. The averaged normalized intensity, I_{enha} is shown as black, red and green solid lines for the first, second and third SiC layer respectively. For comparison we show

[4] In other words the absorptance peak is closer, but still quite far away from the PC-band-edge frequency. This implies a large number of building blocks are necessary for the light to get absorbed.

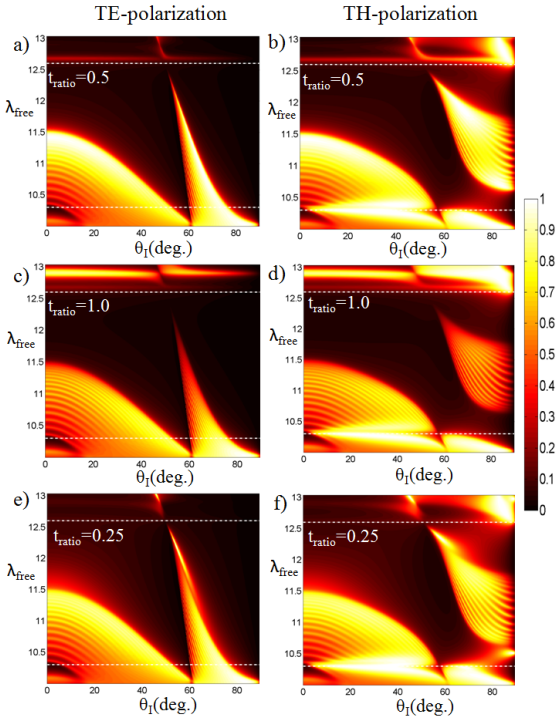

Figure 3.7: Absorptance versus incident angle, θ_I and free space wavelength λ_{free} for TE-polarization (figures in the left) and TH-polarization (figures in the right) for different termination ratios: t_{ratio}=0.5 in (a) and (b), t_{ratio}=1.0 (implying a fully periodic PC) in (c) and (d) and t_{ratio}=0.25 in (e) and (f)

also in Fig. 3.5 the corresponding result for the first SiC layer of the periodic PC as the dashed blue lines. Evidently, the truncation does not have any impact on the spectral response of the intensity enhancement. The actual value of the latter increases across spectrum with the truncation, as more light couples into the structure. This is true for both SiC and air layers. This affirms our previous assertion that the truncation facilitates the in-coupling and thus optimizes the absorptance by manipulating the spatial profile of the light's energy velocity at the entry.

It is very interesting to explore the angular and polarization dependency of the near-perfect absorptive property of the truncated SiC PC. We do so in the following section.

3.7 Angular and polarization response of the truncated PC design: Achieving polarization insensitive and polarization selective efficient absorptance

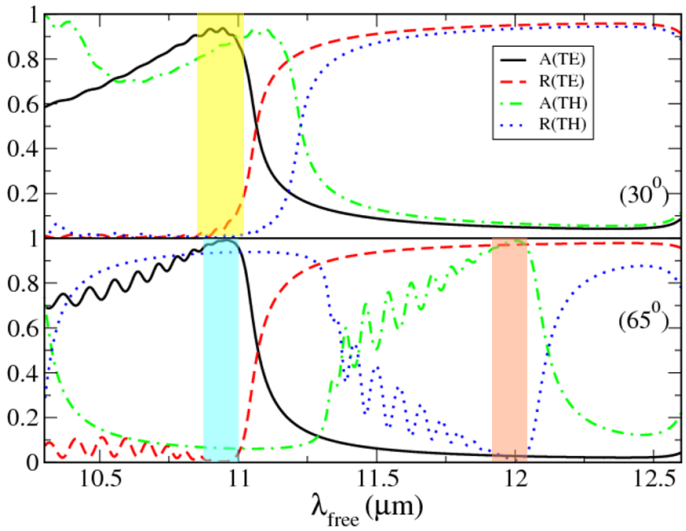

Figure 3.8: (a) Polarization insensitive absorptance when incident angle is 30 deg. (yellow shaded region) (b) Polarization selective absorptance when incident angle is 65 deg. (cyan region for a TE-mode absorber and salmon region for a TH-mode absorber). In all cases, the black solid and dashed green lines represent the absorptance for the TE- and TH-modes respectively, while the red dashed and blue dotted represent the reflectance for TE- and TH-modes respectively.

At normal incidence, TE and TH polarization are degenerate. However, for off-normal incidence these decouple. We depict TE and TH polarization incidence at the truncated PC in Figs. 3.6(a) and 3.6(b) respectively. We calculate then with the TMM for a truncated PC with $t_{\text{ratio}} = 0.5$ and thickness of 20 cells, the absorptance versus the angle of incidence θ_I, and free space wavelength, λ_{free}, and we show the results in Figs. 3.7(a) and 3.7(b) respectively. We note that at each incident angle and frequency the truncation with $t_{\text{ratio}} = 0.5$ may not be always the optimum one. However, we find that overall that the optimum termination is close to a termination ratio of $t_{\text{ratio}} = 0.5$ across the spectrum of incident angles and frequencies within the phonon-polariton gap regime. Indicatively, we show for comparison the respective absorptance versus incident angle and free space wavelength for the fully periodic structure ($t_{\text{ratio}} = 1.0$), and a truncated PC with $t_{\text{ratio}} = 0.25$. The respective TE-polarization cases are shown in Figs. 3.7(c) and 3.7(e) and the respective TH-polarization cases in Figs. 3.7(d) and 3.7(f).

Indeed, looking closely we observe a near-perfect absorptance for the truncated PC design with $t_{\text{ratio}} = 0.5$ for different frequency-angle regimes. This implies that by tuning the angle of incidence we can manipulative the absorptive response of the PC structure. To see this more clearly we highlight this behavior by showing the absorptance versus free space wavelength for two particular incident angles: 30 deg. shown in Fig. 3.8(a) and 65 deg. shown in Fig. 3.8(b). At normal incidence, the two polarizations are degenerate, which means that we would get a near-perfect absorptance for both polarizations. The results in Fig. 3.8(a) suggest that this polarization insensitivity of the absorptance seems to survive even for a larger incident angle, but blue-shifts spectrally. The yellow shaded region in Fig. 3.8(a) represents a spectral regime where we can obtain more than 80% absorptance for both polarizations.

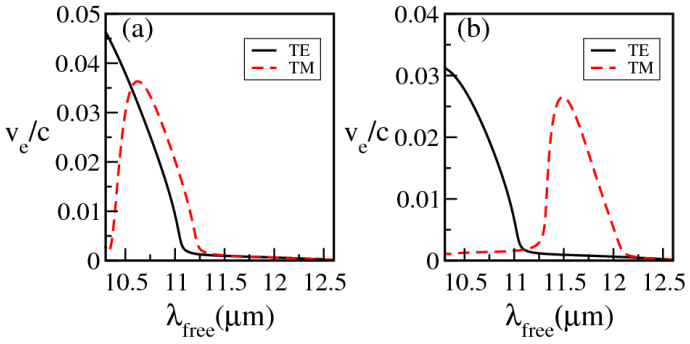

Figure 3.9: Energy velocity, v_e along the propagation direction x versus free space wavelength, λ_{free} for the infinite PC, with a non-zero wave vector along z [defined in Fig. 3.1(a)] , k_z. In (a), (b) k_z corresponds to the mode that couples at an incident angle of 30 deg. and 65 deg. respectively. In all cases, the solid black line represents the TE polarization result and the dashed red lines represents the TH polarization result.

Now for an incident angle of 65 deg., the PC band-gap frequency regimes do not spectrally overlap for the TE and TH polarization cases. We can confirm this by calculating the infinite-PC energy velocity along the propagation direction (x) versus the free space wavelength, for cases having a wavevector component along the z-direction [defined in Fig. 3.1(a)] that corresponds to an angle of incidence of 30 deg. and 65 deg. The results for the former case are shown in Fig. 3.9(a) while the results for the latter in Fig. 3.9(b) with a solid line for TE-polarization and a red dashed line for TH-polarization. As discussed in Section 3.5, the band-gap region can be identified by regions where v_e is ultra-slow approaching zero. Thus, we observe in Fig. 3.9(a) that the band-edge is close for both TE and TH polarizations. This made it possible to get an efficient absorptance at about 10.9 μm, which is in the vicinity but away from the band-edge for both polarizations, as we saw in Fig. 3.8(a). On the other hand, this is not true for the case that corresponds to a 65 deg.

incidence. We observe in Fig. 3.9(b) a spectral region until a free space wavelength of 11 μm where we have allowed TE-modes but forbidden TH modes. Conversely, within the spectral region of $\sim$ 11.5-12 μm the results of Fig. 3.9(b) suggest the existence of forbidden TE-modes but allowed TH modes.

These angle- and polarization-dependent allowed-band regions translate into an angle- and polarization-dependent absorption efficiency. We see clearly in Fig. 3.8(b) in the regime around 10.9 μm (cyan shaded region) an absorptance of more than 95% for TE-polarization and less than 10% for TH-polarization. Conversely, we observe around 12 μm (salmon shaded region) an absorptance of more than 95% for TH-polarization and less than 10% for TE-polarization. The later result demonstrates that our proposed truncated SiC PC can act as a polarization selective absorber at an angle of incidence of 65 deg.

3.8 Conclusions

In conclusion, we report here for the first time a non-metallic route to mid-IR near-perfect absorption with a SiC one-dimensional photonic crystal around the frequency of the bulk SiC phonon-polariton mid-gap. We have achieved the near-perfect absorption by considering ultrathin SiC slices–that allow for reduced reflectivity–and in addition by tailoring the width of the input interface. Our careful investigation reveals that a slow light propagation simultaneously facilitates and impedes absorption, by allowing a larger light-matter interaction time and inducing a high reflection respectively. We find that efficient absorption occurs when the coupled mode is slow, but yet at least an order of magnitude faster than in the bulk SiC material. Also, we find that the absorptance peak can be spectrally well away [5] from the PC band edge contrary to previous reports in metallic PCs [16].

Moreover, we demonstrate that a proper interface truncation manipulates the spatial distribution of the energy velocity at the interface. Our results show that a slow mode with decreasing energy velocity in the interface facilitates an efficient in-coupling and thus induces near-perfect absorption. We further show that by controlling the angle of incidence our proposed structure can act both as a polarization

[5] This means constructing a PC with lossy constituents is not sufficient to achieve a high absorption enhancement at the PC band-edge as suggested in Ref. [16]. The quick EM wave die-off within the PC–characteristic of near-band-edge frequencies–actually competes with having a low reflection. In other words, only EM energy that is not reflected will be quickly absorbed inside the lossy PCs. This inevitably pushes the absorption peak away from the band-edge where reflection is lower. We will explore this limitation in detail for the construction of a compact PC-based absorber in Chapter 5.

insensitive and as a polarization selective absorber. Our truncated PC paradigm opens a new avenue for absorption engineering within the phonon-polariton gap region of semiconductor and ionic crystal materials. We believe our study will inspire new highly efficient non-metallic absorber designs pertinent to mid-IR detection devices.

Bibliography

[1] P. Yeh, *Optical waves in layered media* (Wiley-Interscience, 2005).

[2] P. Yeh, A. Yariv, and C. S. Hong, "Electromagnetic propagation in periodic stratified media 1. General theory," J. Opt. Soc. Am. **67**, 423-438 (1977).

[3] H. A. Atwater and A. Polman, "Plasmonics for improved photovoltaics," Nat. Mat. **9**, 205–213 (2010).

[4] J. Zhu, Z. Yu, G. F. Burkhard, C. M. Hsu, S. T. Connor, Y. Xu, Q. Wang, M. McGehee, S. Fan, and Y. Cui, "Optical Absorption Enhancement in Amorphous Silicon Nanowire and Nanocone Arrays," Nano Lett. **9**, 279–282 (2009).

[5] J. S. White, G. Veronis, Z. Yu, E. S. Barnard, A. Chadran, S. Fan, and M. L. Brongersma, "Extraordinary optical absorption through subwavelength slits," Opt. Lett. **34**, 686–688 (2009).

[6] G. Veronis, R. W. Dutton, and S. Fan, "Metallic photonic crystals with strong broadband absorption at optical frequencies over wide angular range," J. of Appl. Phys. **97**, 093104 (2005).

[7] R. A, Pala, J. White, E. Barnard, J. Liu, and M. L. Brongersma, "Design of Plasmonic Thin-Film Solar Cells with Broadband Absorption Enhancements," Adv. Mat. **21**, 3504–3509 (2009).

[8] C. Min, J. Li, G. Veronis, J.-Y. Lee, S. Fan, and P. Peumans, "Enhancement of optical absorption in thin-film organic solar cells through the excitation of plasmonic modes in metallic gratings," Appl. Phys. Lett. **96**, 133302 (2010).

[9] Y. Cui, K. Hung Fung, J. Xu, H. Ma, Y. Jin, S. He, and N. X. Fang, "Ultra-broadband Light Absorption by a Sawtooth Anisotropic Metamaterial Slab," Nano Lett. **12**, 1443-1447 (2012).

[10] K. Aydin, V. E. Ferry, R. M. Briggs, and H. A. Atwater, Broadband polarization-indepedent resonant light absorption using ultrathin plasmonic super absorbers," Nat. Comm. **2**, 517 (2011).

[11] I. Prieto, B. Galiana, P. A. Postigo, C. Algora, L. J. Martinez, and I. Rey-Stolle, "Enhanced quantum efficiency of Ge solar cells by a two-dimensional photonic crystal nanostructured surface," Appl. Phys. Lett. **94**, 191102 (2009).

[12] A. Ganjoo, H. Jain, C. Yu, J. Irudayaraj, and C. G. Pantano, "Detection and fingerprinting of pathogens: Mid-IR biosensor using amorphous chalcogenide films," J. of Non-Crystalline Solids **354**, 2757–2762 (2008).

[13] S. J. Lee, Z. Y. Ku, A. Barve, J. Montoya, W. Y. Jang, S. R. J. Brueck, M. Sundaram, A. Reisinger, S. Krishna, and S. K. Noh, "A monolithically integrated plasmonic infrared quantum dot camera," Nat. Comm. **2**, 286 (2011).

[14] C. J. Hill, A. Soibel, S. A. Keo, J. M. Mumolo, D. Z. Ting, and S. D. Gunapala, "Demonstration of large format mid-wavelength infrared focal plane arrays based on superlattice and BIRD detector structures," Infrared. Phys. Tech. **52**, 348–352 (2009).

[15] L. Hutchinson, "Breast cancer: Challenges, controversies, breakthroughs," Nat. Rev. Clin. Onco. **7**, 669–670 (2010).

[16] S. Y. Lin, J. G. Fleming, Z. Y. Li, I. El-Kady, R. Biswas, and K. M. Ho, "Origin of absorption enhancement in a tungsten, three-dimensional photonic crystal," J. Opt. Soc. Am. B **20**, 1538–1541 (2003).

[17] S. Foteinopoulou and C. M. Soukoulis, "Electromagnetic wave propagation in two-dimensional photonic crystals: A study of anomalous refractive effects," Phys. Rev. B **72**, 165112 (2005).

[18] J. A. Mason, S. Smith, and D. Wasserman, "Strong absorption and selective thermal emission from a midinfrared metamaterial," Appl. Phys. Lett. **98**, 241105 (2011).

[19] J. A. Mason, G. Allen, V. A. Podolskiy, and D. Wasserman, "Strong coupling of molecular and mid-infrared perfect absorber resonances," IEEE Phot. Tech. Lett. **24**, 31–33 (2012).

[20] C. Kittel, *Introduction to Solid State Physics* (John Wiley and Sons, 2005).

[21] J. M. Bakker, L. M. Aleese, G. Meijer and G. von Helden, "Fingerprint IR spectroscopy to probe amino acid conformations in the gas phase," Phys. Rev. Lett. **91**, 203003 (2003).

[22] J. D. Joannopoulos, S. G. Johnson, J. N. Winn, and R. D. Meade, *Photonic Crystals: Molding the Flow of Light* (Princeton University Press, 2008).

[23] P. B. Catrysse and S. Fan, "Near-complete transmission through subwavelength hole arrays in phonon-polaritonic thin films," Phys. Rev. B **75**, 075422 (2007).

[24] S. Foteinopoulou, J. P. Vigneron, and C. Vandenbem, "Optical near-field excitations on plasmonic nanoparticle-based structures," Opt. Express **15**, 4253–4267 (2007), http://www.opticsinfobase.org/oe/abstract.cfm?URI=oe-15-7-4253.

[25] S. Foteinopoulou, M. Kafesaki, E. N. Economou, and C. M. Soukoulis, "Two-dimensional polaritonic photonic crystals as terahertz uniaxial metamaterials," Phys. Rev. B **84**, 035128 (2011).

[26] K. Sakoda, *Optical Properties of Photonic Crystals* (Springer, Berlin, 2001).

[27] R. Ruppin, "Electromagnetic energy density in a dispersive and absorptive material," Phys. Lett. A **299**, 309–312 (2002).

[28] G. Torrese. J. Taylor, H. P. Schriemer, and M. Cada, "Energy transport through structures with finite electromagnetic stop gaps," J. Opt. A: Pure Appl. Opt. **8**, 973–980 (2006).

[29] R. Loudon, "The propagation of electromagnetic energy through an absorbing dielectric," J. Phys. A **3**, 233–245 (1970).

[30] M. Bergmair, M. Huber, and K. Hingerl, "Band structure, Wiener bounds, and coupled surface plasmons in one dimensional photonic crystals," Appl. Phys. Lett. **89**, 081907 (2006).

[31] R. Moussa, S. Foteinopoulou, L. Zhang, G. Tuttle, K. Guven, E. Ozbay, and C. M. Soukoulis, "Negative refraction and superlens behavior in a two-dimensional photonic crystal," Phys. Rev. B **71**, 085106 (2005).

[32] S. Xiao, M. Qiu, Z. Ruan, and S. He, "Influence of the surface termination to the point imaging by a photonic crystal slab with negative refraction ," Appl. Phys. Lett. **85**, 4269-4271 (2004).

4

Photonic Crystal absorbers: Bragg vs. Effective medium regime

4.1 Chapter Overview

In the previous Chapter we achieved near-perfect absorptance with low-filling-ratio semiconductor photonic crystals (PCs) with a lattice constant roughly of the order of the free space wavelength of operation. In the following, we will refer to these larger lattice constant PCs as PCs in the Bragg regime. In this Chapter, we will investigate the absorption performance of PCs with a deep-subwavelength lattice constant. These PCs essentially behave as effective optical materials. Our objective is to evaluate and compare the Bragg and the effective medium PC routes to absorption enhancement and gain insight for further designs of superabsorbing structures.

Before proceeding to our results and analysis we briefly recap the methods employed in this chapter. The results in this chapter have been calculated with computer programs that have been developed based on Yariv and Yeh's Transfer Matrix Method (TMM) [1–4] that we have presented in Chapter 2, adapted to the specific parameters of the structures studied here.

4.2 Absorption control with natural polaritonic materials

The superabsorbing structures should have a large extinction coefficient that coexists with a small reflection. The latter allows most of the incident light to enter inside these structures. Once the light is inside, the large extinction coefficient ensures light absorption within a small distance within the structure by providing a strong power-loss rate. Therefore, it is advantageous to construct such superabsorbing structures from strongly absorbing constituents such as polaritonic materials. The latter have a large extinction coefficient in the Reststrahlen-band frequency regime. However, due to the extreme permittivity values of the polaritonic materials in this frequency regime, they are also typically highly reflective in bulk form. This high-reflection behaviour can be explained after considering the frequency dependent permittivity of the polaritonic materials. The polaritonic material permittivity can be described with a Lorentzian function [5],

$$\varepsilon = \varepsilon_\infty \left(1 + \frac{\omega_L^2 - \omega_T^2}{\omega_T^2 - \omega^2 - i\omega\Gamma}\right), \tag{4.1}$$

where ω is the angular frequency of the incident EM wave, Γ is the intrinsic damping parameter, ω_T is the transverse optical (TO) phonon frequency and ω_L is the longitudinal optical (LO) phonon frequency. The latter two frequencies are related by the Lyddane-Sachs-Teller relation (LST) [5] as:

$$\frac{\omega_L^2}{\omega_T^2} = \frac{\varepsilon_{st}}{\varepsilon_\infty}, \tag{4.2}$$

where ε_{st} and ε_∞ are the static permittivity and permittivity at very high frequencies of the polaritonic material respectively. We can separate the real and imaginary parts of the permittivity of the polaritonic material as:

$$\varepsilon = \varepsilon^{'} + i\,\varepsilon^{''}, \tag{4.3}$$

where

$$\varepsilon' = \varepsilon_\infty \left(1 + \frac{({\omega_L}^2 - \omega_T^2)(\omega_T^2 - \omega^2)}{(\omega_T^2 - \omega^2)^2 + (\omega\Gamma)^2}\right), \tag{4.4}$$

and

$$\varepsilon'' = \varepsilon_\infty \left(1 + \frac{({\omega_L}^2 - \omega_T^2)\omega\Gamma}{(\omega_T^2 - \omega^2)^2 + (\omega\Gamma)^2}\right). \tag{4.5}$$

We can identify from Eq. 4.4, that ε' becomes negative in the frequency regime between ω_T and ω_L (see also Fig. 2.2 in Chapter 2). Therefore, propagation of

light is prohibited in this region, implying a very high reflection. This frequency regime is referred to as the phonon-polariton gap or the Reststrahlen band [5] of the material. The precise reflectance, R, of a semi-infinite block made from this polaritonic material, can be evaluated from [6]:

$$\mathrm{R} = \frac{(n-1)^2 + \kappa^2}{(n+1)^2 + \kappa^2}, \tag{4.6}$$

where n and κ are the real and imaginary parts of the refractive index of the polaritonic material. From this reflectance, R we can evaluate the absorptance, A as $\mathrm{A} = 1 - \mathrm{R}$, since $\mathrm{T} = 0$ for the semi-infinite block. As an example, we plot in Fig. 4.1 the reflectance and absorptance of a semi-infinite block made of SiC versus the free space wavelength, λ_{free}, with red and black lines, respectively. We indicate the wavelengths corresponding to the LO and TO phonon frequencies with the green dashed lines in Fig. 4.1. As discussed above, the spectral region between these two frequencies represents the Reststrahlen band of SiC, indicated with the yellow shading in Fig. 4.1. We notice the high, near-unity reflectance in most part of this spectral region as expected.

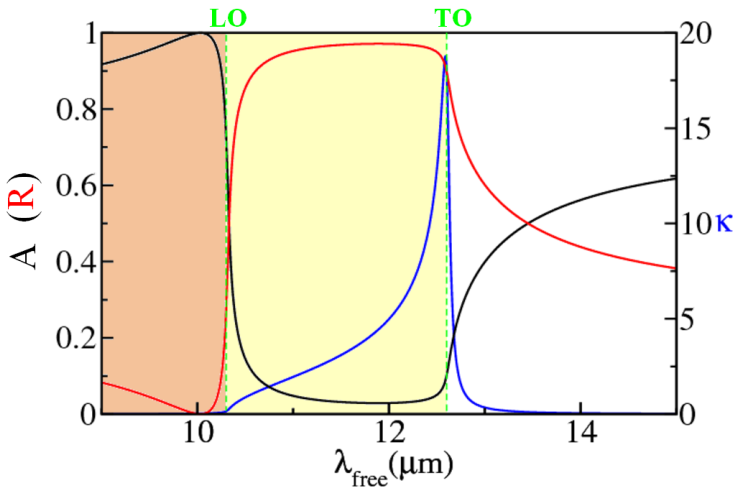

Figure 4.1: Spectral response of absorptance A (black line), reflectance R (red line) and extinction coefficient, κ (blue line) of a semi-infinite SiC block. The green dashed lines indicate the wavelengths corresponding to the LO and TO phonon frequencies in Eq. 4.1. The low and high reflectance region are indicated with the orange and yellow shadings respectively.

Now we draw the attention of the reader to the orange shaded region in the left side of the LO phonon wavelength, $\lambda_L = \frac{2\pi c}{\omega_L}$, in Fig. 4.1. In this spectral regime, polaritonic materials have low values of ε' and negligible values of ε'', (see Fig. 2.2 in Chapter 2) and κ as we see in Fig. 4.1. As a result, the reflectance becomes low according to Eq. 4.6. This low reflectance regime typically exists for polaritonic

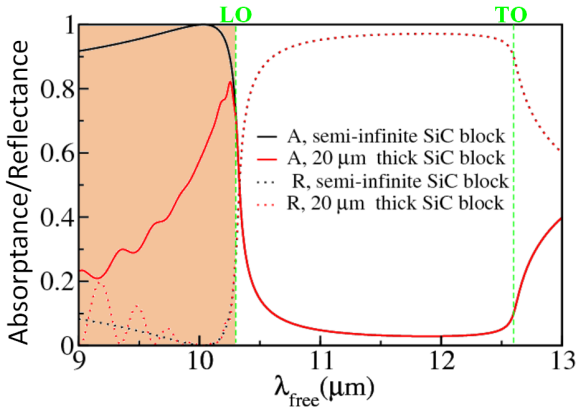

Figure 4.2: Spectral response of absorptance, A of a semi-infinite SiC block (black-solid line), and a 20 μm thick SiC block (red-solid line). The corresponding reflectance results of these two structures are shown with a black-dotted line and a red-dotted line respectively. The orange colour shading indicates the low reflectance spectral regime corresponding to $0 < \varepsilon' \leq 1$. The green dashed lines indicate the wavelengths corresponding to the LO and TO phonon frequencies in Eq. 4.1.

materials in the frequency regime where $0 < \varepsilon' \leq 1$, with the minimum reflectance occurring at $\varepsilon' = 1$. From now on, we refer to this particular frequency regime, as the low reflectance regime. In Fig. 4.1, we can see that for SiC this low reflectance regime spans between 10 μm and 10.3 μm. If we take a sufficiently thick material, then absorptance becomes very high in this low reflectance regime and the peak of the absorptance coincides with the reflectance minimum. In Fig. 4.1, we can observe this near-perfect absorptance peak for SiC at 10 μm.

If we take a thinner layer of polaritonic material, then the peak of the absorptance red shifts towards the higher values of ε'' away from the reflectance minimum. To make this evident we plot the spectral response for the absorptance (reflectance) from a semi-infinite SiC block and a 20 μm thick SiC block in Fig. 4.2, with a black solid (dotted) line and a red solid (dotted) line respectively. We can clearly observe that the absorption peak of the narrower SiC block is red-shifted towards the LO phonon frequency, ω_L. For practical reasons thinner structures are desirable. Accordingly we should expect in these thinner structures a red-shifted absorption peak away from the frequency where $\varepsilon' = 1$. Still, as Fig. 4.2 suggests, a large absorptance can be obtained, of more than 80% for the case of SiC.

So far we have discussed that natural polaritonic materials have a low reflectance regime, where absorptance can be as high one. However, for a specific natural polaritonic material this low reflectance window is fixed. Therefore, we cannot tailor the spectral position of the absorption window on demand. Therefore, in the

following, we will investigate the possibility to construct SiC metamaterials with an on-demand absorption window based on judicious design.

4.3 Effective polaritonic PC metamaterials for tunable absorption control

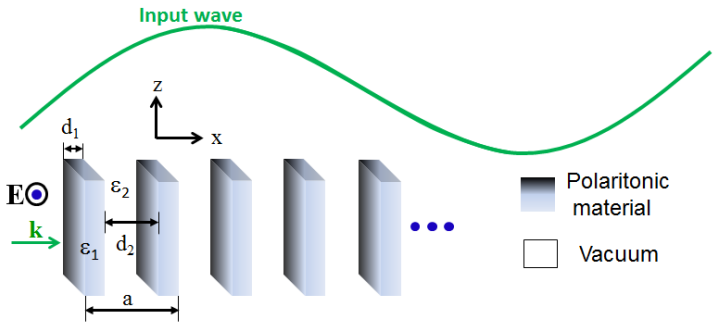

Figure 4.3: Schematics of the 1D-PC metamaterial with the geometric and material parameters indicated. The lattice constant, a, is much smaller than the impinging EM wave's (green curve) wavelength, λ_{free}.

In Section 2.2 of Chapter 2, we discussed that we can treat the 1D-PCs with a deep-subwavelength lattice constant as effective homogeneous media. Consequently we can assign a frequency dependent effective permittivity value $\varepsilon_{eff}(\omega)$, [7–15] as:

$$\varepsilon_{eff}(\omega) = \varepsilon_1(\omega) f_r + \varepsilon_2(1 - f_r), \tag{4.7}$$

where $\varepsilon_1(\omega)$ and ε_2 are the dielectric functions of the polaritonic medium and vacuum respectively, that comprise the PC (see schematics of Fig. 4.3). In the above equation, $f_r = \dfrac{\mathrm{d}_1}{\mathrm{a}}$ represents the filling ratio and $\mathrm{a} = \mathrm{d}_1 + \mathrm{d}_2$ represents the lattice constant of the PC, where d_1 and d_2 are the respective thicknesses of the constituent materials. As we mentioned in Chapter 2, Eq. 4.7 is an approximate relation valid when electric fields vary quasi-statically within the building blocks of the PC. This is a valid assumption for the geometry and size-scale of the building blocks which are less than ten times the wavelength of operation [14]. Furthermore, validation of this assumption is verified by comparing the absorption/reflection spectra corresponding to the effective medium model with exact calculations, which we discuss in detail in section 4.5.

With the use of the polaritonic material permittivity from Eq. 4.1, Eq. 4.7 yields the effective permittivity of the PC metamaterial [13]:

$$\varepsilon_{eff}(\omega) = \varepsilon_\infty \left(1 + \frac{\omega_L^2 - \omega_T^2}{\omega_T^2 - \omega^2 - i\omega\Gamma}\right) f_r + (1 - f_r). \tag{4.8}$$

The above equation can be expanded as:

$$\varepsilon_{eff}(\omega) = \frac{(\omega_T^2 - \omega^2 - i\omega\Gamma)\varepsilon_\infty f_r + (\omega_T^2 - \omega^2 - i\omega\Gamma)(1 - f_r)}{\omega_T^2 - \omega^2 - i\omega\Gamma}. \tag{4.9}$$

By rearranging the terms in Eq. 4.9 we get:

$$\varepsilon_{eff}(\omega) = \frac{(\varepsilon_\infty f_r + (1 - f_r))(-\omega^2 - i\omega\Gamma) + \omega_L^2 \varepsilon_\infty f_r + (1 - f_r)\omega_T^2}{\omega_T^2 - \omega^2 - i\omega\Gamma}. \tag{4.10}$$

With the use of LST relation from Eq. 4.2, the above equation can be rewritten as:

$$\varepsilon_{eff}(\omega) = \frac{(\varepsilon_\infty f_r + (1 - f_r))\,(-\omega^2 - i\omega\Gamma) + \omega_L^2 \left(\varepsilon_\infty f_r + (1 - f_r)\frac{\varepsilon_\infty}{\varepsilon_{st}}\right)}{\omega_T^2 - \omega^2 - i\omega\Gamma}, \tag{4.11}$$

and simplified to:

$$\varepsilon_{eff}(\omega) = \frac{\varepsilon_{\infty,eff}(-\omega^2 - i\omega\Gamma) + \omega_L^2 \alpha}{\omega_T^2 - \omega^2 - i\omega\Gamma}, \tag{4.12}$$

where $\varepsilon_{\infty,eff}$ and α are given by the following equations:

$$\varepsilon_{\infty,eff} = \varepsilon_\infty f_r + (1 - f_r), \tag{4.13}$$

and

$$\alpha = \varepsilon_\infty \left(f_r + \frac{(1 - f_r)}{\varepsilon_{st}}\right). \tag{4.14}$$

Finally, by introducing $\omega_{L,eff}$ as:

$$\omega_{L,eff} = \omega_L \sqrt{\frac{\alpha}{\varepsilon_{\infty,eff}}}, \tag{4.15}$$

we obtain the dielectric permittivity of the effective PC metamaterial as:

$$\varepsilon_{eff}(\omega) = \varepsilon_{\infty,eff} \left(1 + \frac{{\omega_{L,eff}}^2 - \omega_T^2}{\omega_T^2 - \omega^2 - i\omega\Gamma}\right). \tag{4.16}$$

We can identify from Eq. 4.16 that the permittivity of the effective metamaterial has a similar Lorentzian response as the constituent polaritonic material, with a new $\varepsilon_{\infty,eff}$ and a new LO phonon frequency $\omega_{L,eff}$, but with the same TO phonon frequency, i.e.

$$\omega_{T,eff} = \omega_T, \tag{4.17}$$

and the same intrinsic damping parameter:

$$\Gamma_{eff} = \Gamma. \tag{4.18}$$

Furthermore, after applying the LST relation, we get for the static permittivity $\varepsilon_{st,eff}$ of the effective PC metamaterial:

$$\varepsilon_{st,eff} = \varepsilon_{\infty,eff}\frac{\omega_{L,eff}^2}{\omega_{T,eff}^2}. \tag{4.19}$$

With the use of $\omega_{L,eff} = \omega_L\sqrt{\frac{\alpha}{\varepsilon_{\infty,eff}}}$ and $\omega_{T,eff} = \omega_T$ in the above equation, we get:

$$\varepsilon_{st,eff} = \alpha\frac{\omega_L^2}{\omega_T^2} \implies \varepsilon_{st,eff} = \alpha\frac{\varepsilon_{st}}{\varepsilon_\infty}. \tag{4.20}$$

Now with the use of α from Eq. 4.14, Eq. 4.20 yields for $\varepsilon_{st,eff}$:

$$\varepsilon_{st,eff} = \varepsilon_{st}f_r + (1 - f_r). \tag{4.21}$$

From Eqs. 4.13 and 4.21, we can infer that both the static permittivity, $\varepsilon_{st,eff}$ and the high frequency permittivity $\varepsilon_{\infty,eff}$ of the effective medium PC obey the same mixing rule as the effective permittivity of the PC, ε_{eff} in Eq. 4.7.

Moreover, we notice that the LO frequency of the effective PC metamaterial, $\omega_{L,eff}$, is smaller than the original LO frequency, ω_L of the constituent polaritonic material, since the value of $\sqrt{\frac{\alpha}{\varepsilon_{\infty,eff}}}$ is always less than one for any filling ratio. As a result the phonon-polariton gap spectrum of these structures, $\omega_{L,eff} - \omega_T$, is narrower than that of the constituent polaritonic material. That means the deep-subwavelength PCs behave as homogenized metamaterials with a narrowed engineered phonon-polariton gap determined by their filling ratios. This implies that a frequency regime that would be within the Reststrahlen band of the natural polaritonic material and thus repel light may now allow light propagation and in this manner enable absorption.

Note that as we mentioned in Chapter 2, the longitudinal phonon frequency, $\omega_{L,eff}$, in Eq. 4.16 represents the frequency where the real part of the effective permittivity, ε'_{eff}, becomes zero, but does not emanate from a physical coupling between the phonon and photon modes as the EM modes couple to the transverse optical phonon modes only. On the other hand, ω_T represents the frequency of the transverse optical phonon that couples with the transverse incident EM waves resulting in the phonon-polariton dispersion. When we consider normal incidence, the direction of the transverse-phonon-oscillation amplitude would be along the

interface (i.e. parallel to the electric field of the incident EM waves) as seen in the schematics of Fig. 4.3. In this direction, there is no structural boundary perceived in both the cases of the bulk medium and the multilayer structures. Therefore, the ω_T value is the same for both the bulk material and the multilayer structures. However, the $\omega_{L,eff}$ value will be different for the bulk material and the multilayer structures, since the net polarization, $\mathbf{P}$, averaged within the layers changes in the case of multilayer structures giving rise to a different permittivity and thus a different spectral position where such permittivity, ε'_{eff} is zero, i.e. a different value for $\omega_{L,eff}$. We see how the value of $\omega_{L,eff}$ depends on the PC parameters in Eq. 4.15 with the use of Eqs. 4.13 and 4.14.

In section 2, we have discussed that a low reflectance regime exists for polaritonic materials between the LO phonon frequency ω_L and the frequency at which ε' equals one. In the following we will show that the frequency at which ε'_{eff} becomes one does not change with the filling ratio of the effective medium PC and remains the same as for the original polaritonic material. This would imply that the absorption window that extends between the frequency where $\varepsilon' = 1$ and the LO frequency, has only one tunable bound, that of the LO frequency that can change with the filling ratio of the PC metamaterial.

For this purpose we rewrite the expression for ε'_{eff} here:

$$\varepsilon'_{eff} = \varepsilon_{\infty,eff}\left(1 + \frac{(\omega_{L,eff}{}^2 - \omega_T^2)(\omega_T^2 - \omega^2)}{(\omega_T^2 - \omega^2)^2 + (\omega\Gamma)^2}\right). \tag{4.22}$$

Suppose ε'_{eff} becomes one at $\omega = \omega_0$. That means:

$$\varepsilon_{\infty,eff}\left(1 + \frac{(\omega_{L,eff}{}^2 - \omega_T^2)(\omega_T^2 - \omega_0^2)}{(\omega_T^2 - \omega_0^2)^2 + (\omega_0\Gamma)^2}\right) = 1. \tag{4.23}$$

We can rewrite the above equation as:

$$\varepsilon_{\infty,eff}\left(1 + (\omega_{L,eff}{}^2 - \omega_T^2)F(\omega_0)\right) = 1, \tag{4.24}$$

where

$$F(\omega_0) = \frac{(\omega_T^2 - \omega_0^2)}{(\omega_T^2 - \omega_0^2)^2 + (\omega_0\Gamma)^2}. \tag{4.25}$$

Notice that $F(\omega_0)$ is independent of the filling ratio of the effective medium PC and depends only on the parameters of the constituent polaritonic material. From

Eq. 4.24, if ${\varepsilon'}_{eff}$ is to be equal to 1, we see that $F(\omega_0)$ should be equal to

$$F(\omega_0) = \frac{1 - \varepsilon_{\infty,eff}}{\varepsilon_{\infty,eff}\left({\omega_{L,eff}}^2 - \omega_T^2\right)}. \tag{4.26}$$

Thus, if we show that $F(\omega_0)$ in the above equation is independent of the filling ratio of the effective medium PC, then we essentially show that the frequency where ${\varepsilon'}_{eff} = 1$ is independent of the filling ratio of the effective metamaterial PC. By using that $\omega_{L,eff} = \omega_L\sqrt{\frac{\alpha}{\varepsilon_{\infty,eff}}}$ in Eq. 4.26, we get:

$$F(\omega_0) = \frac{1 - \varepsilon_{\infty,eff}}{\left(\varepsilon_{st,eff} - 1 - \varepsilon_{\infty,eff}\right)\omega_T^2}. \tag{4.27}$$

Finally, with the use of the respective expressions for $\varepsilon_{\infty,eff}$ and $\varepsilon_{st,eff}$ from Eqs. 4.13 and 4.21, we get from Eq. 4.27:

$$F(\omega_0) = \frac{1 - \varepsilon_{\infty}}{\left(\varepsilon_{st} - \varepsilon_{\infty}\right)\omega_T^2}. \tag{4.28}$$

Indeed, the term on the right hand side of Eq. 4.28 depends purely on the parameters of the constituent polaritonic material and is independent of the structural parameters of the effective PC metamaterials of Fig. 4.3. So, the frequency where ${\varepsilon'}_{eff} = 1$ is the same as the frequency where ${\varepsilon'}_1 = 1$. This implies that the low-reflectance regime is widened for the effective metamaterial PCs, as the low wavelength bound remains the same, but the high wavelength bound extends to higher values within the phonon-polariton gap. In this manner, effective medium polaritonic PCs offer us a route to enhance the absorption within the Reststrahlen band of the constituent polaritonic material.

4.4 Absorption enhancement with SiC based polaritonic metamaterials

To investigate the absorption potential of these effective metamaterial PCs that we discussed in the previous section, we study a SiC-air 1D-PC in the Reststrahlen band frequency range of SiC. The permittivity of SiC is given by Eq. 4.1 with parameters ε_∞=6.7, ω_T =$2\pi\times$23.79 THz, ω_L =$2\pi\times$29.07 THz and Γ =$2\pi\times$0.1428 THz in accordance with Ref. [16]. We have chosen this particular SiC PC system to compare the absorption results of the effective metamaterial PCs with that of the SiC Bragg PCs we studied in the previous Chapter.

We consider three SiC-air 1D-PCs with a deep-subwavelength lattice constant a of 1μm. We consider three filling ratios 0.05, 0.15 and 0.30 respectively. Since

Filling ratio of the metamaterial PC	$\sqrt{\frac{\alpha}{\varepsilon_{\infty,eff}}}$	$\varepsilon_{\infty,eff}$	$\varepsilon_{st,eff}$	$\omega_{L,eff}$ ($2\pi\times$ THz)	$\omega_{T,eff}$ ($2\pi\times$ THz)	Γ_{eff} ($2\pi\times$ THz)
fr=0.05	0.87	1.285	1.45	25.27	23.79	0.1428
fr=0.15	0.92	1.85	2.35	26.78	23.79	0.1428
fr=0.30	0.96	2.71	3.70	27.80	23.79	0.1428
Bulk SiC	1.0	6.7	10.00	29.07	23.79	0.1428

Table 4.1: Parameters in the effective permittivities of the SiC effective metamaterial PCs. Corresponding values of bulk SiC are also given for comparison.

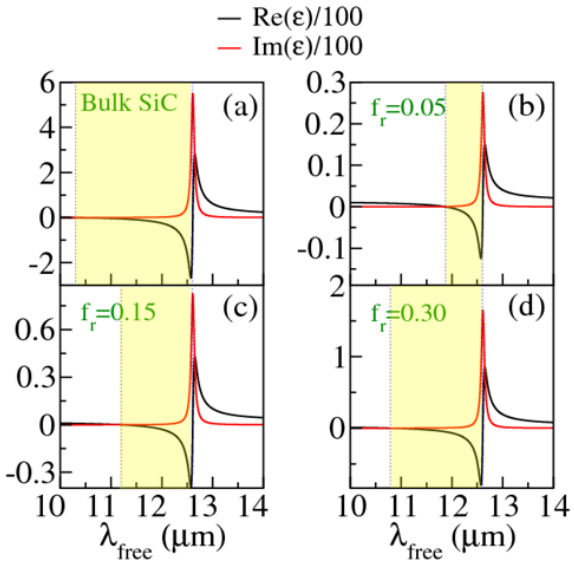

Figure 4.4: (a) The dielectric function of bulk SiC. (b), (c) and (d) same as (a), but for the effective medium PC corresponding to the three filling ratios: $f_r = 0.05$, $f_r = 0.15$ and $f_r = 0.30$. The shaded region in panel (a) indicates the phonon-polariton gap of SiC. The shaded regions in panel (b), (c) and (d) indicate the phonon-polariton gap of the effective homogenised PC metamaterials. Note, that the dielectric function values are scaled down 100 times relative to their original values.

the lattice constant of these PCs is about ten times smaller than the operating wavelengths in the Reststrahlen band of SiC, we can determine the effective permittivity of these PCs from Eq. 4.7. We plot the effective permittivity results of these PCs versus the free space wavelength, λ_{free}, in Figs. 4.4(b), 4.4(c) and 4.4(d) respectively. We also show the permittivity of bulk SiC in Fig. 4.4(a) for comparison. We designate the Reststrahlen band regimes for each of the effective PC metamaterials with a yellow shaded region in Fig. 4.4. We can identify that the effective permittivities of these PCs have similar Lorentzian profiles to that of bulk SiC as we expected. Furthermore, we can see that the width of their Reststrahlen band is reduced compared to the bulk SiC Reststrahlen-band width. We present the parameters of the effective polaritonic metamaterial PCs in Table 4.1, where we also include the effective static permittivity, $\varepsilon_{st,eff}$, and effective permittivity

at very high frequencies, $\varepsilon_{\infty,eff}$. As we explained in the previous section, the ω_T values of both bulk SiC and the effective metamaterial PCs are same. However, the $\omega_{L,eff}$ values change with the filling ratio of the PCs as given by Eq. 4.15. We see some specific values for $\omega_{L,eff}$ for specific filling ratios in Table 4.1.

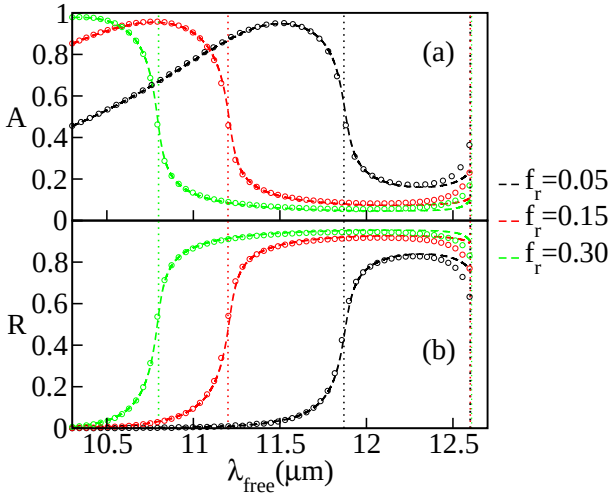

Figure 4.5: (a) Absorptance A, versus free the space wavelength, λ_{free}, for three 200 μm thick homogeneous media corresponding to the metamaterials constructed from the PCs with filling ratios $f_r = 0.05$ (black circles), $f_r = 0.15$ (red circles) and $f_r = 0.30$ (green circles) respectively. We show the respective TMM absorption results of the corresponding precise PC structures with a lattice constant a, of 1 μm as black-dashed line, red-dashed line and green-dashed line respectively. (b) same as (a), but for the reflectance R, versus the free space wavelength.

In order to investigate the absorption properties of the three effective metamaterial PCs, we evaluate their absorptance and reflectance from the analytical relations in Appendix. G, by using their corresponding effective permittivities from Eq. 4.16 with the parameters of Table. 4.1. We consider a total thickness of 200 μm which is close to 20 times the free space wavelength. We show the results in Figs. 4.5 (a) and 4.5(b) respectively. We plot the results versus the free space wavelength λ_{free}, as black, red and green circles for $f_r = 0.05$, $f_r = 0.15$ and $f_r = 0.30$ cases respectively. In Fig. 4.5, we also indicate with black, red and green dotted lines the respective bounds of the Reststrahlen bands of the polaritonic PC metamaterials corresponding to $f_r = 0.05$, $f_r = 0.15$ and $f_r = 0.30$.

We can clearly see that all these PC metamaterials have a low reflectance outside their respective Reststrahlen band wavelength regime until ε' becomes one as we predicted above. It is remarkable to observe more than 90% absorptance in this low reflectance regime in all cases. However, it is important to note that the absorption maxima for these effective media do not coincide with their

corresponding reflectance minima. This is because the thickness of these effective polaritonic metamaterials is not sufficient to completely absorb the light passing through them. As a result the absorption peak red shifts as we also observed in section 2 for bulk SiC.

We notice that simply by changing the filling ratio of the PCs, we can shift the absorptance peak of the corresponding effective metamaterial anywhere within the Reststrahlen band of SiC. These results demonstrate that we can achieve near-perfect absorptance within the highly reflecting Reststrahlen frequency regime of natural polaritonic materials by creating new artificial PCs behaving as polaritonic effective metamaterials. In the following section, we will verify that indeed such absorption in these subwavelength structures is purely an effective medium effect and not a photonic crystal effect.

4.5 Verification of the effective medium behaviour for the polaritonic PC metamaterials

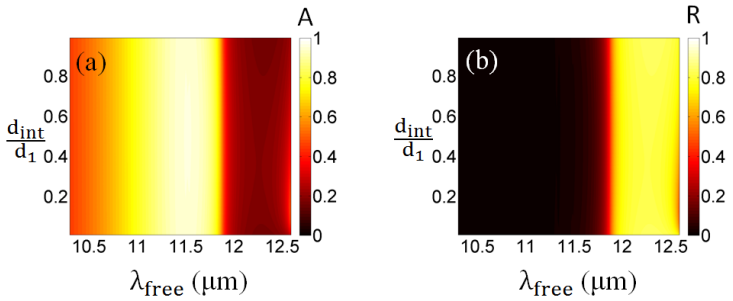

Figure 4.6: (a) Absorptance A, versus the free space wavelength λ_{free}, and the termination ratio $t_{ratio} = \frac{d_{int}}{d_1}$, for the 200 μm thick homogeneous metamaterial PC of filling ratio $f_r = 0.05$. (b) same as (a), but for the reflectance R, versus the free space wavelength λ_{free}, and the termination ratio t_{ratio}.

To verify the claimed effective medium behaviour of the polaritonic PC metamaterials, we evaluate the absorptance and reflectance of the underlying PC structures by employing the TMM [1–4] method described in Chapter 2, and plot them also in Figs. 4.5 (a) and 4.5(b). We indicate the results corresponding to the underlying PCs with $f_r = 0.05$, $f_r = 0.15$, and $f_r = 0.30$ and lattice constant a, of 1 μm as black, red and green dashed lines respectively. We notice a perfect match between results of the exact PC structures and the effective homogeneous polaritonic metamaterials, given by the corresponding circles in the figure.

Furthermore, in the following we provide additional evidence that the high absorption of the deep-subwavelength PCs arises from their effective medium behaviour, and is not a photonic crystal effect. We found in Chapter 3 that terminating the first SiC layer of the Bragg PCs can dramatically alter their absorption performance [17]. Therefore, we evaluate the influence of termination on the absorptance A, by employing the TMM method [1–4] for the PC metamaterial with $f_r = 0.05$. We show the results in Fig. 4.6 (a), versus the free space wavelength, λ_{free}, and the termination ratio $t_{ratio} = \frac{d_{int}}{d_1}$. Here d_{int} is the thickness of the terminated SiC layer at the input layer of the PC. We show the similar plot for the reflectance in Fig. 4.6 (b). We notice that the termination of the first SiC layer has essentially no effect on both the absorptance and reflectance across the spectrum. These results attest that the mechanism for absorption control in these effective polaritonic metamaterial PCs is distinctly different from the Bragg regime PCs.

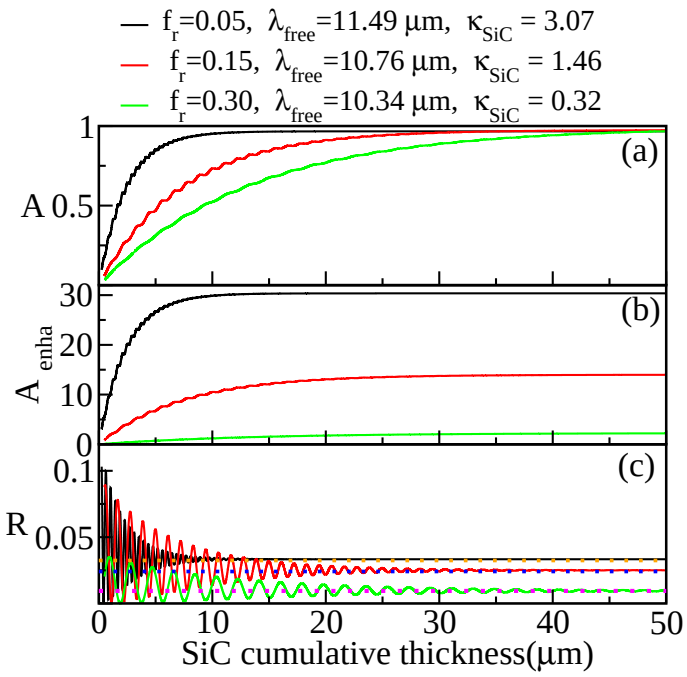

Figure 4.7: (a) Absorptance, A of homogeneous media corresponding to the metamaterials constructed from the PCs with filling ratios $f_r = 0.05$ (black line), $f_r = 0.15$ (red line) and $f_r = 0.30$ (green line) is plotted versus the SiC cumulative thickness. (b) and (c) same as (a), but for the absorption enhancement, A_{enha}, and the reflectance, R respectively versus the SiC cumulative thickness. The free space wavelengths, λ_{free}, at which we evaluated each of these cases are indicated. These wavelengths are chosen at the absorption peak values of the 200 μm thick homogeneous metamaterial PCs of Fig. 4.5. We also indicate the extinction coefficient values, κ_{SiC} of bulk SiC at these wavelengths.

4.6 Performance evaluation of the SiC based polaritonic metamaterial absorbers

We saw that near-perfect absorption can be achieved with all the three effective PC metamaterials that we considered, with parameters given in Table 4.1. Here we evaluate and compare their performance. For this purpose, we calculate the absorption, and the absorption enhancement of the above three metamaterial PCs with respect to a 200 μm thick block of bulk SiC at the wavelengths of their corresponding absorption peaks seen in Fig. 4.5. We show the results in Fig. 4.7(a) and (b) versus the cumulative SiC thickness that the EM wave crosses through each of these structures. We designate the $f_r = 0.05$ case with a black line, $f_r = 0.15$ case with a red line and the $f_r = 0.30$ case with a green line respectively.

We notice from Fig. 4.7(a) and (b) that the effective medium PC with $f_r = 0.05$ demonstrate both the highest absorption and the highest absorption enhancement among the three PCs. Moreover, we can see that both the absorption and the absorption enhancement of this low filling ratio PC reach their saturation values by employing less SiC material. This is due to the larger extinction coefficient of SiC at the absorption peak wavelength of this low filling ratio PC compared to the other two PCs with larger filling ratios (see the labels in Fig. 4.7).

We also plot the corresponding reflectance versus the cumulative SiC thickness in Fig. 4.7(c). We can observe that all the three effective metamaterial structures have reflectance lower than 10%. Note, the high slab thicknesses results converge with the semi-infinite results shown as dotted lines in the same figure. This clearly confirms that the slower saturation for the $f_r = 0.30$ case is due to the low extinction coefficient, κ for SiC at that frequency and not due to a higher reflectance.

4.7 Comparison of the absorptance performance between the effective metamaterial and the Bragg regime polaritonic photonic crystals

We saw that the effective metamaterial PCs can yield near-perfect absorptance, corresponding to an absorption enhancement as high as 30. Therefore, it is interesting to compare the absorption performance of this low filling ratio effective metamaterial PC with the large lattice constant PCs of the Bragg regime that we studied in Chapter 3. In Chapter 3, we demonstrated that we can achieve near-perfect absorp-

tance with a SiC PC within the Reststrahlen band frequency regime of SiC. Our approach was based on exciting the quickly-vanishing lossy Floquet-Bloch modes together with carefully manipulating the energy velocity and the energy velocity gradient at the interface of the PC [17].

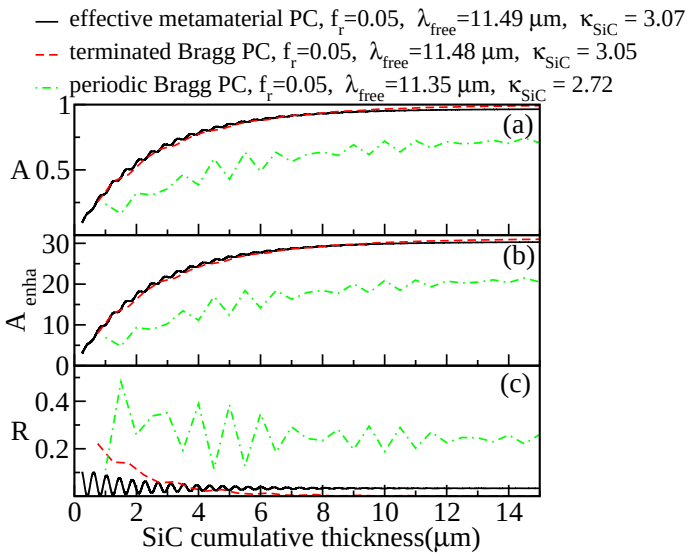

Figure 4.8: Absorption, A versus SiC cumulative thickness for an homogeneous medium corresponding to the metamaterial constructed from a PC with a lattice constant of 1 μm and a filling ratio of 0.05 (black-solid line), a terminated Bragg PC with a lattice constant of 10 μm and a filling ratio of 0.05 (red-dashed line), and a periodic Bragg PC with a lattice constant of 10 μm and a filling ratio $f_r = 0.05$ (green dot-dashed line). (b) and (c) same as (a), but for the absorption enhancement, A_{enha}, and the reflectance, R respectively, versus the SiC cumulative thickness. The free space wavelengths, λ_{free}, at which we evaluated each of these cases are indicated. These wavelengths are chosen to coincide with the absorption peak values of the PCs with 200 μm total thickness. We also indicate the extinction coefficient values, κ_{SiC} of bulk SiC at these wavelengths.

For this comparative study, we consider two Bragg PCs with a lattice constant of 10 μm and a filling ratio of 0.05. The first Bragg PC has its front SiC layer terminated to half of its original size, while the second Bragg PC is completely periodic. We refer to these PCs as terminated Bragg PC and periodic Bragg PC respectively. In Fig. 4.8(a), we show the absorption versus the cumulative SiC thickness for these two Bragg PCs as well as for the effective metamaterial PC with $f_r = 0.05$ we studied in the previous section at their respective absorption peak wavelengths. We notice that the absorptance of the periodic Bragg PC is oscillatory and lower than the other PCs. We attribute its oscillatory behaviour to the Fabry-Perot reflections. However, when we terminate the front SiC layer of the Bragg PC, we achieve a reflectionless conditions at the absorption peak, as explained in Chapter 3. As a result, the terminated Bragg PC exhibits a better absorption performance than the periodic Bragg PC. More importantly, we observe

that the peak absorptance performance of the terminated Bragg PC is almost the same as the one demonstrated by the effective metamaterial PC with $f_r = 0.05$. We can also make a similar observation for the absorption enhancement of these three PCs from Fig. 4.8(b).

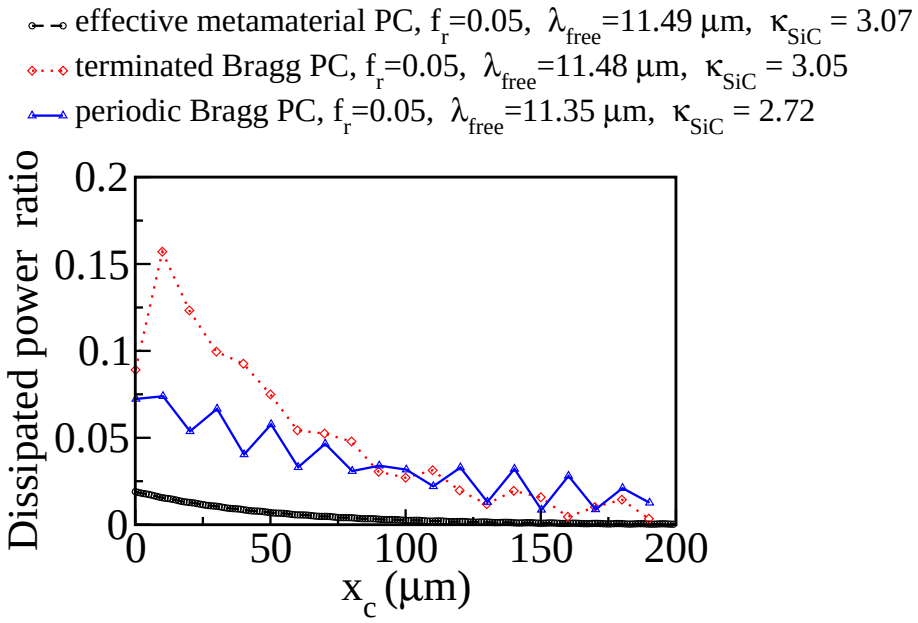

Figure 4.9: (a) Dissipated to incident power ratio in the individual SiC layers, versus the position of the center of the SiC layer x_c, for three SiC-air 1D-PCs: a two-hundred-unit-cell effective metamaterial PC with a lattice constant of 1 μm and a filling ratio of 0.05 (black circles), a twenty-unit-cell terminated Bragg PC with a lattice constant of 10 μm and a filling ratio of 0.05 (red diamonds) and a twenty-unit-cell periodic Bragg PC with a lattice constant of 10 μm and filling ratio of 0.05 (blue triangles). The free space wavelengths, λ_{free}, at which we evaluated the power dissipation ratio for each case are same as in Fig. 4.8.

These results imply that the effective medium PC route does not appear to surpass the performance at peak wavelength of the Bragg PC route, when the reflectionless condition is engineered. In fact, for a given thickness of SiC material, we would require more number of SiC layers in the effective metamaterial PC to obtain the same absorption or absorption enhancement with that of the terminated Bragg PC at the peak wavelength. Furthermore, the corresponding reflectance results shown in Fig. 4.8(c) indicate that the terminated Bragg PC has the lowest reflectance. To understand better the absorption performance of these PCs, in the following, we will also evaluate where the power is absorbed inside each of these PCs.

For this purpose, we evaluate the ratio of dissipated to incident power within each SiC layer of these PCs by using Eq. 2.52 and employing the TMM method [1–4] as we explained in Chapter 2. We plot the results versus the position x_c

of the centre of the SiC layer of these PCs at their peak wavelengths in Fig. 4.9. We notice that power is dissipated throughout the effective metamaterial PC and the periodic Bragg PC as indicated with black circles and blue triangles respectively. However, inside the terminated Bragg PC, most of the power is dissipated within the first few building blocks as shown with red diamonds. These results explain that effective metamaterial structures require large number of building blocks to achieve high absorption enhancement, while the terminated Bragg PC requires fewer building blocks. This implies the latter would be a more appropriate route for compact designs that we will explore further in the subsequent Chapter.

4.8 Conclusion

We explored a polaritonic PC-based effective medium route to absorption enhancement. We found that near-perfect absorptance can be achieved within the highly reflecting Reststrahlen band regime of SiC with deep sub-wavelength SiC-air PC structures that behave as effective media. Other variations can be considered with Mid-IR transparent materials such as BaF_2 or ZnSe [18, 19] as the spacer material. We demonstrated that simply by changing the filling ratio of the effective medium PCs, we can create new artificial polaritonic materials with tailored phonon-polariton gap regime, and thereby control the spectral location of the absorption peak. Our results suggest that for a given SiC material thickness, we require many thin SiC layers to achieve the high absorption enhancement with effective medium PCs. Recent advances in self-assembly type of fabrication methods could make such effective medium approach to absorption possible with other polaritonic materials such as LiF [20]. However, with semiconductor microstructures the fabrication of several layers appears rather challenging. On the other hand, the large lattice constant photonic crystal route seems promising where a strong absorption performance effect is observed with a fewer number of SiC layers. We therefore explore this latter PC route further in the next Chapter entitled "Compact photonic-crystal superabsorbers from strongly absorbing media".

Bibliography

[1] A. Yariv and P. Yeh, *Optical Waves in Crystals: Propagation and Control of Laser Radiation* (Wiley-Interscience, Hoboken 1984).

[2] P. Yeh, *Optical waves in layered media* (Wiley-Interscience, 2005).

[3] P. Yeh, A. Yariv, and C. S. Hong, "Electromagnetic propagation in periodic stratified media. I. General theory*," J. Opt. Soc. Am. **67**, 423-438 (1977).

[4] A. Yariv and P. Yeh, "Electromagnetic propagation in periodic stratified media. II. Birefringence, phase matching, and x-ray lasers," J. Opt. Soc. Am. **67**, 438-447 (1977).

[5] C. Kittel, *Introduction to Solid State Physics* (John Wiley and Sons, 2005).

[6] F. Wooten, *Optical properties of Solids*, (Academic press, Newyork, 1972).

[7] D. E. Aspnes, "Local-field effects and effective-medium theory: A microscopic perspective ," Am. J. Phys. **50**, 704-709 (1982).

[8] D. A. G. Bruggeman, "Berechnung verschiedener physikalischer Konstanten von heterogenen Substanzen. I. Dielektrizitaetskonstanten und Leitfaehigkeiten der Mischkoerper aus isotropen Substanzen," Ann. Phys. (Leipzig) **24**, 636-664 (1935).

[9] J. C. M. Garnett, "Colours in Metal Glasses and in Metallic Films," Philos. Trans. R. Soc. London A **203**, 385-420 (1904).

[10] J. C. M. Garnett, "Colours in Metal Glasses, in Metallic Films, and in Metallic Solutions. II," Philos. Trans. R. Soc. London A, **205**, 237-288 (1906).

[11] A. Kirchner, K. Busch and C. M. Soukoulis, "Transport properties of random arrays of dielectric cylinders," Phys. Rev. B, **57**, 277 (1998).

[12] W. Cai and V. Shalaev, *Optical Metamaterials Fundamentals and Applications*, (Springer, New York, 2010).

[13] S. Foteinopoulou "Photonic crystals as metamaterials," Physica B **407**, 4056-4061 (2012).

[14] S. Foteinopoulou, M. Kafesaki, E.N. Economou and C.M. Soukoulis, "Two-dimensional polaritonic photonic crystals as terahertz uniaxial metamaterials," Phys. Rev. B **84** 035128 (2011).

[15] M. Born and E. Wolf, *Principles of Optics : Electromagnetic Theory of Propagation, Interference, and Diffraction of Light*, (University Press, Cambridge, 2006).

[16] P. B. Catrysse and S. Fan, "Near-complete transmission through subwavelength hole arrays in phonon-polaritonic thin films," Phys. Rev. B **75**, 075422 (2007).

[17] G. C. R. Devarapu and S. Foteinopoulou, "Mid-IR near-perfect absorption with a SiC photonic crystal with angle-controlled polarization selectivity ," Opt. Express **20**, 13041-13054 (2012).

[18] W. Kaiser, W. G. Spitzer, R. H. Kaiser, and L. E. Howarth, "Infrared Properties of CaF_2, SrF_2, and BaF_2," Phys. Rev. **127**, 1950-1954 (1962).

[19] H. H. Li, "Refractive Index of ZnS, ZnSe, and ZnTe and Its Wavelength and Temperature Derivatives," J. Phys. Chem. Ref. Data **13**, 103 (1984).

[20] M. F. Acosta, S. Ganschow, D. Klimm, S. Serrano-Zabaleta, . Larrea and R. I. Merino, "Directional solidification of the eutectic LiFLiYF4 using Bridgman and micro-pulling down techniques: Microstructural study and some properties," J. Euro. Ceramic Soc. **34**, 2051-2059 (2014).

5

Compact photonic-crystal superabsorbers from strongly absorbing media

5.1 Chapter overview

In the previous Chapter, we compared the absorption performance of SiC Bragg PCs and effective metamaterial PCs. We found that from fabrication point of view, the former structures are advantageous as they require fewer SiC layers to achieve a high absorptance. However, still the Bragg PC we studied in Chapter 3, has a total thickness of roughly twenty-free-space-wavelengths, which makes it quite bulky. Therefore, in this Chapter[1,2] we optimise the SiC 1D-PC design to make it compact and practically realisable, by tuning its structural parameters, so that the reflectionless conditions that was derived in Chapter 3 occurs very close to the PC-band edge, leading to a quick absorption within the photonic crystal.

[1]Per Section 2.2 of code of practice for presentation of Theses, this chapter is presented as published in the paper: Ganga Chinna Rao Devarapu and Stavroula Foteinopoulou, "Compact photonic-crystal superabsorbers from strongly absorbing media," J. Appl. Phys. **114**, 033504 (2013). [© 2013 AIP Publishing LLC. See `http://dx.doi.org/10.1063/1.4811521`].

[2]Copyright 2013 American Institute of Physics. This article may be downloaded for personal use only. Any other use requires prior permission of the author and the American Institute of Physics. The following article appeared in J. Appl. Phys. **114**, 033504 (2013) and may be found at `http://dx.doi.org/10.1063/1.4811521`.

Before proceeding to our results and analysis we briefly recap the methods employed in this chapter. The results in this Chapter have been calculated using computer programs that have been developed based on Yariv and Yeh's Transfer Matrix Method (TMM) [1–3] that we have presented in Chapter 2, adapted to the specific parameters of the structures studied here.

Abstract

We present a route to near-perfect absorption in compact photonic-crystal (PC) structures constructed from strongly absorbing media that are typically highly reflective in bulk form. Our analysis suggests that the key underlying mechanism in such PC superabsorbers is the existence of a PC-band-edge reflectionless condition. Although the latter is by default uncharacteristic in photonic crystals, we propose here a clear recipe by which such condition can be met by tuning the structural characteristics of one-dimensional lossy PC structures. Based on this recipe we constructed a realizable three-layer SiC-BaF_2-SiC PC operating within the Reststrahlen band of SiC. We demonstrate near-perfect absorption in this prototype of total thickness smaller than $\lambda/3$, where more than 90% of the impinging light is absorbed by the top deep-subwavelength layer of thickness $\sim \lambda/1100$. We believe our study will inspire new photonic-crystal-based designs for extreme absorption harnessing across the electromagnetic spectrum.

5.2 Introduction

Absorbers are crucial components in photovoltaic and bolometric light detectors [4–6], and thus invaluable for a wide range of applications such as energy conversion systems [7, 8], IR imaging devices [9, 10] for early-stage cancer diagnosis [14–16] as well as bio-sensing [11–13]. This immense applications potential has spurred intensive research efforts for new efficient absorber designs across the EM spectrum. Traditional architectures may involve a top anti-reflection coating [6] to enhance the in-coupling of light and a back-reflector that facilitates a second light pass [5]. Many current works go beyond the latter approach with focused efforts around absorption optimization by nano/micro-structuring the absorber and/or its environment [17–20], including structures aiming for plasmon-mediated near-field enhancement in the vicinity of the absorber [7, 8, 11, 12, 14, 21].

Photonic-crystals have been researched for absorption control both as back-reflector components [22–24] and directly as the absorptive medium [25–29]. The latter

cases seem promising schemes for one-step absorption platforms where the lossy photonic crystal could facilitate the in-coupling of all impinging light and at the same time would mold the coupled mode in a fashion that enables all light to get absorbed. This one-step process is highly attractive, but also particularly challenging, even more so for thin sub-wavelength structures. Compact PC-based superabsorbers should demonstrate a strong power-loss rate; so they should be constructed from strongly absorbing media. Yet strong absorbers, i.e. media with a large extinction coefficient κ, are typically highly reflective as bulk materials. In Ref. [29] Devarapu and Foteinopoulou derived theoretically a condition for zero reflection at the interface of a lossy one-dimensional (1D) PC[3]. Relying on this condition they demonstrated a SiC-air PC paradigm which is reflectionless even within the Reststrahlen band of SiC. This feature had been subsequently utilized to achieve a near-perfect absorption with a thick structure of about $\sim 20\lambda$ [29].

In this paper, we investigate control of the spectral occurrence of the aforementioned reflectionless condition with the structural characteristics of 1D PCs. Relying on the insight gained from the analysis of the latter design principle we propose compact realizable PC structures exhibiting dramatic absorption enhancement. In particular, in Section 5.3 we explore how the PC's structural features should be tuned for the spectral control of the reflectionless condition. In Section 5.4 we analyze the key importance of the spectral position of the reflectionless condition with respect to the PC band-edge on extra-ordinary absorption control. By applying the insight gained by this analysis, we explore extreme absorption harnessing with a compact three-layer PC in Section 5.5. Finally, we present practically realizable compact designs in Section 5.6 and discuss our conclusions in Section 5.7.

5.3 Photonic Band-edge and reflectivity

In Ref. [25] S. Y. Lin et al. presented a metallic photonic crystal absorber, where the observed optimal –close to 50%– absorption was attributed to the low energy velocity, v_e at the PC band-edge, providing longer light-matter interaction times. However, very recently the theoretical analysis [29] of Devarapu and Foteinopoulou uncovered a complex relation between energy velocity and reflection [4]. They showed that actually optimal absorption occurs when the PC is reflectionless, which is atypical for band-edge frequencies. In this section, we explore whether it is possible by tuning the PC's characteristics to push such reflectionless condition very close to the band-edge.

[3]Please refer to Eqs. 3.8 and 3.10 in Chapter 3 of this thesis.
[4]Please refer to section 3.5 in Chapter 3 of this thesis.

For this purpose, and for completeness, we briefly recap the reflectionless condition that was derived in Ref. [29]. For a one-dimensional lossy PC to be reflectionless, the energy velocity at its interface should be equal to:

$$\mathrm{v_{e0}} = \frac{2c}{\varepsilon^{'} + \frac{2\omega\varepsilon^{''}}{\Gamma} + 1}, \tag{5.1}$$

with c being the speed of light. The quantity $\varepsilon^{'} + 2\omega\varepsilon^{''}/\Gamma$ appearing in the denominator of Eq. 5.1 is characteristic of a Lorentzian absorber [30] of dispersive permittivity $\varepsilon(\omega)$, with ω and Γ being the impinging electromagnetic (EM) wave's and material's damping frequencies respectively. This factor is correlated with the lossy medium's stored electric energy density [31]. Note that throughout this paper the prime and double-prime will designate the real and imaginary part of the permittivity respectively. Eq. 5.1 suggests that the optimal energy velocity value at the interface that is required for the PC structure to be reflectionless is dictated only by the lossy material that is placed at the interface. However, tailoring the energy velocity at the interface of the PC does depend highly on all its constituents and its structural particulars.

For the PC to be reflectionless, Eq. 5.1 is a necessary but not a sufficient condition. In addition, the impinging light must be slowing down as it enters the PC with a negative spatial energy velocity gradient that is given by:

$$\left(\frac{d\mathrm{v_e}}{dx}\right)_0 = \frac{\varepsilon^{''}\omega}{\mathrm{c}}\mathrm{v_{e0}}\left[-1 + \frac{\mathrm{v_{e0}}}{c}\right], \tag{5.2}$$

where $\mathrm{v_{e0}}$ is the required optimal interface-energy-velocity value given by Eq. 5.1. We proceed by studying a SiC-air 1D PC system as in Ref [29], depicted in the schematics of Fig. 5.1(a) with all relevant geometric features designated in the figure- with "1" and "2" labeling the properties of the SiC and air layer respectively. The corresponding permittivities are $\varepsilon_1 = \varepsilon(\omega)$ and $\varepsilon_2 = 1$, with the dispersive dielectric $\varepsilon(\omega)$ given by:

$$\varepsilon(\omega) = \varepsilon_\infty\left(1 + \frac{\omega_L^2 - \omega_T^2}{\omega_T^2 - \omega^2 - i\omega\Gamma}\right), \tag{5.3}$$

where ε_∞=6.7, ω_T =$2\pi\times$23.79 THz, ω_L =$2\pi\times$29.07 THz and Γ =$2\pi\times$0.1428 THz in accordance with Ref. [32]. Eq. 5.3 with these parameters gives a permittivity model close to the experimental optical Palik data [33] for SiC that is appropriate for EM waves varying as $e^{-i\omega t}$ with time, t[34, 35]. The SiC permittivity is shown in Fig. 5.1(b), where we have highlighted the Reststrahlen band where our subsequent

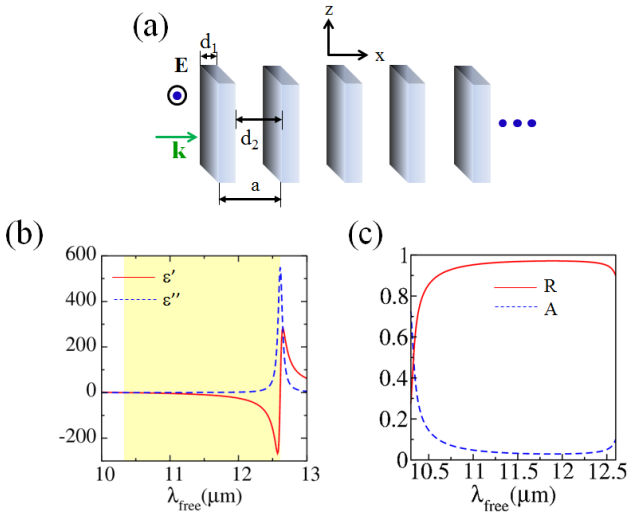

Figure 5.1: (a) Schematics of the SiC-air 1D-PC with the geometric parameters indicated. (b) Spectral response of the real (solid) and imaginary (dashed) parts of the SiC permittivity model of Eq. 5.3. (c) Absorption (dashed line) and reflection (solid line) for a thick bulk SiC block.

investigation focuses. In the Reststrahlen regime, light does not couple efficiently inside the bulk material. It gets reflected with very little light getting absorbed as one can see in Fig. 5.1(c).

For the SiC-air 1D PC there are two main structural characteristics that can be tuned to control its behavior. One is its inter-layer separation, a, known as lattice constant, and the other the SiC filling ratio, f, given by d_1/a. We focus in the following only on a low filling ratio PC, with $f = 0.05$. This is because we found that as the PC's filling ratio increases it start resembling the behavior of bulk SiC [29]. So the primary "tuning knob" to control the PC's properties will be the lattice constant, a. We alert the reader that the familiar scalability law applicable to dielectric PCs [36] does not extend to our PC system under investigation, because it is made of dispersive constituents. In other words, changes in the PC's lattice constant can in principle affect very different PC behaviors in contrast with a mere frequency shift of the same behavior which one expects for dielectric PCs.

Accordingly, we investigate in the following the interface energy velocity $v_{e,\,int}$ with changing lattice constant a for a semi-infinite PC [37]. It can be shown that it can be evaluated by the following expression [31]:

$$v_{e,int} = \frac{\frac{1}{2}\mathrm{Re}[E_y(0)H_z^*(0)]}{\frac{1}{4}[\varepsilon_0\left(\varepsilon' + \frac{2\omega\varepsilon''}{\Gamma}\right)|E_y(0)|^2 + \mu_0|H_z(0)|^2]}, \tag{5.4}$$

where ε_0 and μ_0 are the vacuum permittivity and permeability respectively. E_y and H_z represent the relevant $y-$ and $z-$ components of the electric and magnetic field [see Fig. 5.1(a)]. The fields are evaluated at the interface, i.e at $x = 0$, using the Transfer Matrix Method (TMM) [1–3].

Three characteristic cases for the spectral response of the energy velocity at the PC interface, $v_{e,int}$, are shown as solid lines in Figs. 5.2 (a), 5.2(b) and 5.2(c), that correspond to PCs with lattice constants a=5 μm, 8 μm and 10 μm respectively. Note, $v_{e,int}$ is expressed as a fraction of the speed of light, c and is plotted versus the free space wavelength λ_{free} of the incoming EM wave. We can identify the PC band-edge in each case of Fig. 5.2 with the region where the energy velocity drops to nearly zero, but we note that this is not sharply defined for lossy media. We also show the reflectionless condition by plotting the required interface-energy-velocity optimum, $v_{e,0}$, with the dotted lines. The intersection between the $v_{e,int}$ and the $v_{e,0}$ curves signifies the free-space wavelength where the PC can be reflectionless. We highlight more clearly this region in the insets of each figure.

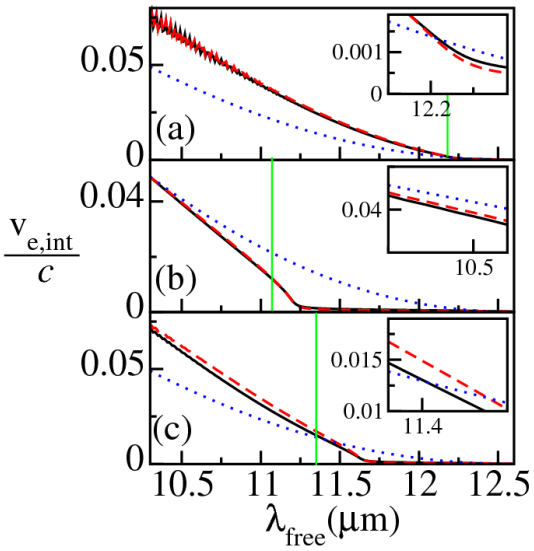

Figure 5.2: Spectral response of the energy velocity at the interface $v_{e,int}$ of a semi-infinite SiC-air PCs structure is shown as solid lines. The dashed lines depict the corresponding values for the same PCs but with 50% of their entry face being cut-off. The results in (a), (b) and (c) represent the PC cases with a lattice constant of a equal to 5 μm, 8 μm and 10 μm, respectively. In all cases, the interface-energy velocity value of the reflectionless condition, $v_{e,0}$ of Eq. 5.1, is depicted with dotted lines. Note, all energy velocity values are expressed in terms of the speed of light c. The vertical solid lines represent the spectral position of the absorption peaks that we will observe in Fig. 5.5.

We observe three distinct behaviors with respect to the relation between the $v_{e,int}$ and $v_{e,0}$ curves. The eight-micron structure case, seems to be completely different

from the case of the five- and ten-micron structures[5] . In particular, we see that the two energy velocity curves pass close together without intersecting, at an extended wavelength region around 10.5 μm and far from the band-edge. Based on this observation, we predict that the eight-micron design would not be the most suitable for an enhanced absorption performance, which we will confirm in Section 5.4. The behavior of the five-micron and ten-micron designs looks similar where we see that the $v_{e,int}$ and $v_{e,0}$ curves intersect, which means both can potentially operate as reflectionless PCs at the intersection wavelength. Yet, there is a small, but very important difference. For the five-micron PC design the intersection between $v_{e,int}$ and $v_{e,0}$ curves occurs at the close vicinity of the band-edge. On the other hand, this intersection occurs somewhat further from the band-edge for the ten-micron PC design, whose behavior is similar to the case studied in Ref. [29]. We will see in the following section, that even this seemingly small spectral difference in the intersection occurrence with respect to the band-edge will have an enormous impact on the respective PCs performances as absorbers.

We would like to remind the reader, that the existence of an intersection between $v_{e,int}$ and $v_{e,0}$ is only a necessary condition. Light should also slow down as it enters the PC structure with an appropriate spatial gradient given by Eq. 5.2. Altering only the entry-layer thickness, without modifying the remaining PC characteristics, tunes the interface energy velocity gradient [29] without changing much the value of $v_{e,int}$. We can see that by observing the dashed line curves in Fig. 5.2, which correspond to the same semi-infinite PCs, but with 50% of their entry SiC layer being cut-off.

This effect can be clearly seen in Fig. 5.3, where dv_e/dx is calculated [1–3] as a function of the location, x within the entry SiC layer of the semi-infinite PC. This is done at the free space wavelength where the $v_{e,int}$ and $v_{e,0}$ curves intersect. This is 12.20 μm for the PC with a=5 μm and 11.48 μm for the PC with a=10 μm. We show the results for both the cases of complete and terminated—missing 50% of the entry layer– structures, as thick and thin solid lines respectively. Fig. 5.3(a) features the PC case of 5 μm lattice constant. Conversely, Fig. 5.3(b) shows the corresponding result for the PC case of 10 μm lattice constant. The dotted lines represent dv_e/dx for the terminated PC cases, but plotted with a $x-$coordinate shift that places the terminated PC's front-layer in the center of the complete PCs front-layer. Notice the remarkable agreement between the complete PC result and the coordinate-shifted terminated-PC result. This makes it evident why one can essentially get the desired

[5]In Appendix H the band structure properties of the SiC-air PC versus the lattice constant are presented and discussed in more detail.

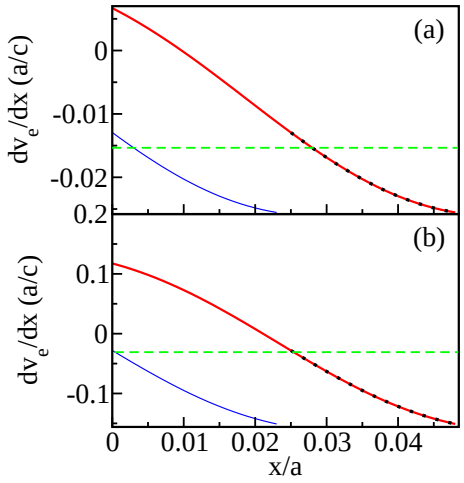

Figure 5.3: The energy-velocity gradient is shown for two PC systems with a lattice constant equal to 5 μm and 10 μm in panels (a) and (b) respectively.[6]The horizontal dashed line represents the reflectionless condition value dictated by Eq. 5.2. Note the coordinate within the PC entry layer, $x-$ is expressed in terms of the lattice constant a, while the energy velocity gradient is expressed in terms of c/a, with c being the speed of light.

dv_e/dx value (seen as horizontal dashed lines), that is dictated by the reflectionless condition of Eq. 5.2, just by "cutting-off" sufficient material from the front SiC layer.

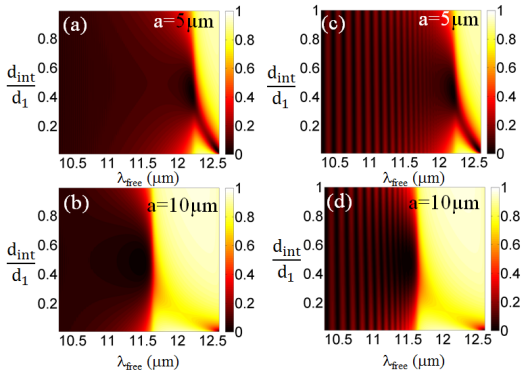

Figure 5.4: Reflection (in color-map) versus termination ratio, d_{int}/d_1 and free space wavelength, λ_{free} calculated from TMM. Panels (a) and (b) represent the result corresponding to the semi-infinite PCs with lattice constant a, of 5 μm, and 10 μm respectively. Same is shown in (c) and (d) but for 200 μm-thick PCs.

The above theoretical analysis suggests that both PCs with lattice constants of 5 and 10 μm will be reflectionless for an impinging wave with a wavelength

[6]Note that the red and blue solid-lines represent the respective energy-velocity gradient values inside the first SiC layer of a full periodic and a terminated PC. To aid the comparison, the black dotted line is drawn to represent the blue line result, but plotted with an $x-$coordinate shift that places the terminated PC's front-layer in the center of the complete PC's front-layer.

of 12.20 μm and 11.48 μm respectively, when their front-face is terminated at 44% and 50% of its complete size, respectively. To verify the predictions of our energy-velocity-based design principle we calculate with the TMM [1–3] the reflection for these semi-infinite PC cases within the entire Reststrahlen band and for different front-layer terminations, given by the thickness ratio of the truncated versus complete PC entry layer, d_{int}/d_1. We show the results in Figs. 5.4(a) and 5.4(b) for the respective PCs of lattice constants 5 and 10 μm. Notice, the complete agreement for near-zero reflectivity between the predictions deduced from the principles represented by Eqs. 5.1 and 5.2 and the actual TMM results. It should be noted the reflectionless PC parameters (free space wavelength and termination) are relatively robust and do not change while transitioning to a finite 200 μm-thick PC structure. For comparison, we also show the corresponding TMM results for the 200 μm-thick structures in Figs. 5.4(c) and 5.4(d).

To recap, the main "tuning-knob" to obtain a potential near-band-edge reflectionless semi-infinite PC is the lattice constant, a. The lattice constant should be tuned, while maintaining a low PC filling ratio, so that the energy velocity at the interface equals the optimum value given by Eq. 5.1 at a frequency that is very close to the band-edge. Near-band-edge near-zero reflection can then be achieved, by fine-tuning the size of the entry PC layer, so that the energy velocity gradient at the interface becomes equal to the optimum value determined by Eq. 5.2. We will explore in the following how the aforementioned design recipe can enable extreme absorption control towards our target of compact realizable PC absorbing structures.

5.4 Near-band edge near-zero reflection and absorption harnessing

Naturally, one would expect near-perfect absorption for the thick 200μm-PCs of Fig. 5.4 at free space wavelength and termination where reflection is near-zero. To compare the two designs of 5 and 10 μm lattice constant respectively we adopt from here-on a common 50% termination, which is near-optimum for both the cases. We calculate with TMM the absorptance, A=1-T-R, with T and R being transmission and reflection respectively and show the results in Fig. 5.5 as dot-dashed line for the case of a=5 μm and solid line for the case of a=10 μm.

Indeed, we observe a near-perfect absorption for both these PC designs with spectral occurrence in excellent agreement with the intersection-wavelength prediction of Fig. 5.2. This excellent agreement can be easily seen by noticing the

vertical solid lines in Fig. 5.2 designating the spectral positions of the absorption peaks observed in Fig. 5.5. For comparison, we also show the PC case with a=8 μm, which did not achieve a near-perfect absorption. For the latter case, absorption peaks away from the spectral region where the $v_{e,int}$ and the $v_{e,0}$ curves of Fig. 5.2(b) are close to each other. This is because the aforementioned spectral regime, is too far from the band-edge. We checked that this remains true for any termination, and is consistent with our predictions in the previous section that this design would not be appropriate for dramatic absorption control. We therefore focus only on the 5 and 10 μm lattice constant PC designs from here on.

We discussed in Section 5.3, that although the above mentioned PC designs show quite a similar behavior, in the sense that the $v_{e,int}$ and the $v_{e,0}$ curves intersect spectrally in the neighborhood of the band-edge, there is still a difference. That is such intersection being in one case much closer spectrally to the band-edge than in the other – roughly 0.4% and 1.4% for the respective cases of 5 and 10 μm lattice constant. Although, on a superficial look this difference may not seem so large we will find out that it does make an enormous difference towards our goal for compact absorbing structures.

We can understand why by looking at the complex photonic band structures for the two PC cases in Fig. 5.6. These bandstructure calculations are performed by using the TMM and applying the Bloch boundary conditions, with a complex Bloch wavevector q, [1–3]. The free space wavelength versus the real and imaginary parts of q are shown respectively in sub-figures (a) and (b) for the PC with a=5 μm and

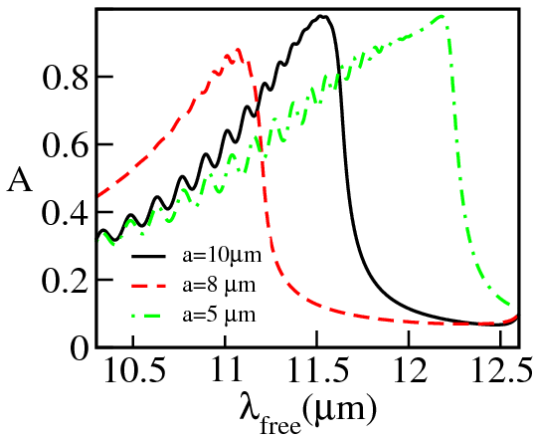

Figure 5.5: Absorptance versus free space wavelength, λ_{free}, for three 200 μm thick SiC-air PCs of 0.05 filling ratio and 50% front layer truncation. The solid, dashed and dot-dashed curves correspond to PCs with a lattice constant a equal to 10 μm, 8 μm, and 5 μm respectively. The front SiC layer is terminated to half its original size.

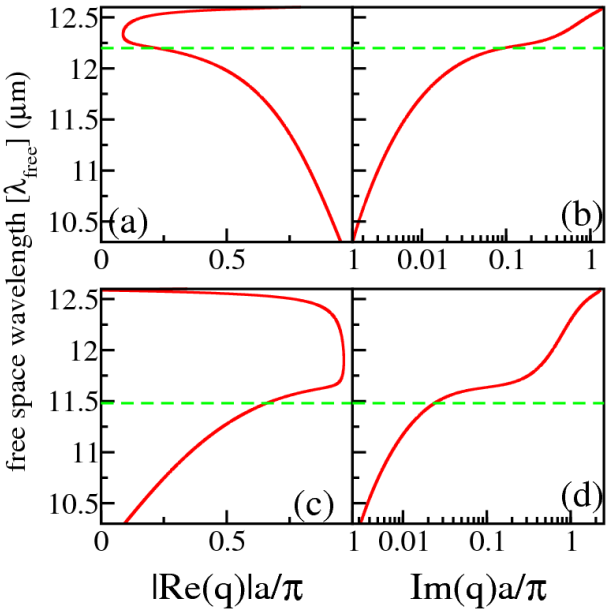

Figure 5.6: Complex band structure (free space wavelength versus Bloch wavevector q) for the PC cases of lattice constant a, 5 μm [in (a) and (b)] and 10 μm [in (c) and (d)] . The respective reflectionless-condition wavelengths are indicated with horizontal dashed lines. Note, both the real and imaginary parts of the Bloch wave vector q is expressed in terms of π/a.

in sub-figures (c) and (c) for the PC with a=10 μm. We also indicate the $v_{e,int}$-$v_{e,0}$ intersection wavelength of Fig. 5.2, representing the reflectionless condition, with horizontal dashed lines. Notice, that indeed as we mentioned before the bandedges are not as sharply defined as in lossless dielectric PCs.

Fig. 5.6 clearly demonstrates the implications of having the reflectionless condition in the close vicinity of the band-edge. At the reflectioness condition wavelength (dashed lines) we find an Im(q) = 0.094π/a for the PC with lattice constant a= 5 μm. Conversely, for the PC with lattice constant a= 10 μm we have Im(q) = 0.024π/a. The complex Bloch wave vector q, implies an e^{iqx} envelope for the electric fields spatial maps across the PC, determining a relative amplitude and phase between points with a separation that is an integer multiple of the lattice constant a[38, 39]. Thus we anticipate, that the larger Im(q) is, the quicker the electric-field amplitude decay within the PC; hence the merit of having the reflectionless condition as close to the band-edge as possible.

In the following, we evaluate the above two PC candidates potential as compact absorbers. We further investigate where is the light getting absorbed while crossing the PC structure. For this purpose, we calculate the ratio of dissipated to incident

power within the jth SiC layer, P(j), by applying Poynting's theorem [21, 40]:

$$\mathrm{P(j)} = \frac{\omega \varepsilon^{''}}{\mathrm{c}|E_0|^2} \int_{x_1}^{x_2} |E_y(x)|^2 dx, \tag{5.5}$$

where x_1, x_2 represent the coordinate limits of the j^{th} SiC layer, given by:

$$[x_1, x_2] = \begin{cases} [0, \frac{\mathrm{d}_1}{2}] & \mathrm{j} = 1 \\ [(\mathrm{j\text{-}1})\ \mathrm{a} - \frac{\mathrm{d}_1}{2}, (\mathrm{j\text{-}1})\ \mathrm{a} + \frac{\mathrm{d}_1}{2}] & \mathrm{j} \neq 1\ . \end{cases}$$

$E_y(x)$ represents the electric field distributions in the PC that are calculated using TMM [1–3] with $|E_0|$ being the incident electric field amplitude.

We briefly digress here to note that a thicker slab does not necessarily imply a higher power loss. By making the crude – yet reasonable for subwavelength blocks– assumption that the electric field does not vary too much within a certain slab, and noting that $\mathrm{P}_{\max} = 1$ we can obtain from Eq. 5.5 an upper bound for the field enhancement $|\mathrm{E}_{\mathrm{enha}}|$. This is given by:

$$|\mathrm{E}_{\mathrm{enha,\ max}}|^2 \approx \frac{\lambda_{\mathrm{free}}}{2\pi\varepsilon^{''}\mathrm{d}_1}. \tag{5.6}$$

Basically the above equation implies that thinner slabs may be capable of a higher field enhancement. Thus, there is no physical limitation in them yielding a higher power loss. In fact, we will find out exactly that in the following, namely a higher power loss in the thinner-slab five-micron PC.

We proceed in calculating what fraction of the incident power was dissipated while the EM wave has crossed through the first $\mathrm{N_c}$ SiC layers of the PC, that we represent in the following as $\mathrm{P}^c(\mathrm{N}_c)$. Thus:

$$\mathrm{P}^c(\mathrm{N}_c) = \sum_{\mathrm{j=1}}^{\mathrm{N_c}} \mathrm{P(j)}. \tag{5.7}$$

We plot the results for $\mathrm{P}^c(\mathrm{N}_c)$ for the two candidate PCs; the 5 μm lattice constant case in Fig. 5.7(a) and the 10 μm lattice constant case in Fig. 5.7(b). For reference we plot also the absorptance A (dark solid line). The figure verifies, that absorptance is equal to the dissipated power through the entire PC (dotted line). Notice, how quicker is power getting absorbed within the five-micron PC design. It is actually very impressive to observe that 60% of the impinging light at the peak wavelength is dissipated within first two SiC layers.

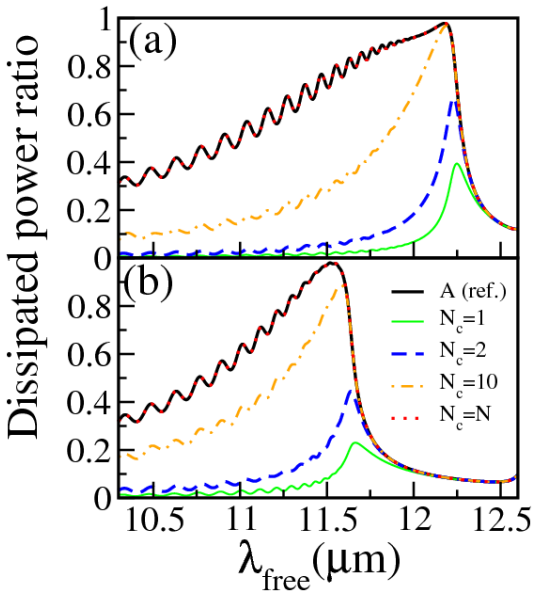

Figure 5.7: Dissipated to incident power ratio versus free space wavelength, λ_{free}, for the 200μm thick SiC-air PCs with 50% truncated front layer, within the first N_c PC unit cells. The result in (a) [(b)] corresponds to the PC case with 5 μm [10 μm] lattice constant. The respective absorptance is shown for reference with the dark solid line. Note, the total number of PC unit cells, N, is 40 for the case in (a) and 20 for the case in (b).

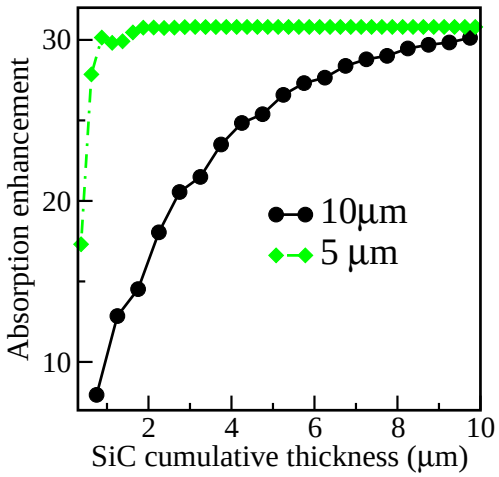

Figure 5.8: Absorptance enhancement of the two terminated SiC-air PCs with lattice constant a, 5 μm (dot-dashed line with diamonds), and 10 μm (solid line with filled circles) with respect to the absorption of a SiC block about a wavelength-thick is plotted against the total thickness of SiC encountered by the EM wave as it travels through the PC.

So, the power loss in the 5 μm-lattice-constant PC of 200 μm thickness is much higher than in the 10 μm-lattice-constant one. This may imply a stronger potential of the former PC structure as a compact absorber. In order to verify this, we test the PC's absorbing performance as it shrinks in thickness, comprising from a smaller number of unit cells. We take the absorption given by a thick bulk slab of SiC as a measure of comparison and evaluate the absorption enhancement with respect to that given by the two PC systems under investigation. We let their respective thicknesses vary, while maintaining the same 50% front-layer termination, and consider from compact two-unit-cell structures, to multiple-wavelength thick PCs. We plot our results in Fig. 5.8, versus the cumulative SiC thickness the EM wave crosses in each case. The dot-dashed line with diamonds designates the PC case of 5 μm lattice constant, while the solid line with filled circles designates the PC case of 10 μm lattice constant. Indeed, the 5 μm-lattice constant PC yields a remarkable absorption enhancement factor over 15 even with just two unit cells, that quickly reaches saturation at a value of $\sim$ 30. We will further look then into the properties of such a compact absorbing PC structure in the following section.

5.5 Compact sub-λ PC-based absorber

Given the favourable results in Fig. 5.8, we take the extreme case of truncating the 5 μm-lattice-constant PC down to only two unit cells and analyze it further. This compact design, depicted in Fig. 5.9(a), is essentially made of just two SiC layers that are d_{sp} apart, with d_{sp} being equal to d_2 – the air-layer thickness of the full periodic structure depicted in Fig. 5.1(a). The back layer has thickness equal to d_1, the SiC- layer thickness of the full periodic PC, while the front layer is truncated to thickness d_{int}, that is a percentage of the back-layer thickness.

It is quite remarkable, how thickness-robust the PC system is. We observe in Fig. 5.9(b) that it retains a low reflectivity close to the original reflectionless condition of the semi-infinite system, i.e at close to 50% termination at about 12.2 μm free space wavelength. In addition, we also observe a near-zero reflection at much smaller termination ratio ($\sim$ 0.05) at about 12.50 μm free space wavelength. If we look back at Fig. 5.2(a), we identify a second regime where the reflectionless condition applies. The existence of such second regime is unique to the five-micron PC design only and we did not observe it for the ten-micron PC case of Fig. 5.4(b). It emanates from a second intersection between the $v_{e,int}$ and $v_{e,0}$ curves that occurs closer to the adjacent band where Im(q) is much larger. This second reflectionless PC regime requires much more SiC material to be "shaved-off" from the front layer

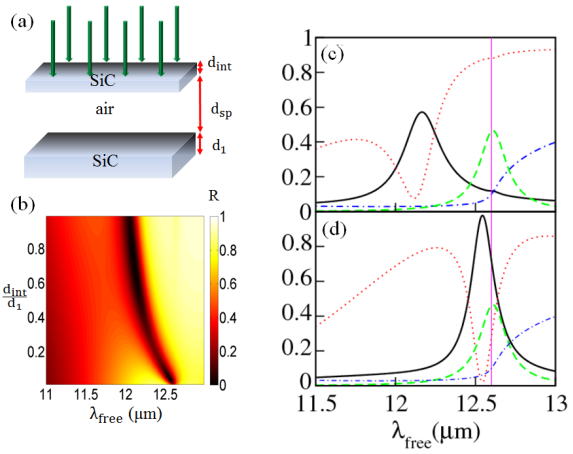

Figure 5.9: (a) Schematics of the compact PC-based design with all structural information indicated. (b) Reflectance (color-map) versus free space wavelength λ_{free} and front-layer truncation ratio d_{int}/d_1. (c) Absorptance (solid lines) and reflectance (dotted lines), for the design in (a) with (c) [(d)] showing the case of $d_{int}/d_1 = 0.5$ [$d_{int}/d_1 = 0.05$]. For comparison absorptance through a single layer is also shown for bulk SiC (dot-dashed) and an ultra-thin SiC film as thick as the front layer of the structure of Fig. 5.9(d). The vertical line designates the SiC Reststrahlen band-edge.

in order to obtain the optimum energy velocity gradient of Eq. 5.2.

Indeed, we can observe clearly a small reflection at about 12.2 μm free space wavelength for the compact design of Fig. 5.9(a), with $d_{int} = 0.5d_1$ seen as dotted line in Fig. 5.9(c). Conversely, we observe a near-zero reflection at about 12.5 μm free space wavelength for the compact design of Fig. 5.9(a), with $d_{int} = 0.05d_1$, that we show with a dotted line in Fig. 5.9(d). The corresponding absorptances are shown as solid lines in the same sub-figures. The absorptance peak-reflection dip offset observed in Fig. 5.9(c) comes from the fact that reflection is small yet non-near-zero at minimum. The peak-absorptance for the case of Fig. 5.9(d) correlated with the second reflectionless-PC regime is near-perfect, and much stronger in comparison to the case of Fig. 5.9(c). This is because the second reflectionless regime is associated with a larger imaginary part of the Floquet-Bloch wave vector, q.

We show in Fig. 5.10 the electric field profiles in the compact PC for the two aforementioned cases, versus the coordinate x, along the propagation direction; in (a) the case with $d_{int} = 0.05d_1$ and in (b) the case with $d_{int} = 0.5d_1$. We compare this profile with the Bloch-phase envelope for the electric amplitude |E|, $e^{-\mathrm{Im(q)}x}$, shown as dotted lines in both sub-figures. The Bloch-envelope captures the relative phase for PC points that are spaced by integer multiples of the lattice constant, a [38, 39]. In other words, it provides a prediction for the electric field amplitude

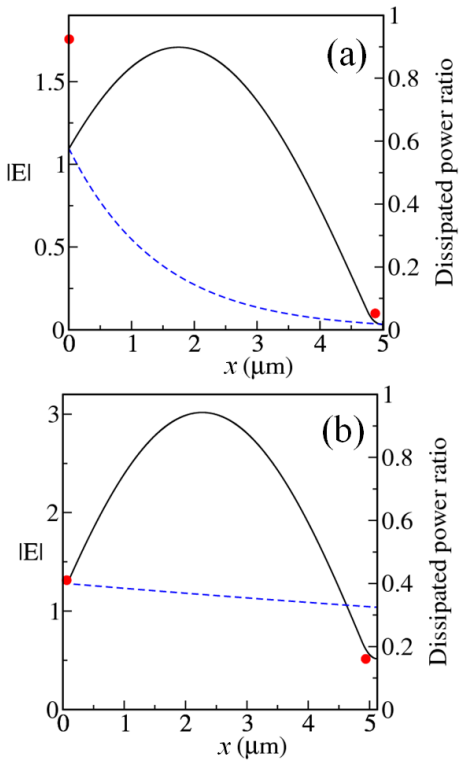

Figure 5.10: Electric field amplitude, |E|, profiles (left vertical axis) versus the coordinate x within the compact superabsorber design. The depicted profiles are normalized with the incident electric field amplitude $|E_0|$. The dotted lines represent the |E|-decay, from the front to the back layer, as predicted by the complex band structure of Fig. 5.6. The solid circles represent the ratio of incident power that is absorbed in each layer (see right vertical axis for values). Panel (a) and (b) represent the respective cases with front-to-back-layer truncation ratio of 0.05 and 0.5.

decay as the EM wave propagates from unit cell to unit cell of a semi-infinite PC. It is impressive to observe, how well this prediction captures the electric field decay from the front to the back layer for the case of Fig. 5.10(a). This is because the PC although compact, is reflectionless, so it emulates the propagation characteristics of its semi-infinite counterpart. This is not true however for the case of Fig. 5.10(b), hence the disagreement between Bloch-phase prediction and observed electric field amplitude decay.

In order to evaluate the performance of the proposed compact SiC PC-based absorber we compare it with that of a single SiC block in the same frequency regime. We show with dot-dashed line in Fig. 5.9 the absorption from bulk SiC, being more than a wavelength thick . Conversely, we show with dashed lines the absorption from an ultra-thin 12.5 nm-thick SiC film, which is as thick as the top layer of the structure of Fig. 5.9(d). The two extremes capture the bounds for the absorptance behavior of a SiC slab of intermediate thicknesses. For the

ultra-thin slab, we do observe a peak of $\sim 40\%$ at 12.6 μm free space wavelength, at the edge of the SiC Reststrahlen band. We emphasize that the physics of such an absorption peak for the single thin film slab is entirely different from the ones observed in the design of Fig. 5.9(a). In the latter cases the peaks are a photonic crystal effect while in the former it is a combination of thin-film behavior and the extreme SiC optical parameters at the Reststrahlen band-edge. This can in fact be easily checked by applying the thin-film approximation into the expressions [35] for transmission, T, and reflection, R of an absorbing block of thickness L, and complex refractive index $\mathrm{n} + \mathrm{i}\kappa$, where n and κ are much larger than 1.

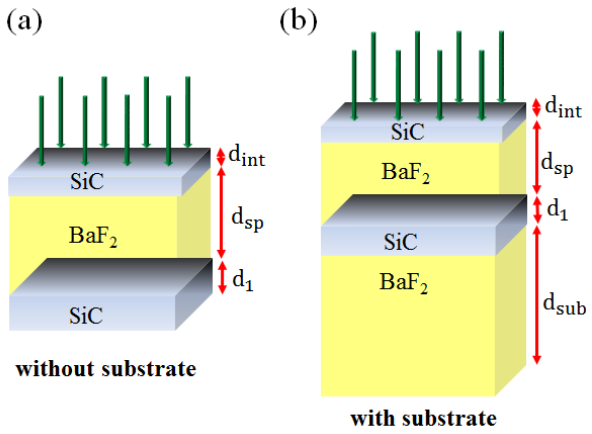

Figure 5.11: (a) Schematics of the realizable compact PC with all structural information indicated. (b) Same as the design in (a) but resting on a substrate made from the spacer material.

We observe a very large absorption enhancement when compared to the capabilities of a single SiC slab, in both cases. It is interesting to check where is the power getting absorbed in our compact system. The filled circles in Fig. 5.10 depict the ratio of incident power that is absorbed in in each SiC layer of our proposed compact design. In both the cases of Fig. 5.10(a) and (b) we find that the thinner front slab absorbs more light. However, the case of Fig. 5.10(a) attest a truly astonishing absorbing phenomenon, where more than 90% of the incident light gets absorbed by the front 12.5 nm-thick layer. This most extraordinary absorbing behavior would be highly attractive for applications. Thus we explore, in Section 5.6, practically realizable designs.

5.6 Practically realizable superabsorber designs

Here we investigate some variations of the compact superabsorber of Section 5.5, that would suggest potential for practical realization. We introduce a transparent material spacer instead of air, as can be seen in the schematics of Fig. 5.11(a). As an example for the transparent material spacer we consider BaF_2, which has a refractive index of ~ 1.36 in the frequency regime of interest [41]. In addition, we will investigate the influence of a substrate that is made from the same transparent material as the dielectric spacer [schematics of Fig. 5.11(b)]. In Figs. 5.11(a) and 5.11(b) we have identified symbolically all the pertinent geometric features, that we intend to "tweak" in the following with the aim towards superabsorbing behavior.

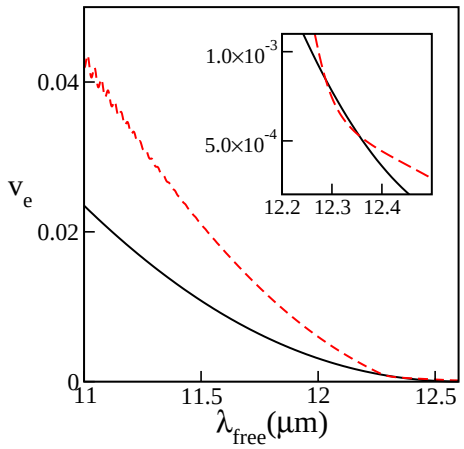

Figure 5.12: Energy velocity versus free space wavelength at the interface of a semi-infinite SiC-BaF_2 PC of lattice constant a=3.5 μm and SiC filling ratio equal to 0.065 (dashed lines). The required optimum of Eq. 5.1 is shown with a solid line. The inset highlights the wavelength region where the interface energy velocity intersects with the required optimum value.

In order to determine the parameters for which the designs of Fig. 5.11 can act as a superabsorber we go back again to the corresponding semi-infinite PC. i.e. we consider a SiC-BaF_2 photonic crystal and look into the spectral behavior of energy velocity at the interface, $v_{e,int}$. We search for parameters that yield an intersection between $v_{e,int}$ at the theoretically mandated optimum $v_{e,0}$. Again, this intersection wavelength should be in the proximity of the PC band-edge, when targeting absorptance performance with the compact structure.

As a paradigm we present the case of filling ratio f=0.065 and lattice constant a=3.5 μm, for which we plot the interface energy-velocity versus free space wavelength with dashed lines in Fig. 5.12. The required optimum of Eq. 5.1, $v_{e,0}$, is also indicated with a solid line. We can clearly identify two intersections between the

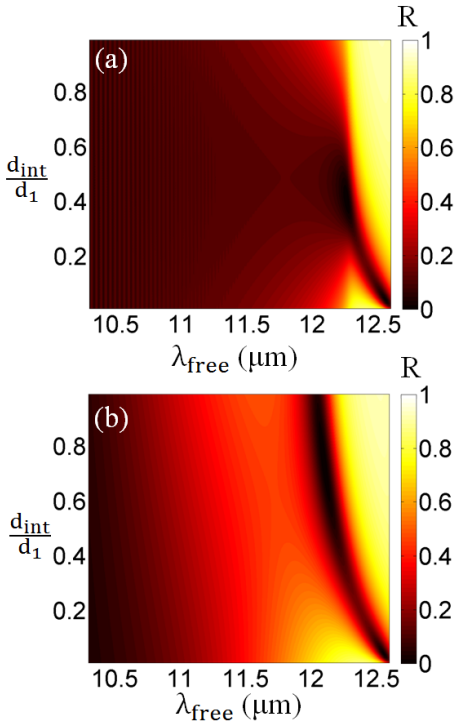

Figure 5.13: Reflectance (color-map), versus free space wavelength λ_{free}, and front-layer truncation ratio, d_{int}/d_1 for the SiC-BaF_2 system. In (a) the result of the semi-infinite PC is shown. In (b) the corresponding compact system of Fig. 5.11(a) is shown.

$v_{e,int}$-v_0 curves that are close to each other spectrally, (see blow-up of this frequency region in the inset), and in the proximity of the PC band-edge. This means that there are potentially two near-band-edge reflectionless frequencies. We note, that usually one can find a termination for which both the energy velocity and the spatial gradient of energy velocity at the interface meet the mandated optimum values of Eqs. 5.1 and 5.2 at frequencies that nearly coincide, but this may not always happen. One should also keep in mind that the $v_{e,int}$ values may shift somewhat with termination as well. This effect is ofcourse stronger for the smaller termination ratios.

In this SiC-BaF_2 PC we find two regimes of near-reflectionless behavior; one near a half-terminated front-layer and another for a very large front-layer truncation. These can be seen as the very dark regions in the reflectance map of Fig. 5.13(a), where reflectance, R, is plotted versus free space wavelength, λ_{free}, and front-layer termination ratio d_{int}/d_1. For comparison, the reflectance for the compact structure of Fig. 5.11 is also shown in Fig. 5.13(b). Indeed, these near-reflectionless λ_{free}-d_{int}/d_1regimes are quite robust with shrinking PC size. In particular, we observe that both near-reflectionless regimes survive until the extreme case of the compact three-layer structure, where the near-zero-reflection property emerges at

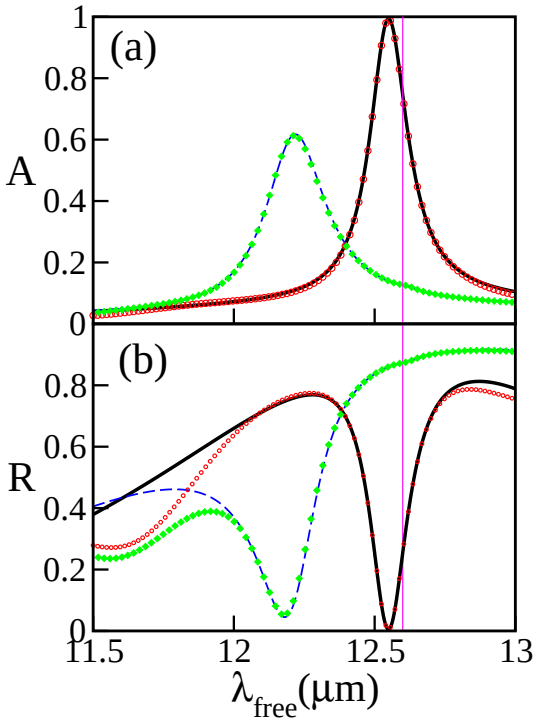

Figure 5.14: Absorptance [(a)] and Reflectance [(b)] versus free space wavelength λ_{free} for the compact SiC-BaF_2-SiC system corresponding to a PC with a lattice constant a=3.5 μm and a SiC filling ratio of f=0.065. Two cases of front-layer truncation are shown: the case of 0.05 truncation ratio with solid lines and the case of 0.5 truncation ratio with dashed lines. The corresponding circles and diamonds represent the respective result when the compact three-layer system rests on a 40μm thick substrate made of BaF_2.

front-layer truncation ratios of 0.05 and 0.50.

We show for these above mentioned cases the absorptance, A and reflectance, R in Figs. 5.14(a) and 5.14(b) respectively. The solid lines represent the case of a 0.05 truncation ratio, while the dashed lines represent the case of a 0.50 truncation ratio. The corresponding symbols –circles and diamonds– represent the respective result when the compact three-layer structure is placed on a forty-micron-thick substrate. We observe that the substrate has almost no influence at all to the absorptance. This is a promising result towards the realization of the compact absorber system depicted in Fig. 5.11.

We find a remarkable absorption performance for the compact design for both truncation ratios, which we describe in more detail in Table 5.1. We were able

[7]The optimal termination value for achieving the reflectionless condition is influenced by the number of SiC layers in the PC and the wavelength of operation. There is no rule of thumb regarding a particular value of the front-layer truncation ratio. However, changing the front-layer truncation ratio allows us to control the Fabry-Perot interference between the PC layers, so that the reflectance at the interface is suppressed at a particular frequency.

Table 5.1: Outline of performance of the compact superabsorber of Fig. 5.11(a) for two front-layer truncation ratios [A stands for absorptance, and DPR stands for dissipated power ratio]

Truncation Ratio	*Total A at peak wavelength*	*DPR in front layer*	*DPR in back layer*	*% of total A in front layer*	*% of total A in back layer*
$d_{int}/d_1 = 0.05$ [7]	0.993	0.925	0.0680	0.93	0.068
$d_{int}/d_1 = 0.5$	0.617	0.428	0.19	0.69	0.30

to observe also with the realizable SiC-BaF_2 the extra-ordinary near-perfect absorption, that we saw in previous section in the SiC-air system. Our proposed compact SiC-BaF_2 system has a total thickness of about $\sim \lambda_{free}/3$. At the wavelength of near-perfect absorption, more than 92% of the incoming light is getting absorbed by the top layer, which is less than $\sim \lambda_{free}/1000$ thick. This is a truly astonishing performance for this simple three-layer paradigm. It should be noted, that we found that by tweaking the geometric parameters of our proposed compact design for a reflectionless condition slightly away from the band-edge, it is possible to obtain an extra-ordinary absorption enhancement that depending on front-layer truncation can swap all the phonon-polariton band-gap region[8]; however near-perfect absorption was not reached in such a case for any front-layer truncation.

To recap, we demonstrated here a realizable compact superabsorber where almost all the incoming light is absorbed by the top layer which is less than a thousandth of the wavelength in thickness. The superabsorber comprises a highly absorbing (large κ) material and a transparent medium. We note, in passing that very recently compact absorbers in a planar geometry have been also reported by M. A. Kats et al. [42] and W. Streyer et al. [43], with designs that rely on the mutual optical properties of two lossy materials in the former work or a high index dielectric and an engineered metal of $\varepsilon \sim -1$ in the latter work. In our proposed compact design the underlying mechanism is a PC effect, where absorption is facilitated by a reflectionless funneling to a photonic-crystal mode, with a highly lossy Floquet-Bloch phase. This mechanism leads to compact structures made of a single-type of highly lossy medium in a planar geometry, and any transparent

[8] Although reflection can be suppressed for a particular termination, this optimal termination works only for one frequency. Slightly changing the termination will yield a suppressed or near-suppressed reflection at a different spectral position. This different spectral position of the suppressed reflection would be in a different position with respect to the PC band-edge, and thus correspond to a different die-off length of the wave within the PC so it may not get fully absorbed in the compact structure, i.e. absorption would not be near-perfect for all truncation ratios. Therefore, with the same compact layer structure, by changing the termination value of the front layer, we can achieve absorption enhancement of different values at different spectral positions throughout the phonon-polariton gap of SiC.

medium, that can function as highly efficient absorbers by suitable adjustment of the out-of-plane constituent slab thicknesses.

5.7 Conclusion

We have presented here a new paradigm of a practically realizable SiC-BaF_2 layered system. We demonstrated with a compact design, which is a third-of-the wavelength thick, a near-perfect absorption, where more than 92% of the incoming light is absorbed in the top SiC ultra-thin layer, having a thickness a thousand times less than the impinging wavelength. The reported super-absorber effect emanates from a special photonic-crystal behavior of the corresponding photonic lattice. In particular, the underpinning mechanism is the achievement of near-zero reflection in the proximity of the photonic 1D lattice band-edge, by a special truncation of the front layer. This enables funneling all incoming light into an ultra-slow mode, that allows the rapid decay of the EM fields within the PC, manifested by the large imaginary part of the complex Floquet-Bloch phase. We believe, our proposed platform offers new avenues for absorption harnessing across the EM spectrum and will inspire new designs where absorption occurs in a one-step process without anti-reflection coating and/or back-reflector [18] and within a single kind of highly absorbing material.

5.8 Acknowledgments

Financial support for the Ph.D. studentship of G. C. R. Devarapu by the College of Engineering, Mathematics and Physical Sciences (CEMPS) University of Exeter is acknowledged.

Bibliography

[1] P. Yeh, *Optical waves in layered media* (Wiley-Interscience, 2005).

[2] P. Yeh, A. Yariv, and C. S. Hong, "Electromagnetic propagation in periodic stratified media. I. General theory," J. Opt. Soc. Am. **67**, 423-438 (1977).

[3] A. Yariv and P. Yeh, "Electromagnetic propagation in periodic stratified media. II. Birefringence, phase matching, and x-ray lasers," J. Opt. Soc. Am. **67**, 438-447 (1977).

[4] E. L. Dereniak and D. G. Crowe, *Optical radiation detectors*, (John Wiley and Sons, Inc., New York, 2008).

[5] *Handbook of Optics Volume I: Fundamentals, Techniques, and Design*, ed. by M. Bass, E. W. Van Stryland, D. R. Williams, W. L. Wolfe (McGraw-Hill, New York, 1995).

[6] A. Nedelcu, V. Guériaux, L. Dua and X. Marcadet, "A high performance quantum-well infrared photodetector detecting below 4.1 m," Semicond. Sci. Technol. **24** 045006, (2009).

[7] H. A. Atwater and A. Polman, "Plasmonics for improved photovoltaic devices," Nat. Mat. **9**, 205 (2010).

[8] R. A Pala, J. White, E. Barnard, J. Liu, and M. L. Brongersma, "Design of Plasmonic Thin-Film Solar Cells with Broadband Absorption Enhancements," Adv. Mat. **21**, 3504 (2009).

[9] C. J. Hill, A. Soibel, S. A. Keo, J. M. Mumolo, D. Z. Ting, and S. D. Gunapala, "Demonstration of large format mid-wavelength infrared focal plane arrays based on superlattice and BIRD detector structures," Infrared. Phys. Tech. **52**, 348-352 (2009).

[10] A. V Barve, S. J. Lee, S. K. Noh, and S. Krishna, "Review of current progress in quantum dot infrared photodetectors," Laser Photon. Rev.**4**, 738-750 (2010).

[11] J. A. Mason, S. Smith, and D. Wasserman, "Strong absorption and selective thermal emission from a midinfrared metamaterial," Appl. Phys. Lett. **98**, 241105-3 (2011).

[12] J. A. Mason, G. Allen, V. A. Podolskiy, and D. Wasserman, "Strong Coupling of Molecular and Mid-Infrared Perfect Absorber Resonances," IEEE Phot. Tech. Lett. **24**, 31-33 (2012).

[13] A. Ganjoo, H. Jain, C. Yu, J. Irudayaraj, and C. G. Pantano, "Detection and finger-printing of pathogens: Mid-IR biosensor using amorphous chalcogenide films," J. of Non-Crystalline Solids **354**, 2757-2762 (2008).

[14] S. J. Lee, Z. Ku, A. Barve, J. Montoya, W. Y. Jang, S. R. J. Brueck, M. Sundaram, A. Reisinger, S. Krishna, and S. K. Noh, "A monolithically integrated plasmonic infrared quantum dot camera," Nat. Commun.2, **286** (2011).

[15] J. F. Head, F. Wang, C. A. Lipari, and R. L. Elliot, "The important role of infrared imaging in breast cancer," IEEE Eng. Med. Biol. **19**, 52 (2000).

[16] L. Hutchinson, "Breast cancer: Challenges, controversies, breakthroughs," Nat. Rev. Clin. Onco.**7**, 669-670 (2010).

[17] W. Dai, D. Yap and G. Chen, "Wideband enhancement of infrared absorption in a direct band-gap semiconductor by using nonabsorptive pyramids," Opt. Express **20**, A519 (2012).

[18] D. Liang, Y. Huo, Y. Kang, K. X. Wang, A. Gu, M. Tan, Z. Yu, S. Li, J. Jia, X. Bao, S. Wang, Y. Yao, H. -S. P. Wong, S. Fan, Y. Cui, and J. S. Harris, "Optical absorption enhancement in freestanding GaAs thin film nanopyramid arrays," Advanced Energy Materials **2**, 1254 (2012).

[19] J. Zhu, Z. Yu, G. Burkhard, C. -M. Hsu, S. T. Connor, Y. Xu, Q. Wang, M. McGehee, S. Fan, and Y. Cui, "Optical Absorption Enhancement in Amorphous Silicon Nanowire and Nanocone Arrays," Nano Letters **9**, 279-282 (2009).

[20] J. Buencuerpo, L. E. Munioz-Camuniez, M. L. Dotor, and P. A. Postigo, "Optical absorption enhancement in a hybrid system photonic crystalthin substrate for photovoltaic applications," Opt. Express **20**, A452 (2012).

[21] K. Aydin, V. E. Ferry, R. M. Briggs, and H. A. Atwater, "Broadband polarization-independent resonant light absorption using ultrathin plasmonic super absorbers," Nat. Comm. **2**, 517 (2011).

[22] B. Curtin, R. Biswas and V. Dalal, "Photonic crystal based back reflectors for light management and enhanced absorption in amorphous silicon solar cells," Appl. Phys. Lett. **95**, 231102 (2009).

[23] P. Bermel, C. Luo, L. Zeng, L. C. Kimerling, and J. D. Joannopoulos, "Improving thin-film crystalline silicon solar cell efficiencies with photonic crystals," Opt. Express **15**, 16986 (2007).

[24] R. B. Wehrspohn and J. Ü̈pping, "3D photonic crystals for photon management in solar cells,," J. Opt. **14**, 024003 (2012).

[25] S. Y. Lin, J. G. Fleming, Z. Y. Li, I. El-Kady, R. Biswas, and K. M. Ho, "Origin of absorption enhancement in a tungsten, three-dimensional photonic crystal," J. Opt. Soc. Am. B **20**, 1538–1541 (2003).

[26] G. Veronis, R. W. Dutton, and S. Fan, "Metallic photonic crystals with strong broadband absorption at optical frequencies over wide angular range," J. of Appl. Phys. **97**, 093104 (2005).

[27] C. Lin and M. L. Povinelli, "Optical absorption enhancement in silicon nanowire arrays with a large lattice constant for photovoltaic applications," Opt. Express **17**, 19371 (2009).

[28] Y. Park, E. Drouard, O. El-Daif, X. Letartre, P. Viktorovitch, A. Fave, A. Kaminski, M. Lemiti, and. C. Seassal, "Absorption enhancement using photonic crystals for silicon thin film solar cells," Opt. Express **17**, 14312 (2009).

[29] G. C. R. Devarapu and S. Foteinopoulou, "Mid-IR near-perfect absorption with a SiC photonic crystal with angle-controlled polarization selectivity," Opt. Express. **20**, 13041-13054 (2012).

[30] R. Loudon, "The propagation of electromagnetic energy through an absorbing dielectric," J. Phys. A **3**, 233 (1970).

[31] R. Ruppin, "Electromagnetic energy density in a dispersive and absorptive material," Phys. Lett. A **299**, 309-312 (2002).

[32] P. B. Catrysse and S. Fan, "Near-complete transmission through subwavelength hole arrays in phonon-polaritonic thin films," Phys. Rev. B **75**, 075422-5 (2007).

[33] E. D. Palik, *Handbook of Optical Constants of Solids*(Academic Press, 1985)

[34] S. Foteinopoulou, J. P. Vigneron, and C. Vandenbem, "Optical near-field excitations on plasmonic nanoparticle-based structures," Opt. Express **15**, 4253 (2007).

[35] S. Foteinopoulou, M. Kafesaki, E. N. Economou, and C. M. Soukoulis, "Two-dimensional polaritonic photonic crystals as terahertz uniaxial metamaterials," Phys. Rev. B **84**, 035128 (2011).

[36] J. D. Joannopoulos, S. G. Johnson, J. N. Winn, and R. D. Meade, *Photonic Crystals: Molding the Flow of Light* (Princeton University Press, 2008).

[37] We emulate a semi-infinite PC behavior by considering a thick two-hundred-cell structure. In this way, essentially all light is absorbed when it meets the end-face, and backreflection, which is inevitable in finite systems, is eliminated. See also Ref. [38]

[38] S. Foteinopoulou and C. M. Soukoulis, "Electromagnetic wave propagation in two-dimensional photonic crystals: A study of anomalous refractive effects," Phys. Rev. B **72**, 165112 (2005).

[39] C. Engström, C. Hafner and K. Schmidt, "Computations of lossy bloch waves in two-dimensional photonic crystals," J. of Com. Theor. Nanoscience **6**, 1 (2009).

[40] J. D. Jackson, *Classial Electrodynamics*, Wiley, Third edition, (1999).

[41] W. Kaiser, W. G. Spitzer, R. H. Kaiser, L. E. Howarth, "Infrared Properties of CaF_2, SrF_2, and BaF_2," Phys. Rev. **127**, 1950-1954 (1962).

[42] M.A. Kats, R. Blanchard, P. Genevet and F. Capasso, "Nanometre optical coat-ings based on strong interference effects in highly absorbing media," Nature Materials **12**, 20-24 (2013).

[43] W. Streyer, S. Law, G. Rooney, T. Jacobs, and D. Wasserman, "Strong absorption and selective emission from engineered metals with dielectric coatings," Opt. Express **21**, 9113 (2013).

6

Broadband Mid-IR superabsorption with aperiodic polaritonic photonic crystals

6.1 Chapter Overview

In the previous chapter, we have demonstrated near-unity absorption in a sub-wavelength thick SiC microstructure. However, this structure has a narrow operational bandwidth. On the other hand, applications such as bolometers require absorption enhancement over a broadband range of wavelengths. Therefore, in this chapter[1], we propose an aperiodic PC approach to achieve broadband absorption enhancement, inspired by chirped gratings which are widely used in the optical fibre community to obtain broadband transmittance/reflectance. In particular, we investigate two types of SiC aperiodic 1D-PCs, and evaluate their relative merits in detail. In addition, we also study the importance of order of the building blocks in these aperiodic PCs. The insights gained in this chapter will be applied in the next chapter to design a compact broadband absorber with a total thickness of about one-third of the wavelength of operation. Moreover, the design insights obtained by this study are transferable for the construction of broadband absorbers with different materials throughout the EM spectrum.

[1]Per Section 2.2 of code of practice for presentation of Theses, this chapter is presented as published in the paper: Ganga Chinna Rao Devarapu and Stavroula Foteinopoulou, "Broadband Mid-IR superabsorption with aperiodic polaritonic photonic crystals," J. Euro. Opt. Soc. Rap. Pub. **9**, 14012 (2014) [© The Authors. See `10.2971/jeos.2014.14012`].

Before proceeding to our results and analysis we briefly recap the methods employed in this chapter. Bandstructure and transmission results have been calculated with computer programs that have been developed based on Yariv and Yeh's Transfer Matrix Method (TMM) [1–3] that we have presented in Chapter 2, adapted to the specific parameters of the structures studied here. Particular expressions for the transfer matrix of the aperiodic system as well as power loss expressions have been derived based on Yariv and Yeh's TMM method and presented in sections 6.4 and 6.5 of this chapter respectively.

Abstract

We propose an approach for broadband near-perfect absorption with aperiodic-polaritonic photonic crystals (PCs) operating in the phonon-polariton gap of the constituent material. In this frequency regime the bulk polaritonic materials are highly reflective due to the extreme permittivity values, and so their absorption capabilities are limited. However, we are able to achieve absorptance of more than 90% almost across the entire phonon-polariton gap of SiC with a SiC-air aperiodic one-dimensional(1D)-PC with angular bandwidth that covers the range of realistic diffraction-limited sources. We explore two types of aperiodic PC schemes, one in which the thickness of the SiC layer increases linearly[2], and one in which the filling ratio increases linearly[3] throughout the structure. We find that the former scheme performs better in terms of exhibiting smoother spectra and employing less SiC material. On the other hand, the second scheme performs better in terms of the required total structure size.We analyze the principles underpinning the broadband absorption merit[4] of our proposed designs, and determine that the key protagonists are the properties of the entry building block and the adiabaticity of the aperiodic sequencing scheme. Further investigation with derivative lamellar sequences–resulting by interchanging or random positioning of the original building blocks–underline the crucial importance of the building block arrangement in an increasing order of thickness. If we relax the requirement of near-perfect absorption, we show that an averaged absorption enhancement across the SiC phonon-polariton gap of ~ 10 can be achieved with much shorter designs of the order of two free-space wavelengths. Our findings suggest that our aperiodic polaritonic PC route can be promising to

[2]The structural specifics of the building blocks of this type of aperiodic structure can be seen in Fig. 6.2 (a) and (b).

[3]The structural specifics of the building blocks of this type of aperiodic structure can be seen in Fig. 6.2 (c) and (d).

[4]By "broadband absorption merit" here we mean the property of near-perfect absorption with a wide bandwidth that spans the entire Reststrahlen band of SiC.

design broadband electromagnetic absorbers across the spectrum.

6.2 Introduction

Absorbers are crucial components in electromagnetic (EM) wave detection and energy harvesting devices such as photovoltaics [4, 5], thermophotovoltaics [6–10], bolometers [11–13] and imaging devices [14–16]. Therefore, many current research efforts are focusing on optimizing EM absorption with different mechanisms such as near-field enhancement through plasmonic resonances [4, 5, 17, 18] or impedance-matching by metamaterial structures [19–22]. In all these schemes the absorptance enhancement in the absorbing material is facilitated by the metallic structures which are integrated with the absorbing material.

An alternative route has been explored with photonic crystals (PCs) relying solely on the excitation of lossy Floquet-Bloch modes in a structure with a single kind of absorbing material [23–28]. In the Mid-IR regime mostly PCs with metallic constituents have been explored [26]. However, metals have a small skin depth [29], thus thick PC structures would be required to get high absorption enhancement [26].

On the other hand, polaritonic materials have a larger skin depth in the Mid-IR region thus offering the possibility of a larger light-matter interaction path. Therefore polaritonic materials could be a promising constituent materials for engineering absorption. However, overcoming the ultrahigh reflection within the phonon-polariton gap, also known as the Reststrahlen band [29] is a major challenge.

However, the recent results of Devarapu and Foteinopoulou [27, 28][5] demonstrating near-perfect absorption with a SiC PC system seem promising in this direction. The underlying mechanism was a combination of a quickly vanishing lossy Floquet-Bloch mode [28, 30] and tailoring of the energy velocity at the interface [27, 28][6]. Careful engineering of such phenomena has led to a compact-superabsorber design where 90% of light gets absorbed within the top absorbing layer of thickness $\lambda/1000$ [28][7]. Nevertheless the operation bandwidth in the latter PC structure was narrow. An important aspect in many applications such as bolometers and thermophotovoltaics, is to have absorption enhancement over a broad range of wavelengths. Therefore, here we explore a possibility to obtain a broadband near-perfect absorption by utilizing polaritonic PCs. For this purpose we employ aperiodic-polaritonic 1D-PCs

[5]These results refer to the results of Chapters 3 and 5 in this thesis.
[6]These results refer to the results of Chapters 3 and 5 in this thesis.
[7]These results refer to the results of Chapter 5 in this thesis.

with varying building block sizes, inspired by the broadband reflection/antireflection property observed in chirped gratings [31–33].

In particular this paper is organized as follows. In Section 6.3, we describe the aperiodic polaritonic 1D-PCs under study. In Section 6.4, we present the methodology we adopted for evaluating the absorptance performance of the proposed aperiodic PCs. In Section 6.5, we discuss our results of near-perfect absorptance of the two aperiodic PCs under study and compare their performance. In Section 6.6, we investigate the robustness of the broadband absorption merit under angular illumination. In Section 6.7, we determine the key operation principles underpinning the broadband functionality of our proposed designs. In Section 6.8, we analyse the significance of the particular order of the building blocks in the aperiodic PC. Based on the determined principles, we present in Section 6.9, a shrinked aperiodic PC design which demonstrates an averaged–within the SiC Reststrahlen band–absorption enhancement with a value close to 10. Finally, we present our conclusions in Section 6.10.

6.3 System under study

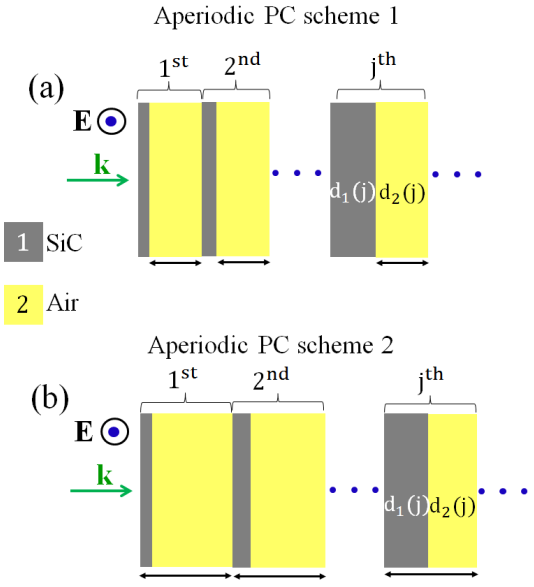

Figure 6.1: Schematic diagrams of the two types of aperiodic SiC-air 1D-PC structures. (a) The thickness of the SiC layer in each building block changes linearly while the thickness of the air layers remains the same. (b) The filling ratio in each building block changes linearly while the lattice constant remains the same.

We will consider two aperiodic 1D-PC structures comprising of alternating layers

of SiC and air as shown schematically in Figs. 6.1(a) and 6.1(b). The respective thicknesses of the SiC and air layers in the j^{th} building block of the aperiodic PC are $d_1(j)$ and $d_2(j)$. We denote the permittivity of air as ε_2, with its value being one. The permittivity of SiC is denoted as ε_1, and modelled with the Lorentzian function [29],

$$\varepsilon_1(\omega) = \varepsilon_\infty \left(1 + \frac{\omega_L^2 - \omega_T^2}{\omega_T^2 - \omega^2 - i\omega\Gamma}\right), \tag{6.1}$$

where ω is the angular frequency of the incident EM wave. The parameters in the Lorentzian function—taken from Ref. [34]—are ε_∞=6.7, ω_T =2$\pi\times$23.79 THz, ω_L =2$\pi\times$29.07 THz and Γ =2$\pi\times$0.1428 THz. We have particularly chosen SiC as the constituent of the aperiodic PCs, since the Reststrahlen band of the SiC spans from 10.3 μm to 12.6 μm, where many pathogens and bio-molecules have their fingerprints [35–37]. Moreover, this frequency regime is an important atmospheric N-band window that facilitates the study of astronomical objects that are colder than 500 K [38–40].

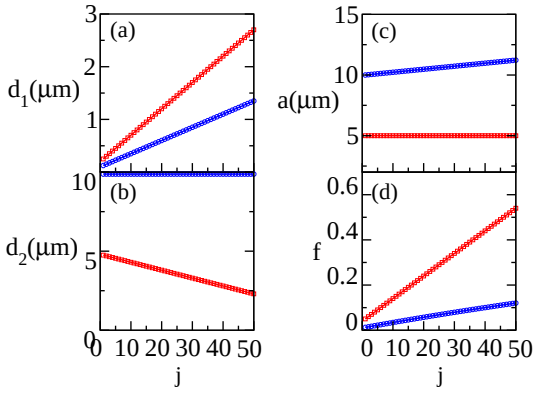

Figure 6.2: Structural parameters of the aperiodic PCs of Fig. 6.1(a) (blue circles) and Fig. 6.1(b) (red squares) in each building block j. (a) thickness of the SiC layers, (b) thickness of air layers, (c) lattice constant and (d) filling ratio.

In the first type of aperiodic PC shown in Fig. 6.1(a), the thickness of the SiC layer in each building block changes linearly as:

$$d_1(j) = d_1(1) + \frac{1}{5}(j-1)\cdot d_1(1), \tag{6.2}$$

where $d_1(1) = 0.125\mu$m is the thickness of the first SiC layer in the aperiodic PC. The thickness of the air layers d_2 is 9.875 μm and it remains constant throughout the aperiodic PC.

On the other hand, in the second type of aperiodic PC shown in Fig. 6.1(b), the filling ratio for each building block changes linearly. The filling ratio of the j^{th}

building block is given by:

$$\mathrm{f(j)} = \mathrm{f(1)} + \frac{1}{100}(\mathrm{j} - 1), \tag{6.3}$$

where f(1) = 0.05 is the filling ratio of the first building block. Note, the lattice constant a = 5 μm is constant throughout the aperiodic PC, implying that the thickness of SiC and air layer in the j^{th} building block of the PC would be $\mathrm{d_1(j)} = \mathrm{a} \cdot \mathrm{f(j)}$ and $\mathrm{d_2(j)} = \mathrm{a} - \mathrm{d_1(j)}$ respectively.

In Fig. 6.2, we show the variation of the structural parameters from one building block to the next one in the first and second type of the aperiodic PCs as blue circles and red squares respectively. In Figs. 6.2(a) and 6.2(b), we show the SiC and air thicknesses respectively in each building block j. In Figs. 6.2(c) and 6.2(d), we show the lattice constant and filling ratio in each building block j, respectively.

6.4 Methodology

In this section, we present the methodology we adopted to study the aperiodic SiC-air lamellae sequence. To evaluate the absorption performance of the two types of aperiodic PCs described above, we need spectral information on their absorptance A. For this reason we calculate with the Transfer Matrix Method (TMM) [1–3] the absorptance A as A=1-T-R. T and R represent respectively the transmittance and reflectance of the aperiodic lamellar structures, determined from the transmission and reflection amplitudes as T= $|t|^2$ and R = $|r|^2$ since our entire structure is embedded in air. In particular,

$$\begin{bmatrix} 1 \\ \\ r \end{bmatrix} = M^{total} \begin{bmatrix} t \\ \\ 0 \end{bmatrix}, \tag{6.4}$$

where M^{total} is the total transfer matrix through the aperiodic PC with N building blocks given by:

$$M^{total} = \left(\prod_{\mathrm{j=1}}^{\mathrm{N\text{-}1}} M^{21} P^{1}(\mathrm{j}) M^{12} P^{2}(\mathrm{j}) \right) M^{21} P^{1}(\mathrm{N}) M^{12}. \tag{6.5}$$

In the above equation, M^{12} and M^{21} are the transfer matrices that relate the amplitude of the EM waves going from medium 1 (SiC) to medium 2 (air) and vice versa

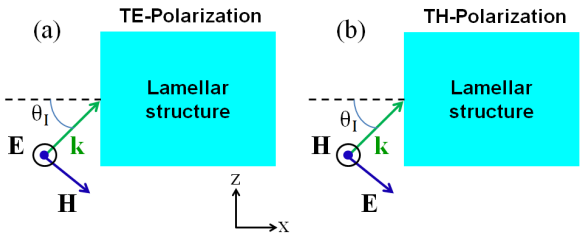

Figure 6.3: EM waves incident on a multilayer structure with lamellae along the yz-plane (a) TE-polarization case (b) TH-polarization case.

and are given by:

$$M^{12} = \frac{1}{2}\begin{bmatrix} 1+\chi^{12} & 1-\chi^{12} \\ 1-\chi^{12} & 1+\chi^{12} \end{bmatrix}, \tag{6.6}$$

and

$$M^{21} = \frac{1}{2}\begin{bmatrix} 1+\chi^{21} & 1-\chi^{21} \\ 1-\chi^{21} & 1+\chi^{21} \end{bmatrix}, \tag{6.7}$$

where the parameters χ^{12} and χ^{21} relate to the SiC permittivity ε_1 and angle of incidence θ_I as follows:

(i) For Normal incidence ($\theta_I = 0$) both polarizations are degenerate and we have,

$$\chi^{12} = \frac{1}{\sqrt{\varepsilon_1}} \quad \text{and} \quad \chi^{21} = \sqrt{\varepsilon_1}. \tag{6.8}$$

(ii) For incidence at an angle $\theta_I \neq 0$ and TE polarization [see schematics of Fig. 6.3 (a)] we have,

$$\chi^{12} = \sqrt{\frac{1-\sin^2\theta_I}{\varepsilon_1 - \sin^2\theta_I}} \quad \text{and} \quad \chi^{21} = \sqrt{\frac{\varepsilon_1 - \sin^2\theta_I}{1-\sin^2\theta_I}}. \tag{6.9}$$

(iii) For incidence at an angle $\theta_I \neq 0$ and TH polarization [see schematics of Fig. 6.3 (b)] we have,

$$\chi^{12} = \varepsilon_1\sqrt{\frac{1-\sin^2\theta_I}{\varepsilon_1 - \sin^2\theta_I}} \quad \text{and} \quad \chi^{21} = \frac{1}{\varepsilon_1}\sqrt{\frac{\varepsilon_1 - \sin^2\theta_I}{1-\sin^2\theta_I}}. \tag{6.10}$$

Then, $P^1(\mathrm{j})$ and $P^2(\mathrm{j})$ in Eq. (6.5), are the respective propagation matrices in the

SiC and air layers within the j$^{\text{th}}$ building block and are given by:

$$P^1(\mathrm{j}) = \begin{bmatrix} e^{-ik_{1x}\mathrm{d}_1(\mathrm{j})} & 0 \\ 0 & e^{ik_{1x}\mathrm{d}_1(\mathrm{j})} \end{bmatrix}, \tag{6.11}$$

and

$$P^2(\mathrm{j}) = \begin{bmatrix} e^{-ik_{2x}\mathrm{d}_2(\mathrm{j})} & 0 \\ 0 & e^{ik_{2x}\mathrm{d}_2(\mathrm{j})} \end{bmatrix}, \tag{6.12}$$

with k_{1x} and k_{2x} representing the x-component of the wavevectors inside the SiC and air layers respectively. Thus, for normal incidence,

$$k_{1x} = \sqrt{\varepsilon_1}\frac{\omega}{c} \quad \text{and} \quad k_{2x} = \frac{\omega}{c}, \tag{6.13}$$

and for off-normal incidence at an angle $\theta_I \neq 0$,

$$k_{1x} = \sqrt{\varepsilon_1 - \sin^2\theta_I}\,\frac{\omega}{c} \quad \text{and} \quad k_{2x} = \sqrt{1 - \sin^2\theta_I}\,\frac{\omega}{c}, \tag{6.14}$$

where ω represents the frequency of the impinging wave and c represents the vacuum speed of light.

Furthermore, in order to gain insight where the light gets absorbed within the aperiodic PC, we will also look into the electric-field distributions –for the case of normal incidence. These are given by:

$$\begin{aligned}
E(x) &= e^{ik_{2x}x} + re^{-ik_{2x}x}, \qquad \text{for} \qquad x \leq 0 \\
E(x) &= A(\mathrm{j})e^{ik_{1x}(x-S_{\mathrm{a}}(\mathrm{j}))} + B(\mathrm{j})e^{-ik_{1x}(x-S_{\mathrm{a}}(\mathrm{j}))}, \\
&\qquad\qquad \text{for } S_{\mathrm{a}}(\mathrm{j}) \leq x \leq S_{\mathrm{a}}(\mathrm{j}) + \mathrm{d}_1(\mathrm{j}) \\
E(x) &= C(\mathrm{j})e^{ik_{2x}(x-S_{\mathrm{a}}(\mathrm{j})-\mathrm{d}_1(\mathrm{j}))} + D(\mathrm{j})e^{-ik_{2x}(x-S_{\mathrm{a}}(\mathrm{j})-\mathrm{d}_1(\mathrm{j}))}, \\
&\qquad\qquad \text{for } S_{\mathrm{a}}(\mathrm{j}) + \mathrm{d}_1(\mathrm{j}) \leq x \leq S_{\mathrm{a}}(\mathrm{j}+1) \\
E(x) &= te^{ik_{2x}(x-S_{\mathrm{a}}(\mathrm{N}-1)-\mathrm{d}_1(\mathrm{N}))}, \text{ for } x \geq S_{\mathrm{a}}(\mathrm{N}-1) + \mathrm{d}_1(\mathrm{N}).
\end{aligned} \tag{6.15}$$

With $S_{\mathrm{a}}(\mathrm{j})$, we denote the location of the front SiC face at the j$^{\text{th}}$ building block. i.e $S_{\mathrm{a}}(\mathrm{j}) = \sum_{\mathrm{i}=1}^{\mathrm{j}-1} \mathrm{a}(\mathrm{i})$ for j $>$ 1 and $S_{\mathrm{a}}(\mathrm{j})$=0 for j=1, where a(i) is the size of the i$^{\text{th}}$ building block in the aperiodic PC. Moreover, as indicated in Fig. 6.4, $A(\mathrm{j})$ and $B(\mathrm{j})$ are the electric-field amplitudes of the forward and backward going waves within the SiC layer of the j$^{\text{th}}$ building block in the aperiodic PC. Similarly $C(\mathrm{j})$ and $D(\mathrm{j})$ are the electric-field amplitudes of the forward and backward going waves within the air layer of the j$^{\text{th}}$ building block. These are determined by the following recursive

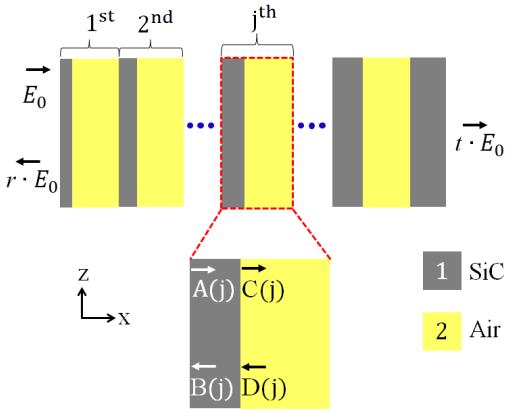

Figure 6.4: Schematic of an aperiodic PC indicating field amplitudes upon entrance and exit at normal incidence. The amplitudes within the SiC and air layers of an arbitrary building block j of the aperiodic PC are also shown. E_0 is the incident electric field amplitude.

relations,

$$\begin{bmatrix} A(\mathrm{j}) \\ \\ B(\mathrm{j}) \end{bmatrix} = P^1(\mathrm{j}) M^{12} P^2(\mathrm{j}) M^{21} \begin{bmatrix} A(\mathrm{j}+1) \\ \\ B(\mathrm{j}+1) \end{bmatrix}, \tag{6.16}$$

and

$$\begin{bmatrix} C(\mathrm{j}) \\ \\ D(\mathrm{j}) \end{bmatrix} = P^2(\mathrm{j}) M^{21} P^1(\mathrm{j}+1) M^{12} \begin{bmatrix} C(\mathrm{j}+1) \\ \\ D(\mathrm{j}+1) \end{bmatrix}, \tag{6.17}$$

with $1 \leq \mathrm{j} < \mathrm{N}$, together with the use of their values at $\mathrm{j} = \mathrm{N}$. The latter are given by:

$$\begin{bmatrix} A(\mathrm{N}) \\ \\ B(\mathrm{N}) \end{bmatrix} = P^1(\mathrm{N}) M^{12} \begin{bmatrix} t \\ \\ 0 \end{bmatrix}, \tag{6.18}$$

and

$$\begin{bmatrix} C(\mathrm{N}) \\ \\ D(\mathrm{N}) \end{bmatrix} = \begin{bmatrix} t \\ \\ 0 \end{bmatrix}. \tag{6.19}$$

Moreover, in Section 6.7 we analyze how the properties of the aperiodic photonic crystals may correlate with the properties of the corresponding periodic photonic crystals made from the underlying building blocks of the aperiodic lamellae. In particular, we discuss the correlation of the broadband absorption to the coupling to allowed modes in the corresponding periodic PCs.

The photonic modes in a periodic medium are subject to Bloch's theorem just like electrons in a natural crystal [1–3, 41–43]. This means that the fields at the entrance of the j^{th} cell of a periodic PC structure would be equal to the fields at the entrance of the $(j+1)^{th}$ cell times a phase factor $e^{-\mathrm{iqa}}$ with q being the Floquet-Bloch wavevector and a the lattice constant of the periodic stack. This means:

$$\begin{bmatrix} E^{+}(\mathrm{j}) \\ E^{-}(\mathrm{j}) \end{bmatrix} = e^{-\mathrm{iqa}} \begin{bmatrix} E^{+}(\mathrm{j}+1) \\ E^{-}(\mathrm{j}+1) \end{bmatrix}, \tag{6.20}$$

where the superscripts $(+)$ and $(-)$ denote the respective wave amplitudes along the $+x$- and $-x$- direction.

In purely dielectric media the Bloch wave vector q is purely real in regimes of allowed EM propagation and completely imaginary outside [1, 42, 43]. However, in lossy photonic crystals the Floquet-Bloch phase, q, is complex throughout the spectrum and an abrupt distinction between allowed "band" modes, and forbidden "gap" modes cannot be made [28, 30]. Typically, forbidden propagation regions in lossy photonic crystals are characterized by a quick transition to ultra-high Im(q) values [28].

The fields in the left and right hand side of Eq. 6.20 can be related by the transfer matrix of the elementary building block, M^{BB}, which is equal to $M^{21}P^{1}M^{12}P^{2}$. Thus, $e^{-\mathrm{iqa}}$ should be an eigenvalue of the elementary building block transfer matrix, which yields:

$$e^{-\mathrm{iqa}} = \frac{1}{2}(M_{11}^{BB} + M_{22}^{BB} \pm \sqrt{\Delta}), \tag{6.21}$$

with $\Delta = (M_{11}^{BB} + M_{22}^{BB})^2 - 4det(M^{BB})$ and $det(M^{BB})$ being the determinant of the M^{BB} matrix. Eq. 6.21 yields two possible roots for q, with only one being acceptable that satisfies the requirement for passivity. As we are looking for modes propagating in the $+x-$direction the passivity requirement takes the form of $\mathrm{Im(q)} > 0$ [44, 45]. Note that the matrix elements of the M^{BB} matrix are frequency dependent, due to the frequency dependent permittivity of SiC, as given in Eq. 6.1. Solving Eq. 6.21 is equivalent to obtaining $\mathrm{q}(\omega)$, i.e. the the band structure of the periodic stack.

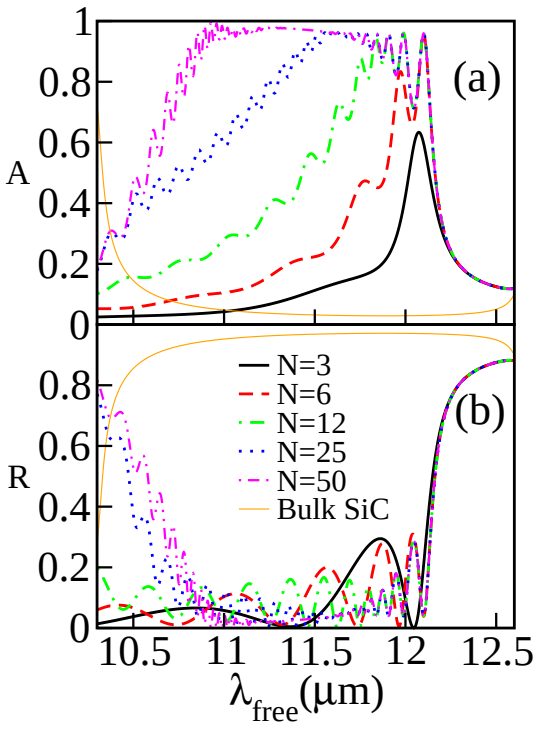

Figure 6.5: (a) Absorptance A, versus free space wavelength, λ_{free}, for the aperiodic PC of Fig. 6.1(a). We show the results for N = 3 (black solid), 6 (red dashed), 12 (green dot-dashed), 25 (blue dotted) and 50 (magenta dot-dashed-dot) building blocks. (b) same as (a), but for reflectance R, versus free space wavelength. For comparison we also show the absorptance and reflectance from a bulk SiC block with solid-orange lines.

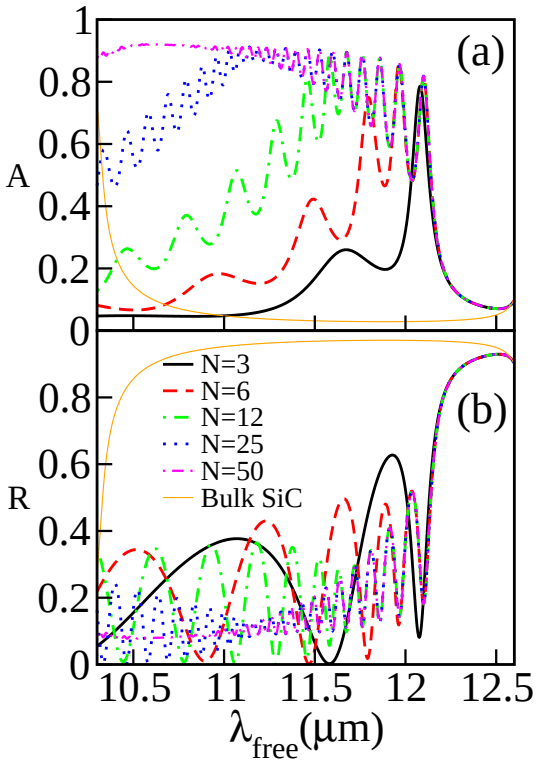

Figure 6.6: Same as in Fig. 6.5, but for the aperiodic PC of Fig. 6.1(b)

6.5 Broadband near-perfect absorptance with aperiodic SiC PCs in the Reststrahlen band: Results and Discussion

In this section, we present our results for the absorption of the aperiodic PCs of section 6.3, calculated with the TMM method as we described above. In particular, in Figs. 6.5(a) and 6.5(b) we show the respective spectral response of absorptance and reflectance of the first type of aperiodic PC depicted in Fig. 6.1(a). We observe in Fig. 6.5(a) a near-perfect absorptance when we take 50 building blocks that covers most of the Reststrahlen band (dot-dash-dot magenta line in Fig. 6.5(a)). This is related to the broadband low reflectance seen in Fig. 6.5(b). Conversely, we present the corresponding results of absorptance and reflectance for the aperiodic PC of Fig. 6.1(b) in Figs. 6.6(a) and 6.6(b) respectively.

Although we successfully demonstrated the broadband absorptance with the two aperiodic PCs with large number of building blocks, it is interesting to check to which extent such broadband absorptance survives when a smaller number of building blocks are taken. For this purpose, we show in the same figures, the absorptance and reflectance for a lower total number of building blocks, N.

In particular, we take N = 3, 6, 12 and 25 and show the results in Figs. 6.5 and 6.6 for the respective cases of Fig. 6.1(a) and Fig. 6.1(b), as black-solid line, red-dashed line, green dot-dashed line and blue-dotted line, respectively. We observe that the low reflectance property remains reasonably broadband even with a small number of building blocks. This is especially true for the first type of aperiodic PC. In the second type we see much stronger Fabry-Perot oscillations in the reflectance spectrum. This is because in the latter PC, the filling ratio increases quite rapidly from one building block to the next one as we have seen in Fig. 6.2 (d). The results of Ref. [27][8] suggest that the lower the filling ratio of a PC is, the less the reflection is. Actually, in the same work it was shown that the higher filling ratio PC structures are essentially approaching the bulk SiC behaviour [27][9]. The above findings imply that the low reflectance merit of the aperiodic PC of Fig. 6.1(a) can be attributed to the low filling ratio. Such low reflectance with the small strength of Fabry-Perot oscillations is important for a smoother spectral response of the absorption. Obviously, any reflection peaks inadvertently will manifest as dips in the absorption spectrum which are undesirable.

[8]These results refer to the results of Chapter 3 in this thesis.
[9]These results refer to the results of Chapter 3 in this thesis.

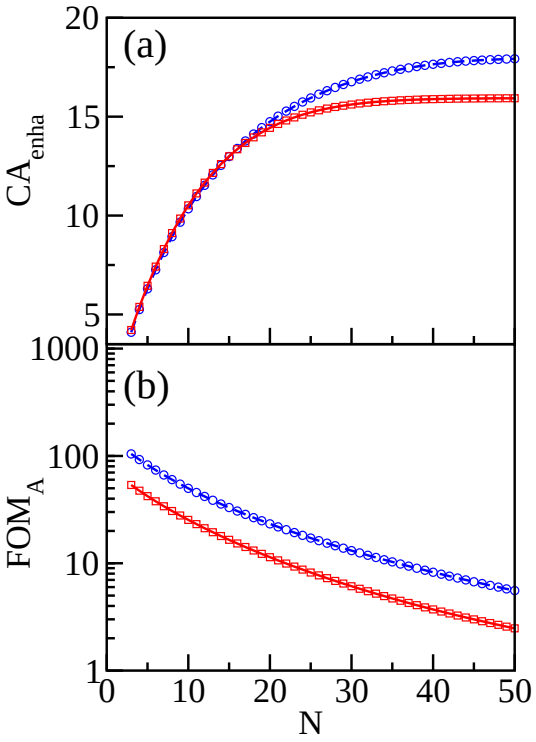

Figure 6.7: (a) Cumulative absorptance enhancement CA_{enha}, of the aperiodic PCs of Figs. 6.1(a) (blue circles) and 6.1(b) (red squares) versus the total number of building blocks N. (b) Same as (a) but for the absorptance figure of merit FOM_A.

In order to obtain a quantitative measure of the performance of the aperiodic PC schemes, we estimate the cumulative absorptance enhancement CA_{enha}, across the Reststrahlen band as follows:

$$CA_{enha} = \frac{1}{\lambda_2 - \lambda_1} \int_{\lambda_1}^{\lambda_2} \frac{A_{PC}(\lambda)}{A_{SiC}(\lambda)} d\lambda, \tag{6.22}$$

where λ_1 and λ_2 represent the bounds of the Reststrahlen band of SiC, and $A_{PC}(\lambda)$ and $A_{SiC}(\lambda)$ are the respective absorptance of the aperiodic PC and a 200 μm thick block of SiC at the specified wavelength. We show the results in Fig. 6.7(a) for the aperiodic PCs of Fig. 6.1(a) and Fig. 6.1(b) indicated with blue circles and red squares respectively. We notice that both the aperiodic PCs have almost same cumulative absorptance enhancement for less than 20 building blocks. However, when the number of building blocks exceeds 20, we can clearly observe that the first type of aperiodic PC exhibits a higher cumulative absorptance enhancement. We attribute this result to the better reflectance performance of the first type of aperiodic PC due to the consistently lower filling ratio throughout the aperiodic PC as we discussed.

It is also interesting to see which of the two aperiodic PC schemes exhibits a high cumulative absorptance with less absorbing material. Therefore we introduce an absorptance figure of merit $\mathrm{FOM_A}$, as follows:

$$\mathrm{FOM_A} = \mathrm{CA_{enha}} \frac{(\lambda_1 + \lambda_2)}{2 \cdot \mathrm{d_{thick}}}, \tag{6.23}$$

where $\mathrm{d_{thick}}$ is the total thickness of the SiC in the entire aperiodic PC structure and λ_1, λ_2, and $\mathrm{CA_{enha}}$ have the same meaning as in Eq. 6.22. We plot the $\mathrm{FOM_A}$ in Fig. 6.7(b) for the aperiodic PCs of Fig. 6.1(a) and Fig. 6.1(b) indicated with blue circles and red squares respectively. We can clearly identify the advantage of the first aperiodic PC scheme where a higher $\mathrm{FOM_A}$ is achieved consistently with the same number of building blocks.

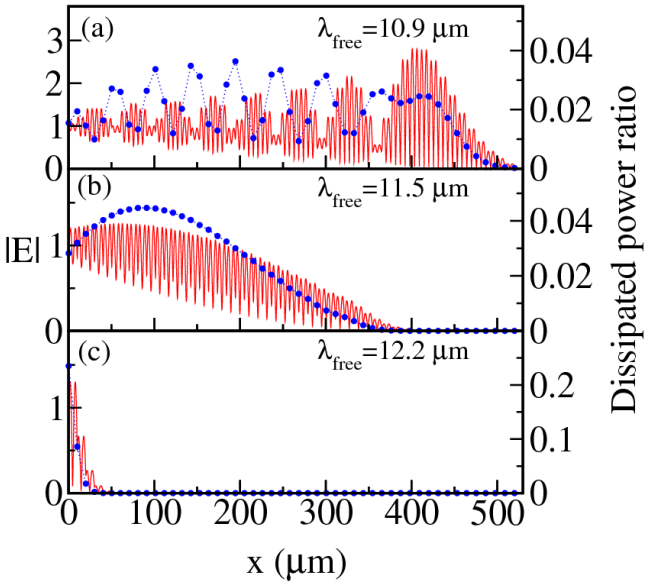

Figure 6.8: Spatial electric-field distributions (red solid lines) and dissipated to incident power ratio in the individual absorbing layers (blue circles) versus the location x, within the aperiodic PC of Fig. 6.1(a), with 50 building blocks. Results for these are plotted at three free space wavelengths, λ_{free} as indicated in the above individual panels (a), (b) and (c).

We note in passing that we did explore another type of aperiodic PC in which the lattice constant changed linearly, while keeping the filling ratio constant. We explored this route and found that the aforementioned aperiodic PC does not perform any better than the aperiodic PCs of Fig. 6.1(a) and Fig. 6.1(b) that we discussed above. We attribute this result to the large Fabry−Perot reflections arising from the increased air layers thickness between the absorbing SiC layers. Accordingly, we did not pursue this scheme further, and we will focus only on the schemes of Fig. 6.1(a) and Fig. 6.1(b) from now on.

To gain more insight into the performance of the two aperiodic PCs, we also calculate the spatial electric-field distributions inside the two aperiodic PC structures and indicate the results with red-solid lines in Figs. 6.8 and 6.9 respectively. The panels (a), (b) and (c) in both Figs. 6.8 and 6.9, represent wavelengths around the blue edge, middle and red edge of the SiC Reststrahlen band. We notice from Figs. 6.8 and 6.9, that around the blue edge of the SiC Reststrahlen, electric fields are oscillating across the aperiodic PC structure and attenuated nearly at the end of the aperiodic PC. On the other hand, around the middle wavelength of the SiC Reststrahlen band, the oscillating electric fields are slowly decreasing and strongly attenuated when reaching the middle of the PC. Finally, around the red edge of the SiC Reststrahlen band, the electric field is rapidly attenuated within the first few building blocks of the aperiodic PC.

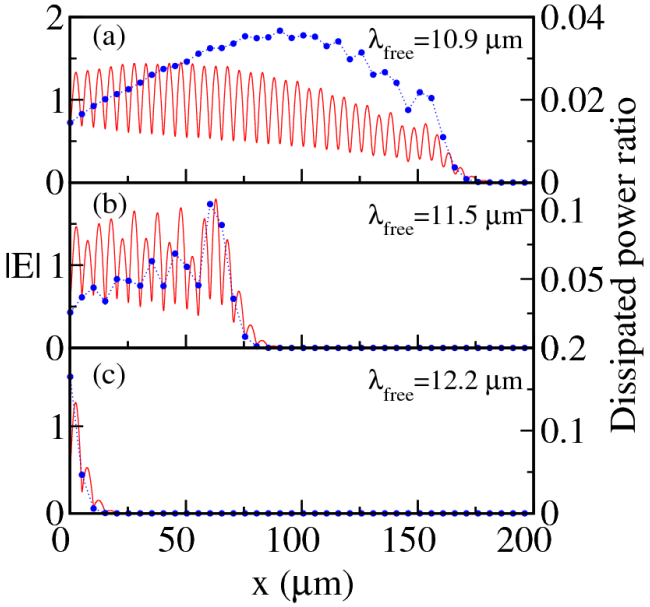

Figure 6.9: Same as in Fig. 6.8, but for the aperiodic PC of Fig. 6.1(b). First 40 building blocks are zoomed.

In order to understand how these electric-field variations correlate to the overall absorption, we evaluate the ratio of dissipated to incident power within the SiC layers. From Poynting's theorem [46] it can be shown that such dissipated to incident power ratio for the j$^{\text{th}}$ layer inside the aperiodic PC is given by:

$$\mathrm{P(j)} = \frac{\omega \varepsilon_1''}{c|E_0|^2} \int_{S_a(\mathrm{j})}^{S_a(\mathrm{j})+d_1(\mathrm{j})} |E(x)|^2 dx, \tag{6.24}$$

where ε_1'' represents the imaginary part of ε_1. With the use of the expressions for

the electric-field distributions $E(x)$ within the SiC layers given by Eq. 6.15, we obtain:

$$\mathrm{P(j)} = \frac{\omega\varepsilon_1''}{c|E_0|^2}\left[\frac{|A(\mathrm{j})|^2}{2k_{1x}''}(1-e^{-2k_{1x}''\mathrm{d_1(j)}}) + \frac{|B(\mathrm{j})|^2}{2k_{1x}''}(e^{2k_{1x}''\mathrm{d_1(j)}}-1)\right.$$

$$\left. +2Re[\frac{A(\mathrm{j})B^*(\mathrm{j})}{2ik_{1x}'}(e^{2ik_{1x}'\mathrm{d_1(j)}}-1)]\right], \tag{6.25}$$

where $k_{1x}{}'$ and $k_{1x}{}''$ are the real and imaginary parts of the wavevector k_{1x}, inside SiC. The A(j) and B(j) coefficients in the above equation are calculated from Eqs. (16)-(19).

We plot the results calculated from Eq. 6.25, for the power dissipation ratio within the j$^{\mathrm{th}}$ SiC layer versus the position of the center of this layer– $x_{\mathrm{c}}(\mathrm{j}) = S_{\mathrm{a}}(\mathrm{j})+\mathrm{d_1(j)}/2$– with the blue circles in Fig. 6.8 for the aperiodic PC of Fig. 6.1(a). Conversely, we show the respective result for the aperiodic PC of Fig. 6.1(b) in Fig. 6.9. It is interesting to notice in Figs. 6.8 and 6.9, that the power dissipation ratio variation does not follow the electric-field variations. This at first seems rather odd. However, we should keep in mind that the power dissipation ratio applies only to the SiC layers. On the other hand, electric fields are plotted for both the SiC and air layers. Moreover, the SiC layer thickness increases from one building to the next one throughout the structure. Therefore, thick SiC layers at the far end of the aperiodic PC will absorb more light due to the larger light-matter interaction length for the same electric-field amplitudes in comparison to the thin SiC layers at the front end of the aperiodic PC.

We notice from Figs. 6.8 and 6.9 that for the wavelengths around the blue edge of the Reststrahlen band, power is dissipated throughout the aperiodic PC. For wavelengths in the middle of the Reststrahlen band, power dissipation is high at the front end of the PC. For the wavelengths around the red edge of the Reststrahlen band, most of the power is dissipated within the first few SiC layers of the aperiodic PC. These results explain why the presence of a large number of building blocks is more important for the blue side of the Reststrahlen band spectrum, as we have seen in Figs. 6.5 and 6.6.

We assert that there is a strong correlation between the location of where most power is getting absorbed and the propagation properties of the corresponding building block at such location. Such propagation properties can be characterised by the imaginary part of the Bloch phase q, Im(q), of the corresponding periodic PC. The imaginary part of Bloch phase, Im(q), would signify regions of "forbidden" and

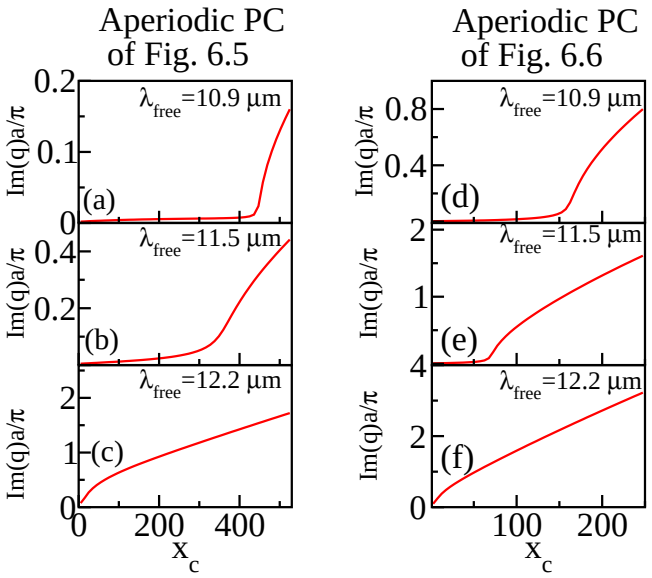

Figure 6.10: Band structure properties of the aperiodic PC building blocks versus the location x_c of their respective centres. The imaginary part of the Floquet-Bloch phase of the corresponding periodic structure, Im(q), is plotted at a certain free space wavelength that is designated inside each panel. Im(q) is scaled with a/π with a being the respective building block size. The panels in the left [(a), (b), and (c)] represent the case of the aperiodic PC of Fig. 6.5. Conversely, the panels in the right [(d), (e), and (f)] represent the case of the aperiodic PC of Fig. 6.6.

"allowed" EM propagation, although such distinction is not as sharp in the case of lossless PCs [28, 30]. In order to uncover such a correlation we calculate the Im(q) versus x_c –for the same wavelength values of the impinging EM wave as in Figs. 6.8 and 6.9– for the case of periodic PCs that correspond to the building blocks located at the x_c position.

We plot the results, in Figs. 6.10(a), 6.10(b) and 6.10(c) at these specified wavelengths (indicated within each panel) for the aperiodic PC of Fig. 6.5. Conversely, in Figs. 6.10(d), 6.10(e) and 6.10(f) we plot the corresponding results at the same wavelengths for the aperiodic PC of Fig. 6.6. Note that Im(q) is shown scaled with a/π, with $a = d_1 + d_2$ being the building block size, which is constant and equal to 5 microns for the PC of Fig. 6.6 but varies with building block location for the case of Fig. 6.5. Clearly, the results in Fig. 6.10 suggest that at a certain free-space wavelength most power is getting absorbed at the vicinity of building blocks with high Im(q) values, i.e. in the vicinity of the gap regime of the corresponding periodic PCs.

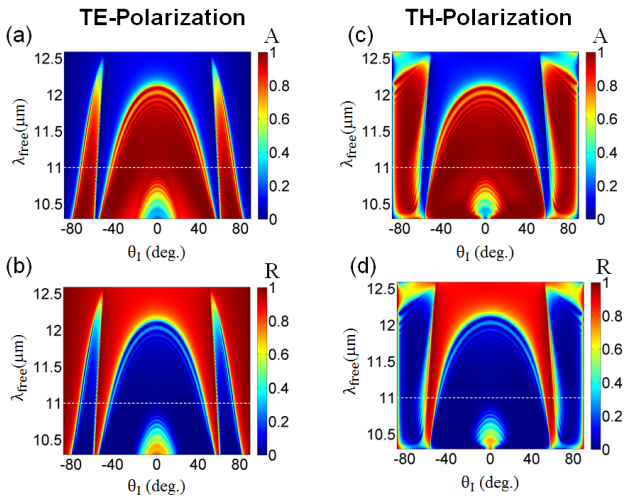

Figure 6.11: Angular response of the aperiodic PC of Fig. 6.5. The absorptance, A and reflectance, R are shown versus the impinging's wave angle of incidence θ_I and wavelength λ_{free} for both polarisations. The results in (a) and (b) represent absorptance and reflectance for the TE-polarisation case while the results in (c) and (d) represent absorptance and reflectance for the TH-polarisation case.

6.6 Angular robustness of the broadband superabsorption

Realistic beams are finite in lateral extend; they are not plane waves. For example a diffraction-limited beam with a Gaussian lateral profile would be equivalent to a superposition of impinging waves at different incident angles, θ_I, within a range spanning roughly between -10^0 to 10^0. It is therefore interesting to check the robustness of the superabsorptance bandwidth we observed for normal incidence with a plane wave under angular illumination conditions.

While the two polarisations are degenerate for normal incidence they are not so for the case of non-normal incidence. For this reason we explore the angular absorptance response of our designs under both TE- and TH- illumination conditions that we depicted in Fig. 6.3. We show in Figs. 6.11(a) and 6.11(b) respectively the absorptance and reflectance versus incident angle and free space wavelength for a TE-polarised impinging wave on the aperiodic PC structure of Fig. 6.5 The corresponding results for the case of a TH-polarised wave are shown in Figs. 6.11(c) and 6.11(d). The results were calculated with the TMM method, as we described in the methodology section for the case of a general incidence with $\theta_I \neq 0$. Likewise, we also investigate off-normal incidence for the PC of Fig. 6.6 and show our results in an analogous manner in Fig. 6.12.

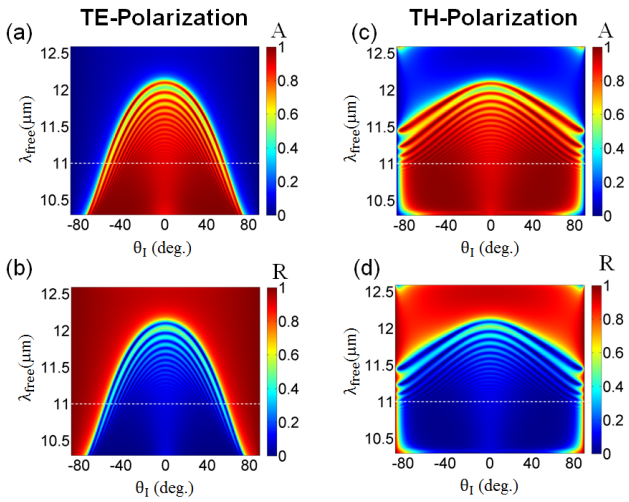

Figure 6.12: Same as in Fig. 6.11 but for the aperiodic PC of Fig. 6.6.

All cases demonstrate an impressive angular bandwidth[10]. throughout the phonon-polariton spectrum that well exceeds the angle-span of a diffraction-limited Gaussian beam. These results suggest that our proposed aperiodic PC platforms would be entirely functional under realistic illumination conditions.

6.7 Broadband aperiodic superabsorbing PCs: Design operation and optimisation

In the previous section we considered two particular aperiodic PC designs. We constructed these two designs based on the intuition we obtained from the study of corresponding periodic structures [27, 28][11]. We considered for the first building block such parameters that give a low filling ratio and a total size equal to the lattice constant of some of the high performing PCs that were previously investigated [28][12]. In fact, the first building block of our second aperiodic PC design is exactly the same as one of such periodic designs reported in Ref. [28][13]. Subsequently, we construct the aperiodic sequence of lamellae with two different

[10]The abrupt increase in reflectance, R and decrease in absorptance, A at near-grazing incidence, i.e. incidence with an angle close to 90^0 with the interface normal, observed for TH-polarized light in Figs. 6.12 (c) and 6.12 (d) respectively, is not uncommon in optics. It typically also occurs for grazing incidence of TH-polarized light at the interface of a dielectric bulk material [e.g see C. A. Balanis, *Advanced engineering electromagnetics*, (Wiley, Canada, 1968)]. It is a result of the low interaction of the EM wave with the PC, as the EM wave essentially passes almost parallel to the PC interface, with its electric field almost perpendicular to the interface. This yields a low field penetration within the structure resulting from the conservation of the normal component of the electric displacement vector **D** and leads accordingly to a high reflectance.

[11]These results refer to the results of Chapters 3 and 5 in this thesis.

[12]These results refer to the results of Chapter 5 in this thesis.

[13]These results refer to the results of Chapter 5 in this thesis.

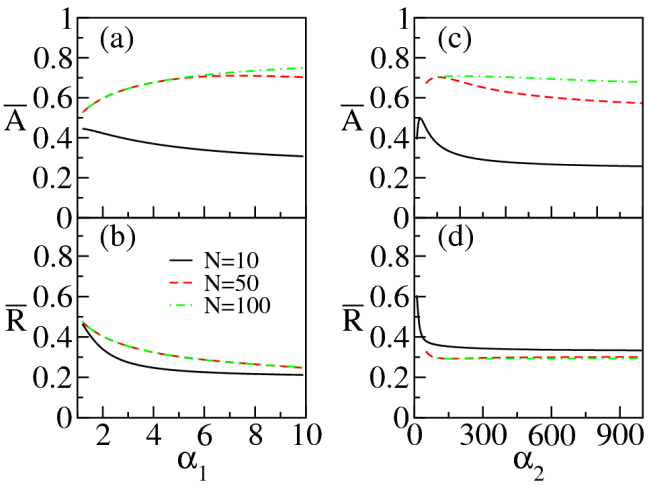

Figure 6.13: Aperiodic design performance versus degree of adiabaticity, α_1, for the aperiodic lamellar sequencing of Eq. 6.28 [panels (a) and (b)] and versus α_2 for the aperiodic lamellar sequencing of Eq. 6.29 [panels (c) and (d)]. The remaining parameters are the same as in the respective cases of Figs. 6.5 and 6.6. Both the averaged absorptance, $\overline{\mathrm{A}}$, and the averaged reflectance, $\overline{\mathrm{R}}$ over the entire Reststrahlen band of SiC are shown.

scenarios –linearly increasing SiC slab thickness with air thickness kept constant and linearly increasing filling ratio with building block size being kept constant–. Again, the linear sequencing slope parameters, 1/5 for the first scenario and 1/100 in the second, were chosen intuitively so that they would produce an adiabatic, yet reasonably significant, increase in the SiC slabs thickness.

In this section we investigate further the broadband merit of such aperiodic polaritonic PCs beyond the intuitive construction of the designs of Fig. 6.5 and 6.6. Our purpose is to gain further understanding on the principles of operation of such structures. Moreover, we will investigate the structural parameter tolerance of the broadband absorptance feature of the aperiodic designs and compare our initial intuitively conceived designs with optimised structures.

First, we study the impact of only the sequencing slope on the broadband absorption merit. As a quantitative measure of the latter we consider the averaged absorption, $\overline{\mathrm{A}}$ over the phonon-polariton regime calculated from:

$$\overline{\mathrm{A}} = \frac{1}{\lambda_2 - \lambda_1} \int_{\lambda_1}^{\lambda_2} \mathrm{A_{PC}}(\lambda) d\lambda. \tag{6.26}$$

We will also look at the averaged reflection, $\overline{\mathrm{R}}$, given by:

$$\overline{\mathrm{R}} = \frac{1}{\lambda_2 - \lambda_1} \int_{\lambda_1}^{\lambda_2} \mathrm{R_{PC}}(\lambda) d\lambda. \tag{6.27}$$

In the above equations, $A_{PC}(\lambda)$ and $R_{PC}(\lambda)$ represent respectively the absorptance and reflectance of the aperiodic PC structures at a certain free space wavelength λ. Also, λ_1 and λ_2 represent the blue and red edge of the phonon-polariton spectrum of SiC.

We essentially start from the same building blocks as in the designs of Fig. 6.5 and 6.6 and change only the slope of the monotonically increasing functions of Eqs. 6.2 and 6.3. In particular we take:

$$d_1(j) = d_1(1) + \frac{1}{\alpha_1}(j-1) \cdot d_1(1), \tag{6.28}$$

and

$$f(j) = f(1) + \frac{1}{\alpha_2}(j-1), \tag{6.29}$$

with $d_1(1) = 0.125\mu$m, and $f(1) = 0.05$ as in the designs of Fig. 6.5 and 6.6. We will refer in the following to α_1 and α_2 as adiabatic parameters since they control how adiabatic is the increase in SiC thickness as we progress within the lamellae sequence. The larger the α parameters are the more adiabatic such change is.

We plot our results for $\overline{A}$ and $\overline{R}$ versus the adiabatic parameter α_1 in Figs. 6.13(a) and 6.13(b) for the aperiodic sequence of the type of Eq. 6.28 with the remaining structural parameters taken the same as in Fig. 6.5. Conversely, we show the corresponding results for $\overline{A}$ and $\overline{R}$ versus the adiabatic parameter α_2 in Figs. 6.13(c) and 6.13(d) for the aperiodic sequence of the type of Eq. 6.29 with the remaining structural parameters taken the same as in Fig. 6.6. We do so for three different cases of total building blocks, N. We take N=10, 50 and 100 and show the corresponding results in Fig. 6.13 with solid black, dashed red and dot-dashed green lines respectively. Note that there is a minimum value for the range of the α_2 parameter that depends on the total number of building blocks as the filling ratio cannot exceed the value of 1 for any building block.

As our intuition would have expected the averaged reflection, $\overline{R}$, monotonically decreases with increasing α parameters i.e. with increasing adiabaticity of the aperiodic lamellae sequencing. However, clearly we do not see this behavior for the averaged reflectance to be transferred to the averaged absorptance. A monotonically decreasing $\overline{R}$ should perhaps yield a monotonically increasing $\overline{A}$ with increasing α values. Indeed, we observe so for the large, hundred-building-block, structures.

However, the other cases typically have a maximum for $\overline{A}$ at a particular value of α or even show a decreasing behavior of $\overline{A}$ with increasing α as for example the

case of Fig. 6.13(a) for N=10. This is actually not too surprising, as transmission maybe non-zero for the thinner structures. As the degree of adiabaticity becomes larger, a larger number of building blocks are required to completely absorb the EM energy passing through.

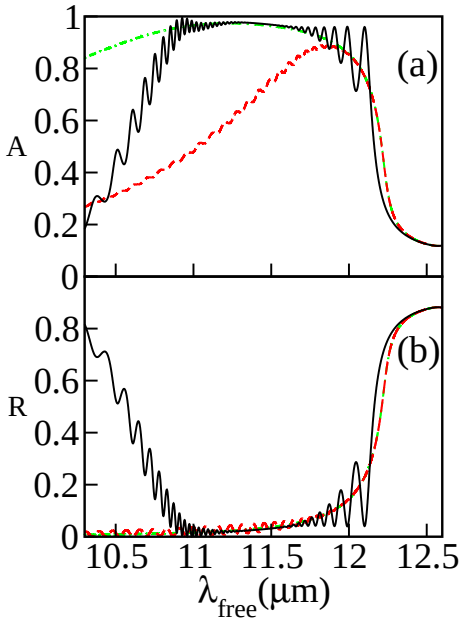

Figure 6.14: Comparison of the absorptance spectra [in (a)] and reflectance spectra [in (b)] between the cases of the aperiodic PC of Fig. 6.5 with 50 building block (black solid lines) and its periodic counterpart constructed from the entry building block. The red-dashed lines represent the result for the periodic PC with 50 building blocks while the green dot-dashed lines represents the result for the periodic PC with 295 building blocks which corresponds to the same total SiC thickness as the aperiodic structure.

Evidently, as $\alpha_1 \to \infty$ and $\alpha_2 \to \infty$ the aperiodic lamellar sequences of Eq. 6.28 and 6.29 fall back to a periodic photonic crystal having an elementary unit cell the same as the first building block of these sequences. The asymptotic behavior of the averaged absorptance versus the adiabatic parameters then suggests that these corresponding periodic photonic crystal structures should be capable of a broadband low-reflective and high-absorbing behavior. However, we had not observed that in our prior investigations[14] in Refs. [27] and [28] . This has prompted us to look into this further.

We replot in Fig. 6.14 the absorptance and reflectance versus the free space wavelength for the aperiodic PC of Fig. 6.5 for fifty building blocks as black solid lines to compare it with the corresponding periodic PC constructed from the first building block of the aperiodic structure (shown as red-dashed lines in

[14]These results refer to the results of Chapters 3 and 5 in this thesis.

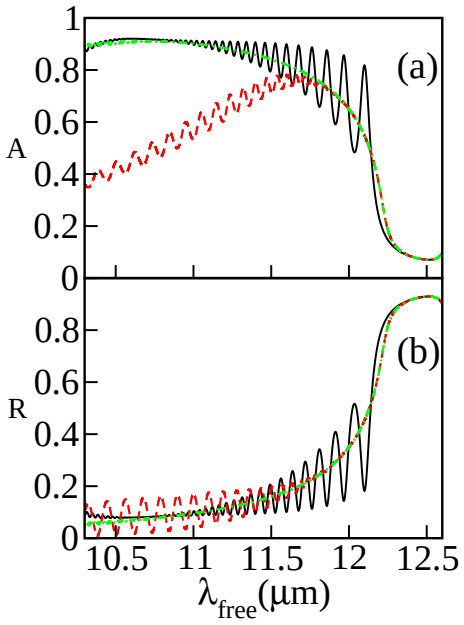

Figure 6.15: Same as in Fig. 6.14 but for the case of the aperiodic PC of Fig. 6.6 and the corresponding periodic PC counterparts.

the same figures). We will refer to such structure simply as the "corresponding periodic PC" from hereon. These results clearly manifest that fifty building blocks sequenced according to Eq. 6.28 for $\alpha_1 = 5$ absorb almost all impinging EM energy in most of the spectral range within the Reststrahlen band. Nevertheless, fifty identical building blocks with the same parameters as the first building block of the aperiodic sequence do not. The result is even worse for periodic structures with a unit cell corresponding to any other building from the aperiodic lamellar structure.

Yet, the analysis of Fig. 6.13 suggests that the corresponding periodic PC should possess broadband near-perfect absorptance as well. We do in fact notice a broadband low reflectance in Fig. 6.14(b). This clearly points out that the lack of absorptance bandwidth in the corresponding periodic PC is because of insufficient SiC material in the fifty-cell structure. Thus, we subsequently consider a corresponding periodic PC that would have as much SiC material as the aperiodic structure of fifty building blocks, N. This means that such periodic PC would need to have a N^{eq} number of unit cells given by:

$$N^{eq} = N + \frac{1}{10}N(N-1), \tag{6.30}$$

where $N = 50$, i.e. it should be comprised of 295 unit cells. We show the corresponding spectra for this long periodic PC in Fig. 6.14 with green dot-dashed lines. Indeed, a broadband absorptance behavior is now observed.

We make a similar comparison in Fig. 6.15 for the corresponding periodic PC case

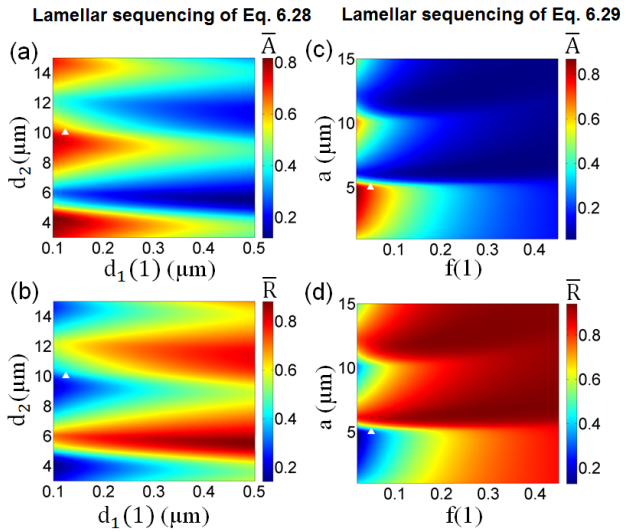

Figure 6.16: (a) Spectrally averaged absorptance, $\overline{A}$, of the aperiodic lamellar sequence of Eq. 6.28 versus thickness of the entry lamella, $d_1(1)$, and inter-lammelar spacing, d_2, kept constant throughout the sequence. The adiabaticity, α_1, equals to 5. (b) Same as in (a) but for the spectrally averaged reflectance, $\overline{R}$. (c) Spectrally averaged absorptance, $\overline{A}$, of the aperiodic lamellar sequence of Eq. 6.29 versus filling ratio of the entry building block, f(1), and unit cell size, a, kept constant constant throughout the sequence. The adiabaticity, α_2, equals to 100. (d) same as in (c) but for the spectrally averaged reflectance $\overline{R}$.The white triangles designate the parameters of the respective aperiodic PCs of Figs. 6.5 and 6.6.

Table 6.1: Performance evaluation and comparison of the aperiodic PCs of Figs. 6.5 and 6.6 and their periodic counterparts constructed from their entry building block. The absorptance figure of merits, FOM_A and $FOM_A{}'$ as defined in Eqs. 6.23 and 6.32 respectively, as well as the cumulative enhancement, CA_{enha} as defined in Eq. 6.22 are employed for such purpose.

Type of Lamellar Structure	**Building Block No**	**Total structure thickness (μm)**	**SiC thickness (μm)**	**FOM_A**	**$FOM_A{}'$**	**CA_{enha}**
Aperiodic PC of Fig. 6.5	50	530.625	36.875	5.56	0.387	17.92
Corresponding periodic PC	50	500	6.25	26.12	0.326	14.26
Corresponding periodic PC	295	2950	36.875	5.80	0.073	18.69
Aperiodic PC of Fig. 6.6	50	250	73.75	2.47	0.730	15.93
Corresponding periodic PC	50	250	12.5	11.94	0.597	13.03
Corresponding periodic PC	295	1475	73.75	2.46	0.123	15.85

of the aperiodic lamellar sequence of Eq. 6.29, with the parameters of Fig. 6.6. We show the results for the absorptance and reflectance for this aperiodic PC and its periodic counterpart with N=50 buildings blocks as black solid lines and red-dotted lines respectively. As in the case of Fig. 6.14 we also see here that fifty cells are inadequate to absorb the incoming EM energy over a broad bandwidth in the Reststrahlen band for periodic PC structure. The number of N^{eq} unit cells we need here in order to have the same amount of SiC material in the corresponding periodic PC as in the aperiodic structure of Fig. 6.6 is given by:

$$N^{eq} = \frac{1}{f(1)} \left(f(1)N + \frac{1}{200} N(N-1) \right), \tag{6.31}$$

with N=50 and f(1)=0.05, which also is equal to 295. We plot in Fig. 6.15 the spectra for the corresponding periodic PC with 295 unit cells as green dot-dashed line.

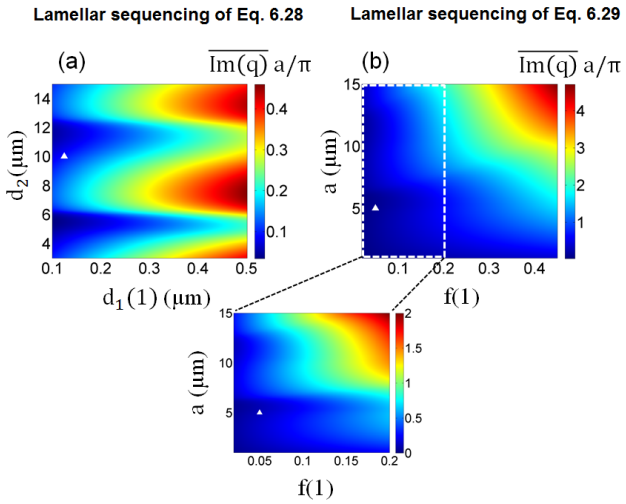

Figure 6.17: Same as in Fig. 6.16(a) and 6.16(c) but for $\overline{\mathrm{Im(q)}}$ evaluated from Eq. 6.33. The $\overline{\mathrm{Im(q)}}$ is scaled with a/π, with a being the lattice constant of the corresponding periodic PC. For the case in (a) $a = d_1(1) + d_2$. For the case in (b) a is explicitly given in the vertical axis.

Indeed, the results in Figs. 6.14 and 6.15 verify that the corresponding periodic PC counterparts exhibit broadband absorptance behavior when a very large number of unit cells is taken that provides a sufficient amount of SiC material. Thus, the above analysis suggests that if we take a block of SiC material and slice it to equal very thin slices sufficiently spaced apart at equal distances we can obtain efficient broadband absorption in the Reststrahlen band of SiC. Note that the total length L of such periodic structure is really very large. In particular, it is close to 300 free

space wavelengths for the case of Fig. 6.14 and close to 150 free space wavelengths for the case of Fig. 6.15. On the other hand, if we allow to slice the same amount of SiC material in unequal slices and position them so that their thickness gradually increases we can obtain a similar absorption over a broad spectral range with much more compact structures. In particular, the length of the structures in Fig. 6.5 and 6.6 are close to 50 and 25 wavelengths respectively.

From the practical point of view, it is important to also consider the total length of the structure when evaluating the merits of a certain design. Hence, it becomes then clear that $\mathrm{FOM_A}$, we defined in Eq. 6.23 may not by itself be an adequate measure of performance of a certain design. We therefore introduce an additional figure of merit, $\mathrm{FOM_A}'$ defined as follows:

$$\mathrm{FOM_A}' = \mathrm{CA_{enha}} \frac{(\lambda_1 + \lambda_2)}{2L}, \tag{6.32}$$

with L being the total thickness of the structure. We emphasize that these figures of merit are useful for a comparative analysis between designs, in the sense that they help to identify the advantages and disadvantages of a certain design. However, one should bear in mind that they are always trade-offs to consider in each case.

For example it appears that the periodic structures can yield smooth broad spectra of efficient absorptance but they involve a much higher number of lamellae and are much longer (about six times) than their aperiodic counterparts. The more compact we try to make a broadband design, the thicker SiC blocks we need to introduce which inevitably lead to more prominent Fabry-Perot fringes and less smooth spectra. For example, the aperiodic PC of Fig. 6.5 shows more interference fringes than its ultra-long corresponding periodic PC counterpart but less interference fringes in comparison with the more compact aperiodic PC of Fig. 6.6. Table 6.1 encapsulates such comparisons, where both introduced absorptance figure of merits, FOM_A and FOM_A', are given for the designs we analysed above.

We proceed below in evaluating further the robustness of the broadband absorptance merit of the aperiodic PCs. Fig. 6.13 attests that the adiabaticity parameter values of α_1=5 and α_2=100 are near the optimum values that yield the maximum averaged absorptance, $\overline{\mathrm{A}}$ when fifty building blocks are taken in the lamellar sequences of Eqs. 6.28 and 6.29 respectively. Accordingly, below we fix these parameters at these values.

Then for the lamellar sequence emanating from Eq. 6.28, we calculate how the averaged absorptance changes with $d_1(1)$ and inter-SiC lamellae spacing d_2 which is kept constant throughout the entire sequence. Conversely, for the lamellar sequence emanating from Eq. 6.29, we calculate how the averaged absorptance is changing with the filling ratio of the entry building block, f(1), and the building block size, a, which is kept constant throughout the entire sequence. We plot the results in Figs. 6.16(a) and 6.16(c) respectively. The accompanying results for the averaged reflectance, $\overline{R}$, are shown in Figs. 6.16(b) and 6.16(d) respectively.

We observe that there is a wide range in parameter space of near-optimum performance in both cases attesting for the robustness of the designs. This is especially true for the designs emanating from the sequence of Eq. 6.28. We observe that the performance of both designs deteriorates with increasing filling ratio. The white triangles in the parameter space designate the parameters of the designs considered in Fig. 6.5 and 6.6. It is impressive to observe that both designs that we conceived intuitively are very close to the optimised aperiodic PC designs.

In the following, we try to understand further the particular structure of the absorptance behavior we observed in Fig. 6.16 in the parameter space of the lamellar sequences. We argue that the performance of the aperiodic PC designs is strongly correlated to the properties of their entry building block. In particular, we argue that the spectral extend of the allowed modes of a periodic PC constructed from the entry building block is of crucial significance. As a measure of the latter we consider the average value of the imaginary part of the Floquet-Bloch phase q, $\overline{\mathrm{Im(q)}}$. The larger this is the lower the extend of allowed modes within the SiC Restrahlen band for the periodic PC comprised of the entry building block of the aperiodic structure. In other words it would be the minima of $\overline{\mathrm{Im(q)}}$ that would suggest a strong absorptance performance.

We evaluate $\overline{\mathrm{Im(q)}}$ from:

$$\overline{\mathrm{Im(q)}} = \frac{1}{\lambda_2 - \lambda_1} \int_{\lambda_1}^{\lambda_2} \mathrm{Im(q}, \lambda) d\lambda, \tag{6.33}$$

where $\mathrm{Im(q}, \lambda)$ is calculated with the TMM method as we discussed in the methodology section. The parameter space of Figs. 6.16 defines different entry building blocks and for each we calculate such $\overline{\mathrm{Im(q)}}$ value for the corresponding PC medium. We plot the result in Fig. 6.17(a) for entry building blocks corresponding to the sequencing of Eq. 6.28. Conversely, we show in Fig. 6.17(b) the result for entry building blocks corresponding to the sequencing of Eq. 6.29. Fig. 6.17(c) is a zoom

of Fig. 6.17(b) around the region of lower filling ratios. It is remarkable to observe that the landscape of $\overline{\mathrm{Im(q)}}$ in the parameter space resembles closely that of the averaged reflectance $\overline{R}$ we observed in Fig. 6.16.

This strongly supports our claim that the properties of the entry building block strongly define the broadband absorption performance of the periodic structure provided a proper adiabatic parameter in the lamellar sequence is taken. We stress that the behavior of a certain building block well within the aperiodic sequence can be dramatically different from the corresponding periodic photonic crystal. For example let's take the 41^{th} building block of the aperiodic structure of Fig. 6.5 located at $x_c \sim 425\,\mu\mathrm{m}$. An EM wave incident with a wavelength of 10.9 μm wavelength would fall in the vicinity of the band-gap for the corresponding periodic PC made from such building block. As a result at this wavelength the latter PC is highly reflective, more than $\sim 80\%$. Yet, at the same impinging wavelength light is directed with a high efficiency to the same building block within the aperiodic sequence to get absorbed thereafter[15].This further supports our claim that it is the entry unit cell that most crucially influences the absorptance performance of the aperiodic designs.

These observations simultaneously imply that the spatial order of the building blocks of the lamellar sequence would be of crucial significance. We investigate this in detail in the following section.

6.8 Significance of the aperiodic PCs building block sequence

We have seen that a large number of absorbing layers is necessary for optimising cumulative absorption enhancement. Both the aperiodic PCs of Fig. 6.1(a) and Fig. 6.1(b) employ these building blocks in an increasing order of thickness. Accordingly, it is natural to wonder how important is the sequence of building blocks in these microstructures. For this reason, we will explore changing the building block sequencing of the aperiodic PC structures and its impact on the absorption spectra.

We start from the case of Fig. 6.1(a) and we just interchange the first two SiC

[15]In other words, a building block that can be highly absorbing when embedded in an aperiodic sequence, actually leads to high reflectance, when a part of a periodic PC that is made of such building block.

layers of our original aperiodic PC of Fig. 6.1(a). We show the absorptance and reflectance of this modified aperiodic PC structure with the green-dashed lines in Figs. 6.18(a) and 6.18(b) respectively. We compare these results with those of the original aperiodic PC seen with red-solid lines. We notice that the absorptance is decreased at the higher wavelength end of the absorptance spectra, corresponding to the converse increase in the reflectance.

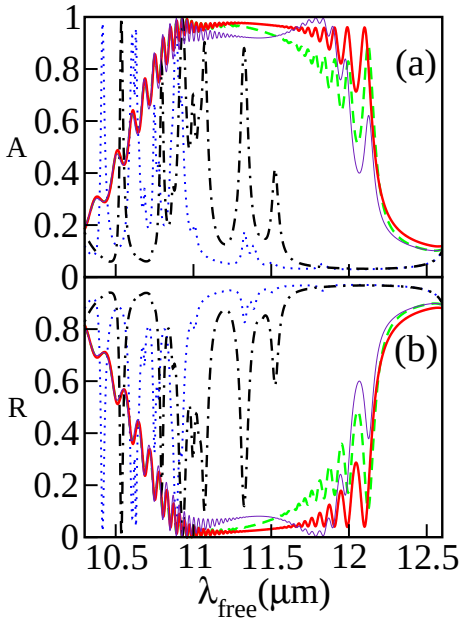

Figure 6.18: (a) Spectral response of the absorptance for the modified PCs from the original aperiodic PC of Fig. 6.1(a). We show the results for the modified PCs in which the first two and the first three SiC layers are interchanged with green-dashed line and violet-solid line respectively. The results for two random multilayer structures, comprised of the same building blocks of the original aperiodic PC of Fig. 6.5(a), are represented with blue-dotted line and black dot-dashed line. (b) same as (a), but for the reflectance versus free space wavelength. For comparison, we also show the absorptance and reflectance of the original aperiodic PC of Fig. 6.1(a) with red-solid lines.

Subsequently, we interchange the SiC layers of the first three building block so that original first, second and third layer are placed in the third, first and second building block respectively of the new modified aperiodic PC. We can clearly identify a further dip in the absorptance and converse increase in the reflectance of this PC as indicated with the violet-solid lines in Figs. 6.18(a) and 6.18(b) respectively. These results suggest that even slightly altering the order of the absorbing layers in the original aperiodic PC negatively affects the cumulative absorptance within the SiC Reststrahlen band.

Now we consider the extreme case where the original building blocks are randomly located. In particular, we apply the Knuth shuffle algorithm [47] on the original ape-

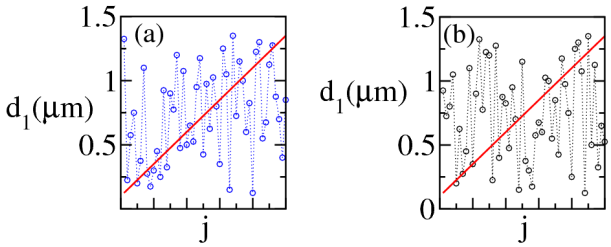

Figure 6.19: SiC lamellae thickness in the random sequences versus building order j. (a) case of the blue dotted line of Fig. 6.18. (b) case of the black dot-dashed line of Fig. 6.18. In both cases, the corresponding values of the SiC lamellae thickness of the original aperiodic PC are shown for comparison with a red solid line.

riodic PC building blocks. We show the absorptance of such two random multilayer structures in Fig. 6.18(a), indicated with blue-dotted and black dot-dashed lines respectively. The corresponding reflectance is shown in Fig. 6.18(b). We also show the SiC lamellae thickness at each building block with the building block order j for these two random sequences in Fig. 6.19. In panel (a) the case of the blue dotted line of Fig. 6.18 is shown with blue circles. Conversely, in panel (b) the case of the black dot-dashed line of Fig. 6.18 is shown with black circles. In both cases, the corresponding values of the SiC lamellae thickness of the original aperiodic PC are shown for comparison with a red solid line.

Table 6.2: Performance evaluation and comparison of the structures of Fig. 6.20. The absorptance figure of merits, $\mathrm{FOM_A}$ and $\mathrm{FOM_A}'$ as defined in Eqs. 6.23 and 6.32 respectively, as well as the cumulative enhancement, $\mathrm{CA_{enha}}$ as defined in Eq. 6.22 are employed for such purpose.

Type of Lamellar Structure	**Building Block No**	**Total structure thickness (μm)**	**SiC thickness (μm)**	**$\mathrm{FOM_A}$**	**$\mathrm{FOM_A}'$**	**$\mathrm{CA_{enha}}$**
Aperiodic PC of Fig. 6.20	5	22.80	5.14	18.10	4.081	8.13
Corresponding periodic PC	5	22.80	1.140	50.52	2.526	5.03
Corresponding Terminated PC	5	22.686	1.026	78.79	3.563	7.06

We can identify multiple high absorptance peaks in the absorptance spectrum of these random multilayer structures. However, these do not exhibit a broadband absorption. Thus the cumulative absorption is much lower than the one exhibited by their aperiodic PC counterpart. This is because of the high reflectance exhibited by the structures with randomly sequenced building blocks. We carried out the same investigations for the aperiodic PC of Fig. 6.1(b) and we observed similar results. Therefore, our findings suggest that although SiC layers with different

thicknesses absorb best different wavelengths of light, these should be arranged in the increasing order of thickness in order to obtain large cumulative absorption within the entire SiC Reststrahlen band.

6.9 Shrinking the size of the broadband aperiodic PC superabsorbers

Table 6.1 clearly suggests that the first aperiodic scheme [from Eq. 6.28] is better performing with respect to the amount of SiC material used; hence it is characterised by higher FOM_A values. However, the second aperiodic scheme [from Eq. 6.29] performs better with respect to the total structural size. Hence it is characterised by higher $FOM_A{}'$ values. We clearly see when we compared the aperiodic PCs of Figs. 6.5 and 6.6 that the absorption enhancement of the latter saturates quicker with a smaller number of total building blocks [See Fig. 6.7], and performance would not be increased further by adding more building blocks. We see in Figs. 6.9 that for the PC of Fig. 6.6, essentially no more power is getting absorbed after the 35^{th} building block.

In other words, the second aperiodic scheme uses more SiC material, but allows to pack it closer to the entry face yielding a smaller total structural size. On the other hand the first aperiodic scheme uses less SiC material and disperses it within a larger structural size. In the extreme case of a periodic structure at broadband absorption conditions, we found out in Section 6.7 that the SiC material must be very dilute throughout, requiring structures as long ~ 300 free space wavelengths. For practical purposes, it is advantageous to pack as much SiC material as possible to the entry face to obtain compact designs with a fewer number of total building blocks. Yet, that poses a challenge because the more we pack SiC material close to the entry face the higher the reflectance is.
We investigate in the following the possibility to obtain a more compact absorber based on the second lamellar sequencing scheme generated from Eq. 6.29. We would need more SiC material distributed over a smaller number of building blocks which implies the need for a less adiabatic design which unavoidably would be more reflective. We therefore need to relax the requirement of near-perfect absorptance. Thus, we investigate whether it is possible to obtain a good, yet not near-perfect[16], absorption performance throughout the Reststrahlen band with the

[16]Naturally, one should aim for the best absorption performance as close to one as possible. However, there are other constraints such as the practical realisation and utilisation of the structure. Therefore, there is a trade-off between the absorption performance and how compact can the

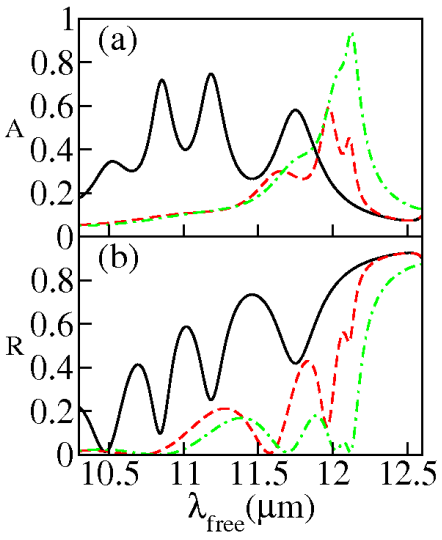

Figure 6.20: Two-wavelength long aperiodic PC structure from the lamellar sequence of Eq. 6.29 with a = 4.56 μm and $\alpha_2 = 11.4$. The absorptance and reflectance are shown with black solid lines in (a) and (b) respectively. For comparison the corresponding spectra of a periodic PC made from the entry building block and with the same total thickness are shown with red long-dashed lines. In addition, we show the effect of a 50% termination in the entry face of the latter periodic PC with green dot-dashed lines.

lamellar sequence of Eq. 6.29. We set a = 4.56 μm, and f(1) = 0.05 which represent near-optimum parameters for the entry building block as we can see in Fig. 6.16. For these parameters we look for the optimum adiabaticity value when a total of five building blocks are considered and we find that to be $\alpha_2 = 11.4$.

We show the results for the absorptance and reflectance versus free space wavelength as black solid lines in Figs. 6.20(a) and 6.20(b) respectively. We observe a strong absorption performance that spans throughout most of the SiC Reststrahlen band, yielding a cumulative enhancement factor of close to 10. We clearly see that this aperiodic scheme outperforms the corresponding periodic PC made from the entry building block–represented with the dashed red lines in the figure. We also compare this performance with the performance of the latter periodic PC with its front face terminated by removing 50% of SiC material. We see that the latter optimisation route, that we discussed in detail in Ref. [27, 28][17], leads to overall comparable absorption enhancement. However, the strong absorption performance of the terminated periodic PC is restricted to a narrow part of the SiC Reststrahlen

absorber structure be. Where the compromise of such trade-off should be met, depends on the particulars of the practical device and application. Here, our aim is to explore the possibility of such trade-off, with a more compact aperiodic structure of five building blocks. Indeed we found a quite high average absorption above 34% that corresponds to cumulative enhancement of 8.13 as defined in Eq. 6.22, throughout the phonon-polaritonic gap of SiC.

[17] These results refer to the results of Chapters 3 and 5 in this thesis.

band. On the other hand, the cumulative absorption enhancement is more evenly distributed across the Reststrahlen band for the aperiodic PC design. We outline the absorption performance comparison between these three designs in Table 6.2. This underlines the strong potential of the aperiodic PC structures for high performing broadband absorbers.

6.10 Conclusions

We proposed an aperiodic absorbing PC route to engineering broadband EM absorption. Our results suggest that this approach is promising even when the PC constituent building blocks have a high extinction coefficient and high reflectance, as the case of the SiC paradigm explored here. In particular, we demonstrated a broadband near-perfect absorption with two types of SiC 1D-aperiodic PCs, one in which the thickness of the SiC layer increases linearly, and one in which the filling ratio increases linearly throughout the structure. Our results suggest that the broadband near-perfect absorption merit is tolerant under angular illumination within a span of at least 20^0. We found that the first aperiodic PC scheme has better performance in terms of smooth absorption profile and high cumulative absorption enhancement with less SiC material. On the other hand the second aperiodic PC scheme has better performance in terms of structural size and is promising for broadband superabsorption with designs of the order of the impinging wave's wavelength

Our analysis indicates that the key structural features leading to the broadband near-perfect absorption functionality are the properties of the entry unit cell and the adiabaticity of the lamellar sequence. Moreover we found, that the particular arrangement of these building blocks in increasing order of SiC thickness is crucial in obtaining the near-perfect broadband absorption. We believe that our aperiodic PC broadband superabsorber paradigm with non-metallic constituents will inspire the design of EM absorbers that can have applications in devices such as bolometers and thermophotovoltaics.

6.11 Acknowledgements

Financial support for the Ph.D. studentship of G. C. R. Devarapu by the College of Engineering, Mathematics and Physical Sciences (CEMPS) University of Exeter is acknowledged.

Bibliography

[1] P. Yeh, *Optical waves in layered media* (Wiley-Interscience, 2005).

[2] P. Yeh, A. Yariv, and C. S. Hong, "Electromagnetic propagation in periodic stratified media. I. General theory," J. Opt. Soc. Am. **67**, 423-438 (1977).

[3] A. Yariv and P. Yeh, "Electromagnetic propagation in periodic stratified media. II. Birefringence, phase matching," and x-ray lasers, J. Opt. Soc. Am. **67**, 438-447 (1977).

[4] H. A. Atwater and A. Polman, "Plasmonics for improved photovoltaic devices," Nat. Mat. **9**, 205-213 (2010).

[5] R. A. Pala, J. White, E. Barnard, J. Liu, and M. L. Brongersma, "Design of Plasmonic Thin-Film Solar Cells with Broadband Absorption Enhancements," Adv. Mater. **21**, 3504-3509 (2009).

[6] E. Rephaeli, and S. Fan, "Absorber and emitter for solar thermo-photovoltaic systems to achieve efficiency exceeding the Shockley-Queisser limit," Opt. Express **17** 15145-15159 (2009).

[7] X. J. Wang, J. D. Flicker, B. J. Lee, W. J. Ready and Z. M. Zhang, "Visible and near-infrared radiative properties of vertically aligned multi-walled carbon nanotubes," Nanotechnology **20**, 215704 (2009).

[8] Y. Guo and Z. Jacob, "Thermal hyperbolic metamaterials," Opt. Express **21**, 15014-15019 (2013).

[9] X. L. Liu, L. P. Wang and Z. M. Zhang, J. Heat, "Wideband Tunable Omnidirectional Infrared Absorbers Based on Doped-Silicon Nanowire Arrays," Trans. **135**, 061602, (2013).

[10] J. G. Fleming, S. Y. Lin, I. El-Kady, R. Biswas and K. M. Ho, "All-metallic three-dimensional photonic crystals with a large infrared bandgap," Nature **417**, 52-55 (2002).

[11] T. Maier and H. Brueckl, "Multispectral microbolometers for the midinfrared," Opt. Lett. **35**, 3766-3768 (2010).

[12] E. L. Dereniak and D. G. Crowe, *Optical Radiation Detectors* (John Wiley and Sons, Inc., New York, 2008).

[13] *Handbook of Optics Volume I: Fundamentals, Techniques, and Design*, 2nd ed., edited by M. Bass, E. W. Van Stryland, D. R. Williams, and W. L. Wolfe (McGraw-Hill, New York, 1995).

[14] A. V. Barve, S. J. Lee, S. K. Noh, and S. Krishna, "Review of current progress in quantum dot infrared photodetectors," Laser and Photonics Reviews **4**, 738-750 (2010).

[15] S. J. Lee, Z. Y. Ku, A. Barve, J. Montoya, W. Y. Jang, S. R. J. Brueck, M. Sundaram, A. Reisinger, S. Krishna and S. K. Noh, "A monolithically integrated plasmonic infrared quantum dot camera," Nat. Commun. **2**, 286 (2011).

[16] C. J. Hill, A. Soibel, S. A. Keo, J. M. Mumolo, D. Z. Ting, and S. D. Gunapala, "Demonstration of large format mid-wavelength infrared focal plane arrays based on superlattice and BIRD detector structures," Infrared. Phys. Tech. **52**, 348-352 (2009).

[17] J. A. Mason, S. Smith, and D. Wasserman, "Strong absorption and selective thermal emission from a midinfrared metamaterial," Appl. Phys. Lett. **98**, 241105-3 (2011).

[18] J. A. Mason, G. Allen, V. A. Podolskiy, and D. Wasserman, "Strong coupling of molecular and mid-infrared perfect absorber resonances," IEEE Phot. Tech. Lett. **24**, 31-33 (2012).

[19] N. I. Landy, S. Sajuyigbe , J. J. Mock, D. R. Smith and W. J. Padilla, "Perfect Metamaterial Absorber," Phys. Rev. Lett. 207402 **100**, (2008).

[20] C. Wu and G. Shvets, "Design of metamaterial surfaces with broadband absorbance," Opt. Lett. **37**, 308-310 (2012).

[21] X. Liu, T. Starr, A. F. Starr and W. J. Padilla, "Infrared spatial and frequency selective metamaterial with near-unity absorbance," Phys. Rev. Lett. **104**, 207403 (2010).

[22] Y. Avitzour, Y. A. Urzhumov and G. Shvets, "Wide-angle infrared absorber based on a negative-index plasmonic metamaterial," Phys. Rev. B **79**, 045131 (2008).

[23] G. Veronis, R. W. Dutton, and S. Fan, "Metallic photonic crystals with strong broadband absorption at optical frequencies over wide angular range," J. Appl. Phys. **97**, 093104 (2005).

[24] C. Lin and M. L. Povinelli, "Optical absorption enhancement in silicon nanowire arrays with a large lattice constant for photovoltaic applications," Opt. Express **17**, 19371 (2009).

[25] Y. Park, E. Drouard, O. El-Daif, X. Letartre, P. Viktorovitch, A. Fave, A. Kaminski, M. Lemiti, and C. Seassal, "Absorption enhancement using photonic crystals for silicon thin film solar cells," Opt. Express **17**, 14312 (2009).

[26] S. Y. Lin, J. G. Fleming, Z. Y. Li, I. El-Kady, R. Biswas, and K. M. Ho, "Origin of absorption enhancement in a tungsten, three-dimensional photonic crystal," J. Opt. Soc. Am. B. **20**, 1538–1541 (2003).

[27] G. C. R. Devarapu and S. Foteinopoulou, "Mid-IR near-perfect absorption with a SiC photonic crystal with angle-controlled polarization selectivity," Opt. Express **20**, 13040-13054 (2012).

[28] G. C. R. Devarapu and S. Foteinopoulou, "Compact photonic-crystal superabsorbers from strongly absorbing media," J. Appl. Phys. **114**, 033504 (2013).

[29] C. Kittel, *Introduction to Solid State Physics* (John Wiley and Sons, 2005).

[30] C. Engström, C. Hafner, and K. Schmidt, "Computations of lossy bloch waves in two-dimensional photonic crystals," J. Comput. Theor. Nanosci. **6**, 1-9 (2009).

[31] A. Katzir, A. C. Livanos, J. B. Shellan, and A. Yariv, "Chirped gratings in integrated optics," IEEE J. Quan. Ele. **13**, 296-304 (1977).

[32] A. Mouldi and M. Kanzari, Optik, "Design of an omnidirectional mirror using one dimensional photonic crystal with graded geometric layers thicknesses," Intl. J. Light and Elctr Opt. **123**, 125-131 (2012).

[33] A. Mouldi and M. Kanzari, "Broad multilayer antireflection coating by apodized and chirped photonic crystal," Opt. Commun. **284**, 4124-4128 (2011).

[34] P. B. Catrysse and S. Fan, "Near-complete transmission through subwavelength hole arrays in phonon-polaritonic thin films," Phys. Rev. B **75**, 075422-5 (2007).

[35] R. W. Waynant, I. K. Ilev and I. Gannot, "Mid-infrared laser applications in medicine and biology," Phil. Trans. R. Soc. Lond. A. **359**, 635-644 (2001).

[36] B. Mizaikoff, "Waveguide-enhanced mid-infrared chem/bio sensors," Chem. Soc. Rev. **42**, 8683-8699 (2013).

[37] J. M. Bakker, L. M. Aleese, G. Meijer, and G. von Helden, "Fingerprint IR spectroscopy to probe amino acid conformations in the gas phase," Phys. Rev. Lett. **91**, 203003 (2003).

[38] R. Assendorp, P. R. Wesselius, D. C. B. Whittet, and T. Prusti, " A study of the Chamaeleon I Dark Cloud and T-association - II: High resolution IRAS maps around HD97048 and HD97300," Astro. Soc. **247**, 624-631 (1990).

[39] H. L. Johnson and W. W. Morgan, "Fundamental stellar photometry for standards of spectral type on the revised system of the Yerkes spectral atlas," Astrophysical Journal **117**, 313-352 (1953).

[40] H. U. Kaüfl, "Ground-based astronomy in the 10 and 20 μm atmospheric windows at ESO - scientific potential at present and in the future," The Messenger, **73**, 8-12 (1993).

[41] S. Foteinopoulou and C. M. Soukoulis, "Electromagnetic wave propagation in two-dimensional photonic crystals: A study of anomalous refractive effects," Phys. Rev. B **72**, 165112 (2005).

[42] J. D. Joannopoulos, S. G. Johnson, J. N. Winn and R. D. Meade, *Photonic crystals: Molding the flow of light*, (Princeton University Press, 2008).

[43] P. Markos and C. M. Soukoulis, *Wave Propagation: From Electrons to Photonic Crystals and Left-Handed Materials*, (Princeton University Press 2008).

[44] S. Foteinopoulou, M. Kafesaki, E. N. Economou and C. M. Soukoulis, "Two-dimensional polaritonic photonic crystals as terahertz uniaxial metamaterials," Phys. Rev. B **84**, 035128 (2011).

[45] S. Foteinopoulou, "Photonic crystals as metamaterials," Physica B **407**, 4056 (2012).

[46] J. D. Jackson, *Classical Electrodynamics*, 3rd edition.

[47] D. E. Knuth, *The art of computer programming vol. 2*, (Addison–Wesley, Third edition, 1998).

7

Subwavelength broadband near-perfect SiC pyramid absorber

7.1 Chapter Overview

In Chapter 6, we demonstrated broadband absorption with an aperiodic 1D-PC. This approach allowed us to increase the absorptance bandwidth to encompass most of the Reststrahlen band of SiC. However, we required very thick PC structures to achieve such broad absorption bandwidth. For example, we showed that a two wavelength thick aperiodic PC can yield cumulative enhancement of $\sim$ 10 [1]. In this Chapter, we propose a SiC near-perfect absorber design that is of subwavelength thickness and has a large bandwidth in the Reststrahlen band of SiC. We aim to achieve cumulative enhancement factor of at least 5, across the entire Reststrahlen band spectrum. To achieve that we would require a higher-order dimensional patterning in the absorber design in order to enable EM control beyond what the multilayer structures can offer. We present in the following our investigations in this direction.

Before proceeding to our results and analysis we briefly recap the methods employed in this chapter. Results in this Chapter have been calculated by setting up the micropyramid structure, as we detailed in the methodology section of this chapter, in a commercial Finite-Difference Time-Domain (FDTD) solver, in particular the

Lumerical EM simulator [2]. Details of the underlying physical principles of such solver have been presented in section 2.6 of Chapter 2.

7.2 System under study: Design conception and specifics

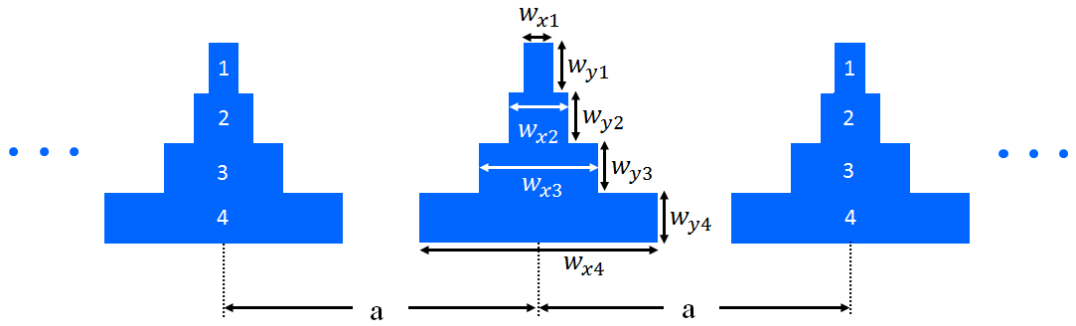

Figure 7.1: (a) Schematic diagram of the grating structure consisting of periodically spaced SiC pyramid absorbing units with all the structural parameters of the pyramid and the grating indicated. Each SiC layer and its structural parameters are indicated with a specific number.

Through our 1D-broadband absorber design discussed in Chapter 6, we understand that absorbing building blocks of different thicknesses effectively absorb the light of different wavelengths. This is what enabled us to extend the absorption bandwidth with aperiodic PCs [1]. Moreover, in Chapter 3, we have seen that a high absorption enhancement is achieved with low filling ratio PCs, as high filling ratio PCs approach the bulk SiC behaviour [3]. Relying on these insights, we conceive a grating absorber design that consists of pyramid shaped SiC building blocks. It has been known that periodic structures with subwavelength pyramid building blocks have low reflectance. In nature, nocturnal Moth insects have pyramid shaped subwavelength structures in their corneas, which suppress reflection of visible light in the night, that enable them to see well while being invisible to their predators [4–8]. This is because, the pyramid shape provides smoothly varying refractive index gradient between the air and the cornea, thus acting as an index-matching anti-reflex [4–8].

Inspired from this pyramid shape, many microstructures are proposed for light harvesting applications both in the role of anti-reflecting structures [6, 8–10] and as direct light absorbers [11–13]. However, mostly these pyramid absorption structures

are explored in the visible regime [6, 8, 10–12] with a few works considering pyramid type of structures in the Mid-IR regime [9, 13]. However, the work in Ref. [9] employs a pyramid structure from non-absorbing material to funnel light into the absorbing material enclosed or below the pyramid. In Ref. [13] the authors use two types of materials one being metal, and the absorptance region is away from the 10 micron regime of interest for biosensing applications. Here, we investigate a SiC-based pyramid design for the Mid-IR regime, made only from the absorbing material. The structure absorbs in a one-step process, acting simultaneously as an impedance-matcher and absorber.

In particular, we consider SiC pyramid building blocks as schematically shown in Fig. 7.1. This micropyramid design is envisaged to mimic the conical shape of the moth-eye structure known for its anti-reflective merits [11]. Moreover, we have particularly chosen the stepped version of the moth-eye structure taking into consideration its easier experimental realisation with certain techniques, such as direct wafer-bonding [14]. At the same time, each block of the micropyramid would behave as a microantenna with emission/absorption spectra in the Mid-IR regime [15]. Combining all the microantenna blocks in a moth-eye type of arrangement would yield enhanced EM in-coupling properties to each SiC block microantenna. This is expected to result in a broadband response. In other words, the design is envisioned to operate simultaneously as a moth-eye antireflector and a broadband micro-antenna.

Now the particular sizes of the blocks are chosen so that to maintain a gradual size variation from one block to the next block and to have a total structural thickness less than $\lambda_m/2$, with $\lambda_m = 11.45\,\mu\text{m}$ being the mid-wavelength of the Reststrahlen band of SiC. At the same time, it is also advantageous from the fabrication point of view to have only a few layers in the structure. Here we have chosen a first exploratory design with a total of four blocks with structural parameters that satisfy the aforementioned criteria. The schematics of such design are shown in Fig. 7.1 with the four SiC layers in the pyramid labelled as 1, 2, 3 and 4. The structural parameters of this design, as designated in the schematics are chosen to be: $w_{x1} = 0.5\,\mu\text{m}$, $w_{y1} = 1\,\mu\text{m}$; $w_{x2} = 1\,\mu\text{m}$, $w_{y2} = 1\,\mu\text{m}$; $w_{x3} = 2\,\mu\text{m}$, $w_{y3} = 1\,\mu\text{m}$; $w_{x4} = 4\,\mu\text{m}$, $w_{y4} = 1\,\mu\text{m}$. We also express them below in terms of the mid-wavelength of the Restrahlen band, λ_m: $w_{x1} = 0.044\,\lambda_m$, $w_{y1} = 0.087\,\lambda_m$; $w_{x2} = 0.087\,\lambda_m$, $w_{y2} = 0.087\,\lambda_m$; $w_{x3} = 0.175\,\lambda_m$, $w_{y3} = 0.087\,\lambda_m$; $w_{x4} = 0.349\,\lambda_m$, $w_{y4} = 0.087\,\lambda_m$. These micropyramids are separated periodically with a lattice constant of 10 μm in the x-direction and extend infinitely in the y-direction to form the structure as shown inFig. 7.1. Of course, a substrate

would be required. However to understand the response of the structure better, we initially do not consider a substrate, but will consider the effect of the substrate later.

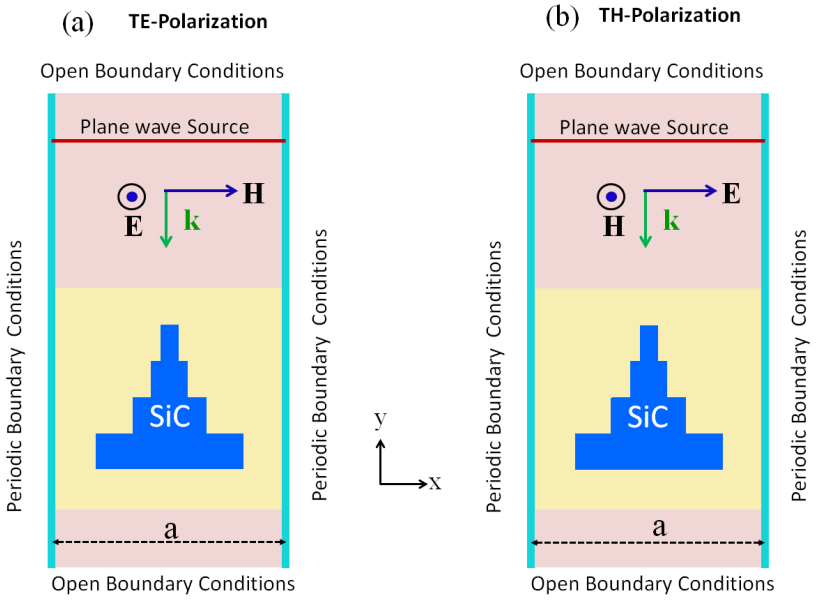

Figure 7.2: Schematic diagram of the set-up for the simulation in the FDTD simulator. The yellow shaded region represents the user-defined mesh region. The brown region represents the default-mesh region in the Lumerical simulator [2]. We designate the lattice constant of the micropyramid grating structure, with a.

7.3 Methodology

To study the absorption potential of the grating absorber, we evaluate the absorptance A, Reflectance R and Transmittance T of these structures. Moreover, to gain more insight into the performance of the absorber, we would require the electric field distribution profiles across the absorber structure. For this purpose, a commercial-grade simulator based on the finite-difference time-domain (FDTD) method was used [2]. We described the method and its implementation in the simulator in Chapter 2. In Fig. 7.2 we show our simulation set-up. By applying periodic boundary conditions in the x-direction, we simulate the infinitely extending structure in this direction, that repeats itself periodically. On the other hand, we apply open boundary conditions in the y-direction. The permittivity of SiC is represented in the simulator with the following Lorentzian function [16]:

$$\varepsilon = \varepsilon_\infty \left(1 + \frac{\omega_L^2 - \omega_T^2}{\omega_T^2 - \omega^2 - i\omega\Gamma}\right), \tag{7.1}$$

with the parameter values being: ε_∞=6.7, ω_T =2$\pi\times$23.79 THz, ω_L =2$\pi\times$29.07 THz and Γ =2$\pi\times$0.1428. The latter were taken from Ref. [17].

Moreover, we used a user-defined mesh with a size as small as 10 nm in both $x-$ and $y-$directions around the pyramid structure. This mesh size is about $\lambda_{\text{free}}/1000$, where λ_{free} is the free-space wavelength. This is because the required mesh size for convergent calculations in FDTD must be much smaller than the wavelength of light inside the material. Given that the refractive index of SiC can be as large as the 20, the wavelength inside SiC can be 20 times smaller than in vacuum. Therefore, we require and considered such a small mesh size for simulating the SiC pyramid structure in FDTD [18]. Furthermore, the mesh size of 10 nm, gives an integer number of grids in all layers of the SiC pyramid, that ensures the accurate representation of the pyramid structure in the simulator. We indicate this user-defined mesh in Fig. 7.2 with the yellow shaded region. The SiC pyramid is surrounded by vacuum. So further away from the pyramid structure, we used Lumerical's default mesh which produces a varying grid size, increasing as we move further away from the pyramid. This mesh has a size of the order of $\lambda_{\text{free}}/30$ [2], which is adequate for vacuum. We represent this mesh in Fig. 7.2 with the brown shaded region. By using this FDTD set-up, we evaluate the performance of the SiC pyramid grating structures. In the following, we present and discuss our results.

7.4 Results and discussion

For this purpose, we will calculate the absorption, A, and reflection, R, of the micropyramid grating with a lattice constant of 10 µm under TE- and TH-polarization illumination conditions. The two different polarizations are schematically shown in Fig. 7.2(a) and Fig. 7.2(b) respectively. We plot the results in Fig. 7.3. The red and blue lines in Fig. 7.3(a) represent the absorption of the respective TE- and TH-polarization cases. It is remarkable to see more than 60% of absorption between 10.3 µm and 11.2 µm for the TH-polarization case. This yields a cumulative absorption enhancement, CA_{enha}, of 3.971, as evaluated from:

$$\text{CA}_{\text{enha}} = \frac{1}{\lambda_2 - \lambda_1} \int_{\lambda_1}^{\lambda_2} \frac{\text{A}_{\text{pyr}}(\lambda)}{\text{A}_{\text{SiC}}(\lambda)} d\lambda, \tag{7.2}$$

where λ_1 and λ_2 represent the bounds of the Reststrahlen band of SiC, and $\text{A}_{\text{pyr}}(\lambda)$ and $\text{A}_{\text{SiC}}(\lambda)$ are the respective absorptances for the micropyramid structure and a 200-µm-thick-block of SiC at the specified wavelength. We show the corresponding reflectance results of the pyramid absorber in Fig. 7.3(b). We notice the low

reflectance for the TH-polarization case in the wavelength regime corresponding to the high absorption in Fig. 7.3(a). However, we see also a low reflectance for the TE-polarization case throughout the SiC Reststrahlen band.

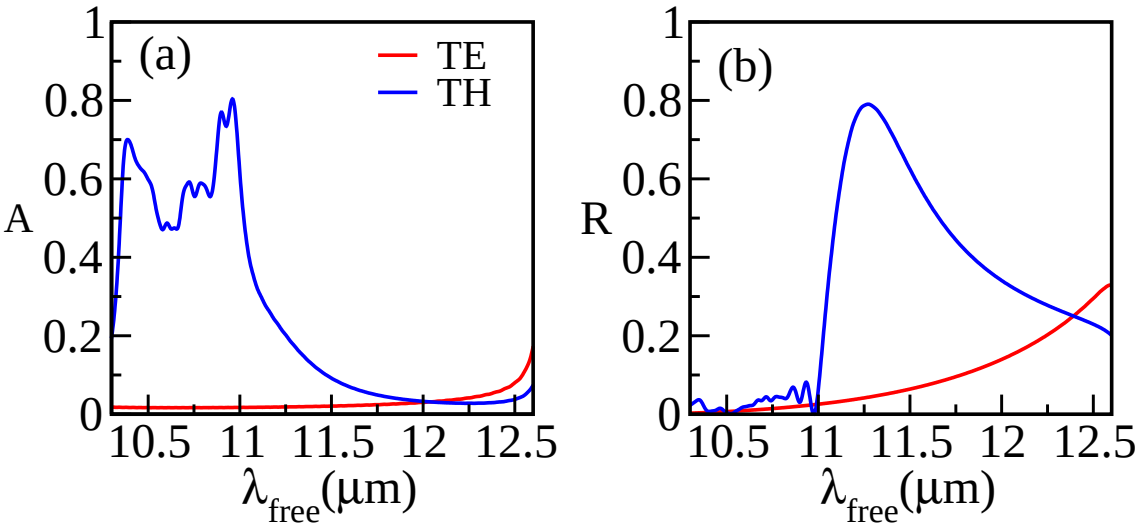

Figure 7.3: Spectral response of the absorptance, A, of the pyramid structure of Fig. 7.1 for the TE- and TH-polarizations are represented with the red and blue lines respectively. (b) same as (a) but for reflectance, R.

This is because in the case of TH-polarization, the phonon-polaritons of SiC are driven by the strong electric fields in the x-direction. That results in coupling of the electric fields between the yz-plane faces in each SiC building block. As a result, more electric field will be pushed inside the SiC building blocks, thus resulting in high absorption. On the contrary, electric fields are zero for the TE-polarization in the x-direction. The length in the y-direction where the electric field is oriented is infinity, meaning that such coupled face-to-face modes cannot exist. Therefore, we see much less absorption for the TE-polarization, as the fields interact very little with the SiC material. Therefore, from now on we focus only on the TH-polarization case.

In order to understand the high absorptance in the TH-polarization case, we evaluate the electric field distributions of the pyramid absorber, $|E(x,y)|^2 = |E_x(x,y)|^2 + |E_y(x,y)|^2$ at three different free-space wavelengths, λ_{free}, within the Reststrahlen band of SiC: $\lambda_{\text{free}} = 10.5\,\mu\text{m}$, $\lambda_{\text{free}} = 11.2\,\mu\text{m}$ and $\lambda_{\text{free}} = 12\,\mu\text{m}$, respectively. We show the respective spatial electric field distributions at these three wavelengths in Fig. 7.4(a), (b) and (c). In addition, in order to be able to clearly see the distribution of these electric-fields, we also plot them in logarithmic scale. We show these logarithmic-scale electric-field plots in Fig. 7.4(d), Fig. 7.4(e) and Fig. 7.4(f) for the same three wavelengths we considered before. We

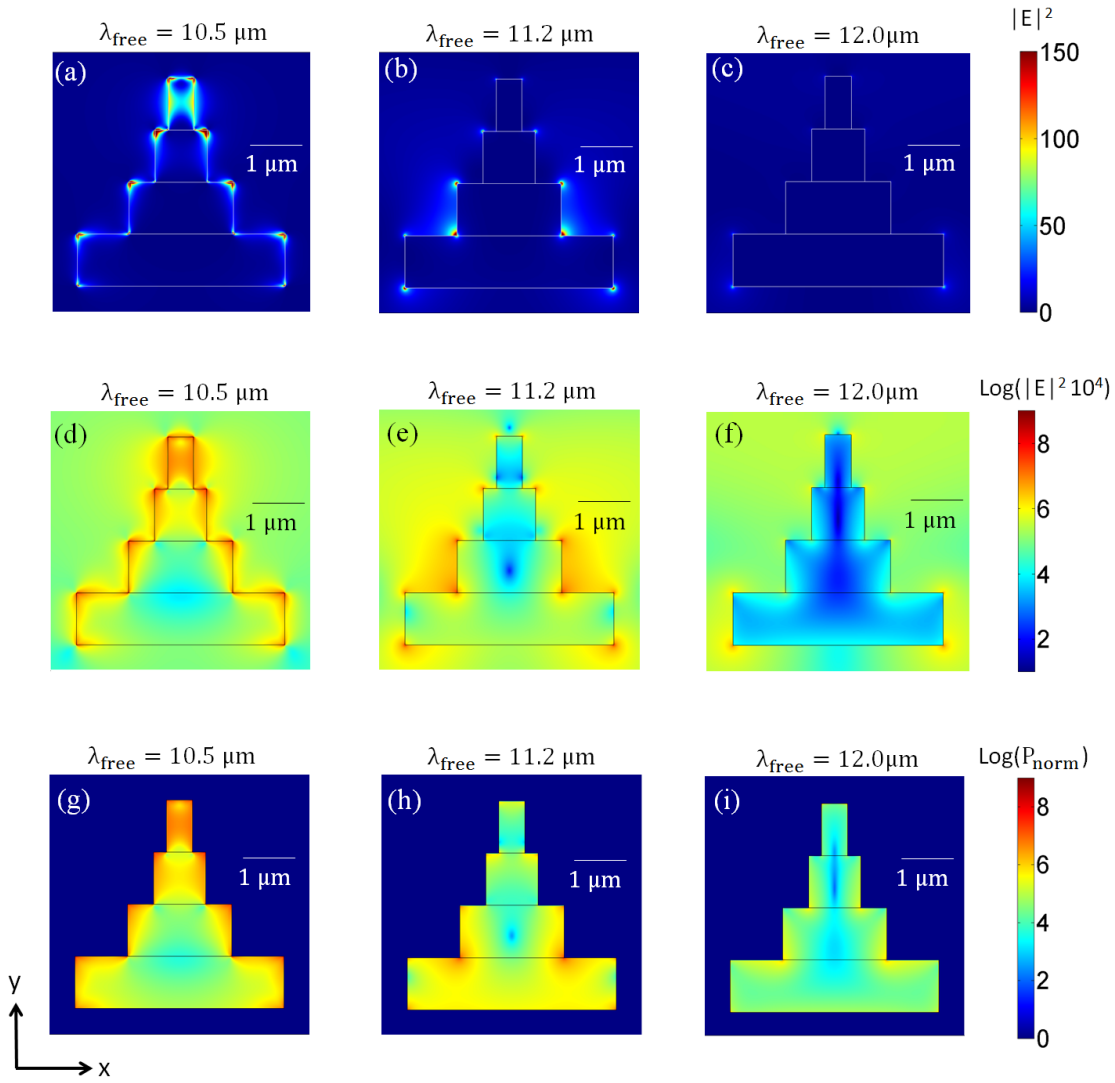

Figure 7.4: (a), (b) and (c) Spatial electric-field distributions of the pyramid structure at three free-space wavelengths λ_{free} as indicated in the respective panels. (d), (e) and (f) same as (a), (b) and (c) respectively, but are plotted in logarithmic scale, after multiplying the electric-fields by a factor of 10^4. (g), (h), (i) Normalised power dissipation ratio from Eq. 7.3 at the three wavelengths.

can identify from Fig. 7.4 that the electric fields of the three different wavelengths are concentrated at different parts of the the SiC absorbing pyramid building block.

For the impinging wavelength of 10.5 µm, there is a high electric fields intensity in all four SiC layers of the pyramid. Consequently we observe a high absorption at this wavelength. For the wavelength of 11.2 µm, there is a high concentration of fields only in the last two layers of the pyramid, thus we observe moderate absorption at this wavelength. Finally, for the wavelength of 12.0 µm, there is an overall low electric field intensity.

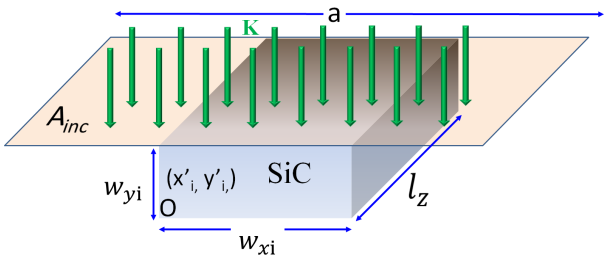

Figure 7.5: Schematic diagram to illustrate the power absorption within the i^{th} SiC layer in the pyramid building block. The geometrical parameters of the SiC layer are indicated. The incident surface area, $A_{inc} = l_z \cdot \mathrm{a}$ and the lattice constant, a of the pyramid grating structure are indicated. We also designate the shifted coordinate system, (x'_i, y'_i), and its origin, O, that we used to compute the power dissipation numerically.

To understand further how these electric-field distributions correlate to the absorption, we evaluate the ratio of dissipated to incident power at each mesh point location of the SiC pyramid structure. From Poynting's theorem [19] it can be shown (see Eq. 2.52 in Chapter 2) that such dissipated power per unit volume at a point (x, y) inside the pyramid, normalised by the incident power per surface area is given by:

$$\mathrm{P}_{\mathrm{norm}}(x, y) = \frac{\varepsilon_r'' \omega}{c} |E_{enha}(x, y)|^2, \tag{7.3}$$

where ε_r'' represents the imaginary part of the relative permittivity and c represents the speed of light in vacuum. We plot the spatial maps of such normalised power dissipation per volume from Eq. 7.3 in Fig. 7.4(g), Fig. 7.4(h) and Fig. 7.4(i) for impinging wavelengths of 10.5 µm, 11.2 µm and 12 µm respectively. Note, these results are plotted in logarithmic scale for clarity. For a wavelength of 10.5 µm, we observe a high power loss in each layer of the SiC pyramid. For a wavelength of 11.2 µm, we see a high power loss in the last two layers of the SiC pyramid. For a wavelength of 12.0 µm, we notice a significant power loss only in the bottom layer of the pyramid.

λ_{free} = 10.5 µm		λ_{free} = 11.2 µm		λ_{free} = 12.0 µm	
Absorption from transmission calculations	Absorption from power dissipation calculations	Absorption from Transmission calculations	Absorption from power dissipation calculations	Absorption from transmission calculations	Absorption from power dissipation calculations
0.5983	A(1)=0.1670 A(2)=0.1282 A(3)=0.0977 A(4)=0.1460 $\sum_{i=1}^{4} A(i) = 0.5388$	0.2342	A(1)=0.0021 A(2)=0.0068 A(3)=0.0573 A(4)=0.1684 $\sum_{i=1}^{4} A(i) = 0.2346$	0.0327	A(1)= 0.0011 A(2)=0.0033 A(3)=0.0084 A(4)=0.0241 $\sum_{i=1}^{4} A(i) = 0.0369$

Table 7.1: Absorption in each layer of the SiC pyramid, evaluated from Eq. 7.4. Here A(1), A(2), A(3) and A(4) represents the absorption in the first, second, third and fourth SiC layer in the pyramid and $\sum_{i=1}^{4} A(i)$ indicates the cumulative absorption from all four SiC layers together. We also represent the corresponding absorption results evaluated from the transmission calculations for comparison.

To quantify these observations, we also evaluate the absorption in each layer of the SiC micropyramid from the normalised power dissipation per volume in that layer. The absorption in i^{th} layer, A(i) is given by:

$$A(i) = \frac{1}{a} \int_0^{w_{xi}} \int_0^{w_{yi}} P_{norm}(x_i', y_i') \; dx_i' dy_i', \tag{7.4}$$

where (x_i', y_i') is a shifted coordinate system such that, the first grid point is always at the bottom left corner of the i^{th} SiC layer in the pyramid with i varying from 1 to 4. The derivation of the formula in Eq. 7.4 is given in Appendix B. The derivation relies on considering the incident power through an area, A_{inc}, designated in the schematics of Fig. 7.5, and the total power dissipated through the volume V enclosed by the SiC log below the specified area, as seen in schematics of Fig. 7.5. The integral in Eq. 7.4 is evaluated numerically by considering the summation of the quantity in the integral on all grid points within the specified SiC slab. The results for the absorption from Eq. 7.4 at the three wavelengths in each layer of the SiC pyramid are shown in the Table. 7.1. We compare the total absorption resulting from all the four layers together and with the corresponding absorption evaluated from the transmission calculations. We notice a very good agreement between the two results [20].

To understand the absorption bandwidth of the pyramid absorber, we evaluate the absorption capabilities of each of the constituent layers in the SiC pyramid, when by itself. For this purpose, we show the spectral response of the absorption of

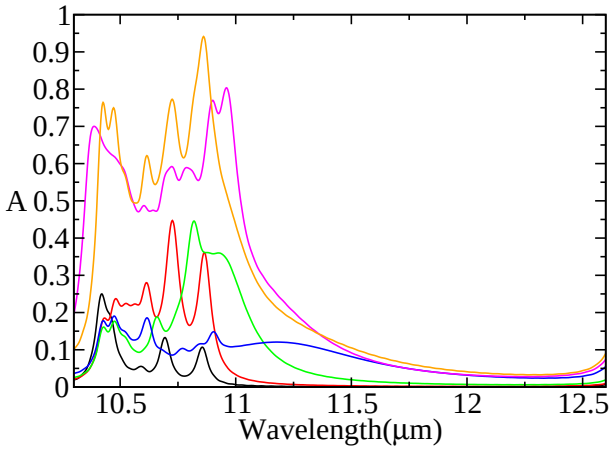

Figure 7.6: Absorptance versus free-space wavelength λ_{free} of the different layers in the SiC pyramid. The black, red, green and blue lines represent the results for the respective first, second, third and fourth SiC layers of the SiC pyramid, when on their own. The orange line indicates the value when the individual absorption of the all four layers is added together. For comparison, the absorptance of the micropyramid structure is shown with the magenta line.

these individual layers, repeated along x-direction with a periodicity a, forming a grating type of structure, in Fig. 7.6. We represent the absorption of these gratings consisting of the first, second, third and fourth SiC layers with black, red, green and blue lines respectively. We indicate in Fig. 7.6 the added absorption of the all the four individual gratings with the orange line. In addition, we also show for comparison the absorption of the corresponding SiC pyramid design with the magenta line. It is evident that the cumulative absorption of the four individual gratings is close to the absorption of the pyramid absorber. This observation suggests that we can understand the absorption bandwidth of the pyramid building block by analysing the optical response of its constituting building block layers.

A more thorough comparison of the absorption between the isolated layers and the micropyramid at each wavelength of 10.5 μm, 11.2 μm and 12.0 μm are shown in Table. 7.2. Note, also that the data of Table. 7.2 suggest that there is a vertical interference between each layer, when they are put together into a pyramid, that they affect the strength of the coupling to the individual layers, with some becoming stronger and some becoming weaker. This can be seen by looking at the electric field distribution at each individual layer and when that layers are part of the pyramid, that we show in Fig. 7.7.

To understand the behaviour of the pyramid absorber further, we show the spectral response of the transmittance, T, of the four underlying grating structures in Fig. 7.8(a). The black, red, green and blue lines represent the respective

	λ_{free} = 10.5 µm		λ_{free} = 11.2 µm		λ_{free} = 12.0 µm	
Absorption Ratio	Isolated	Pyramid	Isolated	Pyramid	Isolated	Pyramid
$A(1)/\sum_{i=1}^{4} A(i)$	0.1407	0.3099	0.0103	0.0090	0.0092	0.0298
$A(2)/\sum_{i=1}^{4} A(i)$	0.3586	0.2379	0.04220	0.0290	0.03983	0.0894
$A(3)/\sum_{i=1}^{4} A(i)$	0.2409	0.1813	0.3510	0.2442	0.1688	0.2276
$A(4)/\sum_{i=1}^{4} A(i)$	0.2598	0.2710	0.5965	0.7178	0.7821	0.6531

Table 7.2: (a) Ratio of absorption in each SiC layer of the pyramid to the cumulative absorption of all four layers together. These absorptions are obtained from transmission calculations. Here A(1), A(2), A(3) and A(4) and $\sum_{i=1}^{4} A(i)$ have same meaning as in Table. 7.1. We also represent the corresponding absorption ratio results evaluated from power dissipation calculations with Eq. 7.4.

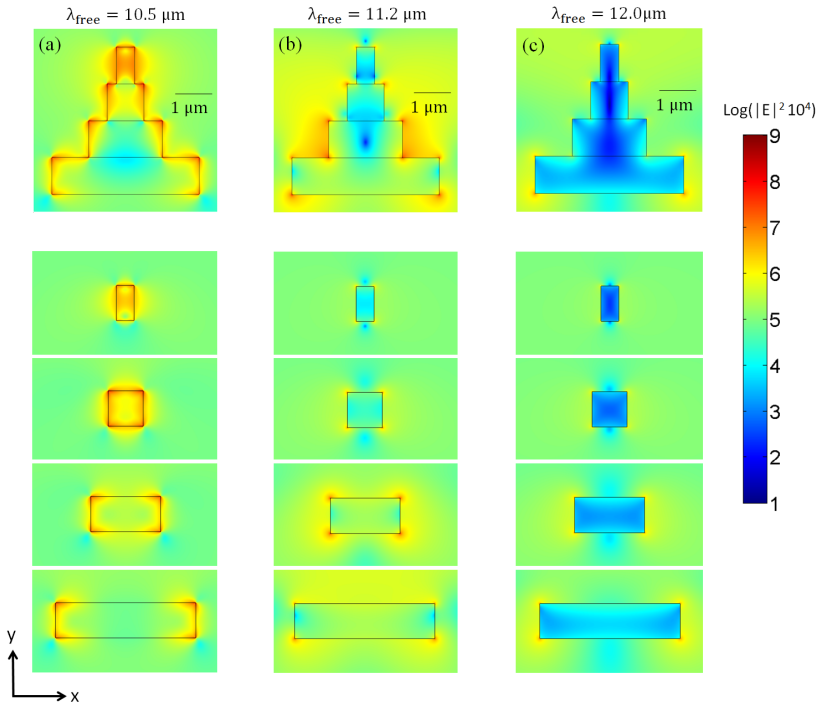

Figure 7.7: (a), (b) and (c) Spatial electric-field distributions of the pyramid absorber at three free-space wavelengths λ_{free} as indicated in the respective panels. The electric-field distributions of the isolated SiC layers in the pyramid are presented below the respective panels. Note, all the electric-field are plotted in logarithmic scale.

transmittance of the first, second, third and fourth SiC grating structures in the SiC micropyramid design. We notice that in the wavelength regime beyond 11 µm,

each layer is clearly transparent. However, between the wavelengths of 10 µm and 11 µm, we notice multiple dips of various strengths in the transmission spectrum of these layers. These dips signify localised resonances that result from the interaction of the phonon-polaritons at each SiC face edge of the layer. When these layers are arranged together as a pyramid, then the collective excitation of these localised resonances in each of these layers leads to a reduced transmittance for the pyramid structure in the wavelength regime from 10 µm to 11 µm, which combined with the near zero-reflectance (see Fig. 7.3(b)) gives high absorption.

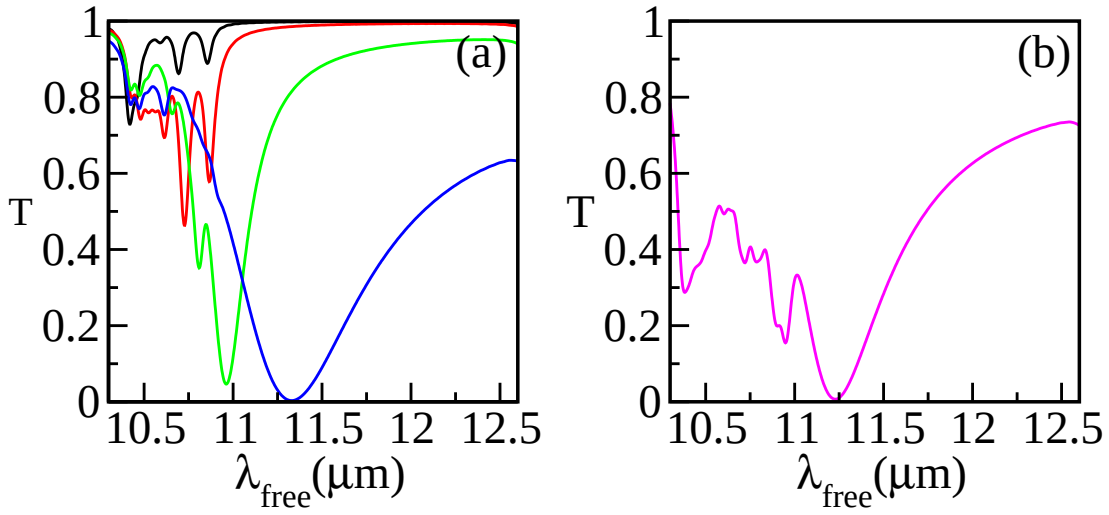

Figure 7.8: (a) Transmittance versus free-space wavelength λ_{free} of the different layers in the SiC pyramid. The black, red, green and blue lines represent the results for the first, second, third and fourth SiC layers in the SiC pyramid respectively. (b) Transmittance of the micropyramid structure versus the free-space wavelength λ_{free}.

Indeed, we show such low transmittance of the pyramid structure in Fig. 7.8(b). In Fig. 7.8(a), we clearly see a spectral regime with structure in the transmission and a spectral regime of relatively smoother high transmission separated by a dip reaching almost zero for layers 3 and 4. The transmission of the entire pyramid shows a similar behaviour as indicated by the magenta line in Fig. 7.8(b). That dip is a characteristic signature of a Fano type of interaction between extended and localised modes [21–23]. The localised modes arise from scattering of light by the SiC layers, while the extended modes arise from the light that is transmitted via the voids between the SiC layers [23]. This Fano type of interference in the same wavelength regime was also observed in perforated SiC layers with subwavelength holes by P. B. Catrysse *et al.* [17]. However, the authors used such structure to achieve transparency and did not focus in the regime where the localised type of resonances dominate to achieve absorptance. On the other hand, our interest lies in the regime where the localised resonances dominate in order to exploit a high

interaction between the SiC material and EM fields that will lead to absorption. We will further analyse this spectral transition from localised resonant behaviour to transparency behaviour below.

To understand better the transition from localised resonances to a broad transparent type of behaviour, we evaluate the x-and y-components of the Poynting vector S_x and S_y respectively at the three wavelengths specified before, for this pyramid structure. We show the results in Fig. 7.9, normalised with the vacuum Poynting vector S_0. In Fig. 7.9(a), (c) and (e) the red and blue regions in the x-component of the Poynting vector S_x, signify the energy propagation of the EM wave in the positive and negative $x-$direction respectively. Conversely, in Fig. 7.9(b), (d) and (f) the red and blue regions in the y-component of the Poynting vector S_y, signify the energy propagation of the EM wave in the positive and negative $y-$direction respectively. The x-and y-components of the Poynting vector plotted across the pyramid structure gives us insight how the energy flows through the pyramid at each wavelength. We can see that at wavelength 10.5 µm in Fig. 7.9(a), and Fig. 7.9(b), the energy flow forms a vortex around each edge of each SiC layer in the pyramid.

To see this vortex energy flow clearly, we focus on the right side of the top SiC layer in the pyramid, where we can see that energy flows towards the right side at the top edge of the layer and towards the left side at the bottom edge of the layer. At the same time, Fig. 7.9(b) suggests that energy flows from top to bottom outside the SiC layer and flows from bottom to top inside the same SiC layer. Now if we look at the combined effect for the energy flow in the $x-$and $y-$directions together, we see clearly a vortex type of energy circulation in each side of the top SiC layer. We can identify the similar vortex energy flow for the other SiC layers of the pyramid at a wavelength of 10.5 µm. This vortex type of energy flow suggests that localised types of cavity modes are excited in each of the layers of the pyramid.

We can see a similar strong vortex type of energy flow only around the third and fourth SiC layers for wavelength of 11.2 µm. This evidence of a resonant behaviour of the different blocks, in combination with the low reflectance of the structure in this frequency region, confirms our initial intuition when envisioning this design regarding its simultaneous operation as a moth-eye type of anti-reflector and a broadband micro-antenna. However, at wavelength 12.0 µm, we see that energy flows around the pyramid edges without forming any vortex, thus completely avoiding interaction with the pyramid. In conclusion, there is a correlation between the formation of vortex type of modes and absorption performance. The stronger these vortex

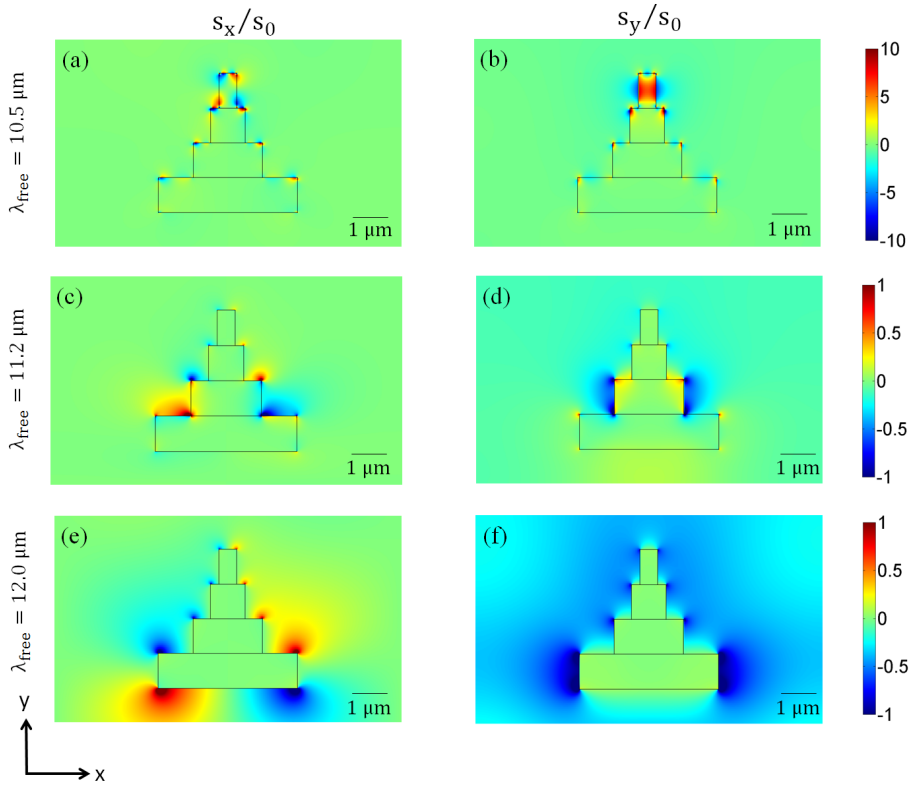

Figure 7.9: (a) and (b) x and y-components of the normalised Poynting vector of the pyramid absorber at a wavelength of 10.5 µm. (c) and (d) same as (a) and (b) respectively but at a the wavelength of 11.2 µm. (e) and (f) same as (a) and (b) respectively but at a wavelength 12.0 µm.

modes in each of the participating layers, the higher the absorption is. When these modes are not excited, the EM wave just avoids the structure, leading to transparency. We assert that this interaction between the localised vortex modes with the extended transparency modes leads to the Fano-interference signature as seen by the transmission dip of Fig. 7.8(b).

7.5 Weakly versus strongly coupled micropyramid modes

So far we achieved absorptance over 60% with the micropyramid grating structure, that we saw was a result of the interaction between the localised vortex modes and SiC. In the following, we will explore whether it is possible to engineer the absorption further without increasing the thickness of the structure. We will therefore investigate whether it is possible to achieve a stronger coupling into this localised vortex type of modes that naturally will result in a larger absorption. One possibility to do so is by changing the lattice constant of the grating structure. To

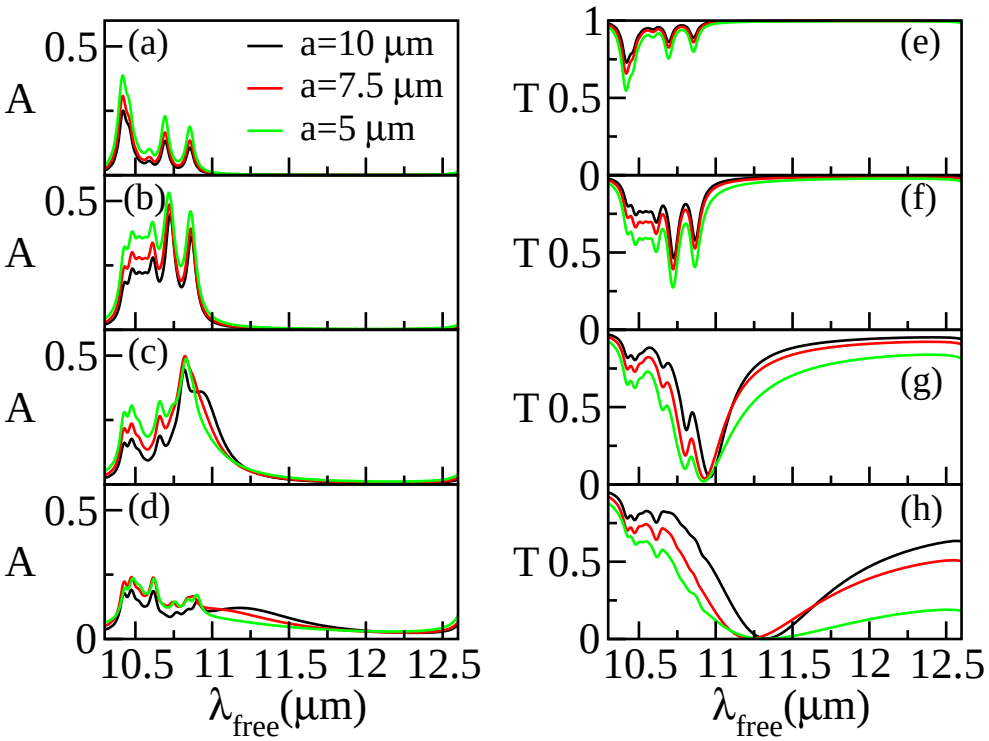

Figure 7.10: (a), (b), (c), (d) Spectral response of absorptance, A of the first, second, third and fourth layers in the SiC pyramid in a grating arrangement. The green, red and black lines indicate the results for the gratings with a lattice constant of 5 μm, 7.5 μm and 10 μm respectively. (e), (f), (g) and (h) same as (a), (b), (c) and (d) but for the transmittance, T.

investigate this, we decompose the pyramid structure into layers and study their individual optical response by varying the lattice constant. For this purpose, we consider three different values for the lattice constant: 5 μm, 7.5 μm and 10 μm. We show in Fig. 7.10 the absorptance, A and transmittance, T of the individual blocks in the SiC pyramid in a grating arrangement for these three lattice constants. The green, red and black lines indicate the results for a lattice constant of 5 μm, 7.5 μm and 10 μm respectively. In Fig. 7.10, we can identify that both the spectral profile of the absorptance and transmittance do not vary a lot with the lattice constant of the grating structure. However, we notice that the strength of the dips in the transmission, or peaks in the absorption increases. This is because, when we decrease the lattice constant, the SiC layers get closer to each other. That results in a stronger coupling of the localised modes of the SiC layers in the lateral direction, that enhances their strength.

We will now check, to see the effect of the stronger coupling of the local resonances in the single layer grating structures, when these are put together to form the micropyramid structure of Fig. 7.1. It is important to achieve that stronger coupling

to the cavity mode, while maintaining the low reflectance property. To check this we evaluate the absorptance and reflectance of the micropyramid grating structure for three different lattice constants, 5 µm, 7.5 µm and 10 µm. We plot the results versus the free-space wavelength λ_{free} in Fig. 7.11. We indicate the case of 5 µm, 7.5 µm and 10 µm grating structures with green, red and black lines respectively. Indeed, we see an increase for the absorptance with decreasing the lattice constant in the same wavelength regime between 10.3 µm to 11.2 µm. It is also evident from Fig. 7.11(b) that the reflectance of the small lattice constant grating structures is almost the same as the 10 µm lattice constant micropyramid grating in this spectral regime. We achieve more than 80% of absorptance with the 5 µm lattice constant structure, which is quite a remarkable enhancement.

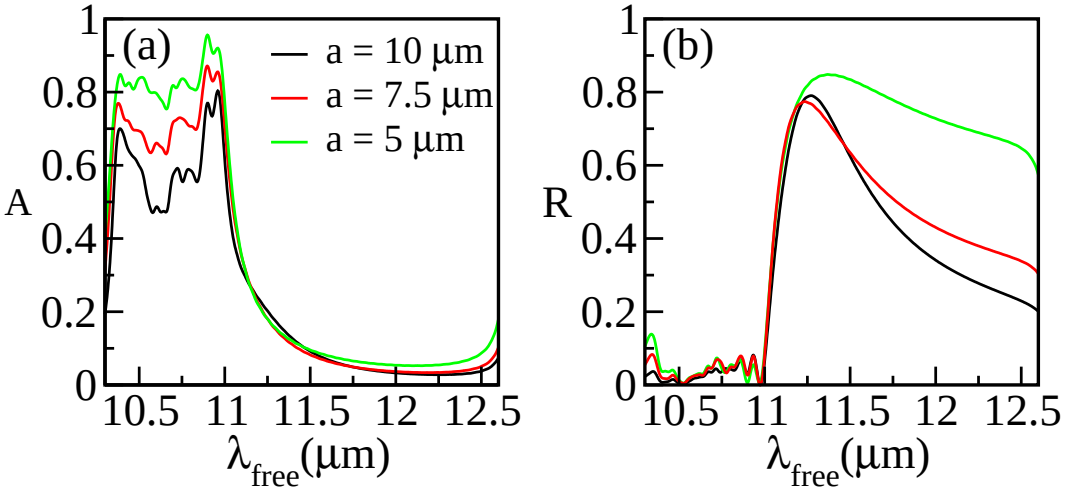

Figure 7.11: (a) Absorptance versus free-space wavelength λ_{free} of the micropyramid grating structure with the three lattice constants. We indicate the results of the 5 µm, 7.5 µm and 10 µm grating structures with green, red and black lines respectively. (b) Same as in (a) but for the reflectance, R.

To obtain a quantitative measure of the performance of these three lattice constant micropyramid gratings, we estimate the cumulative absorptance enhancement CA_{enha}, across the Reststrahlen band using Eq. 7.2. It is also interesting to see which of the three lattice constant gratings exhibits a high cumulative absorptance for the given SiC material. Therefore, we introduce an absorptance figure of merit FOM_{A1}, as follows:

$$FOM_{A1} = CA_{enha}\frac{(\lambda_1 + \lambda_2)^2}{4S}, \tag{7.5}$$

where S is the total area occupied by the SiC material in the micropyramid building block and λ_1, λ_2, and CA_{enha} have the same meaning as in Eq. 7.2. We show both these CA_{enha} and FOM_{A1} results in Table. 7.3. We can identify that the smallest

lattice constant grating structure has both the highest CA_{enha} and FOM_{A1} values, owing to the strong coupling of the localised modes between the neighbouring micropyramids in the grating structure as explained before, that maintains the low reflectance. We argue that the low reflectance comes through the gradual introduction of the SiC material in the pyramid. Therefore, we will study the effect of the order of the participating layers in the micropyramid.

Absorption performance	a = 5 µm	a = 7.5 µm	a = 10 µm
CA	5.12	4.44	3.97
FOM_{A1}	89.5	77.61	69.4

Table 7.3: Comparison of the cumulative enhancement CA_{enha} and the figure of merit FOM_{A1} of the three micropyramid grating structures with three lattice constants.

7.6 Impact of the order of the building blocks

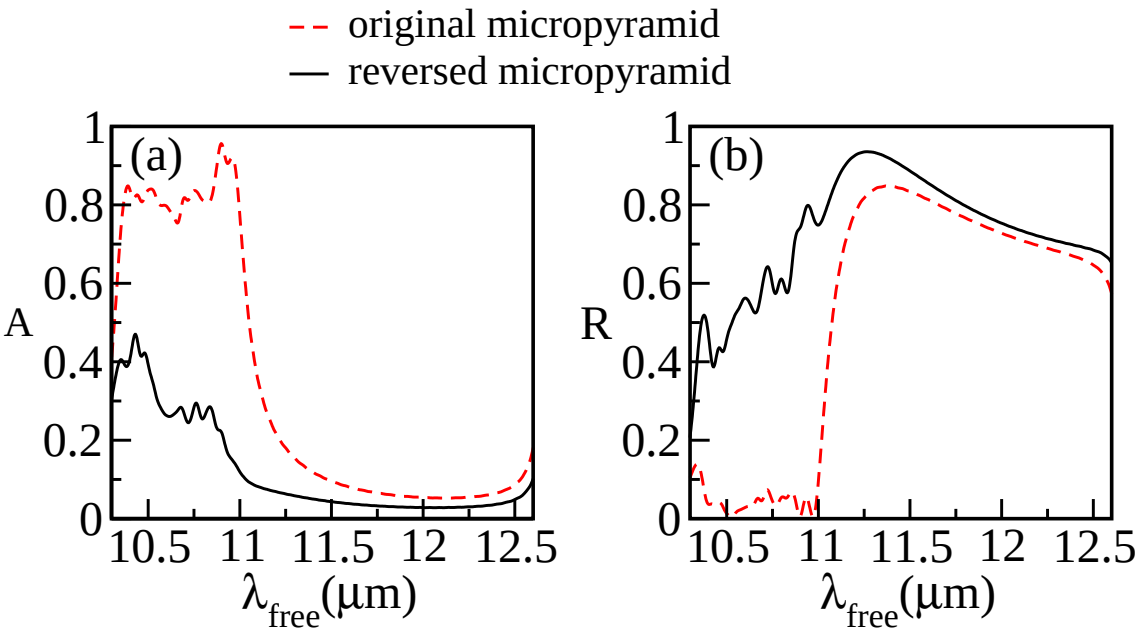

Figure 7.12: (a) Spectral response of the absorptance, A of the reverse micropyramid grating absorber, of lattice constant a = 5 µm, in which the SiC layers are arranged in the exact reverse order of the original micropyramid (black-solid lines). Result of the original micropyramid is shown for the comparison (red-dashed lines). (b) Same as in (a) but for the reflectance, R.

We have already seen in Chapter 6 that it is very important to arrange the

absorbing blocks of the 1D-PC in the increasing order of their thickness to achieve high absorptance [1]. Therefore, in the following we will change the SiC layers sequence within the the micropyramid grating structure and explore its impact on the absorption performance.

For this purpose we investigate a micropyramid grating, in which the the SiC layers are arranged in the exact reverse order of the original micropyramid. We take the lattice constant of this grating to be 5 µm. We evaluate the absorptance and reflectance of this reverse micropyramid grating. We plot the results versus the free-space wavelength λ_{free} in Fig. 7.12 and indicate these with black-solid lines. We also represent the results of the corresponding original micropyramid grating with 5 µm lattice constant as red-dashed lines in Fig. 7.12. We can clearly see that the absorption performance of the reverse pyramid structure is very poor in comparison to the original microstructure. This is due to the increased reflection of the reverse structure as we can see from Fig. 7.12.

In order to understand this increased reflective behaviour of the reverse design, we evaluate the x- and y-components of the normalised Poynting vector, S_x and S_y at the three wavelengths as we did before. We show the results in Fig. 7.13. We also show the results of the original micropyramid structure of lattice constant 5 µm, next to these for an easy comparison. From these Poynting vector plots at wavelength 10.5 µm, it is evident that the power strength is more than two times lower for the reverse structure compared to the original micropyramid structure. Moreover, we can see all cavity modes in each of the SiC layers can be accessed in the case of the original pyramid structure. However, we see that in the reverse structure the modes in the bottom two layers are not accessed by the EM fields. We can see similar observations for the wavelength 11.2 µm. However, at wavelength 12.0 µm, both the reverse and original pyramid designs have similar energy flow behaviour. If we flip the pyramid, then we barely see the difference which way the modes are excited. This is because in this regime, we have extended modes between the micropyramid structure, thus the EM wave goes around the pyramid structure. Indeed we see more or less same absorption and reflectance performance for these two structures at this wavelength.

7.7 Impact of the substrate

So far we have explored the micropyramid grating structure grating as a standalone structure. However, a more realistic absorber design will need a substrate. Hence,

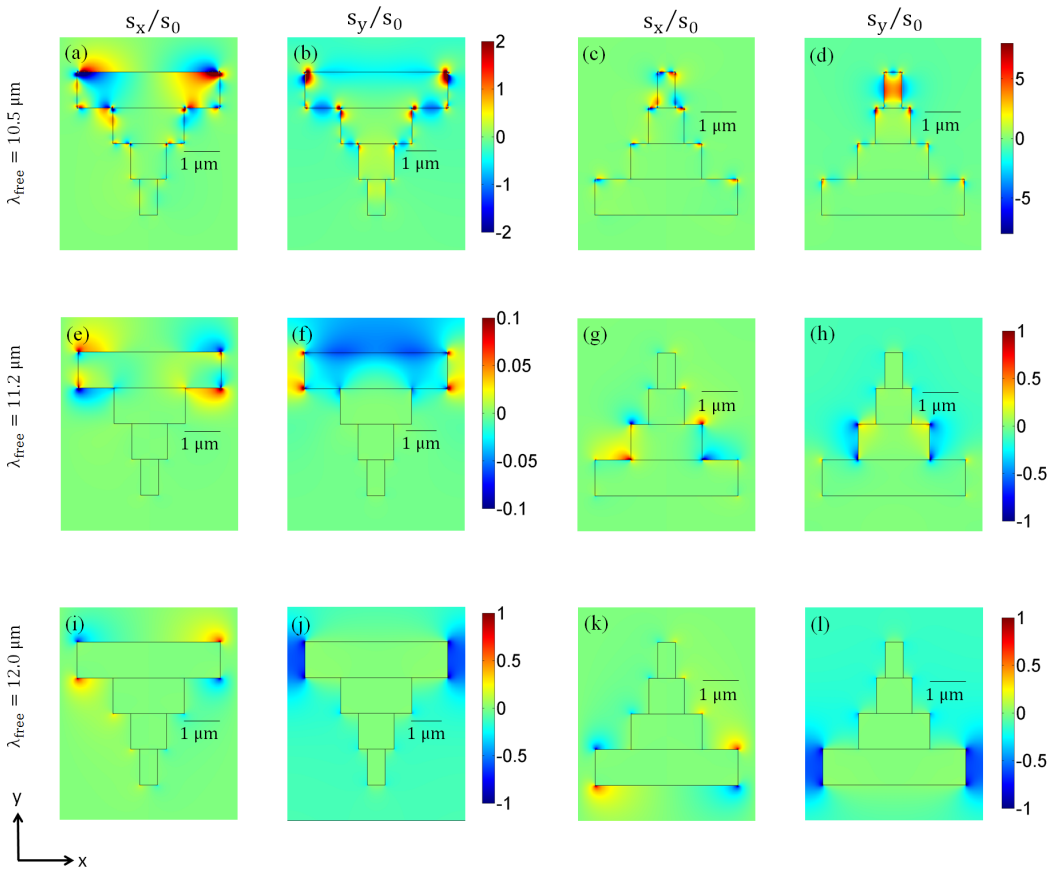

Figure 7.13: (a) and (b) x- and y-components of the normalised Poynting vector, S_x and S_y, of the reverse pyramid absorber with lattice constant 5 µm, at wavelength 10.5 µm. (c) and (d) are same as (a) and (b), but for the corresponding original pyramid absorber with lattice constant 5 µm. (e), (f), (g) and (h) are same as (a), (b), (c) and (d) respectively, but for wavelength 11.2 µm. Similarly, (i), (j), (k) and (l) are same as (a), (b), (c) and (d) respectively, but for wavelength 12.0 µm

we explore in this section, how the absorptance enhancement of these two designs will be affected by adding a 10 µm thick BaF_2 block that is fairly transparent in the Mid-IR. For this purpose, we calculate the absorptance, A and reflectance, R of the pyramid absorber of 5 µm lattice constant with the added BaF_2 substrate, and compare it with the stand alone structure. We show the results in Fig. 7.14(a) and Fig. 7.14(b) respectively. We can identify from Fig. 7.14 that the substrate has almost no influence on both the absorptance and reflectance spectrum of the original structure. This result is similar to what we already observed in our 1D-PC absorber case in Fig. 14 of Ref. [24]. These observations suggest that our proposed micropyramid grating structure design has potential for practical realisation.

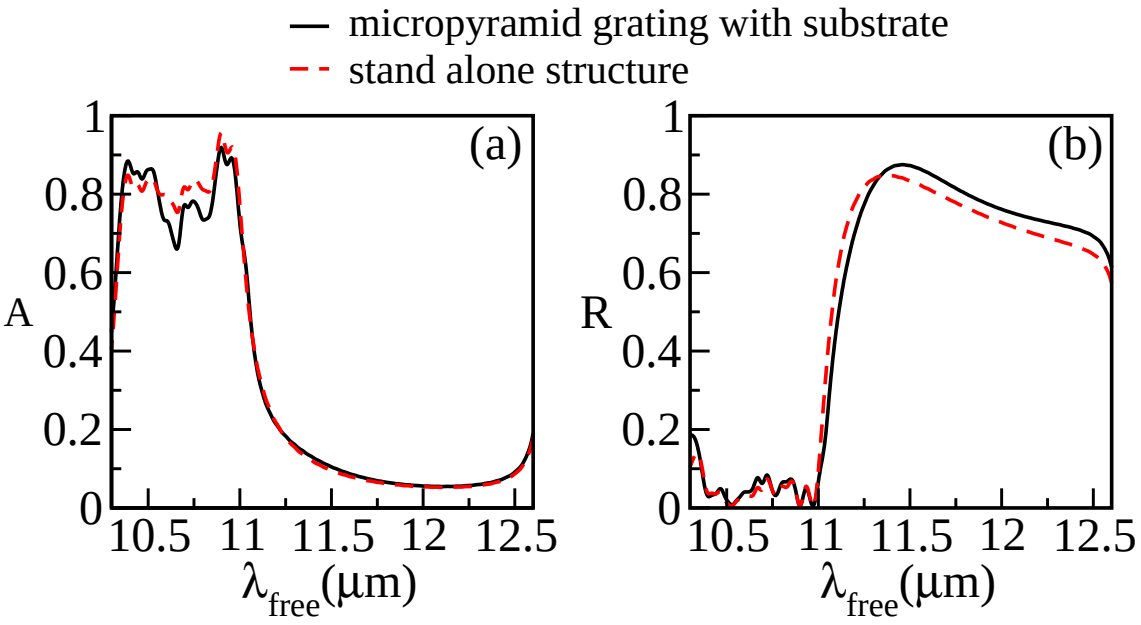

Figure 7.14: (a) Spectral response of the absorptance, A of the micropyramid grating absorber, of lattice constant a = 5 μm, resting on a BaF_2 substrate (black-solid lines). Stand alone structure is shown for the comparison (red-dashed lines). (b) Same as in (a) but for the reflectance, R.

7.8 Conclusion

We proposed practically realizable SiC micropyramid grating paradigm for absorption enhancement within the Reststrahlen band of the SiC. We demonstrated a total absorption of more than 80% over a broad wavelength regime with our compact grating that is a third-of-the impinging wavelength thick. The underlying mechanism for this superabsorption is exciting vortex-like cavity modes in each of the layers in the SiC micropyramids, that result from the coupling between the phonon-polariton modes at each face of the SiC layer. Such coupling can become stronger when the layers are arranged closer in a grating structure of a lower lattice constant. Furthermore, our findings indicate that the particular arrangement of the SiC layers in the increasing order of their lateral width is necessary for a high absorption, while the presence of the transparent substrate does not alter the results.

We note, in passing that very recently B. Neuner III *et al.* [25] have also reported absorption enhancement with a mushroom-like 2D-SiC array in the Reststrahlen band of SiC. However, the maximum absorption achieved with their SiC metasurfaces is only 50%. The near-perfect absorption of our pyramid suggests the possibility of this structure to function as near-perfect thermal emitters according to Kirchhoff's law [26]. Further engineering of the particular structure can make them one-way emitters, given the high asymmetry in the directional absorption of the pyramid

structure. We believe that our micropyramid paradigm which is easily realizable using the standard etching based semi-conductor fabrication techniques [14] will inspire the design of EM absorbers/emitters across the THz/Mid-IR spectrum with the utilisation of phonon-polaritonic materials.

Bibliography

[1] G. C. R. Devarapu and S. Foteinopoulou, "Broadband Mid-IR superabsorption with aperiodic polaritonic photonic crystals," J. Euro. Opi. Soc: Rap. Pub. **9** 14012 (2014).

[2] Lumerical Solutions, Inc. http://www.lumerical.com/tcad-products/fdtd/

[3] G. C. R. Devarapu and S. Foteinopoulou, "Mid-IR near-perfect absorption with a SiC photonic crystal with angle-controlled polarization selectivity," Opt. Express **20**, 13041-13054 (2012).

[4] C. G. Bernhard and W.H. Miller, "A corneal nipple pattern in insect compound eyes," Acta Physiol. Scand. **56**, 385-386 (1962).

[5] C. G. Bernhard, W.H. Miller, and A.R. Moller, "The insect corneal nipple array. A Biological, Broad-band impedance transformer that acts as an antireflection coating". Acta Physiol. Scand. Suppl. **243**, 1-79 (1965).

[6] B. S. Thornton, "Limit of the moths eye principle and other impedance-matching corrugations for solar-absorber design" J. Opt. Soc. Am. **65**, 265-270, (1975).

[7] D. G. Stavenga, S. Foletti, G. Palasantzas, and K. Arikawa, (2006). "Light on the moth-eye corneal nipple array of butterflies," Proc. Royal Soc. B **273**, 661-667, (2006)

[8] C. H. Sun, P. Jiang, and B. Jiang, "Broadband moth-eye antireflection coatings on silicon", App. Phy. Lett. **92**, 061112 (2008).

[9] W. Dai, D. Yap, and G. Chen, "Wideband enhancement of infrared absorption in a direct band-gap semiconductor by using nonabsorptive pyramids", Opt. Express **20**, A519 (2012).

[10] R. Esteban, M. Laroche, and J. -J. Greffet, "Dielectric gratings for wide-angle, broadband absorption by thin film photovoltaic cells," Appl. Phys. Lett. **97**, 221111 (2010).

[11] E. Rephaeli, and S. Fan, "Absorber and emitter for solar thermo-photovoltaic systems to achieve efficiency exceeding the Shockley-Queisser limit", Opt. Express **17**, 15145-15159 (2009).

[12] K. X. Wang, Z. Yu, V. Liu, Y. Cui, and S. Fan, "Absorption enhancement in ultrathin crystalline silicon solar cells with antireflection and light-trapping nanocone gratings," Nano Lett. **12**, 1616-1619 (2012).

[13] Y. Cui, K. H. Fung, J. Xu, Y. Jin, S. He, and N. X. Fang, "Ultrabroadband Light Absorption by a Sawtooth Anisotropic Metamaterial Slab," Nano Lett. **12**, 443-1447 (2012).

[14] G. N. Yushin, A. V. Kvit, R. Collazo, and Z. Sitar, "SiC to SiC wafer bonding," MRS Proc. **742**, (2002).

[15] J. A. Schuller, T. Taubner, and M. L. Brongersma, "Optical antenna thermal emitters," Nat. Photonics **3**, 658–661 (2009).

[16] C. Kittel, *Introduction to Solid State Physics* (John Wiley and Sons, Hoboken, 2005).

[17] P. B. Catrysse and S. Fan, "Near-complete transmission through subwavelength hole arrays in phonon-polaritonic thin films," Phys. Rev. B **75**, 075422 (2007).

[18] S. Foteinopoulou, M. Kafesaki, E. N. Economou, and C. M. Soukoulis, "Two-dimensional polaritonic photonic crystals as terahertz uniaxial metamaterials," Phys. Rev. B **84**, 035128 (2011).

[19] J. D. Jackson, *Classical Electrodynamics* (Third edition, John Wiley and Sons, Hoboken, 1998).

[20] K. Aydin, V. E. Ferry, R. M. Briggs, and H. A. Atwater, "Broadband polarization-independent resonant light absorption using ultrathin plasmonic super absorbers," Nat. Commun. **2**, 517 (2011).

[21] U. Fano, "Effects of configuration interaction on intensities and phase shifts," Phys. Rev. **124**, 1866-1878 (1961).

[22] M. V. Rybin, K. B. Samusev, I. S. Sinev, G. Semouchkin, E. Semouchkina, Y. S. Kivshar, and M.F. Limonov, "Mie scattering as a cascade of Fano resonances," Opt. Express **21**, 825-828 (2013).

[23] P. Fan, Z. Yu, S. Fan, and M. L. Brongersma, "Optical Fano resonance of an individual semiconductor nanostructure," Nat. Mater. (2014).

[24] G. C. R. Devarapu and S. Foteinopoulou, "Compact photonic-crystal super-absorbers from strongly absorbing media," J. Appl. Phys. **114**, 033504 (2013).

[25] B. Neuner III, C. Wu, G. T. Eyck, M. Sinclair, I. Brener, and G. Shvets, "Efficient infrared thermal emitters based on low-albedo polaritonic meta-surfaces," Appl. Phys. Lett. **102**, 211111 (2013).

[26] M. Born and E. Wolf, *Principles of Optics : Electromagnetic Theory of Propagation, Interference, and Diffraction of Light*, (University Press, Cambridge, 2006).

8

Propagation in lossy 1D-PCs: Theory

8.1 Chapter Overview

So far we have investigated one extreme property of lossy PCs namely the capability to demonstrate near-perfect absorption of light. Specifically, in Chapter 5 we demonstrated that more than 90% of light can be absorbed within the top absorbing layer of thickness $\lambda/1000$. Here, we are interested to investigate whether an opposite effect is possible. In particular, we aim to explore whether light can demonstrate ultra-refractive effects while propagating through lossy PC structures, with very little getting absorbed. In other words, we will investigate whether lossy PCs can act as extraordinary translucent photonic media.

This possibility will be highly desirable for device applications in the IR frequency regime where suitable materials for constructing bulk optical components are rare. We will explore and discuss a particular example in the following Chapter. Thus far mostly lossless PCs have been employed to engineer ultra-refractive effects of light [1–10]. However the strong Fabry-Perot interference effects in lossless PCs cause fringes in the transmission, with an oscillatory strength that increases with the filling ratio and an occurrence frequency that increases with the number of unit cells in the PC. As a result, transmission can change rapidly within a narrow spectral region.

In the following, we will explore whether it is possible to overcome this limita-

tion with 1D-lossy PCs. Since the backreflection from the lossy PCs will lose strength due to absorption, we anticipate the strength of the interference fringes to be decreased. This suggests that lossy PCs can have smoother reflection spectra, which are expected to yield significant smooth transmission spectra, if we operate sufficiently away from the photonic crystal band-edge. By smooth transmission spectra we mean transmission spectra with Fabry-Perot fringes [11] of reduced strength, less than 10%. Note, in contrast, the extraordinary absorption phenomenon we discussed in the previous chapters arose from engineering low reflection to occur near the PC band-edge. In order to be able to utilise the lossy PCs as translucent media, we should understand the propagation theory of light in them, which is not systematically studied in the literature thus far.

For this purpose, we develop a new alternate approach to understand the efficient incoupling of light in the lossy 1D-PCs and connect our findings to the Bloch impedance formalism as hitherto explored in the literature [12–20]. Furthermore, we present a complete theory of propagation in lossy PCs with which we can determine the refracted beam for any given impinging wave. This theory is an extension of the comprehensive theory for lossless PCs [1–4]. The fundamental analysis presented here will provide the grounds to extend this theory to 2D and 3D PCs.

Before proceeding to our results and analysis we briefly recap the methods employed in this chapter. Bandstructure and transmission results have been calculated with computer programs that have been developed based on Yariv and Yeh's Transfer Matrix Method (TMM) [21–24] that we have presented in Chapter 2. Furthermore, we have relied on Yariv and Yeh's method to develop a complete framework of the analysis of propagation properties of EM waves in lossy PCs. The new introduced aspects of our analysis includes a method of determining the backward and forward nature of EM waves in lossy PCs, a new expression of Bloch impedance that relies on the Yariv and Yeh's formalism and a method for calculating the group velocity in lossy multilayer systems for off-normal incident light. All these methods are developed based on Yariv and Yeh's TMM method, however they have not been reported before. In addition, the electric-field maps have been calculated by setting up the problem, as we detailed in section 8.3 of this chapter, in a commercial Finite-Difference Time-Domain (FDTD) solver, in particular the Lumerical EM simulator [25]. Details of the underlying physical principles of such solver have been presented in section 2.6 of Chapter 2.

8.2 Transmittance and Bloch impedance in lossy 1D-PCs

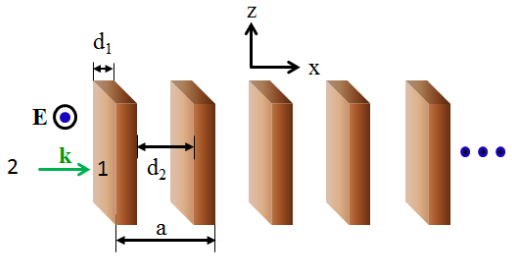

Figure 8.1: Schematics of a 1D-PC structure consisting of two media we designate as medium 1 and medium 2 respectively. We indicate the geometric and material parameters of such structure. We assume that EM waves are incident from medium 2.

In order to demonstrate the transmission limitations of lossless PCs that we discussed above, we consider a dielectric-air 1D-PC system, with the permittivity of the dielectric material equal to 11.56, which is close to the realistic value of Si in the Mid-IR [26]. We show this 1D-PC system schematically in Fig. 8.1, with the dielectric and air medium designated as medium 1 and medium 2 respectively. In particular, we consider a twenty-unit-cell dielectric-air PC with a lattice constant, a of 3 μm. We take three different filling ratios, f_r, 0.05, 0.10 and 0.15 respectively. We evaluate the transmittance, T and reflectance, R by employing the TMM method [21–24] that we have described in Chapter 2. We show the results versus the free space wavelength, λ_{free} in Fig. 8.2. We indicate the results of f_r, 0.05, 0.10 and 0.15 with black, red and blue lines respectively for this structures.

In Fig. 8.2(a), we can clearly see the strong Fabry-Perot interference fringes in the transmission spectrum of these PCs. We notice clearly that the strength of the fringes sharply increases with the filling ratio, even for these low filling ratio PCs. We can observe the corresponding fringes in the reflectance shown in Fig. 8.2(b). It becomes evident from Fig. 8.2 that these fringes in the transmission pose a limitation in utilising the lossless PCs for ultra-refraction applications, since a small change in frequency will result in a large change in transmission. This aspect is crucial where operational bandwidth is required.

To see whether this limitation can be overcome with lossy PCs, we consider a SiC-air 1D-PC system in the Reststrahlen frequency regime of SiC, where the SiC is a highly lossy material. In this frequency regime, the permittivity of SiC that we

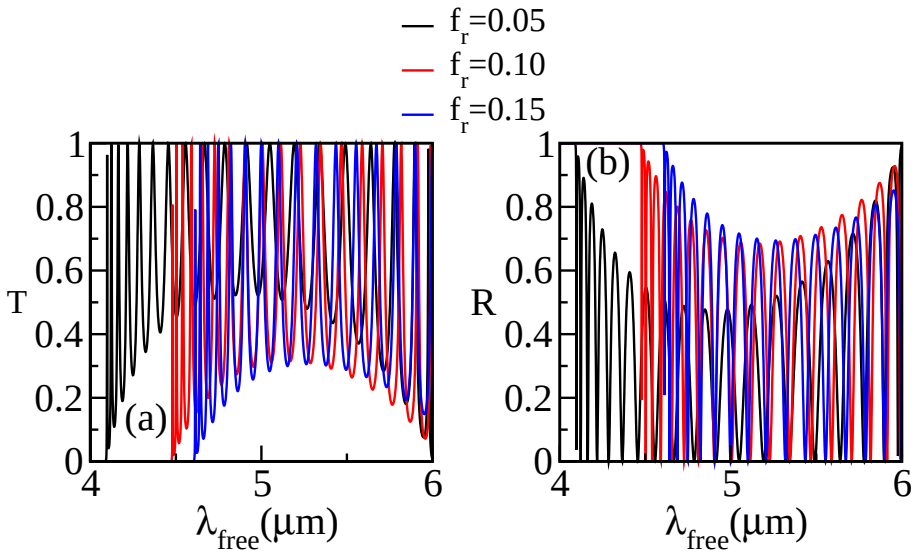

Figure 8.2: (a) Transmittance versus free space wavelength, λ_{free}, for three twenty-unit-cell dielectric-air PCs with filling ratios 0.05 (black line), 0.10 (red line) and 0.15 (blue line). The lattice constant of these PCs is 3 μm. (b) Same as (a), but for the reflectance versus free space wavelength.

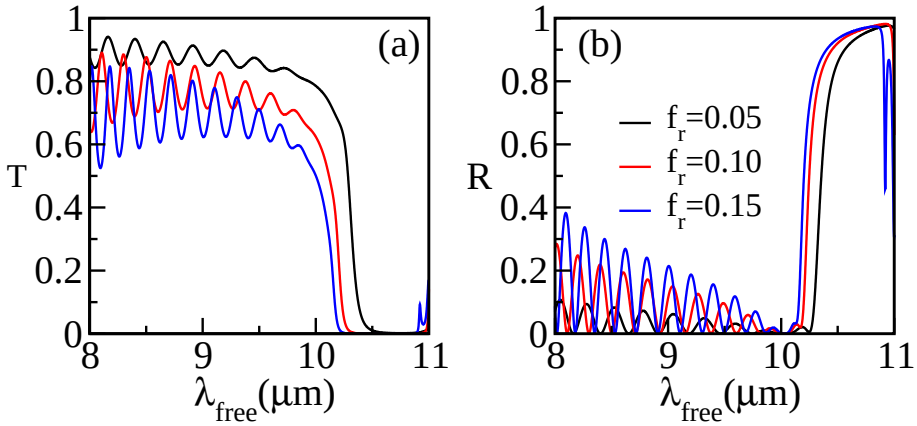

Figure 8.3: Same as in Fig. 8.2, but for a SiC-air PC with a lattice constant of 5.5 μm.

denote with ε_1, can be modelled with a Lorentzian function [27] as:

$$\varepsilon_1(\omega) = \varepsilon_\infty \left(1 + \frac{\omega_L^2 - \omega_T^2}{\omega_T^2 - \omega^2 - i\omega\Gamma}\right), \tag{8.1}$$

where ω is the angular frequency of the incident EM wave. The parameters in the Lorentzian function—taken from Ref. [28]—are ε_∞=6.7, ω_T =2$\pi\times$23.79 THz, ω_L =2$\pi\times$29.07 THz and Γ =2$\pi\times$0.1428 THz. The filling ratio and the number of unit cells of the these SiC-air are the same as the above discussed lossless PC, except the lattice constant, which is taken to be 5.5µm. We show the transmittance and reflectance results of these PCs in Fig. 8.3(a) and (b) respectively. From Fig. 8.3(a), we can observe that the transmittance is relatively less oscillatory and near-unity for the lowest filling ratio PC, compared to the lossless PCs. This suggests that lossy PCs can be translucent with little spectral structure in the transmission spectra, hence promising for broadband optical device applications. As we discussed above, the smoother spectra are anticipated because of the partial absorption of the backreflected EM waves in the lossy PCs.

In order to understand this further, we consider in the following, the reflectivity of a 1D-PC of N unit cells, $r(N)$, in the case where the incoming and the outgoing medium are the same as the second constituent of the PC (see Fig. 8.1). The expression for $r(N)$ is given by Eq. 2.127 derived from the TMM method [21–24] as described in Chapter 2:

$$r(N) = \frac{M_{21}^u U_{N-1}}{M_{11}^u U_{N-1} - U_{N-2}}, \tag{8.2}$$

where

$$U_N = \frac{\sin((N+1)\mathrm{qa})}{\sin(\mathrm{qa})}, \tag{8.3}$$

and M^u is the 2 $\times$ 2 transfer matrix of the PC unit cell in the Yariv and Yeh formulation [21–24]. Note that in Eq. 8.3, q and a represent the Bloch wavevector and lattice constant of the PC respectively. Furthermore, q is related to the elements of the transfer matrix of the unit cell in the PC as:

$$\cos(\mathrm{qa}) = \frac{1}{2}(M_{11}^u + M_{22}^u). \tag{8.4}$$

With the use of Eq. 8.3, we can rewrite Eq. 8.2 as:

$$r(N) = \frac{M_{21}^u}{M_{11}^u - \frac{\sin((N-1)\mathrm{qa})}{\sin(N\mathrm{qa})}}. \tag{8.5}$$

After mathematical simplification, we get:

$$r(N) = \frac{M_{21}^{u}}{M_{11}^{u} - \cos(\mathrm{qa}) + \frac{\sin(\mathrm{qa})}{\tan(N\mathrm{qa})}}. \tag{8.6}$$

Thus far, we still have made no assumption about the nature of the PC's constituent material whether lossy or lossless, thus Eq. 8.6 is general, provided medium 2 is the same as the incoming and outgoing medium.

Now, we consider the case of a semi-infinite lossy PC, where the EM waves have a complex Bloch wavevector $\mathrm{q} = \mathrm{q}' + i\mathrm{q}''$ where q' and q'' represent the real and imaginary parts of the Bloch wavevector respectively. In such a case, we can express $\tan(N\mathrm{qa})$ in Eq. 8.6 as:

$$\tan(N\mathrm{qa}) = \frac{e^{iN\mathrm{q}'\mathrm{a}}.e^{-N\mathrm{q}''\mathrm{a}} - e^{-iN\mathrm{q}'\mathrm{a}}.e^{N\mathrm{q}''\mathrm{a}}}{i\left(e^{iN\mathrm{q}'\mathrm{a}}.e^{-N\mathrm{q}''\mathrm{a}} + e^{-iN\mathrm{q}'\mathrm{a}}.e^{N\mathrm{q}''\mathrm{a}}\right)}. \tag{8.7}$$

Since we consider the $+x$ direction as the propagation direction (see Fig. 8.1), q'' should be always positive to satisfy the passivity requirement. Therefore, for a semi-infinite PC, in the limit of $N \to \infty$, we have $e^{-N\mathrm{q}''\mathrm{a}} \to 0$. That means, we can approximate the $\tan(N\mathrm{qa})$ as:

$$\tan(N\mathrm{qa}) \approx \frac{-e^{-iN\mathrm{q}'\mathrm{a}}.e^{N\mathrm{q}''\mathrm{a}}}{i\left(e^{-iN\mathrm{q}'\mathrm{a}}.e^{N\mathrm{q}''\mathrm{a}}\right)} = i, \tag{8.8}$$

and obtain from Eq. 8.6:

$$r_{semi} \approx \frac{M_{21}^{u}}{M_{11}^{u} - e^{i\mathrm{qa}}}, \tag{8.9}$$

where q is complex valued and r_{semi} is the reflectivity of the semi-infinite PC where one of its constituents is the same with the incoming medium.

Now the reflectivity, r at the interface between two homogeneous media designated as medium 1 and medium 2, with the EM incident from medium 2, can can be written as:

$$r = \frac{Z_1 - Z_2}{Z_1 + Z_2}, \tag{8.10}$$

where $Z_1 = \frac{1}{\sqrt{\varepsilon_1}}$ and $Z_2 = \frac{1}{\sqrt{\varepsilon_2}}$ are the relative impedances of medium 1 and medium 2 respectively, with respect to the vacuum impedance $Z_0 = \sqrt{\frac{\mu_0}{\varepsilon_0}}$, since we consider these media to be non-magnetic. Here ε_0 and μ_0 represent the permittivity and permeability of the vacuum respectively.

It is desirable to characterize the semi-infinite lossy PC medium with an effective

impedance Z_{eff} that yields the PC's reflectivity. Equating the semi-infinite PC's precise reflectivity with that of a semi-infinite homogeneous medium with an effective impedance Z_{eff}, we get:

$$\frac{Z_{eff} - Z_2}{Z_{eff} + Z_2} = r_{semi}, \tag{8.11}$$

since EM waves are incident from medium 2. That implies:

$$Z_{eff} = Z_2 \left(\frac{1 + r_{semi}}{1 - r_{semi}} \right). \tag{8.12}$$

With the use of r_{semi} from Eq. 8.9, we will get:

$$Z_{eff} = Z_2 \left(\frac{M_{11}^u + M_{21}^u - e^{iqa}}{M_{11}^u - M_{21}^u - e^{iqa}} \right). \tag{8.13}$$

We would like to compare this effective impedance that we derived with our approach with the different Bloch impedance Z_B, definitions used thus far in the literature [12–17]. One approach is proposed by Boscolo *et al.*[13]. If the PC has translational symmetry at the interface, their relative Bloch impedance is defined as:

$$Z_B = \frac{1}{Z_0} \frac{E_y(x=0)}{H_z(x=0)}, \tag{8.14}$$

where $E_y(x=0)$ and $H_z(x=0)$ are the y-axis electric and z-axis magnetic field components at the interface of the 1D-PC (see schematics in 8.1). With the use of the EM boundary conditions at the PC interface, it is clear that:

$$E_y(x=0) = E_0 + rE_0 = (1+r)E_0, \tag{8.15}$$

where E_0 designates the incident electric field along the y-axis. From Maxwell's equation, the magnetic field at the interface will be:

$$H_z(x=0) = \frac{(E_0 - rE_0)k_2}{\omega \mu_0} = \frac{(1-r)E_0\sqrt{\varepsilon_2}}{Z_0}, \tag{8.16}$$

where k_2 represents the incident wavevector, while ε_2 represent the permittivity of the incident medium respectively.

From Eqs. 8.14-8.16, we obtain for the Bloch impedance according to Boscolo *et al.*[13]:

$$Z_B = \frac{1+r}{1-r}\sqrt{\frac{1}{\varepsilon_2}} \Rightarrow Z_B = Z_2 \left(\frac{1+r}{1-r} \right). \tag{8.17}$$

We see by comparison from Eqs. 8.12 and 8.17, that our derived effective impedance

from the TMM properties is consistent with the Bloch impedance introduced by Boscolo *et al.*[13], if we substitute r in Eq. 8.17, with the r_{semi} of a semi-infinite lossy PC.

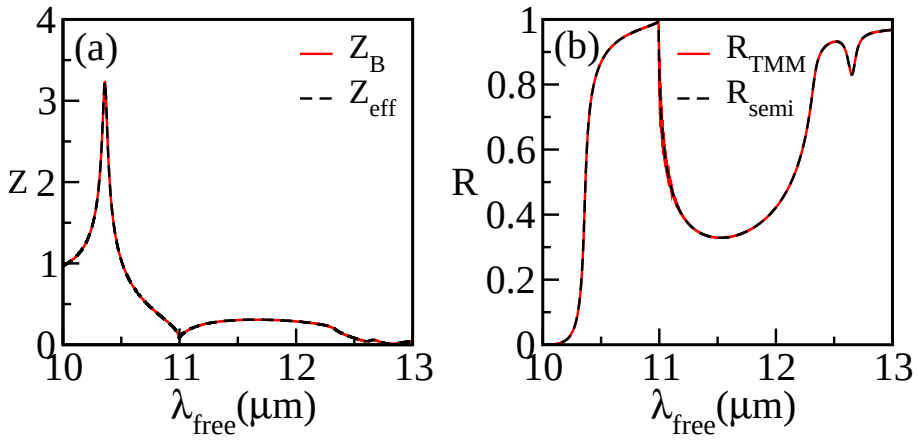

Figure 8.4: (a) Bloch impedance, Z_B (red-solid line) from Eq. 8.18 and effective impedance, Z_{eff} (black-dashed line) from Eq. 8.13 are plotted versus free space wavelength, λ_{free}, of a SiC-air PC with filling ratio 0.05 and lattice constant of 5.5 μm. (b) Reflectance versus free space wavelength, λ_{free}, of the same SiC-air PC. Black-dashed line indicates the reflectance obtained from considering the PC as a homogeneous semi-infinite medium with Z_{eff}, and the red-solid line indicates the reflectance from the actual SiC-air PC from TMM method with a large number of unit cells (500) to emulate a semi-infinite structure.

Another approach commonly used in the literature [12, 17–20], defines the relative Bloch impedance as:

$$Z_B = -\frac{1}{Z_0}\left(\frac{T_{12}^u}{T_{11}^u - e^{-i\text{qa}}}\right), \tag{8.18}$$

where T_{11}^u and T_{12}^u are the elements of the 2×2 characteristic matrix in the Abelès formulation [29, 30]. This matrix is frequently also referred to as the transfer matrix [31, 32]. However, we alert the reader that this matrix is distinctly different from the Yariv and Yeh's transfer matrix [21–24], with the top and bottom elements being the total electric-field and total magnetic-fields components, rather than the forward and backward propagating electric-fields. For the interested reader, we briefly recap the Abelès formulation for the characteristic matrix in Appendix A.

Although the expression for Z_B in Eq. 8.18 looks different from our defined effective impedance, Z_{eff} in Eq. 8.13, it yields the identical result. We plot both these impedances Z_B and Z_{eff} in Fig. 8.4(a), for a SiC-air PC with a lattice constant of 5.5 μm and filling ratio 0.05. Indeed, they coincide exactly. Therefore, from now on we refer to our derived effective impedance also as Bloch impedance. Now with the use of this impedance, we evaluate the corresponding reflectance $R_{semi} = |r_{semi}|^2$

of the semi-infinite PC. We plot the result versus free space wavelength, λ_{free} in Fig. 8.4(b) with a black-dashed line. We compare this with the reflectance from the actual five-hundred-unit-cell SiC-air PC from TMM [21–24], indicated with red-solid line. We consider such a large number of unit cells to emulate a semi-infinite structure [3]. It is remarkable to see from Fig. 8.4(b) that indeed the Bloch/effective impedances from both approaches give the exact reflectance for the semi-infinite lossy PCs.

The importance of introducing our alternative approach is that it makes it clear that the Bloch/effective impedance is expected to give the precise reflectivity for the case of a semi-infinite lossy PCs only. Although not within the subject matter of this section, it might be interesting to look into the meaning of the Bloch/effective impedance for the case of lossless PCs. We present that in Appendix I. Furthermore, our approach allows the definition of a Bloch impedance from the popularly adopted Yariv and Yeh's transfer matrix formalism [21–24]. However, we alert the reader that the definition from Eq. 8.13 is valid only when the incident and outgoing medium are the same as one of the constituents of the PC. In the following, we expand our approach to encompass a general case.

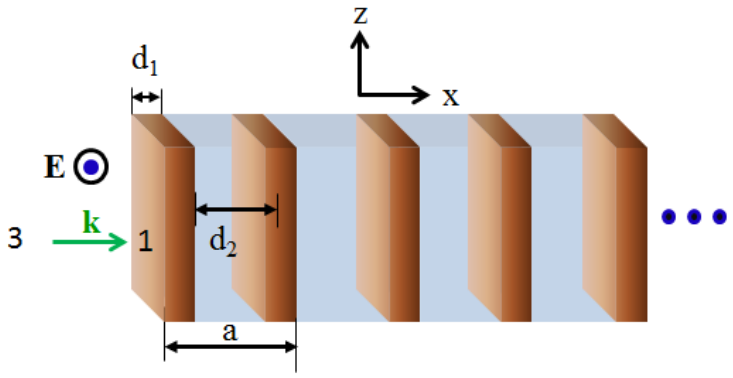

Figure 8.5: (a) Same as Fig. 8.1, but we assume that EM waves are incident from medium 3.

For this purpose, we consider a semi-infinite PC consisting of medium 1 and medium 2. We assume that EM waves are incident from medium 3 in this case, that is different from any of the constituent media of the PC as schematically depicted in Fig. 8.5. The transfer matrix, $M'(N)$ of this PC with N unit cells, can be expressed by employing the TMM method [21–24] as:

$$M'(N) = M^{31}P^{1}M^{12}P^{2}M(N-1), \tag{8.19}$$

since we consider the outgoing medium as medium 2, where M^{31} is the dynamical matrix from medium 3 to medium 1 and M^{12} is the dynamical matrix from medium 1 to medium 2, defined [21–24] as:

$$M^{31} = \frac{1}{2}\begin{bmatrix} 1+\chi^{31} & 1-\chi^{31} \\ 1-\chi^{31} & 1+\chi^{31} \end{bmatrix}, \text{and } M^{12} = \frac{1}{2}\begin{bmatrix} 1+\chi^{12} & 1-\chi^{12} \\ 1-\chi^{12} & 1+\chi^{12} \end{bmatrix}, \tag{8.20}$$

with $\chi^{31} = \frac{k_{1x}}{k_{3x}}$, and $\chi^{12} = \frac{k_{2x}}{k_{1x}}$. Here k_{1x}, k_{2x} and k_{3x} represent the respective wavevectors of the medium 1, medium 2 and medium 3 in the stacking direction along the x-axis. By considering $N \to \infty$, we can emulate a semi-infinite structure. In Eq. 8.19, $M(N)$ is the total transfer matrix of a PC with N unit cells and the same constituents for the PC with transfer matrix $M'(N)$, but with the incident and outgoing medium being medium 2. Note in the case of Fig. 8.5 we have medium 3 as the incoming medium.

With the use of $M^{12}M^{21} = I$, where I is the unity matrix (see Chapter 2), we can express the above transfer matrix from Eq. 8.19 as:

$$M'(N) = M^{31}M^{12}M^{21}P^1M^{12}P^2M(N-1). \tag{8.21}$$

That implies:

$$M'(N) = M^{31}M^{12}M(N), \tag{8.22}$$

since, $M^{21}P^1M^{12}P^2$ is the transfer matrix of the PC unit cell. Further, with the use of $M^{31}M^{12} = M^{32}$ (see Appendix J), we can simplify the above equation as:

$$M'(N) = M^{32}M(N). \tag{8.23}$$

Therefore, we can write $M'(N)$ as:

$$M'(N) = \frac{1}{2}\begin{bmatrix} (1+\chi^{32})M_{11}(N)+(1-\chi^{32})M_{21}(N) & (1+\chi^{32})M_{12}(N)+(1-\chi^{32})M_{22}(N) \\ (1-\chi^{32})M_{11}(N)+(1+\chi^{32})M_{21}(N) & (1-\chi^{32})M_{12}(N)+(1+\chi^{32})M_{22}(N) \end{bmatrix}, \tag{8.24}$$

From the above equation, we can obtain the reflectivity $r'(N)$ of the PC of Fig. 8.5 as:

$$r'(N) = \frac{(1-\chi^{32})M_{11}(N) + (1+\chi^{32})M_{21}(N)}{(1+\chi^{32})M_{11}(N) + (1-\chi^{32})M_{21}(N)}. \tag{8.25}$$

After rearranging the terms in the above equation, we get:

$$r'(N) = \frac{(1-\chi^{32}) + (1+\chi^{32})\frac{M_{21}(N)}{M_{11}(N)}}{(1+\chi^{32}) + (1-\chi^{32})\frac{M_{21}(N)}{M_{11}(N)}}. \tag{8.26}$$

In the above equation, if we let $N \to \infty$ we can identify that $\frac{M_{21}(N)}{M_{11}(N)}$ to be the reflectivity of the semi-infinite PC, r_{semi}, when the incoming medium is medium 2. That implies:

$$r'_{semi} = \frac{(1-\chi^{32}) + (1+\chi^{32})r_{semi}}{(1+\chi^{32}) + (1-\chi^{32})r_{semi}}. \tag{8.27}$$

Thus the effective impedance, Z'_{eff} for this PC will be:

$$\frac{Z'_{eff} - Z_3}{Z'_{eff} + Z_3} = r'_{semi}, \tag{8.28}$$

since EM waves are incident from medium 3. In the above equation $Z_3 = \frac{1}{\sqrt{\varepsilon_3}}$ is the relative impedance of the incident medium, with relative permittivity ε_3. From Eq. 8.28, we can obtain an effective impedance Z'_{eff}, with the use of Eq. 8.27 and Eq. 8.9, for the general case where the incident medium can be different from one of the constituents:

$$Z'_{eff} = \frac{Z_3}{\chi^{32}} \left(\frac{M^u_{11} + M^u_{21} - e^{i\mathrm{qa}}}{M^u_{11} - M^u_{21} - e^{i\mathrm{qa}}} \right), \tag{8.29}$$

To verify the applicability of the above defined effective impedance, we consider a SiC-BaF_2 1D-PC with a lattice constant of 5.5 µm and filling ratio 0.05 and assume that the incident medium is air. We consider this particular PC, because we will employ it in the next chapter to construct a superprism that yields a 90^0 bending of light. We plot the Bloch impedance, Z_B obtained from Eq. 8.18 and the effective impedance Z'_{eff} obtained from Eq. 8.29 in Fig. 8.6(a), with red-solid line and black-dashed line respectively. We can clearly see that both the results are identical. This confirms that our new approach for the effective impedance based on the Yariv and Yeh formalism, applies to the general case where the incoming and outgoing medium are different than the constituents of the PC.

Furthermore, we also compare the corresponding reflectance of the semi-infinite PC obtained from the Bloch/effective impedance and with the actual five-hundred-unit-cell SiC-BaF_2 PC from the TMM method. We plot these results in Fig. 8.6(b). Notice the remarkable agreement between the two results. Also, notice that reflectance is low as well as smooth in the spectral regime where the Bloch impedance is close to the impedance of the incident medium in this case air. As we discussed in section 8.1, this low reflectance spectral regime is key to the design of optical devices.

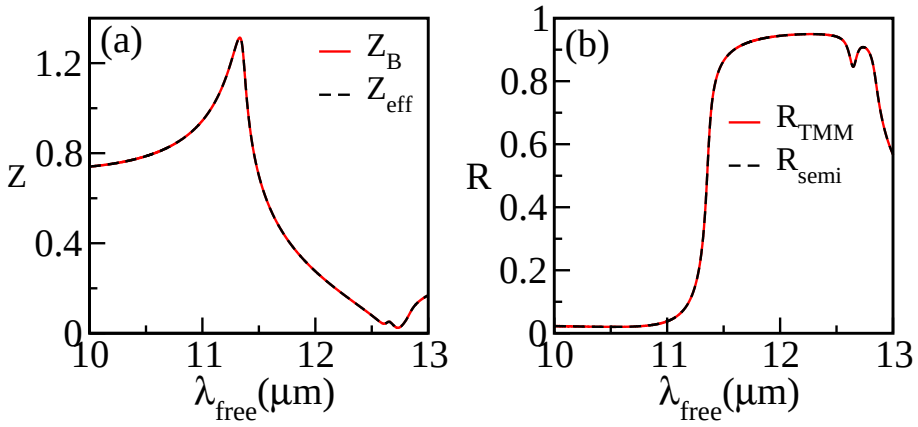

Figure 8.6: (a) Same as Fig. 8.4, but for the SiC-BaF_2 PC when the incident medium is air.

Note that the Bloch/effective impedance exactly predicts the reflectance for semi-nfinite lossy PCs. This is not the case with lossless PCs where the Bloch impedance can only predict a mean reflectance within strong Fabry-Perot oscillations (see Appendix J). This is because a thick lossy PC emulates a semi-infinite medium, since EM wave loses its energy as it propagates inside a semi-infinite structure. Thus as an EM wave gets fully absorbed, there is no reflection from the back interface of the PC. As a result, there are no Fabry-Perot interference fringes in the reflection spectra of semi-infinite lossy PCs. Mathematically, we see that in Eq. 8.6, where for lossy PCs the reflection amplitude, $r(N)$ has a limit as $N \to \infty$, but $r(N)$ does not converge to a limit for lossless PCs. These details are further discussed in Appendix J.

Now that we understood how to analyse the transmission properties of lossy 1D-PCs with the Bloch impedance, we proceed in understanding their propagation properties in the following section.

8.3 Propagation analysis of lossy PCs

8.3.1 Classification of propagation in lossy PCs: band versus gap regions; forward versus backward propagation

In Chapter 2, we presented the propagation theory for lossless 1D-PCs. In the following, we will expand this theory for the case of lossy 1D-PCs. For this purpose, we will study as an example a SiC-BaF_2 1D-PC with a lattice constant of 5.5 μm and filling ratio 0.05, since this is the PC design that we will use for the 90^0 bend structure of Chapter 9.

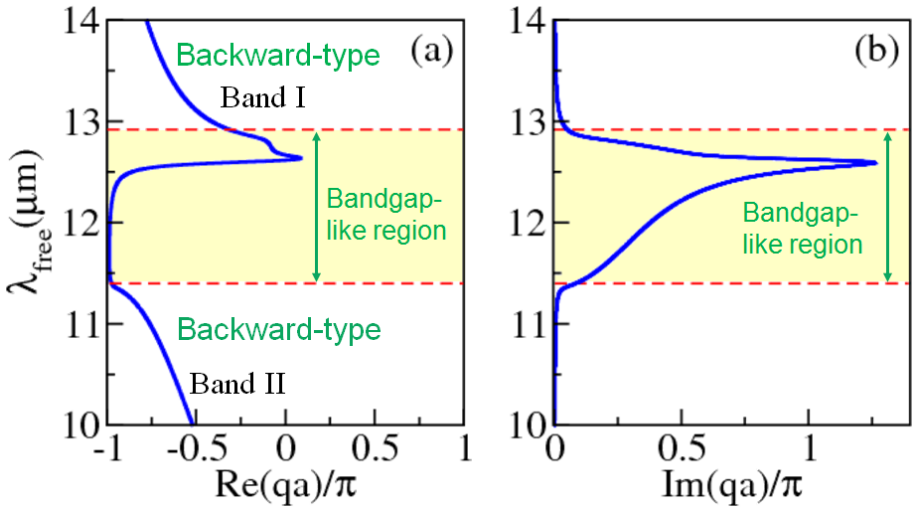

Figure 8.7: Complex bandstructure (free space wavelength, λ_{free} versus Bloch wave vector) of SiC-BaF_2 1D-PC with a lattice constant of 5.5 μm and filling ratio 0.05. An impinging EM wave along the $+x$ direction is assumed, hence the positive Im(q) value is taken to satisfy the passivity requirement. We indicate the bandgap-like region with the yellow shaded region. For the band region, we designate the type of propagation inside the PC, which is backward-type for both bands.

Similar to the case of lossless PCs the dispersion relation i.e. the bandstructure can be evaluated with the TMM method as described in Chapter 2 from:

$$e^{-\text{iqa}} = \frac{1}{2}(M^u_{11} + M^u_{22} \pm \sqrt{\Delta}), \tag{8.30}$$

with $\Delta = (M^u_{11} + M^u_{22})^2 - 4\text{det}(M^u)$ and $\det(M^u)$ being the determinant of the 2×2 transfer matrix of the unit cell of the PC, M^u. Note that unlike the case of lossless PCs, here we cannot have an abrupt separation between the allowed "band" modes and forbidden "gap" modes, for lossy PCs. This is because, the Bloch wavevector, q is complex throughout the spectrum [33–36]. We typically observe regions in the bandstructures that are characterized by a gradual transition from low to high Im(q) values. This implies that the limits of the bandgap region are approximate rather than sharply defined. Therefore we refer to these regions as bandgap-like regions, rather than bandgaps [34], which is the case for lossless PCs, where q transitions from purely real value in the bands to a purely imaginary value in the gaps as we discussed in Chapter 2.

For example we observe in Fig. 8.7, where the bandgap-like regime is shown with yellow shading, that Re(q) is not at the Brillouin Zone (BZ) edge, which was the case for lossless PCs (see Fig. 2.11 in Chapter 2). Also we see that Im(q) increases gradually rather than abruptly. It is also important to note, that a major difference

in the bandgap-like regions is as follows. In lossless PCs in the bandgap, reflectance, R is equal to unity as we discussed in Chapter 2. However, even for a semi-infinite lossy PC, reflectance, R is high, but not equal to unity. We can see it clearly in the yellow shaded region of Fig. 8.8, where we plot the spectral response of reflectance, R for the SiC-BaF_2 1D-PC of Fig. 8.7 with five-hundred-unit-cell, thus emulating a semi-infinite PC.

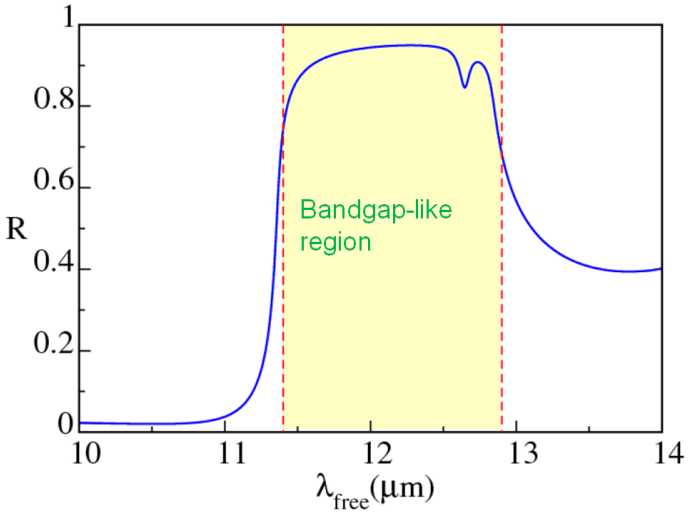

Figure 8.8: Reflectance, R versus free space wavelength, λ_{free} of an essentially semi-infinite SiC-BaF_2 1D-PC with the structural parameters same as Fig. 8.7 (we take 500 unit cells). Bandgap-like region is indicated with the yellow shading.

Now we have understood the bandstructure properties of lossy PCs in the bandgap-like regions, we proceed in understanding the band regions in the bandstructure of lossy PCs. We remind the reader that in the case of lossless PCs as we described in Chapter 2, we could not immediately know which is the sign of q in the band regions, as in principle both roots of Eq. 8.30 were possible. For the choice of the proper root of Eq. 8.30, we had to further look into the group velocity. The proper root choice was based on which root gives a causal propagation direction for the group velocity which is equal to the energy velocity in the lossless PC case. The causal propagation direction is a propagation direction that points away from the source, i.e. along the $+x$ direction for an impinging wave propagating along the $+x$ direction.

In contrast, here in the case of lossy PCs we can immediately determine the sign of Re(q). We can do so, because the Bloch wavevector, q is complex for lossy PCs throughout the spectrum. Thus, if we assume the impinging wave along the $+x$ direction, the wave couples into PC in the $+x$ direction. This means we should accept only the eigenvalue solution, that has a positive Im(q) value, out of the two

possibilities in Eq. 8.30. This is required by passivity, otherwise we would have an increase of EM wave energy while the wave is propagating, which is unphysical. As a result, the bandstructure cannot be symmetric with Re(q) for lossy PCs, contrary to what we know for lossless PCs as we discussed in Chapter 2 (see Fig. 2.11).

The choice of one root from Eq. 8.30 by employing the passivity condition, leads to an immediate determination of the type of EM wave propagation inside the lossy PC. For an impinging wave along the $+x$ direction, if the root with Im(q)>0 has a positive Re(q), that implies a forward-type EM wave, since the energy velocity, $\mathbf{v_e}$ and phase velocity, $\mathbf{v_p}$ will be parallel [3, 4, 7, 8, 37]. On the other hand, if the root with Im(q)>0 has a negative Re(q), that implies a backward-type EM wave, since the energy velocity, $\mathbf{v_e}$ and phase velocity, $\mathbf{v_p}$ will be anti-parallel [3, 4, 7, 8, 37]. We plot the bandstructure of our considered SiC-BaF_2 PC in Fig. 8.7, by taking the correct choice of root with Re(q) that corresponds to positive Im(q) values. Notice that Re(q) is negative in both the branches, which implies that the propagation inside the PC is backward-type for both these bands.

We emphasise that except for the isolated case of Ref. [34], there is a tendency in the literature [12, 35, 36] to show Re(q) in the bandstructure of lossy PCs, without discussing its sign and the selection of the proper root. In particular, in the majority of prior works [12, 35, 36] the bandstructure is plotted with both Re(q) and Im(q) showing positive, although this may not be the case. Even in Ref. [34], where the passivity requirement is applied and the correct the sign of Re(q) is chosen, its importance and implications on the type of wave propagation are not discussed further. However, the information of the sign of Re(q), has very important implications both in designing photonic device applications as well as from the theoretical point of view. From the applications point of view, we will see that the wedged structure in Chapter 9, which bends light through 90^0, relies on the existence of backward-type EM wave propagation, with a Re(q)<0 for an impinging wave along the $+x$-direction. From the theoretical point of view, the sign of Re(q) is important as it captures the correct Bloch phase as the wave propagates from unit cell to unit cell inside the PC [3].

To demonstrate this latter point pictorially, we plot the real and imaginary parts of the y-component of the electric field, E_y, for an essentially semi-infinite SiC-BaF_2 1D-PC with its structural parameters being the same as the SiC-BaF_2 1D-PC of Fig. 8.7 (we take 500 unit cells, after which almost all the EM energy is absorbed that makes the structure acting as semi-infinite). We do so for two wavelengths: $\lambda_{\text{free}} = 13.5\,\mu\text{m}$ that corresponds to band I and $\lambda_{\text{free}} = 11.0\,\mu\text{m}$ that corresponds to

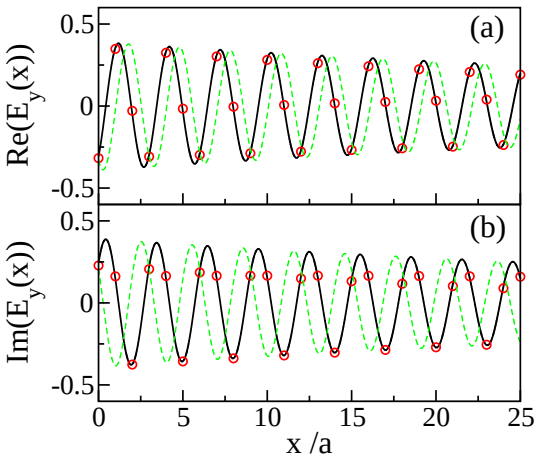

Figure 8.9: (a) Real part of the y-component of the electric field, Re(E_y), at free space wavelength, $\lambda_{\text{free}} = 13.5\,\mu\text{m}$ versus the position, x within an essentially semi-infinite SiC-BaF_2 1D-PC with lattice constant, a = 5.5 µm and filling ratio, $f_r = 0.05$. The open circles represent the result obtained from the TMM method. The black-solid line represents the Bloch phase envelope from Eq. 8.32 with the correct root incorporated for the Bloch wavevector having Re(q)< 0 and Im(q)> 0. The green dashed line represents the Bloch phase envelope from Eq. 8.32, if one takes the positive counterpart of Re(q) that many authors typically use in the literature in lossy-PC bandstructures [12, 35, 36]. (b) Same as in (a), but for the imaginary part of the y-component of the electric field, Im(E_y).

band II. Specifically, we calculate the y-component of the electric-field, E_y using the TMM method (see Section 2.3 in Chapter 2), at the centre of the each SiC layer in the PC. In other words at the j^{th} layer of the PC the field is calculated at the location $x_c(j)$ with:

$$x_c(j) = d_1/2 + (j-1)\text{a}. \tag{8.31}$$

We represent these TMM results with the red-open circles in Figs. 8.9 and 8.10. Then we evaluate the Bloch phase envelope from:

$$E_y(x) = E_y(d_1/2)e^{i\text{q}(x-d_1/2)}, \tag{8.32}$$

where q is the Bloch wavevector at the chosen wavelength, λ_{free}. We show such Bloch phase as black-solid lines in Figs. 8.9 and 8.10.

Note that both the wavelengths considered here correspond to a backward-type EM wave propagation, since Re(q) is negative as we have seen in Fig. 8.7. Thus, we have a negative Re(q) and positive Im(q) in Eq. 8.32. It is remarkable to observe that the Bloch phase captures exactly the actual electric field variation from unit cell to unit cell. However, if we do not carefully incorporate the sign of Re(q), and use its positive counterpart, which is commonly adopted for lossy-PC bandstructures thus

far [12, 35, 36], the Bloch phase completely misrepresents the electric field variation from unit cell to unit cell (see the green dashed lines in Figs. 8.9 and 8.10). These observations emphasise the importance of determining and using the correct sign of Re(q) in lossy PC systems, that is consistent with the passivity requirement. In other words it is important to plot a bandstructure with the correct sign info for Re(q) as plotted in Fig. 8.7.

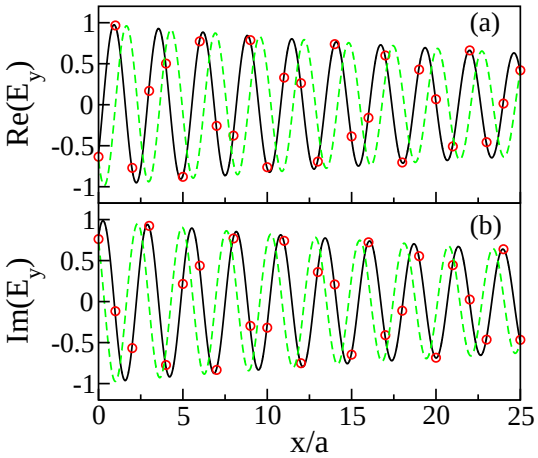

Figure 8.10: Same as Fig. 8.9, but at free space wavelength, $\lambda_{\text{free}} = 11.0\,\mu\text{m}$.

Now that we have understood the correct mode regime, for the wavevector that couples into the lossy PC, we proceed in understanding the velocity of the energy propagation of these modes.

8.3.2 Propagation velocity of EM modes in lossy 1D-PCs: group versus energy velocity

In the case of lossless PCs, we have discussed in Chapter 2 that the energy velocity is equal to the group velocity and that both represent the propagation velocity of EM energy. However, also discussed in Chapter 2 when an EM wave travels even in a bulk-lossy strongly-dispersive material, the pulse shape distorts significantly [38] and the group velocity loses its meaning. In particular, we have compared the group and energy velocity for the particular case of SiC and found that these significantly disagree within the entire Reststrahlen-band frequency region. Therefore, it is interesting to check how the group velocity and energy velocity relate in a PC that has lossy strongly-dispersive constituents, and evaluate within which conditions the use of group velocity is meaningful in such media.

We note that a large number of works just use naively the group velocity as a measure of the propagation velocity without regard of its relation to energy

velocity. Given that highly dispersive constituents are increasingly used in periodic media such as polaritonic PCs [40] and metamaterials with Lorentzian-type of permeability [41–43], it is very important to evaluate the conditions where group velocity can still represent the true energy velocity.

We attempt such comparison for the PC of Fig. 8.7. We make a first inspection by looking at the bandstructure. We remind the reader that in the case of lossless PCs, we discussed that the sign of $\frac{\omega}{\mathrm{q}}\frac{\partial\omega}{\partial\mathrm{q}}$ determines the directionality of the EM wave, forward versus backward-type. Here our intention is to check if this analysis based on the sign of $\frac{\omega}{\mathrm{Re(q)}}\frac{\partial\omega}{\partial\mathrm{Re(q)}}$ agrees with the determination of the directionality based on the passivity requirement for lossy PCs. For this purpose we plot again the bandstructure with dimensionless frequency, fa/c versus Re(q) and Im(q) in Figs. 8.11(a) and (b) respectively, to make it easy to determine the band slope. We denote the band regions in Fig. 8.11 as band I and band II and highlight them with the red and blue shading respectively. We indicate the bandgap-like region with the yellow shading.

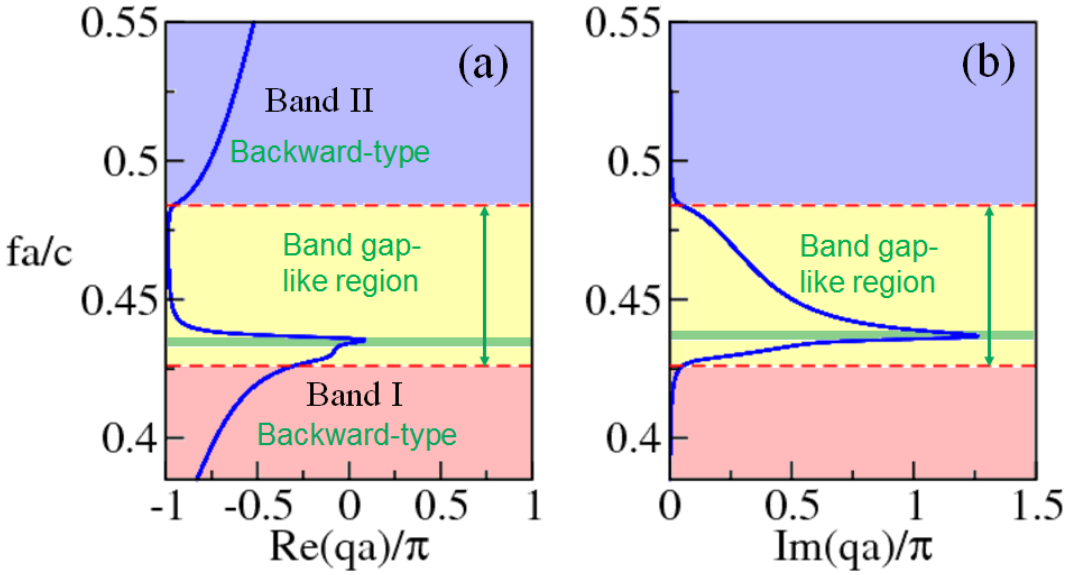

Figure 8.11: Complex bandstructure (dimensionless frequency, fa/c versus Bloch wave vector) for the SiC-BaF_2 1D-PC of Fig. 8.7.

Furthermore, we evaluate $\frac{\omega}{\mathrm{Re(q)}}\frac{\partial\omega}{\partial\mathrm{Re(q)}}$ for the frequency regimes of band I and band II and plot the results in Figs. 8.12(a) and (b) respectively. To aid the reader to identify these two band regimes, we use the same shading for panel (a) and (b) as the shading used for the corresponding band regions in Fig. 8.11. We can clearly observe that the sign of $\frac{\omega}{\mathrm{Re(q)}}\frac{\partial\omega}{\partial\mathrm{Re(q)}}$ is negative for both the band regions. This means that based on the analysis of Chapter 2, we determine that Re(q) should be

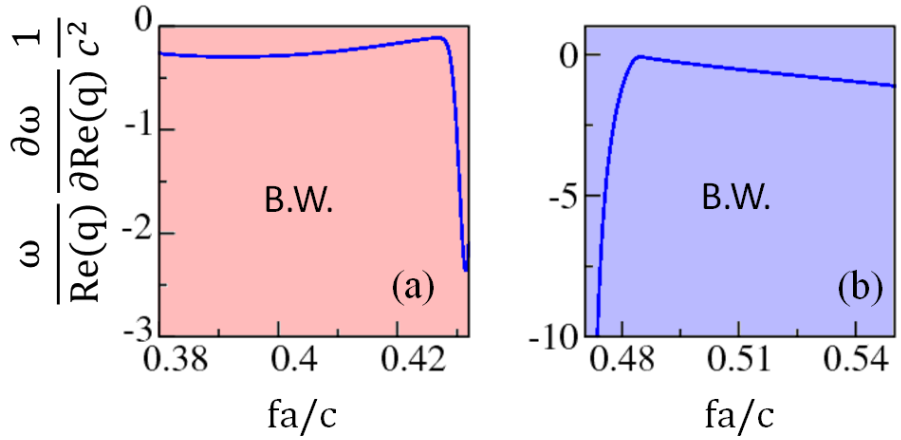

Figure 8.12: (a) $\frac{\omega}{\mathrm{Re(q)}}\frac{\partial\omega}{\partial\mathrm{Re(q)}}$ versus dimensionless frequency, fa/c for the SiC-BaF_2 1D-PC of Fig. 8.7 in the frequency regime of band I. (b) Same as (a), but for band II. In both the panels, B.W. designates that this should be a backward wave based on the analysis from the passivity requirement. The sign of $\frac{\omega}{\mathrm{Re(q)}}\frac{\partial\omega}{\partial\mathrm{Re(q)}}$ agrees with this analysis in both the bands.

negative for these two bands. This observation suggests that the determination of directionality based on the sign of $\frac{\omega}{\mathrm{Re(q)}}\frac{\partial\omega}{\partial\mathrm{Re(q)}}$ agrees with the analysis based on the passivity requirement in the band regions for lossy PCs that we presented in the previous section.

In order to see whether the sign of $\frac{\omega}{\mathrm{Re(q)}}\frac{\partial\omega}{\partial\mathrm{Re(q)}}$ still predicts the directionality in the bandgap-like region, we plot $\frac{\omega}{\mathrm{Re(q)}}\frac{\partial\omega}{\partial\mathrm{Re(q)}}$ for this region and show the result in Fig. 8.13. Note in Fig. 8.13, the orange (green) shaded region represents a frequency regime, where the analysis based on the use of the passivity requirement predicts a backward-type (forward-type) propagation inside the lossy PC. In other words the orange (green) regime corresponds to a negative Re(q) (positive Re(q)) Bloch wavevector. Thus if the analysis of Chapter 2 were valid, we should find a positive $\frac{\omega}{\mathrm{Re(q)}}\frac{\partial\omega}{\partial\mathrm{Re(q)}}$ in the green shaded region and a negative $\frac{\omega}{\mathrm{Re(q)}}\frac{\partial\omega}{\partial\mathrm{Re(q)}}$ in the orange shaded region. We draw the attention of the reader to the two marked spectral regions with a red-dashed box and an unmarked spectral region in Fig. 8.13. Note that in the unmarked spectral region, the directionality of the EM wave determined from the sign of $\frac{\omega}{\mathrm{Re(q)}}\frac{\partial\omega}{\partial\mathrm{Re(q)}}$ agrees with the directionality determined based on the passivity requirement. However, in the marked region, the sign of $\frac{\omega}{\mathrm{Re(q)}}\frac{\partial\omega}{\partial\mathrm{Re(q)}}$ clearly suggests the opposite directionality for the EM wave to the one determined from the passivity requirement.

So we can conclude that the method described in Chapter 2 for determining the directionality of the wave is no longer in general valid for lossy PCs, as it violates

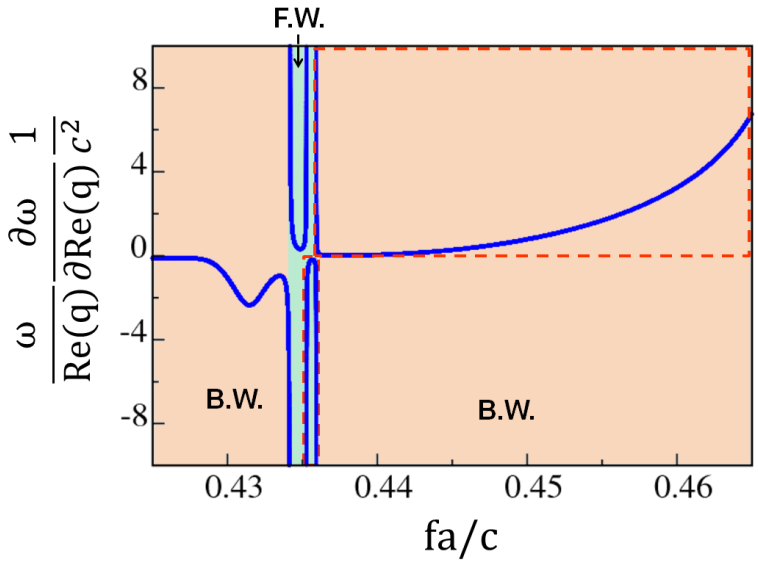

Figure 8.13: Same as Figs. 8.9, but in the bandgap-like region of bandstructure. The red-squares indicate the region where the directionality suggested by the sign of $\frac{\omega}{\mathrm{Re(q)}}\frac{\partial\omega}{\partial\mathrm{Re(q)}}$ disagrees with the determination we have made based on the passivity requirement.

passivity, in some cases. This is because the group velocity is not in general a meaningful quantity for lossy PCs. We will see that further in the following, where we will compare the two velocities quantitatively.

For this purpose, from the dispersion relation, ω (q) we obtained from Eq. 8.30, we numerically evaluate the group velocity, $\mathbf{v_g}$ at each frequency $\omega(i)$, by taking central differences as:

$$\mathbf{v_g} = \mathrm{v}_{gx}\hat{x} = \frac{\partial\omega}{\partial\mathrm{Re(q)}}(i) = \left(\frac{\omega(i+1)-\omega(i-1)}{\mathrm{Re(q}(i+1))-\mathrm{Re(q}(i-1))}\right)\hat{x}, \tag{8.33}$$

where v_{gx} represents the component of the group velocity along x, which is the direction of the propagation. Since we consider normal incidence, we expect both $\mathbf{v_g}$ and $\mathbf{v_e}$ completely aligned in the x-direction. Furthermore, the energy velocity, $\mathbf{v_e}$ can be evaluated [39, 44] with the TMM method as described in Chapter 2 from:

$$\mathbf{v_e} = \mathrm{v}_{ex}\hat{x} = \frac{<\overline{\mathrm{S}_x}>}{<\overline{\mathrm{U}}>}\hat{x}, \tag{8.34}$$

where $\overline{\mathrm{S}_x}$ represents the time-averaged x-component of the Poynting vector, $\overline{\mathrm{U}}$ represents the time-averaged energy density and v_{ex} represents the component of the energy velocity along x. Here $< .. >$ denotes the spatial average of these quantities within a unit cell of the PC. These are calculated from:

$$<\overline{S}_x>=\frac{1}{2}\int_0^{\mathrm{a}}\mathrm{Re}[E_y(x)H_z^*(x)]dx \tag{8.35}$$

and

$$< \overline{U} >= \frac{1}{4}\int_0^a [\varepsilon_0(\varepsilon_1{}' + \frac{2\omega\varepsilon_1''}{\Gamma})|E_y(x)|^2 + \mu_0|H_z(x)|^2]dx, \tag{8.36}$$

where ε_0, μ_0 denote the vacuum permittivity and permeability respectively, while $\varepsilon_1', \varepsilon_1''$ and Γ_e represent the real part, imaginary part and dissipation parameters of the SiC relative permittivity respectively. The y-component of the electric field, E_y and the z-component of the magnetic field H_z are calculated as functions of the location x within the PC by using the TMM method as we have described in Chapter 2.

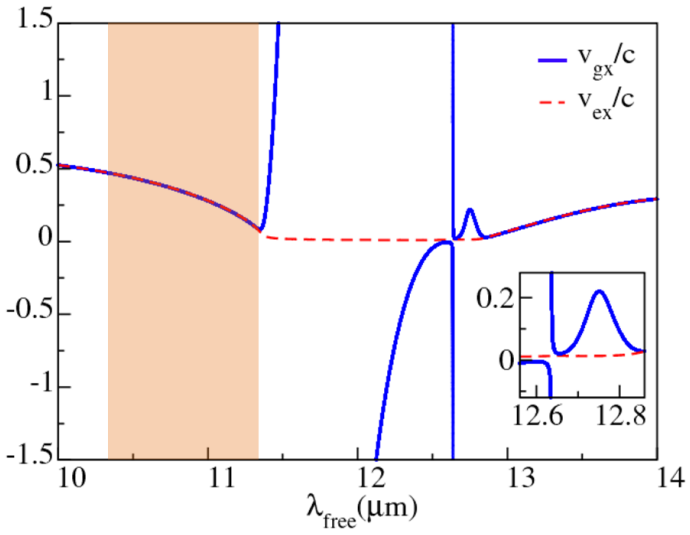

Figure 8.14: Spectral response of the group velocity v_{gx} (blue-solid line), and the energy v_{ex} (red-dashed line). Note, both v_{gx} and v_{ex} are expressed in terms of the speed of light in vacuum c. The orange shaded region represents the part of the Reststrahlen-band regime where v_{gx} agrees with the v_{ex}.

Now we proceed in comparing v_{gx} and v_{ex}. For this purpose, we plot v_{gx} obtained from Eq. 8.33 versus the free space wavelength λ_{free} in Fig. 8.14, with a blue-solid line. In the same figure, we also plot v_{ex} obtained from Eq. 8.34 with a red-dashed line. Note that both v_{gx} and v_{ex} are expressed in units of the speed of the light in vacuum c. It is evident from Fig. 8.14 that v_{gx} is equal to v_{ex} only well within the band regions. However in the band-gap like regions, where Im(q) is high, v_{gx} diverges completely from v_{ex} with its value exceeding the speed of light in vacuum, c, in the wavelength region between 11.4 μm and 12.8 μm. So in such cases clearly the group velocity cannot possibly represent the velocity of the energy propagation which is well bounded by the speed of light in vacuum, c. It is important to notice that it is not only the magnitude of $\mathbf{v_g}$ that is different from $\mathbf{v_e}$, but the sign of v_{gx} is also different from v_{ex} in the wavelength region between 12.1 μm and 12.6 μm

(see inset in Fig. 8.14). Since we assume an impinging wave in the $+x$ direction, causality requires the energy propagation to be towards the $+x$ direction. Thus a negative sign of v_{gx} in Fig. 8.14 is a clear indication that v_{gx} misrepresents the energy propagation direction.

We notice that the large deviation of v_{gx} from v_{ex} in Fig. 8.14 coincides with the large Im(q) for the Bloch mode inside the 1D-PC. We alert the reader that in the case of bulk SiC the imaginary part of the wavevector, Im(k_1) is very large throughout the phonon-polariton gap. Hence we have a large deviation of v_{gx} from v_{ex} for the entire phonon-polariton gap (see Fig. 2.4 in Chapter 2). The PC effect enables allowed modes even within the phonon-polariton gap with a low Im(q). Therefore, we have v_{gx} agreeing with v_{ex} in a wide spectral region within the Reststrahlen band between 10.3 µm and 11.4 µm, that we show with the orange shading in Fig. 8.14. For reference we compare the imaginary part of the Bloch wavevector of the SiC-BaF_2 1D-PC of Fig. 8.7, Im(q), with the imaginary part of the wavevector of bulk SiC, Im(k_1), in Fig. 8.15. We indicate these with a blue line and a red line respectively.

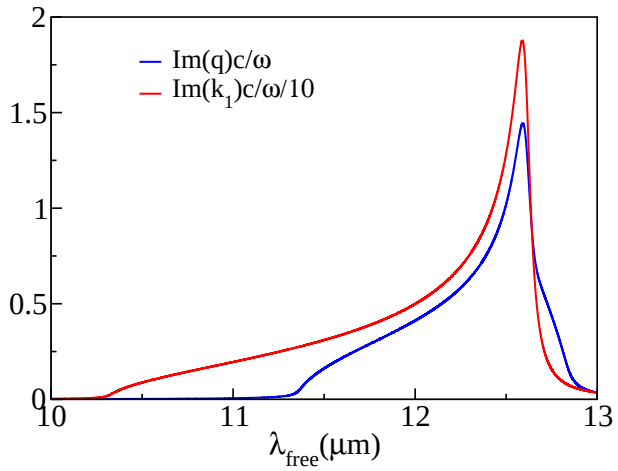

Figure 8.15: Spectral response of the imaginary part of the wavevector inside a bulk SiC, Im(k_1) (red-line), and the imaginary part of the Bloch wavevector, Im(q) (blue-line) for the SiC-BaF_2 1D-PC of Fig. 8.7. Note, both Im (k_1) and Im(q) are expressed in the units of c/ω and Im(k_1) is scaled down 10 times to its original value, to aid the comparison with Im(q).

Furthermore, notice in Fig. 8.14 that the energy velocity is nearly zero in the bandgap-like region. This suggests that the energy velocity can be used to identify the bandgap-like regions for lossy PCs. Remember that in lossless PCs both v_{gx} and v_{ex} are equal and exactly equal to zero in the bandgap region. This is because the Bloch wavevector is purely imaginary in this region for lossless PCs, implying

that only evanescent waves exist inside these PCs, which do not carry any energy. On the other hand, the Bloch wavevector is complex in the bandgap-like regions of lossy PCs. Thus we have wave propagation even in the bandgap-like region. However the wave strongly attenuates as it propagates inside the PC due to the large imaginary part of the Bloch wavevector in this frequency region. However, the EM waves still carry through some energy even in the band-gap like region, hence the small, non-zero energy velocity that we observe in this regime. We have exploited such phenomena successfully to achieve the near-perfect absorption of light in Chapters 3, 5 and 6.

To recap, the group velocity is not always a good measure to capture the energy propagation in lossy PCs. Although the group velocity agrees with the energy velocity in the band regions of lossy PCs, in the bandgap-like regions disagreement can be huge to the point that it suggests the wrong direction for the EM wave propagation. Therefore the general reliable measure of energy propagation will be the energy velocity. We thus conclude that the energy velocity should be used for the propagation analysis of lossy PCs.

8.3.3 EFCs in 1D-lossy PCs

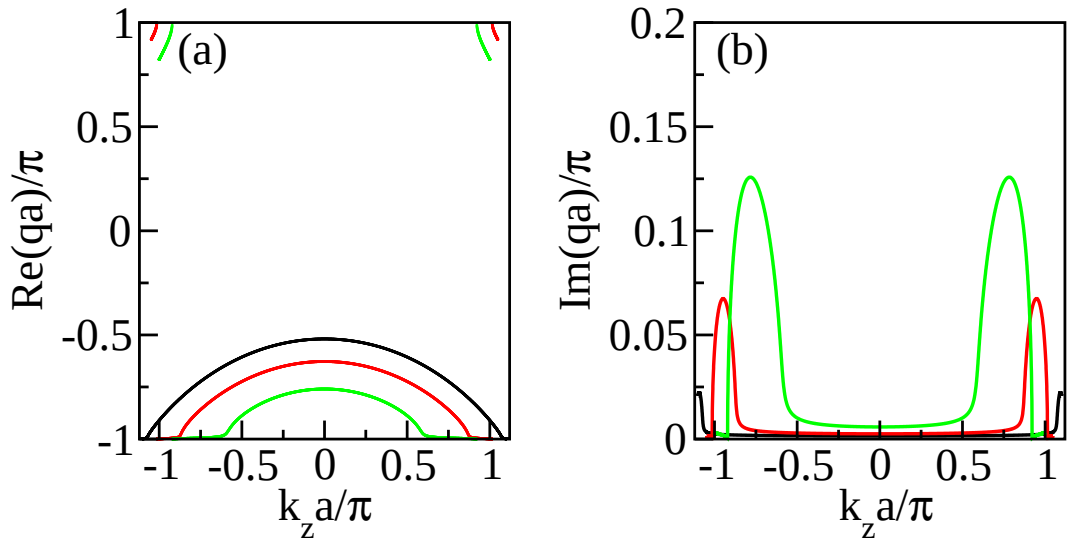

Figure 8.16: Equi-frequency contours of SiC-BaF_2 1D-PC of Fig. 8.7 at wavelengths 10 μm (black lines), 10.5 μm (red lines) and 11 μm (green lines).

We saw in Chapter 2 that the propagation of EM waves at oblique incidence at the interface of lossless PCs can be studied using the Equi-frequency contours (EFCs), which represent the distribution of modes for a given frequency. In this case, we

used the group velocity obtained from the gradient of these EFCs to predict the direction of the refracted beam inside a lossless PC. However, we have seen in the previous section that $\mathbf{v_g}$ does not always captures the direction and magnitude of the propagating wave for lossy PCs. Therefore, we cannot use the wavevector diagram formalism to predict the angle of the refracted beam inside the lossy PCs. However, EFCs would still portray the distribution of modes in the wavevector space.

Thus we plot these to discuss which properties can be understood for the system based on the EFCs. For this purpose, we evaluate the EFCs for our SiC-BaF_2 1D-PC by solving the dispersion relation in Eq. 8.30, for q, for different wavevector values along the z direction, k_z by employing the TMM method [21–24]. Note, k_z is the parallel to the interface component of the incident wavevector i.e. $k_z = k_{||} = \omega/c\,\sin\theta$ and is conserved at the PC interface. We plot the Re(q) and Im(q) versus the parallel component of the incident wavevector, k_z at three wavelengths in Figs. 8.16(a) and (b) respectively. The black, red and green lines represent the EFCs at wavelengths 10 μm, 10.5 μm and 11 μm respectively. Just as we did when determining the bandstructure for normal incidence, we consider the modes that have a positive Im(q), since we assumed the normal direction of the impinging wave to be along the $+x$ direction. Therefore, we do not expect, and indeed do not obtain, mirror symmetric EFCs as we have seen in the case of lossless PCs. Notice that the sign of Re(q) in Fig. 8.16(a) changes with the incident angle. This implies that a mode which is backward-type at normal incidence, can become forward-type at a certain angle of incidence.

Furthermore, we also observe in Fig. 8.16(b) high Im(q) regions for certain incident angle range. These regions are also similar to the bandgap-like region we discussed in the previous section for normal incidence. In other words, very little light will couple inside the PC for angles falling in the range of this region. In these non-normal incidence bandgap-like regions, we would expect to have very low energy velocity just like in the bandgap-like regions we observed at normal incidence.

To make it evident, we show the energy velocity versus the angle of incidence, θ in Figs. 8.17(a), (b) and (c) respectively for the three wavelengths we considered above. We indicate the results with the same coloured lines that we used in the EFC plot in Figs. 8.17 for these three wavelengths. We can clearly see the low energy velocity in the bandgap-like region and we have indicated that with the yellow shading. Indeed we also observe very high reflectance in these regions, at the interface of a semi-infinite PC, as can be seen in Figs. 8.17(d), (e) and (f). Note, reflectance is not exactly equal to unity, similar to what we observed for the normal incidence case.

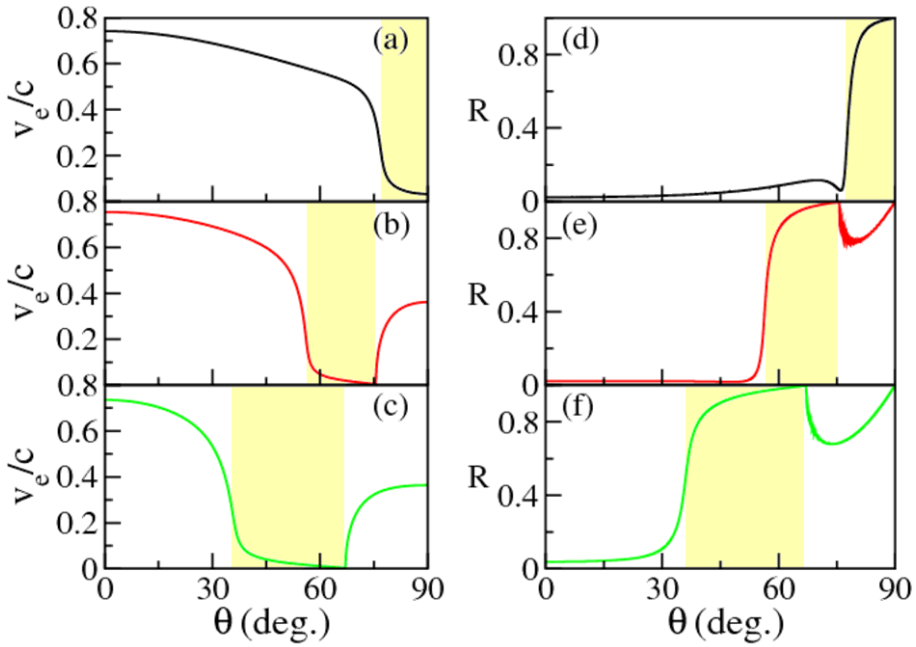

Figure 8.17: (a), (b) and (c) Magnitude of energy velocity, $\mathbf{v_e}$ versus the angle of incidence θ for SiC-BaF_2 1D-PC of Fig. 8.7 at three wavelengths 10 μm (black-lines), 10.5 μm(green-lines) and 11 μm (red-lines) respectively. (d), (e) and (f) are same as (a), (b) and (c) respectively, but for the reflectance, R from an essentially semi-infinite SiC-BaF_2 1D-PC (500 unit cells are taken). The yellow shaded region designate the angular bandgap-like region.

We discussed before that the spectral transition from allowed to bandgap-like region is not abrupt for normal incidence. Likewise the angular transition from allowed bands to bandgap-like behaviour is also not abrupt. It may be useful to attempt to have a quantity to determine which modes fall within a bandgap-like region and which within the band region. Therefore, we use the figure of merit, FOM that has been used in metamaterials [45–48] and photonic crystals [40]. For the particular case of PCs it is defined as [40]:

$$\text{FOM} = \frac{|\text{Re}(q)|}{\text{Im}(q)}. \tag{8.37}$$

We show the results of the FOM versus the angle of incidence in Figs. 8.18(a), (b) and (c), for the same three wavelengths considered above. We indicate the angular bandgap-like regions in Fig. 8.18 with yellow shading, where reflectance was high and energy velocity was small in Fig. 8.17. Although the FOM is much smaller in these shaded regions than the band regions, it is still quite high. Therefore, we find that the FOM may not be a good measure for classification of a photonic crystal region as band-like or bandgap-like. On the other hand, energy velocity is consistently near-zero in the bandgap-like region. Therefore, we are going to rely on the

energy velocity, to make the determination of a region as a band or a bandgap-like region. This low energy velocity regime coincides with the existence of a high Im(q).

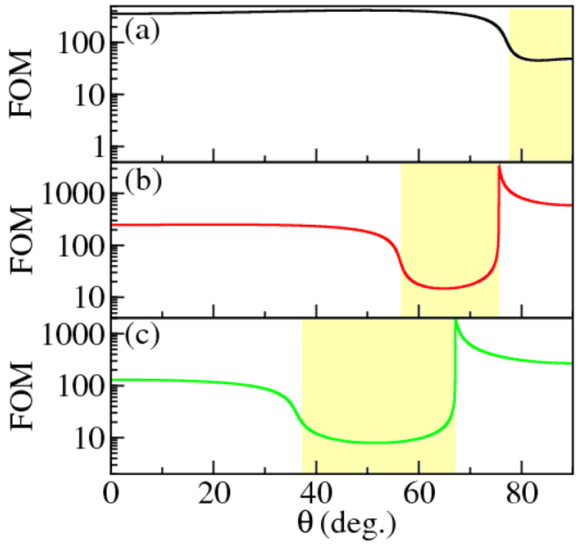

Figure 8.18: (a), (b) and (c) Figure of merit, FOM versus the angle of incidence θ for SiC-BaF_2 1D-PC of Fig. 8.7 at three wavelengths 10 μm (black-line), 10.5 μm(green-line) and 11 μm (red-line) respectively. The yellow shaded region represents the angular bandgap-like region as in Fig. 8.17.

So although EFC may not be appropriate to be employed in a wavevector type of formalism for the determination of the refracted angle, they provide a quick picture for the angular range where one can expect a bandgap-like behaviour, by observing the high Im(q). In the following, we will calculate the predicted angle of refraction by calculating the group velocity, and by calculating the energy velocity, and make a comparison between the two.

8.3.4 Propagation analysis in 1D-loss PCs for non-normal incidence: group and energy velocity predictions

We depict the refraction process in the schematic diagram in Fig. 8.19. In this figure $\mathbf{v_{inc}}$ represents both the group velocity and the energy velocity of the incident wave, since both are the same in air. However, we let the refracted wave velocity $\mathbf{v_{ref}}$ to represent either the energy velocity or the group velocity, which we note can be different inside a lossy PC. This means that the refracted angles ϕ determined from the group velocity and the energy velocity will in general be different. In the following we will calculate both and compare them.

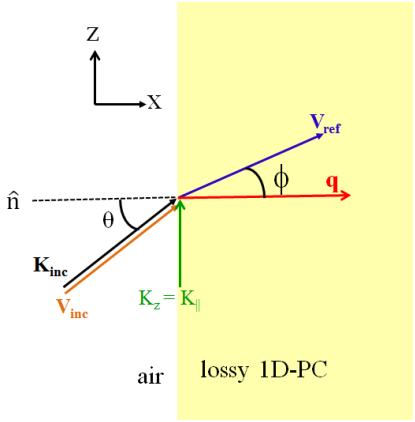

Figure 8.19: Angle of refraction, ϕ inside a lossy 1D-PC for an EM wave incident at an angle θ at the PC interface. The incident wavevector, $\mathbf{k_{inc}}$ (black-arrow), Bloch wavevector, $\mathbf{q}$ (red-arrow) and the parallel component of the incident wavevector, $\mathbf{k}_{||} = \omega/c \sin\theta\hat{z}$ (green-arrow) are indicated. The propagation velocity of the incident wave $\mathbf{v_{inc}}$, (orange-arrow) is indicated. We represent the velocity of the refracted wave, $\mathbf{v_{ref}}$ with the blue-arrow that we let it to represent either the group velocity or the energy velocity.

First we evaluate the angle of refraction, ϕ calculated from the group velocity for an EM wave incident on a lossy PC at an angle, θ. From the schematic diagram in Fig. 8.19, the angle of refraction, ϕ can be obtained as:

$$\tan(\phi) = \frac{\mathrm{v}_{gz}}{\mathrm{v}_{gx}}, \tag{8.38}$$

where $\mathrm{v}_{gx} = \frac{\partial\omega}{\partial \mathrm{Re(q)}}$ and $\mathrm{v}_{gz} = \frac{\partial\omega}{\partial k_z}$ are the x and z components of the group velocity respectively.

Although, the calculation of such angle ϕ from Eq. 8.38 may be quite straightforward for lossless 1D-PCs, it is somewhat more elaborate for lossy 1D-PCs. We will start by splitting the dispersion relation of lossy 1D-PCs into its real and imaginary parts, which was previously adopted in Ref. [49] to calculate the complex dispersion relation of lossy 1D-PCs. However, the group velocity calculations were not performed in Ref. [49] for such case. The dispersion relation of lossy 1D-PCs for angular incidence at angle θ, is given by Eq. 2.104 in Chapter 2:

$$\cos\,(\mathrm{qa}) = \cos(k_{1x})\cos(k_{2x}) - \frac{1}{2}\left(\frac{k_{1x}}{k_{2x}} + \frac{k_{2x}}{k_{1x}}\right)\sin(k_{1x})\sin(k_{2x}), \tag{8.39}$$

where k_{1x} and k_{2x} represent the wavevectors along the stacking direction x inside the two PC constituents, medium 1 and medium 2 respectively. These are given by:

$$k_{1x} = \sqrt{\varepsilon_1 - \sin^2\theta}\,\frac{\omega}{c} \quad \text{and} \quad k_{2x} = \sqrt{\varepsilon_2 - \sin^2\theta}\,\frac{\omega}{c}. \tag{8.40}$$

Since the Bloch wavevector is complex for lossy PCs, we have $\mathrm{q} = \mathrm{q}' + i\mathrm{q}''$ where q' and q'' represent the real and imaginary parts of the Bloch wavevector respectively. Therefore, we can rewrite the above equation as:

$$\cos(\mathrm{q}'\mathrm{a})\cos(\mathrm{q}''\mathrm{a}) - i\sin\,(\mathrm{q}'\mathrm{a})\sin\,(\mathrm{q}''\mathrm{a}) = A + iB, \tag{8.41}$$

where A and B represent the real and imaginary parts of the right-hand-side of Eq. 8.41. In the above equation, by separating the real and imaginary parts, we get:

$$\cos(\mathrm{q}'\mathrm{a})\cos(\mathrm{q}''\mathrm{a}) = A = \mathrm{Re}\left(\cos(k_{1x})\cos(k_{2x}) - \frac{1}{2}\left(\frac{k_{1x}}{k_{2x}} + \frac{k_{2x}}{k_{1x}}\right)\sin(k_{1x})\sin(k_{2x})\right). \tag{8.42}$$

$$-\sin\,(\mathrm{q}'\mathrm{a})\sin\,(\mathrm{q}''\mathrm{a}) = B = \mathrm{Im}\left(\cos(k_{1x})\cos(k_{2x}) - \frac{1}{2}\left(\frac{k_{1x}}{k_{2x}} + \frac{k_{2x}}{k_{1x}}\right)\sin(k_{1x})\sin(k_{2x})\right). \tag{8.43}$$

By differentiating the left-hand-side expressions of the above two equations with respect to angular frequency, ω, we will obtain:

$$\sin(\mathrm{q}'\mathrm{a})\,\frac{\partial(\mathrm{q}'\mathrm{a})}{\partial\omega}\cosh(\mathrm{q}''\mathrm{a}) + \cos(\mathrm{q}'\mathrm{a})\sinh(\mathrm{q}''\mathrm{a})\,\frac{\partial(\mathrm{q}''\mathrm{a})}{\partial\omega} = \frac{\partial A}{\partial\omega}. \tag{8.44}$$

$$-\left(\cos(\mathrm{q}'\mathrm{a})\,\frac{\partial(\mathrm{q}'\mathrm{a})}{\partial\omega}\sinh(\mathrm{q}''\mathrm{a}) + \sin(\mathrm{q}'\mathrm{a})\cosh(\mathrm{q}''\mathrm{a})\,\frac{\partial(\mathrm{q}''\mathrm{a})}{\partial\omega}\right) = \frac{\partial B}{\partial\omega}. \tag{8.45}$$

The above two equations are a system of linear equations with variables $\frac{\partial(\mathrm{q}'\mathrm{a})}{\partial\omega}$ and $\frac{\partial(\mathrm{q}''\mathrm{a})}{\partial\omega}$. Therefore, we can solve for $\frac{\partial(\mathrm{q}'\mathrm{a})}{\partial\omega}$, by expressing these equations in a matrix form as:

$$\begin{bmatrix} \sin(\mathrm{q}'\mathrm{a})\,\cosh(\mathrm{q}''\mathrm{a}) & \cos(\mathrm{q}'\mathrm{a})\sinh(\mathrm{q}''\mathrm{a}) \\ -\cos(\mathrm{q}'\mathrm{a})\sinh(\mathrm{q}''\mathrm{a}) & -\sin(\mathrm{q}'\mathrm{a})\cosh(\mathrm{q}''\mathrm{a}) \end{bmatrix} \cdot \begin{bmatrix} \frac{\partial(\mathrm{q}'\mathrm{a})}{\partial\omega} \\ \frac{\partial(\mathrm{q}''\mathrm{a})}{\partial\omega} \end{bmatrix} = \begin{bmatrix} \frac{\partial A}{\partial\omega} \\ \frac{\partial B}{\partial\omega} \end{bmatrix}. \tag{8.46}$$

That implies:

$$\frac{\partial(\mathrm{q}'\mathrm{a})}{\partial\omega} = \frac{\begin{vmatrix} \frac{\partial A}{\partial\omega} & \cos(\mathrm{q}'\mathrm{a})\sinh(\mathrm{q}''\mathrm{a}) \\ \frac{\partial B}{\partial\omega} & -\sin(\mathrm{q}'\mathrm{a})\cosh(\mathrm{q}''\mathrm{a}) \end{vmatrix}}{\begin{vmatrix} \sin(\mathrm{q}'\mathrm{a})\,\cosh(\mathrm{q}''\mathrm{a}) & \cos(\mathrm{q}'\mathrm{a})\sinh(\mathrm{q}''\mathrm{a}) \\ -\cos(\mathrm{q}'\mathrm{a})\sinh(\mathrm{q}''\mathrm{a}) & -\sin(\mathrm{q}'\mathrm{a})\cosh(\mathrm{q}''\mathrm{a}) \end{vmatrix}}, \tag{8.47}$$

where $|..|$ designates the determinant. Since the denominator in the above equation is equal to one, we can simplify the above equation as:

$$\frac{\partial(\mathrm{q}'\mathrm{a})}{\partial\omega} = -\frac{\partial A}{\partial\omega}\sin(\mathrm{q}'\mathrm{a})\cosh(\mathrm{q}''\mathrm{a}) - \frac{\partial B}{\partial\omega}\cos(\mathrm{q}'\mathrm{a})\sinh(\mathrm{q}''\mathrm{a}). \tag{8.48}$$

Now by multiplying both sides with $\frac{\partial\omega}{\partial k_z}$, we get:

$$\frac{\partial\omega}{\partial k_z}\frac{\partial(\mathrm{q}'\mathrm{a})}{\partial\omega} = -\frac{\partial A}{\partial k_z}\sin(\mathrm{q}'\mathrm{a})\cosh(\mathrm{q}''\mathrm{a}) - \frac{\partial B}{\partial k_z}\cos(\mathrm{q}'\mathrm{a})\sinh(\mathrm{q}''\mathrm{a}). \tag{8.49}$$

That implies:

$$\mathrm{a}\frac{\mathrm{v}_{gz}}{\mathrm{v}_{gx}} = -\frac{\partial A}{\partial k_z}\sin(\mathrm{q}'\mathrm{a})\cosh(\mathrm{q}''\mathrm{a}) - \frac{\partial B}{\partial k_z}\cos(\mathrm{q}'\mathrm{a})\sinh(\mathrm{q}''\mathrm{a}). \tag{8.50}$$

So we get from Eq. 8.38:

$$\phi = \tan^{-1}\left(\frac{-\frac{\partial A}{\partial k_z}\sin(\mathrm{q}'\mathrm{a})\cosh(\mathrm{q}''\mathrm{a}) - \frac{\partial B}{\partial k_z}\cos(\mathrm{q}'\mathrm{a})\sinh(\mathrm{q}''\mathrm{a})}{\mathrm{a}}\right). \tag{8.51}$$

In the above equation, we calculate $\frac{\partial A}{\partial k_z}$ and $\frac{\partial B}{\partial k_z}$ numerically by taking the central differences of A, B in the right-hand-side expressions of Eqs. 8.42 and 8.43 at each k_z respectively. By using the above equation, we evaluate the angle of refraction ϕ for wavelengths 10 µm, 10.5 µm and 11 µm. We plot the results versus angle of incidence θ in Fig. 8.20 with red-solid lines.

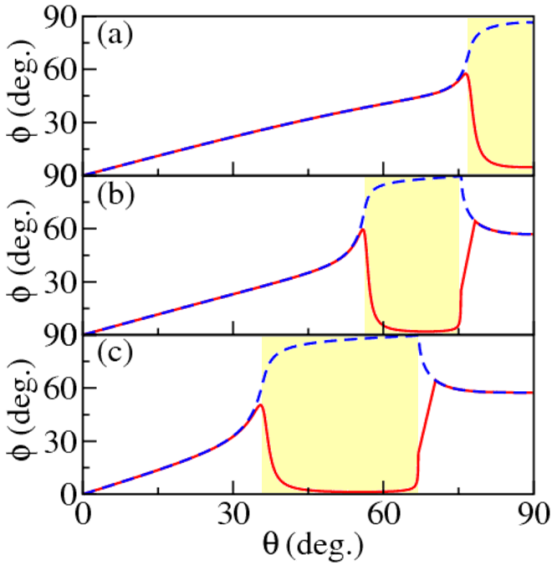

Figure 8.20: (a), (b) and (c) Angle of refraction ϕ, versus angle of incidence θ for SiC-BaF_2 1D-PC of Fig. 8.7 at three wavelengths 10 µm, 10.5 µm and 11 µm respectively. Red-solid and blue-dashed lines indicate the results obtained from Eq. 8.51 and Eq. 8.53 and respectively.

We will compare these angles of refraction, ϕ, results obtained from the group velocity with the angle of refraction determined from the energy velocity in the

following. Similar to Eq. 8.38, the angle of refraction from the energy velocity can be obtained as:

$$\tan(\phi) = \frac{\mathrm{v}_{ez}}{\mathrm{v}_{ex}}, \tag{8.52}$$

where $\mathrm{v}_{ex} = \frac{<\overline{\mathrm{S}_x}>}{<\overline{\mathrm{U}}>}$ and $\mathrm{v}_{ez} = \frac{<\overline{\mathrm{S}_z}>}{<\overline{\mathrm{U}}>}$ are the x- and z-components of the energy velocity respectively. That implies:

$$\phi = \tan^{-1}\left(\frac{<\overline{\mathrm{S}_z}>}{<\overline{\mathrm{S}_x}>}\right), \tag{8.53}$$

where $<\overline{\mathrm{S}_x}>$ and $<\overline{\mathrm{S}_z}>$ represent the x- and z-components of the time-averaged Poynting vectors respectively, which we evaluate using the TMM method. Here $<\ldots>$ designates the spatial average of these quantities within a unit cell of the lossy PC taken similarly as in the case of Eq. 8.35. Now from Eq. 8.53, we evaluate the angle of refraction, ϕ for the same three wavelengths considered above and plot the results in Fig. 8.20 with the blue-dashed lines.

We can clearly notice that the angle of refraction predicted from the group velocity deviates from the angle of refraction predicted from the energy velocity in the angular regimes that correspond to the bandgap-like region identified in Fig. 8.17 and here with a yellow shaded region. However, we can observe that in the angular band regions the refracted angle calculated from the group velocity agrees well with the refracted angle calculated from the energy velocity.

In the following, we will set-up a Finite-Difference Time-Domain (FDTD)-based numerical simulation to verify the predicted results for the angle of refraction. We attempt to conduct these numerical simulations only for the angles in the band regions, since the angles in the bandgap-like region have a very high reflectivity and thus it is not possible to clearly observe these in the numerical simulation.

8.3.5 Propagation analysis in 1D-lossy PCs for non-normal incidence: Numerical observations

For this purpose, a commercial-grade simulator based on the Finite-Difference Time-Domain (FDTD) method was used [25] as we described in the Chapter 2. In this set-up, we simulate a thirty-unit-cell SiC-BaF_2 1D-PC of Fig. 8.7 with a lateral width of 900 µm embedded in vacuum as shown in Fig. 8.21. We apply open boundary conditions in both x- and z-directions. The permittivity of the SiC is

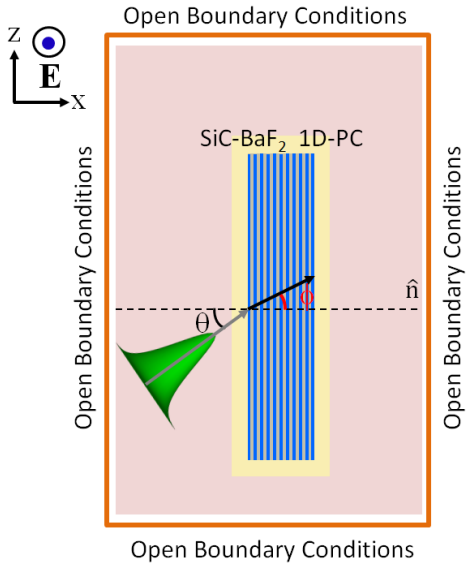

Figure 8.21: Schematic diagram of the simulation set-up in the FDTD simulator. The yellow shaded region represents the region where a user defined mesh has been used. The brown region represents the region where the default mesh of Lumerical simulator [25] has been used. The incident angle, θ, refracted angle, ϕ, incident wave (grey-arrow) and refracted wave (black-arrow) are indicated.

represented in the simulator with a Lorentzian function [27], same as the one in Eq. 1.1, and with the same parameters we used in the TMM method. The permittivity of BaF_2 is taken to be 1.8496. Further, we used a user defined mesh of size 25 nm and 200 nm in the x- and z-directions respectively around the 1D-PC-slab structure. The mesh size of 25 nm in the x-direction allows a sufficient integer number of grids within the SiC layer and BaF_2 layer, that ensures accurate representation of the 1D-PC structure in the simulator. However, in the lateral direction the PC structure is not changing. Therefore, a 200 nm grid size is adequate in this direction. We indicate this user defined mesh in Fig. 8.21 with the yellow shaded region. For the simulation region outside the yellow region, we used the software's default mesh which produces a varying grid size of the order of $\lambda_{\text{free}}/30$ [25], which is adequate for the vacuum region. We represent this mesh with the brown shaded region in Fig. 8.21.

We use a highly collimated Gaussian EM wave incident on this PC at an angle θ, with the interface as shown in Fig. 8.21. We repeat the simulation for different angles of incidence by changing the angle of incidence for this Gaussian source. We chose the particular angles to span the band region observed in Fig. 8.20(b). In each simulation, we obtain the y-component of the electric-field $E_y(x, z)$, throughout the simulation region for $\lambda_{\text{free}} = 10.5\,\mu\text{m}$ with a procedure explained in Section 2.6 of

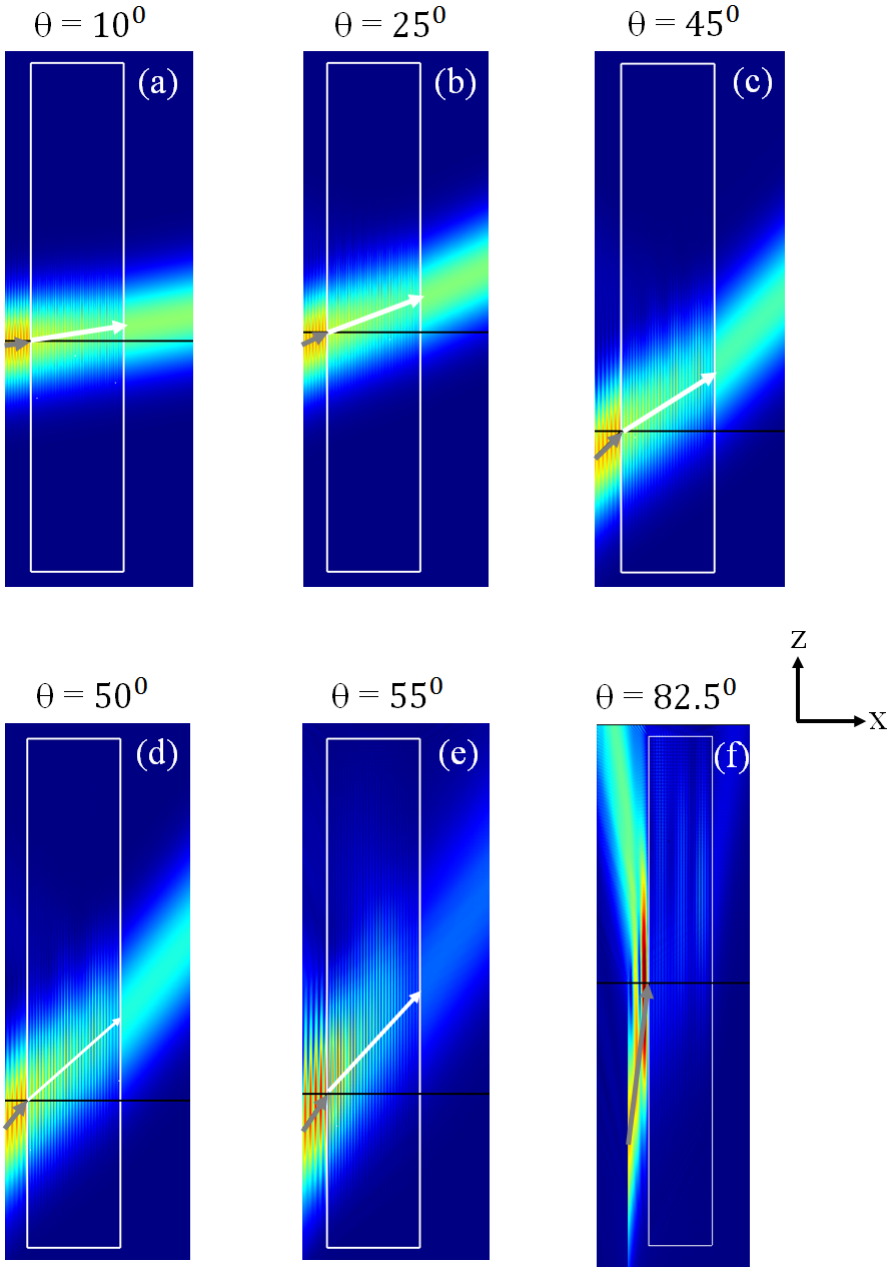

Figure 8.22: The magnitude of the y-component of the electric-field, $|E_y(x,z)|$ in the numerical refraction simulation for a SiC-BaF_2 1D-PC with a lattice constant of 5.5 µm and filling ratio 0.05. The lateral width of the PC is 900 µm. Panels (a)-(f) represent results for an angle of incidence θ, equal to 10^0, 25^0, 45^0, 50^0, 55^0, and 82.5^0 respectively. The white-line rectangle indicate the PC bounds. The grey-arrow and white-arrow indicate the propagation direction of the incident and refracted wave respectively.

Chapter 2. We show these electric-field results in Fig. 8.22. Except for the case of 82.5^0, we measure the angle of refraction for the incident angles that we indicated in Fig. 8.22. However, for the case of an 82.5^0 angle of incidence, the Gaussian beam spread in the lateral direction inside the PC is very large as we can observe in Fig. 8.22(f). The wave essentially creeps almost parallel to the interface hitting the top PC bound which distorts the beam profile. As a result an accurate evaluation of the refraction angle cannot be made for this case.

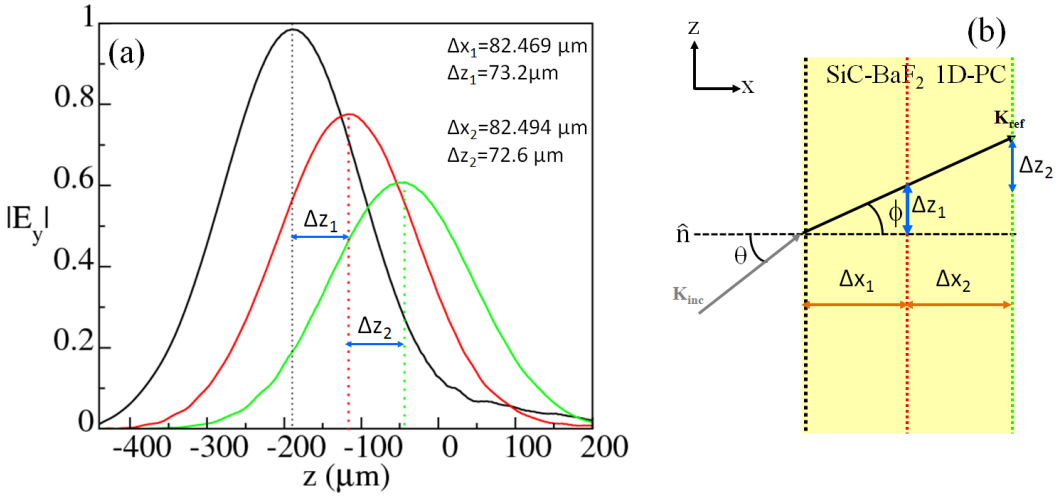

Figure 8.23: (a) Spatial electric-field distributions, $|E_y(x,z)|$ versus the location, z at the entrance (black-dotted line), middle (red-dotted-line) and exit (green-dotted line) of the SiC-BaF_2 1D-PC in the FDTD simulation for the case of an angle of incidence 50^0. (b) Schematics of the refraction process. We indicate the distances Δx_1 and Δx_2 on the x-axis and beam shifts Δz_1 and Δz_2 on the z-axis that we used to determine the angle of refraction ϕ from Eq. 8.53.

For an accurate measurement of the angle of refraction, ϕ, we plot the lateral Gaussian beam profile along z within a distance x, just after the first PC interface, in the middle of the PC and just before the end interface of the PC. i.e we plot the z-profile of the electric-field at $x = 0.0125\,\mu$m, $x = 82.4815\,\mu$m and $x = 164.9755\,\mu$m with $x = 0.0\,\mu$m designating the entrance interface of the PC. We show the results for the case of an incident angle of 50^0 in Fig. 8.23 (a) with a black, red and green line respectively. In the schematic diagram of Fig. 8.23 (b), we indicate the lines where we took the Gaussian beam profiles as black-dotted line, red-dotted line and green dotted line respectively. We denote the distance between the first interface and middle of the PC as Δx_1 and the distance between the middle of the PC to the end interface as Δx_2 as shown in schematics of Fig. 8.23 (b). We measure the corresponding beam shifts as Δz_1 and Δz_2 from the peaks of the Gaussian beam profiles as shown in Fig. 8.23 (a). By using the Δx and Δz measurements, we can obtain the angle of refraction ϕ from:

$$\phi = \frac{\phi_1 + \phi_2}{2} \qquad \text{with } \phi_1 = \tan^{-1}\left(\frac{\Delta z_1}{\Delta x_1}\right) \text{ and } \phi_2 = \tan^{-1}\left(\frac{\Delta z_2}{\Delta x_2}\right). \quad (8.54)$$

By using the above equation, we obtain the angles of refraction for all the angles of incidence indicated in Fig. 8.22, except for the case of 82.5^0. Since an accurate estimation of the refracted angle was not possible in such case due to the large refracted angle. We represent these numerical simulation results as green circles in Fig. 8.24 together with the results obtained before from the group velocity and energy velocity calculations that we represented with the red-solid line and blue-dashed line respectively. We can observe an excellent agreement of these numerical results with the theoretically predicted angle of refraction values, up to the angle of incidence 50^0. However, for the incident angle of 55^0 we observe a small deviation from the FDTD result. We attribute this disagreement to the angular spread of the Gaussian source, in combination with the steep change in reflectance occurring around 55^0, as we see in Fig. 8.17(e).

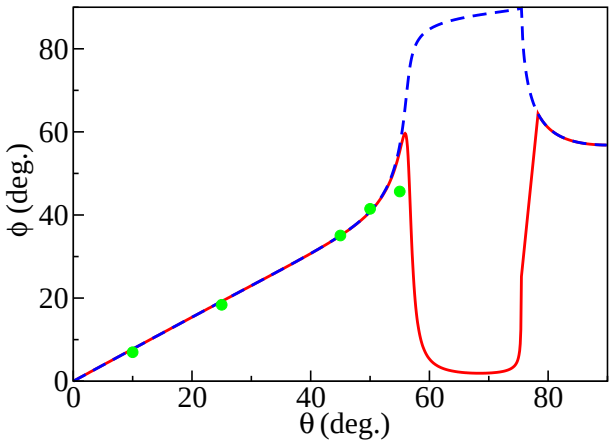

Figure 8.24: Same as Fig. 8.20(b), but now we overlay the FDTD numerical simulation results for the refracted angle, ϕ as green circles.

8.4 Conclusions

We proposed a new alternative approach to define the Bloch impedance even for a general case of lossy 1D-PCs, where the incident medium is different from the constituents of the PC. Our approach for deriving the Bloch impedance is based on the popularly adopted Yariv and Yeh's transfer matrix formalism, which was not done in the literature thus far. This Bloch impedance, allowed us to determine the spectral regions of translucence for a SiC-BaF_2 1D-PC that will be useful for

engineering optical device applications in the Mid-IR regime.

Furthermore, we presented a theory of propagation in lossy 1D-PCs, to determine the propagation type of lossy PC waves, backward-type versus forward-type based on the passivity requirement. We demonstrated the importance of plotting the bandstructure for lossy PCs with the correct sign of the real part of the Bloch wavevector, a practice that is not adopted thus far by the majority of prior studies. In addition, we found that the group velocity is not generally a reliable measure to represent the propagation of EM wave energy in lossy PCs, contrary to the case of lossless PCs. This is because the group velocity can be very different from the energy velocity in some spectral regions with bandgap-like behaviour.

We also demonstrated through the energy velocity calculations that although backward-type modes exist for lossy 1D-PCs, these will not yield negative refraction inside these PCs due to the anisotropy of the modes in the wavevector space. Indeed we observed only positive refraction in the tilted source FDTD numerical simulation. However, we will find out in the next Chapter that we can achieve a negative deflection in a wedged type structure, where the incident light will undergo a 90^0 angle of bending, based on the existence of backward Bloch waves within these lossy 1D-PCs.

Bibliography

[1] P. St. J. Russell, T. A. Birks, and F.DominicLloyd-Lucas, in Confined Electrons and Photons, New Physics and Applications, Vol. **340** of NATO Advanced Studies Institute, Series B: Physics, edited by E. Burstein and C. Weisbuch (Plenum, New York, 1995), p. 585.

[2] M. Notomi, "Theory of light propagation in strongly modulated photonic crystals: Refraction like behavior in the vicinity of the photonic band gap," Phys. Rev. B **62**, 10696 (2000).

[3] S. Foteinopoulou and C. M. Soukoulis, "Electromagnetic wave propagation in two-dimensional photonic crystals: A study of anomalous refractive effects," Phys. Rev. B **72**, 165112 (2005).

[4] S. Foteinopoulou and C. M. Soukoulis, "Negative refraction and left-handed behavior in two-dimensional photonic crystals," Phys. Rev. B **67**, 235107 (2003).

[5] S. Foteinopoulou, E. N. Economou, and C. M. Soukoulis, "Refraction in Media with a Negative Refractive Index," Phys. Rev. Lett. **90**, 107402 (2003).

[6] E. Cubukcu, K. Aydin, E. Ozbay, S. Foteinopoulou, and C. M. Soukoulis, "Negative refraction by photonic crystals," Nature (London) **423**, 604 (2003).

[7] S. Foteinopoulou, M. Kafesaki, E. N. Economou, and C. M. Soukoulis,"Backward surface waves at photonic crystals," Phys. Rev. B **75**, 245116 (2007).

[8] S. Foteinopoulou, G. Kenanakis, N. Katsarakis, I. Tsiapa, M. Kafesaki, E. N. Economou and C. M. Soukoulis, "Experimental verification of backward wave propagation at photonic crystal surfaces," Appl. Phys. Lett. **91**, 214102 (2007).

[9] S. Foteinopoulou, "Electromagnetic wave propagation in two-dimensional photonic crystals," Ph.D thesis, Iowa State University (2003).

[10] H. Kosaka, T. Kawashima, A. Tomita, M. Notomi, T. Tamamura, T. Sato, and S. Kawakami, "Superprism phenomena in photonic crystals," Phys. Rev. B**58**, 10096 (1998).

[11] M. Born and E. Wolf, *Principles of Optics : Electromagnetic Theory of Propagation, Interference, and Diffraction of Light*, (University Press, Cambridge, 2006).

[12] F. Shi, Y. Chen, P. Han, and C. M. Soukoulis, "Investigation of one-dimensional photonic bandgap structures containing lossy double-negative metamaterials through the Bloch impedance," J. Opt. Soc. Am. B **30**, 1473-1478 (2013).

[13] S. Boscolo, C. Conti, M. Midrio, and C. G. Someda, "Numerical Analysis of Propagation and Impedance Matching in 2-D Photonic Crystal Waveguides With Finite Length," J. Lightwave Technol. **20**, 304-310 (2002).

[14] F. J. Lawrence, "Photonic crystal antireflection coatings, surface modes, and impedances," Ph.D thesis, CUDOS and Institute of Photonics and Optical Science (IPOS) (2012).

[15] R Biswas, Z.Y. Li and K.M. Ho. "Impedance of photonic crystals and photonic crystal waveguides," Appl. Phys. Lett. **84**, 1254 (2004).

[16] Z. Lu and D. W. Prather. "Calculation of effective permittivity, permeability, and surface impedance of negative-refraction photonic crystals," Opt. Express **15**, 83408345 (2007).

[17] Ruey-Bing (Raybeam) Hwang, *Periodic Structures: Mode-Matching Approach and Applications in Electromagnetic Engineering* (John Wiley and Sons, IEEE Press, 2012).

[18] C. Sabah, F. Urbani, S. Uckun, "Bloch impedance analysis for a left handed transmission line," J. Electr. Eng. **63**, 310-315 (2012).

[19] D. M. Pozar, *Microwave Engineering* (John Wiley and Sons, New York 2003).

[20] R. E. Collin *Foundation for Microwave Engineering* (McGraw-Hill, New York, 1992).

[21] A. Yariv and P. Yeh, *Optical Waves in Crystals: Propagation and Control of Laser Radiation* (Wiley-Interscience, Hoboken 1984).

[22] P. Yeh, *Optical waves in layered media* (Wiley-Interscience, Hoboken 2005).

[23] P. Yeh, A. Yariv, and C. S. Hong, "Electromagnetic propagation in periodic stratified media. I. General theory*," J. Opt. Soc. Am. **67**, 423-438 (1977).

[24] A. Yariv and P. Yeh, "Electromagnetic propagation in periodic stratified media. II. Birefringence, phase matching, and x-ray lasers," J. Opt. Soc. Am. **67**, 438-447 (1977).

[25] Lumerical Solutions, Inc. http://www.lumerical.com/tcad-products/fdtd/

[26] E. D. Palik, *Handbook of Optical Constants of Solids* (Academic Press, 1985).

[27] C. Kittel, *Introduction to Solid State Physics* (John Wiley and Sons, Hoboken, 2005).

[28] P. B. Catrysse and S. Fan, "Near-complete transmission through subwavelength hole arrays in phonon-polaritonic thin films," Phys. Rev. B **75**, 075422 (2007).

[29] F. Abelès, "Recherches sur la propagation des ondes èlectromagnètiques sinusiodales dans les milieux stratifiès. Applicacion aux couches minces," Annales de Physique **5**, 596640, 706782 (1950).

[30] M. Born and E. Wolf, *Principles of optics: electromagnetic theory of propagation, interference and diffraction of light* (Oxford, Pergamon Press, 1964).

[31] N. Mattiucci, M. J. Bloemer, N. Aközbek, and G. D'Aguanno, "Impedance matched thin metamaterials make metals absorbing," Sci. Reports **3**, 3203 (2013).

[32] N. Mattiucci, G. D'Aguanno, N. Akozbek, M. Scalora, and M. J. Bloemer "Homogenization procedure for a metamaterial and local violation of the second principle of thermodynamics," Opt. Comm. **283**, 16131620 (2010).

[33] G. C. R. Devarapu, and S. Foteinopoulou, "Compact photonic-crystal superabsorbers from strongly absorbing media," J. Appl. Phys. **114**, 033504 (2013).

[34] C. Engström, C. Hafner, and K. Schmidt, " Computations of lossy bloch waves in two-dimensional photonic crystals,"J. Comput. Theor. Nanosci. **6**, 1-9 (2009).

[35] B. Jiang, Y. Zhang, Y. Wang, and W. Zheng, "Band structure of photonic crystal with dispersive and lossy materials using Dirichlet-to-Neumann wave vector eigen equation method," J. App. Phys. **112**, 033112 (2012).

[36] T. W. Chang, J .J. Wu, and C. J. Wu, " Complex photonic band structures in a photonic crystal containing lossy semiconductor InSb," Prog. in Electromagn. Research **131**, 153-167, (2012).

[37] I. V. Lindell, S. A. Tretyakov, K. I. Nikoskinen, S. Ilvonen, "BW media-media with negative parameters, capable of supporting backward waves," Microwave Opt. Tech. Lett. **31**, 163-165 (2001).

[38] J. D. Jackson, *Classical Electrodynamics*, (Wiley, Third edition, 1999).

[39] R. Ruppin, "Electromagnetic energy density in a dispersive and absorptive material," Phys. Lett. A **299**, 309312 (2002).

[40] S. Foteinopoulou, M. Kafesaki, E. N. Economou, and C. M. Soukoulis, "Two-dimensional polaritonic photonic crystals as terahertz uniaxial metamaterials," Phys. Rev. B **84**, 035128 (2011).

[41] J. B. Pendry, A.J. Holden, D.J. Robbins, and W.J. Stewart, "Magnetism from Conductors and Enhanced Nonlinear Phenomena," IEEE Trans. Micro. wave Theo. Tech. **47**, 2075-2084 (1999).

[42] R. A. Shelby, D.R. Smith, and S. Schultz, "Experimental Verification of a Negative Index of Refraction," Science **292**, 77 (2001).

[43] C.M. Soukoulis, M. Wegener, "Past achievements and future challenges in the development of three-dimensional photonic metamaterials," Nat. Photonics **5** 523-530 (2011).

[44] R. Loudon, "The propagation of electromagnetic energy through an absorbing dielectric," J. Phys. A **3**, 233245 (1970).

[45] A. J. Hoffman, L. Alekseyev, S. S. Howard, K. J. Franz, D. Wasserman, V. A. Podolskiy, E. E. Narimanov, D. L. Sivco, and C. Gmachl, "Negative refraction in semiconductor metamaterials," Nature Mater. **6**, 946-950 (2007).

[46] C. M. Soukoulis, S. Linden, and M. Wegener, "Negative Refractive Index at Optical Wavelengths," Science **315**, 47-49 (2007).

[47] J. Valentine, S. Zhang, T. Zentgraf, E. Ulin-Avila, D. A. Genov, G. Bartal, and X. Zhang, "Three-dimensional optical metamaterial with a negative refractive index," Nature (London) **455**, 376-379 (2008).

[48] E. N. Economou, M. Kafesaki, C. M. Soukoulis, and T. Koschny, "The Fourth Quadrant in the ε, μ, Plane: A New Frontier in Optics," J. Comp. Theor. Nanoscience **6**, 1827-1836 (2009).

[49] V. Kuzmiak and A. A. Maradudin, "Photonic band structures of one- and two-dimensional periodic systems with metallic components in the presence of dissipation," Phys. Rev. B **55**, 7427-7444 (1997).

9

Propagation in lossy 1D-PCs: Applications

9.1 Chapter Overview

As we discussed in Chapter 1, there is a need for optical beam manipulation components in the Mid-IR regime. However, suitable materials for constructing such optical components are rare in the Mid-IR regime, compared to the visible regime. This is because, many materials that are transparent in the visible regime become opaque in the Mid-IR regime. However, in the previous Chapter, we have demonstrated that we can expand the material base for translucent Mid-IR devices by smartly designing structures with highly lossy materials, that are opaque in bulk form.

In particular, we discussed in Chapter 8 that low filling ratio 1D-PCs constructed with these lossy materials can exhibit translucence over a wide frequency regime with negligible Fabry-Perot fringes in the spectrum. Furthermore, we found that even these simple low filling ratio structures can exhibit backward wave propagation. In this Chapter, we will exploit these two key qualities of the aforementioned lossy PCs to propose a possible device application in the Mid-IR spectrum. Specifically, we will design a wedged structure that causes an extreme bending of light of 90^0 or more.

Currently there is a huge interest for such kind of extreme bending of light

throughout the EM wave spectrum [1–7]. In particular, in the THz spectral regions superbending has been demonstrated by employing anisotropic metamaterials [1, 2], and dispersion engineered plasmonic structures [3]. Similarly in the optical/near-IR region, this extraordinary deflection has been achieved with negative refractive index metamaterials [4], engineered metamaterial Huygen's surfaces [5], graded photonic crystals [6] and smartly designed corner waveguides [7]. In the Mid-IR region Hoffman *et al.* [8], showed negative refraction with a semiconductor based metamaterials, but a large deflection angle from the incident direction was not demonstrated. To our knowledge a 90^0 bend has not been demonstrated thus far in the Mid-IR spectral regime, which will be the subject matter of investigation in this Chapter.

In particular, in this Chapter we design a wedged structure consisting of SiC 1D-PCs that can bend light that beyond 90^0, by exploiting backward propagation of EM waves in such lossy PCs. Our design is advantageous as it functions with lossy semiconductors. Thus it entails flexibility for the choice of materials to be incorporated, beyond the currently available few materials that are widely used in the Mid-IR frequency regime. Furthermore, our PC-based structure has certain advantages over the metamaterial structures. The latter are either deep-subwavelength multilayers [8] or involve resonant structures with complex designs which are harder to realise. Resonant metamaterials tend also to have properties that are very sensitive to fabrication defects [9]. On the other hand, PC multilayer structures have periodicity about a half of the free space wavelength and are so simpler to fabricate.

Before proceeding to our results and analysis we briefly recap the methods employed in this chapter. Bandstructure and transmission results have been calculated with computer programs that have been developed based on Yariv and Yeh's Transfer Matrix Method (TMM) [10–13] that we have presented in Chapter 2. The design determination of the wedged structure is based on the theoretical framework developed in Chapter 8. The electric-field maps have been calculated by setting up the wedged structure, as we detailed in section 9.4 of this chapter, in a commercial Finite-Difference Time-Domain (FDTD) solver, in particular the Lumerical EM simulator [14]. Details of the underlying physical principles of such solver have been presented in section 2.6 of Chapter 2.

9.2 Designing the 1D SiC PC superbending wedged structure

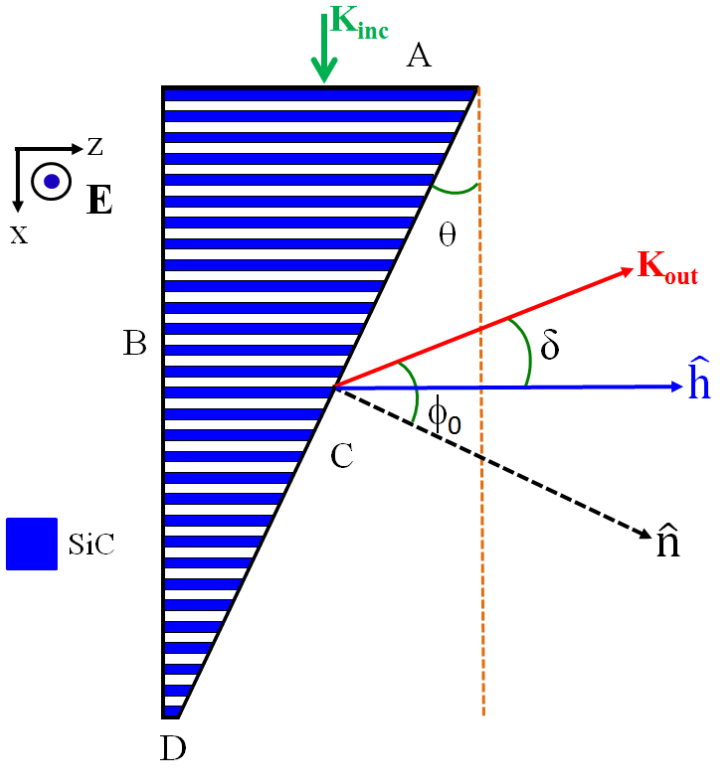

Figure 9.1: Schematics of the wedged structure constructed with a SiC 1D-PC. The blue block regions represent SiC and the white regions represent air. The polarisation of the incident EM wave is indicated. The normal, $\hat{n}$ to the slanted interface is indicated with a black-dashed line. The incident wavevector, $\mathbf{K_{inc}}$ and outgoing wavevector, $\mathbf{K_{out}}$ are indicated with green and red arrows respectively. The angle of the wedge, θ, and the angle of the outgoing wave with the normal, ϕ_0 are also designated. We indicate a horizontal line in the direction 90^0 to the stacking direction of the PC with a blue arrow. The angle of the outgoing beam, with this horizontal line is designated with δ.

We show the schematics of the wedged structure constructed with a SiC 1D-PC in Fig. 9.1. We consider the angle of the wedge as θ, as shown in Fig. 9.1. This is the angle between the slanted interface and the stacking direction x. We consider that EM waves are incident on the entry face of the wedge along the $+x$ direction. We represent this with the incident wavevector, $\mathbf{K_{inc}}$ as indicated with a green arrow in Fig. 9.1. Similarly we represent the outgoing wave with a red arrow with its wavevector, $\mathbf{K_{out}}$. We represent the angle of this outgoing wave with the normal to the exit face of the wedge with ϕ_0. Our aim is to get this outgoing wave at an angle of 90^0, if not more with respect to the incident wave. This would imply that the angle, δ, indicated in the schematics of Fig. 9.1 should be zero or positive. From

the geometry of the schematics, we can observe that, to achieve such superbending, light should undergo extreme deflection from the wedged structure, which is not possible, in wedges made from natural materials. In the following, we will discuss the key requirements and the corresponding controlling parameters for achieving such extreme bending of light with the 1D-PC superprism.

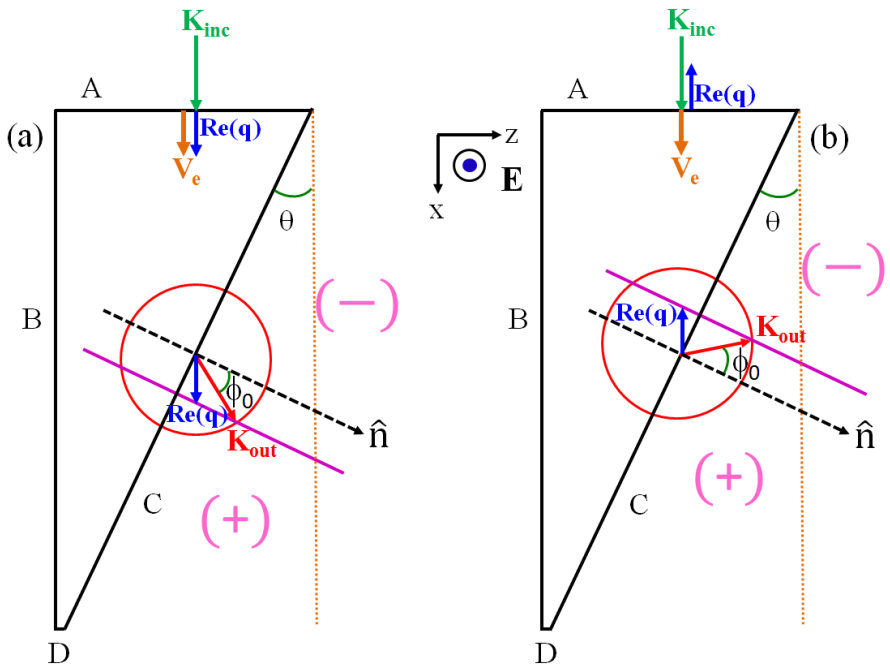

Figure 9.2: (a) Deflection process in a wedged structure is shown schematically for the case of a forward-type EM wave propagation inside the wedged structure. The red circles represent the equi-frequency contours of the air medium. The real part of the Bloch wavevector and the energy velocity are indicated with a blue arrow and an orange arrow respectively. The normal, n̂ to the slanted interface is indicated with a black-dashed line. The incident wavevector, $\mathbf{K_{inc}}$ and outgoing wavevector, $\mathbf{K_{out}}$ are indicated with green and red arrows respectively. The angle of the wedge, θ, and angle of the outgoing wave with the normal, ϕ_0 are also designated. (b) same as (a) but for the case of a backward-type EM wave propagation inside the wedged structure.

For a good broadband performance of the superprism, the PC should be as translucent as possible over a broad frequency regime. We saw in Chapter 8 that this was possible with a low filling ratio SiC-air 1D-PC. The second key requirement is the existence of a backward-type propagation in these PCs [15–19]. To understand this requirement, we show the deflection process in the PC-wedged structure of Fig. 9.1. Suppose, a normally incident EM wave with wavevector, $\mathbf{K_{inc}}$ excites a forward-type propagating wave inside the PC-wedge with a Bloch wavevector Re(q) as shown in Fig. 9.2(a). Re(q) points in the $+x$ direction since it is a forward type Floquet Bloch mode (see blue arrow in Fig. 9.2(a)).

Now to determine the outgoing beam direction at the exit face of the wedge, we apply the conservation principle for the parallel component of the wavevector at this face, $k_{||}$ [20]. To represent this $k_{||}$ conservation we draw a line parallel to the normal of the slanted interface (see magenta line in Fig. 9.2(a)) at a distance equal to $k_{||} = \mathrm{Re(q)}\cos\theta$, from the origin of the wavevector space, where the positive direction of the slanted axis points south-west. From the intersection of this construction line with the EFC of the air medium (red-circle in the figure), the wavevector $\mathbf{K_{out}}$, of the outgoing beam is determined. We indicate this with a red-arrow, in Fig. 9.2(a). We see that this outgoing beam is in the positive hemisphere from the surface normal, just as in the case of any wedge made from a conventional dielectric. Clearly then PC-wedges that enable forward-type EM waves do not offer superprism capabilities.

Thus we consider the case where a normally incident EM wave excites a backward-type propagating wave inside the wedged structure as schematically shown in Fig. 9.2(b). Since we consider a backward-type Bloch wave, Re(q) flips its sign when it crosses the entry face of the wedge, and points in the $-x$ direction. As before, in order to determine the outgoing beam direction, we apply the $k_{||}$ conservation at the slanted interface. However, now that $k_{||} = -|\mathrm{Re(q)}|\cos\theta$, is negative, it will result in an outgoing beam with a wavevector $\mathbf{K_{out}}$ in the negative hemisphere. In other words, the incident beam will make a huge deflection beyond whats possible with natural prisms.

The possibility to have light deflection from a prism in the negative hemisphere has been thoroughly explored both theoretically and experimentally with negative refractive index prisms [4, 21, 22] and also prisms constructed from PCs where backward-type Floquet-Bloch waves propagate [16–18]. However, the possibility to have Mid-IR light superdeflecting prisms demonstrating deflection beyond 90^0, that are made from 1D-PC structures, which are simple to fabricate, has not been reported. This is what we plan to investigate in the following.

In the above analysis we made the silent assumption that only the primary beam emanating from the Floquet Bloch wave outcouples into the outgoing area, after the slanted interface. The truth is that higher order Bragg beam couplings commonly exist whenever periodic interfaces are considered [16, 23, 24]. Therefore it is important that the backward EM mode condition is met concurrently with the condition of suppression of the higher order Bragg couplings [16, 23, 24]. The latter condition is crucial in order to have out-coupling of only a single beam after the

slanted interface of the wedge and thus obtain the desired superbending prism effect. Otherwise, one would have multiple outgoing beams in multiple directions in the area after the slanted interface of the wedge [16].

In the following, we discuss the control parameters of lossy PCs that should be carefully tuned to satisfy the following three requirements: translucence, existence of backward waves, and suppression of higher order Bragg couplings. These are the conditions that must be simultaneously satisfied in the 90^0 bending PC superprism. The main structural parameters of the SiC PC we can change are the filling ratio and the lattice constant. In Chapter 8, we showed that a high filling ratio destroys the translucence, due to the increased reflectance and absorptance and the increased oscillatory strength of the Fabry-Perot fringes. Thus, we will consider only PCs with a low filling ratio. That leaves the lattice constant to be the only parameter that may control the type of propagation, backward versus forward in these PCs. Now coming to the third requirement, i.e. higher order Bragg wave suppression at the exit face, we will demonstrate that the controlling parameters are the angle of the wedged structure, θ, and the lattice constant, a. Therefore, cumulatively the lattice constant and the angle of the wedge appear to be the key controlling parameters for the design of the 90^0 light bending superprism.

Before considering specific cases we should first explore the relation and permissible values between the wedge angle, θ and the lattice constant, a that ensures the suppression of the higher order Bragg coupling. We will assume the backward-type propagation inside the 1D-PC since as we discussed this would be needed for the superprism design. Therefore, from the geometry of the problem as shown in Fig. 9.2(b), and conservation of the parallel component of the wavevector at the slanted interface we have:

$$\sin\phi_0 = \frac{k_{||}}{k_{out}} = \frac{-|\mathrm{Re(q)}|\cos\theta}{\frac{\omega}{c}} = \frac{-\left|\mathrm{Re}\left(\frac{\mathrm{qa}}{2\pi}\right)\right|\cos\theta}{\frac{\mathrm{a}}{\lambda}}, \tag{9.1}$$

where $k_{||} = -|\mathrm{Re(q)}|\cos\theta$ is the parallel component of the wavevector at the slanted wedge interface, ω is the frequency of the incident EM wave, λ is the wavelength of the incident EM wave and c is the speed of light in vacuum. The above relation gives the outgoing angle, ϕ_0, of the primary beam after the exit face of the PC wedge. However, as we discussed above many higher order Bragg beams can also emerge [16, 23, 24]. Higher order beams may couple after the slanted interface with

angles, ϕ_n given by:

$$\sin\phi_n = \frac{\left[-\left|\mathrm{Re}\left(\frac{qa}{2\pi}\right)\right| + n\right]\cos\theta}{\frac{a}{\lambda}}. \tag{9.2}$$

Here n represents the order of the Bragg beam, thus it is an integer that takes values from $-\infty$ to $+\infty$. Note that the negative sign of $-|\mathrm{Re}\ (q)|$ signifies that the primary beam appears in the negative hemisphere.

We note that the existence of higher order Bragg outcouplings is a major hindrance for the functionality of the left handed metamaterial wedges as well [24]. Overcoming this problem and having the desirable primary beam in the negative hemisphere, without having the higher order Bragg couplings is a considerable challenge to meet [16, 23, 24]. From Eq. 9.2 it is evident that to avoid the coupling to the higher order Bragg beams, the value of $|\sin\phi_n|$ should be more than 1 for any $n \neq 0$. It is easy to show that:

$$\left|1 - \left|\mathrm{Re}\left(\frac{qa}{2\pi}\right)\right|\right| < \left|-1 - \left|\mathrm{Re}\left(\frac{qa}{2\pi}\right)\right|\right| < \left|-2 - \left|\mathrm{Re}\left(\frac{qa}{2\pi}\right)\right|\right| < \cdots, \tag{9.3}$$

and

$$\left|1 - \left|\mathrm{Re}\left(\frac{qa}{2\pi}\right)\right|\right| < \left|2 - \left|\mathrm{Re}\left(\frac{qa}{2\pi}\right)\right|\right| < \left|3 - \left|\mathrm{Re}\left(\frac{qa}{2\pi}\right)\right|\right| < \cdots, \tag{9.4}$$

since the maximum value of $\left|\mathrm{Re}\left(\frac{qa}{2\pi}\right)\right|$ is 0.5, which is less than 1. From the above inequalities, it is obvious that, if $|\sin\phi_n| > 1$ is satisfied for $n = 1$, it will be automatically satisfied for any other $n \neq 0$. This is true for a backward-type Floquet-wave only. Therefore, to suppress the coupling to the higher order Bragg beams, it suffices to show that:

$$|\sin\phi_1| = \frac{\left[1 - \left|\mathrm{Re}\left(\frac{qa}{2\pi}\right)\right|\right]\cos\theta}{\frac{a}{\lambda}} > 1, \tag{9.5}$$

On the other hand, to have the primary beam outcoupled from the slanted interface, we should have:

$$|\sin\phi_0| < 1. \tag{9.6}$$

In the following, we will investigate the parameter space within which both these conditions given by Eqs. 9.5 and 9.6 are satisfied simultaneously.

Normally it is very difficult to have translucence for lossy 1D-PCs in a spectral regime close to the transverse-phonon frequency, ω_T, which is at free space wavelength of 12.6 µm for the case of SiC. In the previous Chapter we have seen that for the case of the SiC-air 1D-PC, such translucence regime is possible between

10.0 µm and 11.0 µm, away from the transverse-phonon frequency, ω_T. Therefore, we will consider only this 10.0 µm - 11.0 µm spectral regime while designing the wedged structure. As we discussed in Chapter 1, this Mid-IR spectral regime is especially interesting for bio-sensing applications since pathogens and bio-molecules have their fingerprints [25–27] in this region. With the operational spectrum fixed, we will explore in the following the values for the lattice constant, a, the wedge angle, θ and the normalised Bloch wavevector $\mathrm{Re}\left(\frac{qa}{2\pi}\right)$ where the condition in Eq. 9.5 is satisfied ensuring the suppression of the higher order beams. At the same we will look for the subset of values where in addition $|\sin\phi_0| < 1$ is satisfied to ensure that the primary beam outcouples and does not total internally reflect within the wedge [28].

For this purpose, we consider three wedge angles, θ equal to 30^0, 45^0 and 60^0 respectively. For each of these wedge angles, we consider three wavelengths of operation, 10.0 µm, 10.5 µm and 11.0 µm that cover the spectral regime of interest. We depict the parametric space of the lattice constant, a and the normalised Bloch wavevector $\mathrm{Re}\left(\frac{qa}{2\pi}\right)$, in Fig. 9.3, for each of the wedge angles, θ at these three wavelengths. Note, in Fig. 9.3 we consider only the negative values for $\mathrm{Re}\left(\frac{qa}{2\pi}\right)$, since we will consider only backward-type Bloch waves inside the PC. In Fig. 9.3, the white line essentially separates the parameter space (a, q) into regions when $|\sin\phi_1| < 1$, thus higher order bragg beams exist (blue regions in Fig. 9.3) and regions with $|\sin\phi_1| > 1$ i.e. higher order bragg couplings are suppressed (green and orange regions in Fig. 9.3). Then the orange regions represent the part of the (a, q) parametric space where also the condition $|\sin\phi_0| < 1$ is satisfied ensuring the outcoupling of the primary beam. Therefore, we will look to have the structural parameters falling within this orange region.

We draw the attention of the reader to the left hand side panels (a), (b) and (c) in Fig. 9.3 that correspond to the case of a wedge with angle, θ equal to 30^0. It is obvious that the orange region is larger i.e. we have a larger parametric space where both condition are met for this case, compared to other two cases with larger wedge angles, θ equal to 45^0 and 60^0 respectively. This suggests that if we choose the wedge with a 30^0 angle, we will have more flexibility for the other control parameters namely the lattice constant, a and the normalised Bloch wavevector $\mathrm{Re}\left(\frac{qa}{2\pi}\right)$ when designing the wedged structure. Therefore, in the following we will explore superprism designs with this angle further.

Accordingly, we now proceed in finding suitable parameters satisfying the conditions $|\sin\phi_0| < 1$ and $|\sin\phi_1| > 1$, but at the same time yielding a backward wave

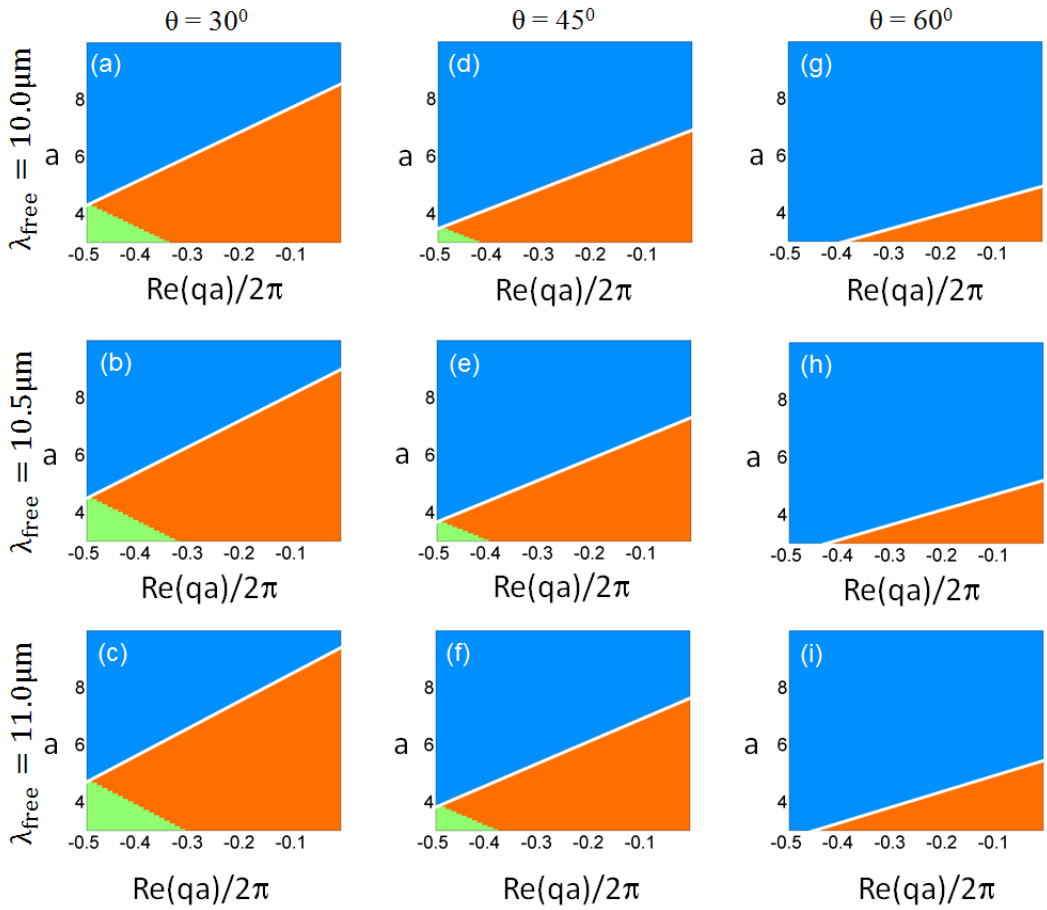

Figure 9.3: The parameter space of the lattice constant, a and the normalised Bloch wavevector Re $\left(\frac{qa}{2\pi}\right)$ is depicted. In the regions above the white line, the higher order Bragg couplings cannot be avoided. Below the white line, all higher order couplings are suppressed. The green regions represent the cases where the primary beam cannot outcouple. Thus the orange regions indicate the part of the parameter space where both the higher order Bragg beams are suppressed and the primary beam outcouples. The panels (a)-(c) represent the results for the wavelengths, 10.0 μm, 10.5 μm and 11.0 μm respectively for the wedge with $\theta = 30^0$. The panels (d)-(f) are the same as (a)-(c), but for $\theta = 45^0$. The panels (g)-(i) are the same as (a)-(c), but for $\theta = 60^0$.

propagation within the PC. So, we consider SiC-air 1D-PCs with a low filling ratio of 0.05, to maintain the translucence. The bandstructures of these PCs are calculated by using the TMM method [10–13] as described in Chapter 2. In particular in Fig. 9.4, we plot the bandstructures of the SiC-air 1D-PCs with lattice constants 3.0 μm, 4.0 μm and 5.0 μm with blue, red and green lines respectively. Note, we assume the impinging EM wave along the $+x$ direction, hence we take only positive Im(q) value in Fig. 9.4, to satisfy the passivity requirement. We can clearly see from Fig. 9.4(a) that Re(q) is positive for these three PCs in the spectral region of interest, which implies a forward-type propagation as we explained in Chapter 8. This means we cannot have a backward-type propagation with these

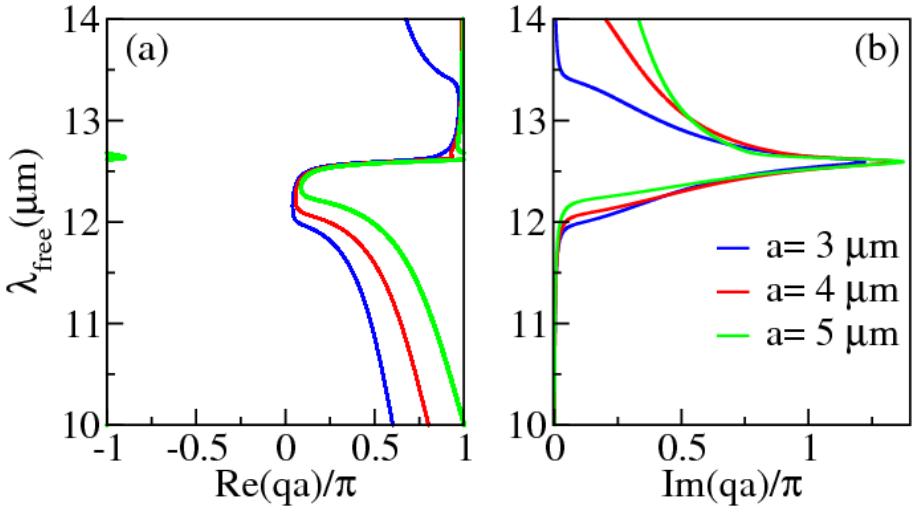

Figure 9.4: Complex bandstructure (free space wavelength, λ_{free} versus Bloch wave vector, q) of SiC-air 1D-PCs of filling ratio 0.05. The blue, red and green lines indicate the results for the PCs with lattice constants 3.0 μm, 4.0 μm and 5.0 μm respectively. An impinging EM wave along the $+x$ direction is assumed, hence the positive Im(q) value is taken to satisfy the passivity requirement as we discussed in the Chapter 8.

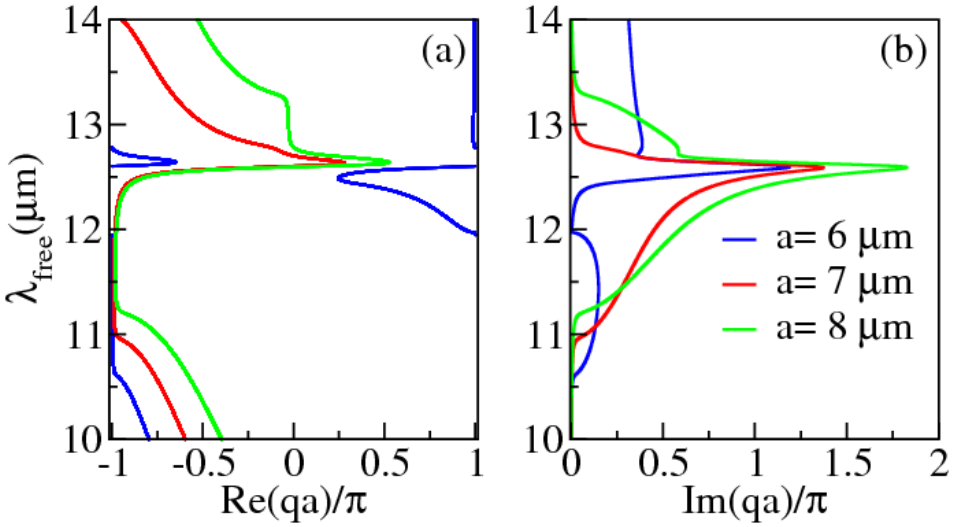

Figure 9.5: Same as Fig. 9.4, but for the SiC-air 1D-PCs with lattice constant, a equal to 6.0 μm (Blue-lines), 7.0 μm (red-lines) and 8.0 μm (green-lines).

low lattice constant PCs, suggesting that we should investigate PCs with a larger lattice constant.

Therefore, we show in Fig. 9.5(a) and (b) the bandstructures of the SiC-air 1D-PCs with a lattice constant equal to 6.0 μm, 7.0 μm and 8.0 μm with blue, red and green lines respectively. For the case of 6.0 μm lattice constant PC, we can observe that an allowed band barely exists within the Reststrahlen-band of the SiC. Therefore, this PC is not a useful design for the wedge superprism in the 10.0 μm-11.0 μm

spectral region that we are interested. On the other hand, SiC-air PCs with a lattice constant equal to 7.0 µm and 8.0 µm have Re(q) within the spectral region of interest. Thus these PCs would look promising for the wedged-superprism design, since we can have backward-type propagation inside them. However, from Fig. 9.3, it is evident that these two cases fall mostly in the blue region of the parametric space (a, q), implying higher order outcouplings, which renders them also unsuitable for the superprism design.

From the above observations, we can conclude that it is not possible to design a wedged-superprism with SiC 1D-PCs, just by changing its lattice constant. That implies, additional control parameters should be sought in designing such wedged structures. Therefore, we explore the possibility of replacing air with a transparent medium in these SiC 1D-PCs. Therefore, we consider BaF_2 as the transparent medium since it has a refractive index of 1.36 in the Mid-IR spectral regime [29]. We particularly chose BaF_2, since it is transparent in the Mid-IR regime, similar to glass in the visible regime. By exploring different lattice constants, we found that SiC-BaF_2 1D-PC with a lattice constant of 5.5 µm and filling ratio 0.05 has a good position in the parametric space yielding only outcoupling of the primary beam after the slanted interface.

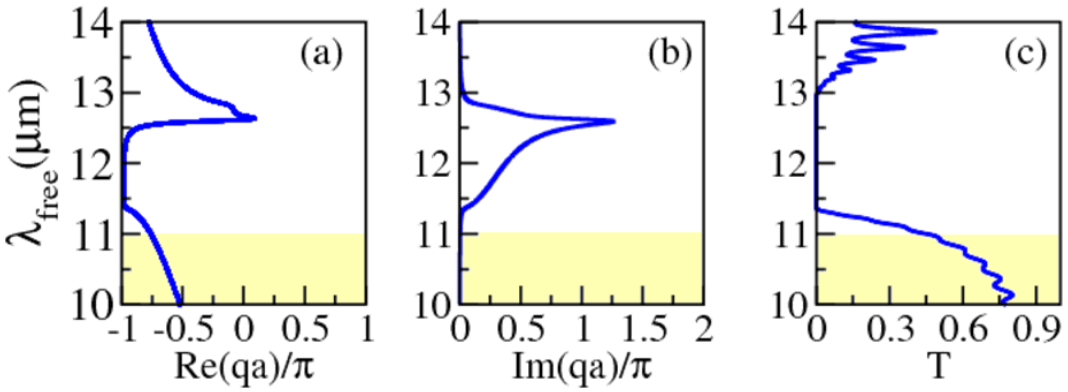

Figure 9.6: (a) and (b): Complex bandstructure (free space wavelength, λ_{free} versus Bloch wave vector, q) for a SiC-BaF_2 1D-PC with a lattice constant of 5.5 µm and filling ratio 0.05. (c) The free space wavelength, λ_{free} versus the transmittance, T for the same PC with twenty unit cells. The yellow shading indicates the spectral region of interest, where the PC has a negative Bloch wavevector, Re(q) and high transmittance, T.

In Fig. 9.6 we show the bandstructure for this PC. It is evident that this PC has a negative Bloch wavevector, Re(q), i.e. pointing towards the $-x$ direction in the spectral region from 10.0 µm to 11.4 µm. Therefore, it supports backward-type propagation for this broad regime, which is very impressive, while simultaneously being translucent, between 10.0 µm to 11.0 µm. To see this clearly, we show in

Fig. 9.6(c), the transmittance spectra of this PC with twenty unit cells (see the yellow shaded region in Fig. 9.6).

Now that we have chosen the precise structure of the 1D-PC for constructing the wedged superprism, it is interesting to check the limits of the wedge angle, θ for this particular PC where the higher order Bragg beams are suppressed, while the primary beam outcouples. By taking $|\sin\phi_0| < 1$ and $|\sin\phi_1| > 1$, it is easy to show that, θ should satisfy the following condition:

$$\left| \frac{\frac{a}{\lambda}}{\left[1 - \left|\mathrm{Re}\left(\frac{qa}{2\pi}\right)\right|\right]} \right| < \cos\theta < \left| \frac{\frac{a}{\lambda}}{\mathrm{Re}\left(\frac{qa}{2\pi}\right)} \right|. \tag{9.7}$$

With this equation, we evaluate the upper limit of $\cos\theta$ i.e. the right hand side expression for our chosen SiC-BaF_2 1D-PC by using the $\mathrm{Re}\left(\frac{qa}{2\pi}\right)$ values from the bandstructure. We show the result in Fig. 9.7(a) with a red line, which indicate that the right hand side of Eq. 9.7 is always above one throughout the spectrum. This means that the primary beam can always outcouple at the slanted interface for any chosen wedge angle θ. In other words, there is no restriction on the minimum wedge angle, as far as the outcoupling of the primary beam is concerned. On the other hand, we evaluate the lower limit of $\cos\theta$ i.e. the left hand side expression of Eq. 9.7 for the same PC, and show the result in Fig. 9.7(a) with a blue line. This lower limit of $\cos\theta$, gives the maximum of the wedge angle, θ_{max} as:

$$\theta_{max} = \cos^{-1}\left(\left| \frac{\frac{a}{\lambda}}{\left[1 - \left|\mathrm{Re}\left(\frac{qa}{2\pi}\right)\right|\right]} \right| \right). \tag{9.8}$$

To see this clearly, we show the result for θ_{max} in Fig. 9.7(b). It is evident that the maximum of the wedge angle allowed in the spectral regime of interest is 36^0. Therefore, in the following we chose the wedge angle of 30^0 for our superprism design.

9.3 Theoretical prediction for the superdeflection angle for the proposed wedged PC superprism design

Now that we have chosen all the control parameters for the wedged-superprism design that satisfy all the three requirements explained above, we proceed in evaluating the performance of the superprism. For this purpose, we determine the direction

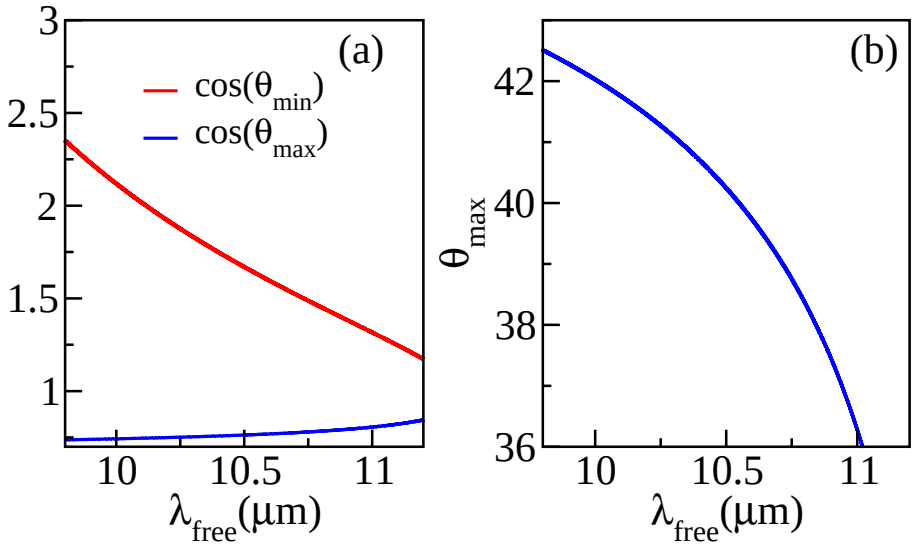

Figure 9.7: (a) The upper limit values (red-line) and lower limit values (blue-line) of cosθ in Eq. 9.7 versus the free space wavelength, λ_{free} for a SiC-BaF_2 1D-PC with a lattice constant of 5.5 μm and filling ratio 0.05. (b) The maximum permissible wedge angle, θ_{max} versus the free space wavelength, λ_{free} for a wedged design from the PC of Fig. 9.6 without higher order Bragg couplings.

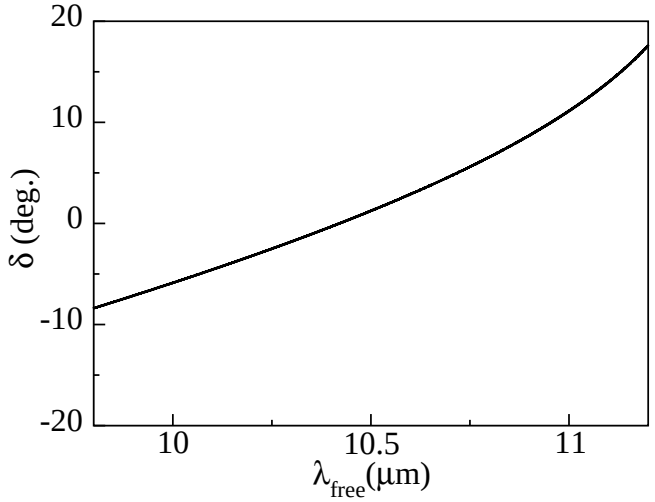

Figure 9.8: The angle, δ calculated from Eq. 9.9 versus the free space wavelength, λ_{free} of a wedged structure of 30^0 angle (see schematics in Fig. 9.1) that is constructed from a SiC-BaF_2 1D-PC with a lattice constant of 5.5 μm and filling ratio 0.05.

of the outgoing beam with respect to the incident beam, by evaluating the angle, δ shown in Fig. 9.1. We can obtain δ from the geometry in Fig. 9.1 as:

$$\delta = |\phi_0| - \theta = \left| \frac{-\left|\mathrm{Re}\left(\frac{qa}{2\pi}\right)\right| \cos\theta}{\frac{a}{\lambda}} \right| - \theta. \tag{9.9}$$

In the above equation, if δ is zero, the outgoing beam is exactly at 90^0 with respect to the incident wave. When δ is positive, the outgoing wave bends more than 90^0, while when δ is negative the outgoing wave bends less than 90^0. We evaluate the spectral response for the angle, δ from Eq. 9.9, by using the $\mathrm{Re}\left(\frac{qa}{2\pi}\right)$ values from the bandstructure in Fig. 9.6. We plot the result in Fig. 9.8. We notice that δ varies from negative to positive values and at wavelength close to $10.5\,\mu m$, it is near zero. That means, if an EM wave is incident on the wedged structure at this particular wavelength, it will bend very close to 90^0. Furthermore, the positive values of δ in Fig. 9.8 imply that bending of light larger than 90^0 is possible with this wedged-PC structure.

In the following, we will set-up a Finite-Difference Time-Domain (FDTD) based numerical simulation to verify the theoretically predicted super-deflection of light with our proposed wedged 1D-PC superprism design.

9.4 Numerical verification of the theoretically predicted superdeflection for the wedged-PC superprism

For this purpose, a commercial-grade simulator based on the Finite-Difference Time-Domain (FDTD) method was used [14] as we described in Chapter 2. We simulate a wedged structure constructed with a SiC-BaF_2 1D-PC as shown in Fig. 9.9. We consider that this wedged structure is embedded in vacuum. The structural parameters of SiC-BaF_2 1D-PC are the same as stated in Fig. 9.6. Following our analysis in the previous section, we consider the wedge angle to be 30^0. The lengths of the sides of the wedge are taken to be $A = 200\,\mu m$, $B = 253\,\mu m$ and $D = 53.93\,\mu m$, which corresponds to 46 cells along the stacking direction. Note that in the numerical set-up the slanted interface has a teeth-like profile, as complete unit cells of different lateral sizes are stacked on top of each other. We apply open boundary conditions in both the x- and z-direction. The permittivity of the SiC is represented in the simulator with a Lorentzian function [30], same as

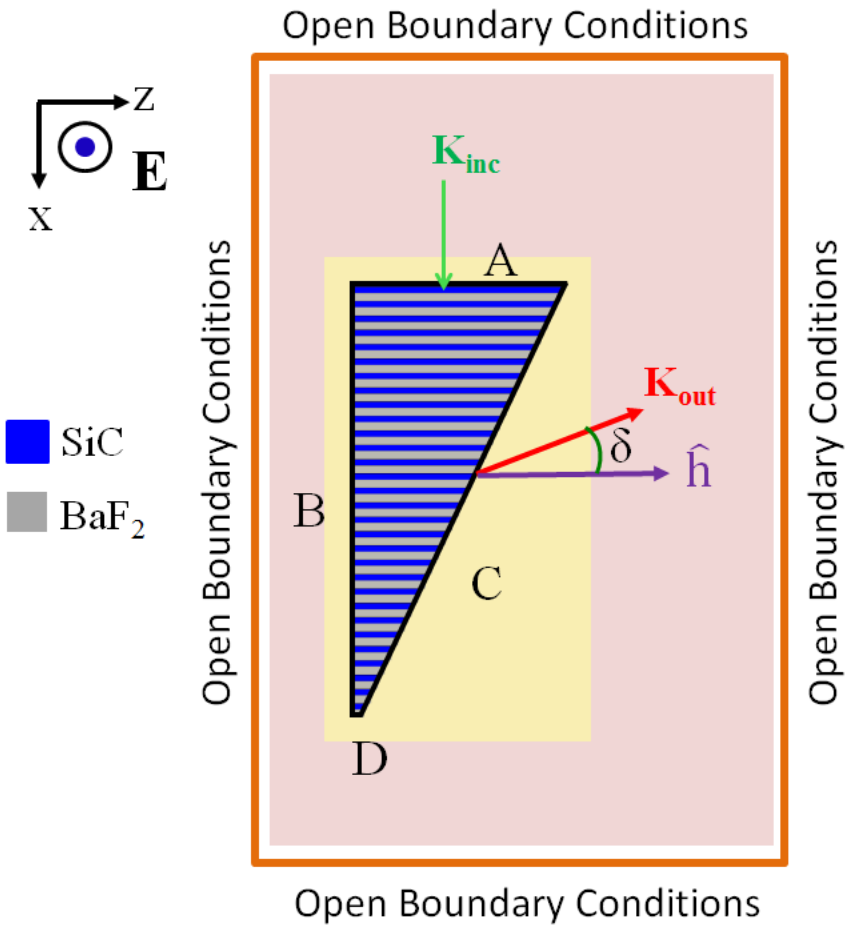

Figure 9.9: Schematic diagram of the simulation set-up in the FDTD simulator. The blue block regions represent SiC and the grey regions represent BaF_2. The polarisation of the incident EM wave is indicated. We designate the sizes of each side of the wedged structure, as A, B, C and D. The yellow shaded region represents the regime where a user defined mesh was used. The brown region represent the region where the default Lumerical simulator [14] mesh has been used. The direction of the incident wave (green-arrow), and outgoing wave (red-arrow) are indicated. The angle, δ of the outgoing beam with respect to the horizontal, $\hat{h}$ (orange-dashed line) is also indicated.

the one in Eq. 8.1. of Chapter 8. The permittivity of BaF_2 is taken to be as 1.8496 [29], that corresponds to a refractive index of 1.36. This is a realistic value for this frequency region. For the similar reasons as in the case of the tilted source set-up in Chapter 8, we used a user-defined mesh of size 25 nm and 200nm in the x- and z-directions respectively around the wedged structure.

We repeat the simulation for three different wavelengths, 10.0 µm and 10.5 µm and 11.0 µm. In each simulation run, we record the y-component of the electric field, $E_y(x, z)$, throughout the simulation region (see Chapter 2). We show these electric-field results in Fig. 9.10. We measure the angle, δ graphically from the

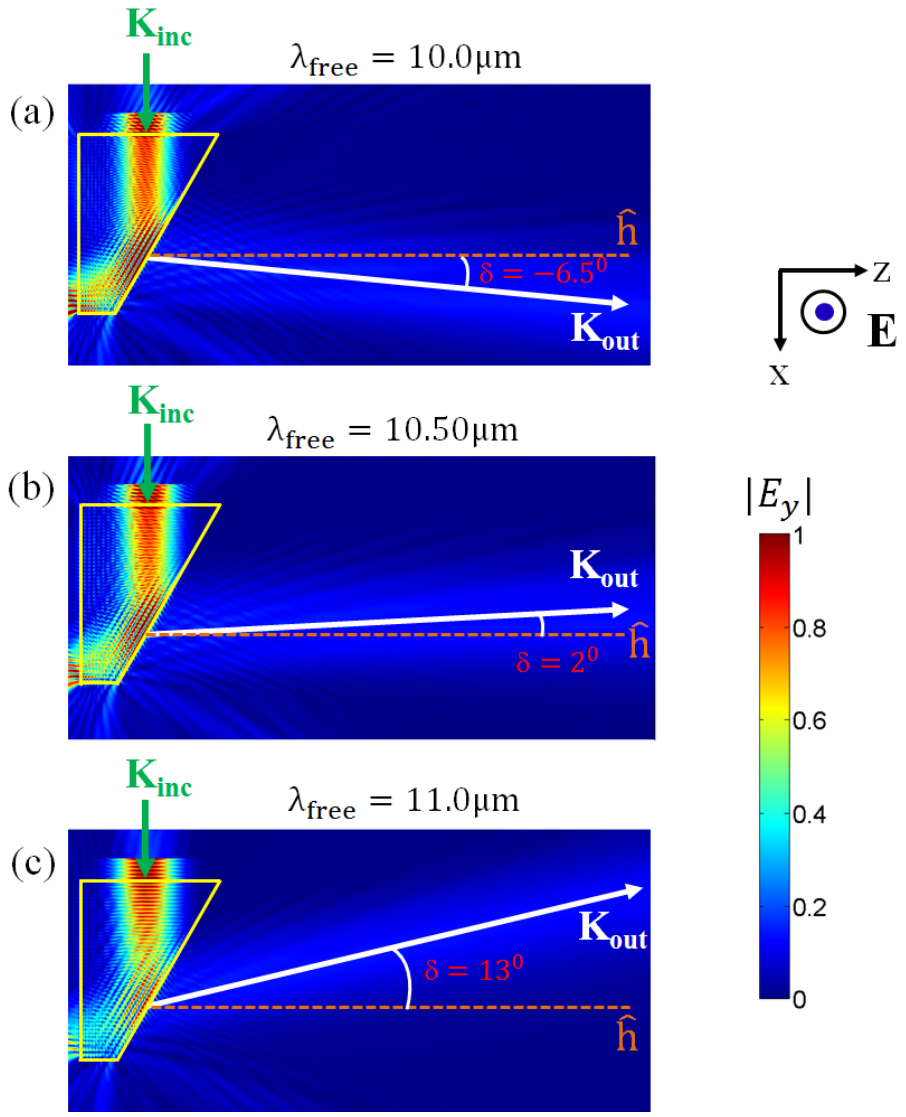

Figure 9.10: The magnitude of the y-component of the electric field, $|E_y(x,z)|$ in the numerical ultra-refraction simulation of a wedged structure constructed from a SiC-BaF_2 1D-PC with a lattice constant of 5.5 µm and filling ratio 0.05. The lengths of the sides of the wedge are taken to be $A = 200\,\mu m$, $B = 253\,\mu m$ and $D = 53.93\,\mu m$. The yellow-lines indicate the wedged structure bounds. Panels (a)-(c) represent the results at wavelengths, 10.0 µm and 10.5 µm and 11.0 µm respectively. As a guide for the eye, we draw a green-arrow and a white-arrow to indicate the propagation direction of the incident and outgoing wave respectively. In each panel we indicate the graphically measured angle, δ of the outgoing beam with respect to the horizontal, $\hat{h}$ (orange-dashed line).

electric-field plots, for the three wavelengths that we indicated in Fig. 9.10. We represent these numerical results in Fig. 9.11 with red circles together with the theoretical predicted results obtained for a 30^0 wedge from Eq. 1.10, that we represented with a black-line. We can clearly observe an excellent agreement of these numerical results with our theoretical predicted results throughout the spectrum. Notice the remarkable almost 90^0 bending of light for incidence at 10.5 μm free space wavelength. Even more impressively, we observe a 103^0 bending of light for incidence at 11.0 μm free space wavelength.

The aim of this first exploratory study is to demonstrate as a proof of concept the possibility to achieve extreme bending of light beyond 90^0, based on backward propagation of EM waves in a PC comprising of opaque constituents. We can see in Fig. 9.10 that multiple reflections occur inside the wedged structure resulting in leaked light from the bottom left-side of the wedged structure. The electric field amplitude of this leaked light is quite high, around two times more than that of the out-coupled bended beam. Although the leaked elecric field is less for the extreme bending case shown in Fig. 9.10 (c), in comparison to the low bending case in Fig. 9.10 (a), it is unavoidable due to reflection within the wedged structure. However, the wedged structure can be optimised further by varying the lattice constant and filling ratio of the PC as well as the angle and shape of the slanted interface of the wedged structure. For example, based on intuition we could argue that if the SiC blocks in each PC layer within the wedged structure are tapered in the side of the wedged interface, then this might lead to better out-coupling of the refracted beam in the area after the slanted interface. These optimisations would be interesting for a future study.

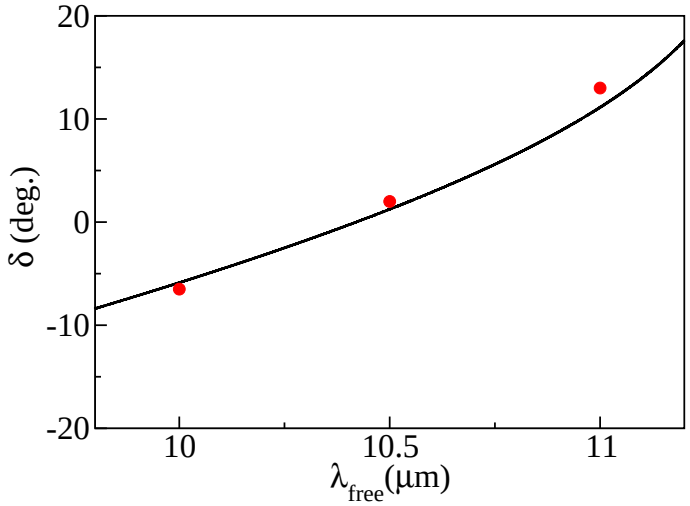

Figure 9.11: Same as Fig. 9.8, but now we overlay the numerical FDTD simulation results for the angle, δ as red circles.

9.5 Conclusions

We have verified numerically the existence of backward-type waves in lossy 1D-PCs, in the Mid-IR frequency region. Our findings demonstrate superbending of light in the Mid-IR spectral regime by employing a simple multilayer design without the need to consider complex 3D structures with an effective-negative refractive index. In particular, we demonstrated more than 90^0 bending of light with a wedged structure constructed from a SiC-BaF_2 1D-PC in the Reststrahlen-band of SiC.

We found that the key requirements to achieve such high deflection of light are the existence of a translucent spectral regime, the existence of backward-type Floquet wave propagation through the underlying PC structure and suppression of the higher order Bragg couplings at the slanted exit interface. We were able to achieve this by considering a low filling ratio, tuning the lattice constant of the lossy PC, tuning the angle of the wedge, as well as incorporation of suitable transparent material between the SiC slabs. The determination of the aforementioned structural parameters is based on the special quantitative conditions we derived for the suppression of the higher order Bragg beams and by considering the bandstructure properties of the underlying PC structure. We believe that our wedged PC design will inspire engineering of translucent optical devices made of opaque media throughout the EM wave spectrum.

Bibliography

[1] N. K. Grady, J. E. Heyes, D. R. Chowdhury, Y. Zeng, M. T. Reiten, A. K. Azad, A. J. Taylor, D. A. R. Dalvit, H. T. Chen, "Terahertz Metamaterials for Linear Polarization Conversion and Anomalous Refraction," Science, **340**, 1304-1307 (2014).

[2] F. Zhou, Y. Bao, W. Cao, C. T. Stuart, J. Gu, W. Zhang, and C. Sun, "Hiding a Realistic Object Using a Broadband Terahertz Invisibility Cloak," Scientific Rep. **1**, 78, (2011).

[3] D. Martin-Cano, M. L. Nesterov, A. I. Fernandez-Dominguez, F. J. Garcia-Vidal, L. Martin-Moreno, and Esteban Moreno "Domino plasmons for subwavelength terahertz circuitry," Opt. Exp. **18**, 754-764, (2010).

[4] N. H. Shen, Th. Koschny, M. Kafesaki, and C. M. Soukoulis, "Robust wedge demonstration to optical negative index metamaterials," Appl. Phys. Lett **102**, 241915 (2013).

[5] C. Pfeiffer, N. K. Emani, A. M. Shaltout, A. Boltasseva, V. M. Shalaev and A. Grbic "Efficient Light Bending with Isotropic Metamaterial Huygens Surfaces," Nano Lett, (2014).

[6] E. Centeno, D. Cassagne, and J. P. Albert, "Mirage and superbending effect in two-dimensional graded photonic crystals," Phys. Rev. Lett. **112**, 068103 (2006).

[7] W. Shin, W. Cai, P. B. Catrysse, G. Veronis, M. L. Brongersma, and S. Fan "Broadband Sharp 90-degree Bends and T-Splitters in Plasmonic Coaxial Waveguides," Nano Lett. **13**, 4753-4758 (2013).

[8] A. J. Hoffman, L. Alekseyev, S. S. Howard, K. J. Franz, D. Wasserman, V. A. Podolskiy, E. E. Narimanov, D. L. Sivco and C. Gmachl, "Negative refraction in semiconductor metamaterials," Nat. Mat. **6**, 946-950 (2007).

[9] C. M. Watts, X. Liu, and W. J. Padilla, "Metamaterial electromagnetic wave absorbers," Adv. Mater. **24**, 98120, (2012).

[10] A. Yariv and P. Yeh, *Optical Waves in Crystals: Propagation and Control of Laser Radiation* (Wiley-Interscience, Hoboken 1984).

[11] P. Yeh, *Optical waves in layered media* (Wiley-Interscience, Hoboken 2005).

[12] P. Yeh, A. Yariv, and C. S. Hong, "Electromagnetic propagation in periodic stratified media. I. General theory*," J. Opt. Soc. Am. **67**, 423-438 (1977).

[13] A. Yariv and P. Yeh, "Electromagnetic propagation in periodic stratified media. II. Birefringence, phase matching, and x-ray lasers," J. Opt. Soc. Am. **67**, 438-447 (1977).

[14] Lumerical Solutions, Inc. http://www.lumerical.com/tcad-products/fdtd/

[15] I. V. Lindell, S. A. Tretyakov, K. I. Nikoskinen, S. Ilvonen, "BW media-media with negative parameters, capable of supporting backward waves," Microwave Opt. Tech. Lett. **31**, 163-165 (2001).

[16] S. Foteinopoulou and C. M. Soukoulis, "Electromagnetic wave propagation in two-dimensional photonic crystals: A study of anomalous refractive effects," Phys. Rev. B **72**, 165112 (2005).

[17] S. Foteinopoulou and C. M. Soukoulis, "Negative refraction and left-handed behavior in two-dimensional photonic crystals," Phys. Rev. B **67**, 235107 (2003).

[18] S. Foteinopoulou, "Electromagnetic wave propagation in two-dimensional photonic crystals," Ph.D thesis, Iowa State University (2003).

[19] M. Notomi, "Theory of light propagation in strongly modulated photonic crystals: Refractionlike behavior in the vicinity of the photonic band gap," Phys. Rev. B **62**, 10696 (2000).

[20] J. D. Jackson, *Classical Electrodynamics*, (Wiley, Third edition, 1999).

[21] R. A. Shelby, D. R. Smith, S. Schultz, "Experimental Verification of a Negative Index of Refraction," Science, **292**, 77-79 (2001).

[22] C. G. Parazzoli, R. B. Greegor, K. Li, B. E. C. Koltenbah, and M. Tanielian, "Experimental Verification and Simulation of Negative Index of Refraction Using Snells Law," Phys. Rev. Lett. **90**, 170401 (2003).

[23] A. Tikhonov, J. Bohn, and S. A. Asher, "Photonic crystal multiple diffraction observed by angular-resolved reflection measurements," Phys. Rev. B**80**, 235125 (2009).

[24] D. R. Smith, P. M. Rye, J. J. Mock, D. C. Vier, and A. F. Starr, "Enhanced Diffraction from a Grating on the Surface of a Negative-Index Metamaterial," Phys. Rev. Lett. **93**, 137405 (2004).

[25] R. W. Waynant, I. K. Ilev and I. Gannot, "Mid-infrared laser applications in medicine and biology," Phil. Trans. R. Soc. Lond. A., **359**, 635-644 (2001).

[26] B. Mizaikoff, "Waveguide-enhanced mid-infrared chem/bio sensors," Chem. Soc. Rev., **42**, 8683-8699 (2013).

[27] J. M. Bakker, L. M. Aleese, G. Meijer, and G. von Helden, "Finger-print IR spectroscopy to probe amino acid conformations in the gas phase," Phys. Rev. Lett., **91**, 203003 (2003).

[28] M. Born and E. Wolf, *Principles of optics: electromagnetic theory of propagation, interference and diffraction of light* (Oxford, Pergamon Press, 1964).

[29] E. D. Palik, *Handbook of Optical Constants of Solids* (Academic Press, 1985).

[30] C. Kittel, *Introduction to Solid State Physics* (John Wiley and Sons, Hoboken, 2005).

10

Conclusions and Future Outlook

Through a series of theoretical investigations on SiC microstructures presented in this thesis, we have overcome the challenge of controlling light within the Reststrahlen band of SiC, where the bulk SiC material is highly reflective. We uncovered new routes to absorption enhancement with these naturally highly reflecting materials. In particular, we demonstrated narrow-band near-unity absorptance with highly compact SiC 1D-PCs and broadband absorption covering the entire Reststrahlen band with bulky aperiodic SiC PCs. Furthermore, by combining the insights from both of these designs, we achieved an absorptance of more than 80% over a broad wavelength regime within the Reststrahlen band of SiC with a subwavelength thick SiC pyramid structures. Since the emissivity is directly related to the absorption by Kirchhoff's law, this SiC pyramid structure entails promise for highly-directional, polarization-selective IR sources. This could be an interesting future direction emanating from the line of research in this thesis. In addition, we demonstrated superabsorption in SiC effective metamaterials by tailoring their effective phonon-polariton gap at will. Our absorption controlling mechanisms that we presented in this thesis could be useful for applications such as detectors, Mid-IR sources and energy conversion devices.

There are other applications in the Mid-IR spectrum such as beam deflecting devices that require Mid-IR refractive materials to realise. However, very few suitable natural materials are available in the Mid-IR regime for such applications. Therefore, in

the second part of the thesis, we explored the Mid-IR refractive properties of SiC microstructures. Specifically, through an effective Bloch impedance analysis, we found that highly translucent Mid-IR optical components can be constructed with SiC 1D-PCs. We further conceived a superprism constructed from a SiC 1D-PC, operating in the Mid-IR, that can deflect light beyond 90^0, which was not reported thus far.

Although we used only SiC as the constituent material, the findings reported in this thesis are in general applicable to any phonon-polaritonic material. Therefore, our findings in this thesis contribute to the growing area of "polaritonics", by offering new ways of controlling EM waves with phonon-polaritonic materials, which were otherwise thought to have only reflection properties. Furthermore, we mostly focussed on 1D-PCs since they allowed us to obtain simple analytical relations between various physical quantities, which was useful to gain fundamental insights for designing superabsorbers and superbending structures. Since now 1D-PCs are thoroughly explored in this thesis, one can expand these investigations to higher order periodic structures. For example, the micropyramid designs can be extended to two-dimensional periodicity (2D grating with micropyramids), which could be desirable for applications requiring polarization independent absorption/emission behaviour. Moreover, we studied microstructures consisting of only one kind of polaritonic media. However inclusion of more than one kind of polaritonic media, could open additional possibilities with multiple operating spectral windows. Therefore, we believe that our work presented in this thesis will inspire the design of a variety of absorptive/emissive and superrefractive devices across the THz/Mid-IR spectrum.

List of Publications

Published papers in refereed international journals

1. **Ganga Chinna Rao Devarapu** and Stavroula Foteinopoulou, "Mid-IR near-perfect absorption with a SiC photonic crystal with angle controlled polarization selectivity," Opt. Express **20**, 13040-13054 (2012).

2. **Ganga Chinna Rao Devarapu** and Stavroula Foteinopoulou, "Compact photonic-crystal superabsorbers from strongly absorbing media," J. Appl. Phys. **114**, 033504 (2013).

3. **Ganga Chinna Rao Devarapu** and Stavroula Foteinopoulou, "Broadband Mid-IR superabsorption with aperiodic polaritonic photonic crystals," J. Euro. Opt. Soc. Rap. Pub. **9**, 14012 (2014).

Papers in preparation for submission in refereed international journals

1. **Ganga Chinna Rao Devarapu** and Stavroula Foteinopoulou, "Subwavelength broadband near-perfect SiC pyramid absorber" (in preparation to be submitted to Phys. Rev. Appl.) *(based on the research presented in Chapter 7).*

2. **Ganga Chinna Rao Devarapu** and Stavroula Foteinopoulou, "Superprism effects in polaritonic photonic crystals," (in preparation to be submitted to Phys. Rev. E) *(based on the research presented in Chapters 8 and 9).*

3. **Ganga Chinna Rao Devarapu** and Stavroula Foteinopoulou, "Superabsorption with SiC effective metamaterials," (in preparation to be submitted to Appl. Opt.) *(based on the research presented in Chapter 4).*

Conference Proceedings

1. **Ganga Chinna Rao Devarapu** and Stavroula Foteinopoulou, "Harnessing

IR absorption with polaritonic PCs", AIP Conf. Proc. **1475**, 122-124 (2012).

2. **Ganga Chinna Rao Devarapu**, and Stavroula Foteinopoulou, "Unconventional infrared absorption with polaritonic photonic crystals", Lasers and Electro-Optics Europe (CLEO EUROPE/ IQEC), Conference on and International Quantum Electronics Conference. IEEE, (2013).

Conference Presentations

1. Poster presentation at Theoretical and Computational Nano-photonics (TaCoNa), **Ganga Chinna Rao Devarapu** and Stavroula Foteinopoulou, "Harnessing IR absorption with polaritonic PCs," Bad Honnef, Germany (Oct-2012).

2. Poster presentation at the European Conference on Lasers and Electro-Optics and the International Quantum Electronics Conference (CLEO-IQEC), **Ganga Chinna Rao Devarapu** and Stavroula Foteinopoulou, "Unconventional infrared absorption with polaritonic PCs," Munich, Germany (May-2013).

3. Poster presentation at Complex NanoPhotonics Science Camp, **Ganga Chinna Rao Devarapu** and Stavroula Foteinopoulou, "Extreme photonic-crystal based absorption control in the infrared," Windsor Great Park, UK (Aug-2013).

Appendices

A

Propagation in 1D-periodic media: Abelès formulation

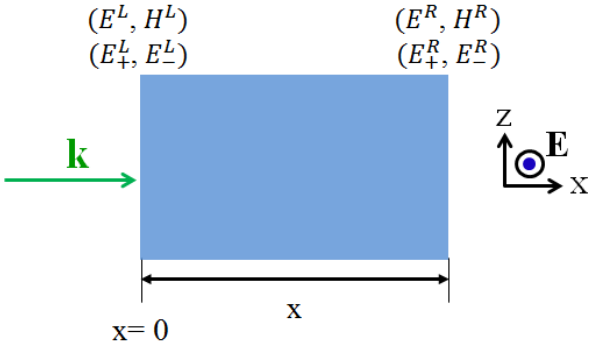

Figure A.1: Amplitudes of the electric and magnetic fields at the entrance and exit of a homogeneous block of thickness, x are shown schematically. Geometric parameters and polarization direction are indicated.

Let us consider a plane electromagnetic (EM) wave with frequency, ω incident normally on a non-magnetic homogeneous medium with polarisation as schematically depicted in Fig. A.1. Now the total electric-field along the x-direction $E_y(x)$, at a point x inside the medium is:

$$E_y(x) = E_+(0)e^{ik_x x} + E_-(0)e^{-ik_x x}, \tag{A.1}$$

where $E_+(0)$ and $E_-(0)$ represent the amplitudes of the forward and backward going electric fields at the entrance, $x = 0$ of the medium. From Maxwell's equation, we have:

$$\nabla \times \mathbf{E} = -\frac{\partial \mathbf{B}}{\partial t} \Rightarrow \nabla \times \mathbf{E} = -\mu_0 \frac{\partial \mathbf{H}}{\partial t}, \tag{A.2}$$

since we consider a non-magnetic medium. Here μ_0 represents the permeability of the vacuum. That implies:

$$H_z(x) = \frac{1}{i\omega\mu_0} \frac{\partial E_y(x)}{\partial x}. \tag{A.3}$$

With the use of Eq. A.1 in the above equation, we get that the total magnetic field along the z-direction, $H_z(x)$ is:

$$H_z(x) = \eta(E_+(0)e^{ik_x x} - E_-(0)e^{-ik_x x}), \tag{A.4}$$

where $\eta = \frac{-k_x}{\mu_0 \omega}$.
By considering $E_+(0)e^{ik_x x}$ and $E_-(0)e^{-ik_x x}$ as E_+ and E_-, we can rewrite Eqs. A.1 and A.4 in matrix form as:

$$\begin{bmatrix} E_y(x) \\ H_z(x) \end{bmatrix} = \begin{bmatrix} 1 & 1 \\ \eta & -\eta \end{bmatrix} \begin{bmatrix} E_+ \\ E_- \end{bmatrix}. \tag{A.5}$$

By inverting we get:

$$\begin{bmatrix} E_+ \\ E_- \end{bmatrix} = \frac{1}{2} \begin{bmatrix} 1 & \frac{1}{\eta} \\ 1 & -\frac{1}{\eta} \end{bmatrix} \begin{bmatrix} E_y(x) \\ H_z(x) \end{bmatrix}. \tag{A.6}$$

Now we consider two points in the homogeneous medium separated by a distance x, as shown in Fig. A.1. By using the above equation, we can relate the total electric and magnetic fields, E^L, H^L at the entrance of the medium with the corresponding forward and backward going electric fields,E^L_+, E^L_- at the entrance as:

$$\begin{bmatrix} E^L \\ H^L \end{bmatrix} = \begin{bmatrix} 1 & 1 \\ \eta & -\eta \end{bmatrix} \begin{bmatrix} E^L_+ \\ E^L_- \end{bmatrix}. \tag{A.7}$$

The forward and backward electric fields at the entrance of the medium can be related to the forward and backward electric fields at a distance x, by using the propagation matrix as:

$$\begin{bmatrix} E^L_+ \\ E^L_- \end{bmatrix} = \begin{bmatrix} e^{-ik_x x} & 0 \\ 0 & e^{ik_x x} \end{bmatrix} \begin{bmatrix} E^R_+ \\ E^R_- \end{bmatrix}. \tag{A.8}$$

From Eqs. A.7 and A.8, we get:

$$\begin{bmatrix} E^L \\ H^L \end{bmatrix} = \begin{bmatrix} 1 & 1 \\ \eta & -\eta \end{bmatrix} \begin{bmatrix} e^{-ik_x x} & 0 \\ 0 & e^{ik_x x} \end{bmatrix} \begin{bmatrix} E^R_+ \\ E^R_- \end{bmatrix}. \tag{A.9}$$

With the use of Eq. A.6 in Eq. A.9, we get:

$$\begin{bmatrix} E^L \\ H^L \end{bmatrix} = \frac{1}{2} \begin{bmatrix} 1 & 1 \\ \eta & -\eta \end{bmatrix} \begin{bmatrix} e^{-ik_x x} & 0 \\ 0 & e^{ik_x x} \end{bmatrix} \begin{bmatrix} 1 & \frac{1}{\eta} \\ 1 & -\frac{1}{\eta} \end{bmatrix} \begin{bmatrix} E^R \\ H^R \end{bmatrix}. \tag{A.10}$$

The above equation can be written simply:

$$\begin{bmatrix} E^L \\ H^L \end{bmatrix} = T \begin{bmatrix} E^R \\ H^R \end{bmatrix}, \tag{A.11}$$

where

$$T = \frac{1}{2} \begin{bmatrix} 1 & 1 \\ \eta & -\eta \end{bmatrix} \begin{bmatrix} e^{-ik_x x} & 0 \\ 0 & e^{ik_x x} \end{bmatrix} \begin{bmatrix} 1 & \frac{1}{\eta} \\ 1 & -\frac{1}{\eta} \end{bmatrix}. \tag{A.12}$$

After some mathematical simplification, we get:

$$T = \begin{bmatrix} \cos k_x x & \frac{-i}{\eta} \sin k_x x \\ -i\eta \cos k_x x & \cos k_x x \end{bmatrix}. \tag{A.13}$$

The matrix T is the characteristic matrix of the dielectric layer, and establishes the relationship between the total electric and magnetic fields separated by a distance x [1, 2].

Now we consider a 1D periodic system consisting of two media A and B. In such periodic system, the total electric and magnetic fields at the entrance and exit of the unit cell can be related by the characteristic matrix, T^u of the entire unit cell, which is also referred to as the transfer matrix [3–5]:

$$\begin{bmatrix} E^i \\ H^i \end{bmatrix} = \begin{bmatrix} T^u_{11} & T^u_{12} \\ T^u_{21} & T^u_{22} \end{bmatrix} \begin{bmatrix} E^{i+1} \\ H^{i+1} \end{bmatrix}, \tag{A.14}$$

where $T^u = T^A T^B$, with T^A and T^B being the the individual characteristic matrices of the media A and B respectively. This results from the continuity of the total E_y and H_z at each boundary, from the EM boundary conditions. Note again that this unit cell transfer matrix, T^u is entirely different from the unit cell transfer matrix, M^u in the Yariv and Yeh formalism that we discussed in Chapters 2 and 8.

By using Bloch's theorem as we discussed in Yariv and Yeh's formalism [6–9] in Chapters 2, we get:

$$\begin{bmatrix} E^i \\ H^i \end{bmatrix} = e^{-i\mathrm{q}a} \begin{bmatrix} E^{i+1} \\ H^{i+1} \end{bmatrix}, \tag{A.15}$$

where $\mathrm{Tr}[T^u] = 2\cos(\mathrm{qa})$, with q and a represent the Bloch wavevector and the lattice constant of the periodic system respectively.
From Eqs. A.14 and A.15, we have:

$$\begin{bmatrix} T^u_{11} - e^{-i\mathrm{q}a} & T^u_{12} \\ T^u_{21} & T^u_{22} - e^{-i\mathrm{q}a} \end{bmatrix} \cdot \begin{bmatrix} E^{i+1} \\ H^{i+1} \end{bmatrix} = 0, \tag{A.16}$$

From the above matrix, we can get:

$$T^u_{11} - e^{-i\mathrm{q}a} E^{i+1} + T^u_{12} H^{i+1} = 0. \tag{A.17}$$

That implies:

$$\frac{E^{i+1}}{H^{i+1}} = \frac{-T^u_{12}}{T^u_{11} - e^{-i\mathrm{q}a}}. \tag{A.18}$$

Since the Bloch impedance, Z_B is defined [5] as:

$$Z_B = \frac{1}{Z_0} \frac{E^{i+1}}{H^{i+1}}, \tag{A.19}$$

where $Z_0 = \sqrt{\frac{\mu_0}{\varepsilon_0}}$ is the impedance of the vacuum. Therefore, we get the expression for Z_B as:

$$Z_B = \frac{1}{Z_0} \left(\frac{-T^u_{12}}{T^u_{11} - e^{-i\mathrm{q}a}} \right). \tag{A.20}$$

Bibliography

[1] F. Abelès, Recherches sur la propagation des ondes èlectromagnètiques sinusiodales dans les milieux stratifiès. Applicacion aux couches minces, Annales de Physique **5**, 596640, 706782 (1950).

[2] M. Born and E. Wolf, *Principles of optics: electromagnetic theory of propagation, interference and diffraction of light* (Oxford, Pergamon Press, 1964).

[3] N. Mattiucci, M. J. Bloemer, N. Aközbek, and G. D'Aguanno, "Impedance matched thin metamaterials make metals absorbing," Sci. Reports **3**, 3203 (2013).

[4] N. Mattiucci, G. D'Aguanno, N. Akozbek, M. Scalora, and M. J. Bloemer "Homogenization procedure for a metamaterial and local violation of the second principle of thermodynamics," Opt. Comm. **283**, 16131620 (2010).

[5] F. Shi, Y. Chen, P. Han, and C. M. Soukoulis, "Investigation of one-dimensional photonic bandgap structures containing lossy double-negative metamaterials through the Bloch impedance," J. Opt. Soc. Am. B **30**, 1473-1478 (2013).

[6] A. Yariv and P. Yeh, *Optical Waves in Crystals: Propagation and Control of Laser Radiation* (Wiley-Interscience, Hoboken 1984).

[7] P. Yeh, *Optical waves in layered media* (Wiley-Interscience, Hoboken 2005).

[8] P. Yeh, A. Yariv, and C. S. Hong, "Electromagnetic propagation in periodic stratified media. I. General theory*," J. Opt. Soc. Am. **67**, 423-438 (1977).

[9] A. Yariv and P. Yeh, "Electromagnetic propagation in periodic stratified media. II. Birefringence, phase matching, and x-ray lasers," J. Opt. Soc. Am. **67**, 438-447 (1977).

B

Absorption within the SiC building blocks in the micropyramid

The power absorbed within the i^{th} SiC building block of the micropyramid, A(i) can be obtained as:

$$A(i) = \frac{\overline{P_{loss}}}{\overline{P_{inc}}}, \tag{B.1}$$

where $\overline{P_{loss}}$ and $\overline{P_{inc}}$ represents the time-averaged power dissipation of the i^{th} SiC building block and the time-averaged incident power on the pyramid respectively. From Eq. 2.46 in Chapter 2, the time-averaged power dissipation per unit volume of a material, $\overline{P_{loss,\mathrm{v}}}$ is given by the Poynting's theorem [1] as:

$$\overline{P_{loss,\mathrm{v}}} = \frac{\omega\varepsilon_0\varepsilon_r''}{2}|E|^2. \tag{B.2}$$

Therefore, the power dissipated within a volume, V of a SiC building block of the micropyramid, $\overline{P_{loss}}$ can be obtained as:

$$\overline{P_{loss}} = \frac{\omega\varepsilon_0\varepsilon_r''}{2}\int |E(x,y)|^2\, dV. \tag{B.3}$$

Since we consider that the pyramid structure is invariant in the z-direction (see schematics in Fig. 7.5), we can consider any arbitrary length, l_z in the z-direction of SiC log. Let's consider the power dissipated in the volume enclosed by l_z and the

SiC face on the xy-plane. This will be:

$$\overline{P_{loss}}(x,y) = \frac{\omega\varepsilon_0\varepsilon_r'' l_z}{2}\int_0^{w_{xi}}\int_0^{w_{yi}} |E(x,y)|^2\, dx_i dy_i. \tag{B.4}$$

For the respective widths w_{xi}, w_{yi} and l_z in i^{th} SiC log (see schematics in Fig. 7.5) Similarly, from Eq. 2.51 in Chapter 2, the time-averaged incident power $\overline{P_{inc}}$ through the A_{inc} surface indicated in the see schematics in Fig. 7.5, is given by:

$$\overline{P_{inc}} = \frac{A_{inc}}{2c\mu_0}|E_{inc}|^2, \tag{B.5}$$

Note, A_{inc} designates the surface area normal to propagation direction of the impinging EM wave. In our case of a periodic structure with period a, the surface area is $A_{inc} = l_z \cdot \mathrm{a}$. Therefore, Eq. B.5 will become:

$$\overline{P_{inc}} = \frac{\mathrm{a}l_z}{2c\mu_0}|E_{inc}|^2. \tag{B.6}$$

Now with the use of Eqs. B.2 and B.6, Eq. B.1 yields:

$$\mathrm{A}(i) = \frac{\varepsilon_r''\omega}{\mathrm{a}c|E_{inc}|^2}\int_0^{w_{xi}}\int_0^{w_{yi}} |E(x,y)|^2 dx_i dy_i = \frac{\varepsilon_r''\omega}{\mathrm{a}c}\int_0^{w_{xi}}\int_0^{w_{yi}} |E_{enha}(x,y)|^2 dx_i dy_i, \tag{B.7}$$

where $E_{enha}(x,y) = \dfrac{E(x,y)}{E_{inc}}$ represents the enhanced electric field, within the SiC log. The above equation can be written as:

$$\mathrm{A}(i) = \frac{1}{\mathrm{a}}\int_0^{w_{xi}}\int_0^{w_{yi}} \mathrm{P}_{\mathrm{norm}}(x_i,y_i)\;\; dx_i dy_i, \tag{B.8}$$

where $\mathrm{P}_{\mathrm{norm}}(x,y)$ is:

$$\mathrm{P}_{\mathrm{norm}}(x,y) = \frac{\varepsilon_r''\omega}{c}|E_{enha}(x,y)|^2. \tag{B.9}$$

(see also Eq. 7.3 in Chapter 7)

Bibliography

[1] J. D. Jackson, *Classical Electrodynamics* (Third edition, John Wiley and Sons, Hoboken, 1998).

C

Proof of $M^{12}M^{21} = 1$

From Eq. 2.98 of Chapter 2, $\det(M^u)$ can be written as:

$$\det(M^u) = \det(M^{21}P^1M^{12}P^2), \tag{C.1}$$

where M^{12} and M^{21} are the respective dynamical matrices given by Eq. 2.88 and Eq. 2.89 in Chapter 2, which we write again here:

$$M^{12} = \frac{1}{2}\begin{bmatrix} 1+\chi^{12} & 1-\chi^{12} \\ 1-\chi^{12} & 1+\chi^{12} \end{bmatrix}, \text{and } M^{21} = \frac{1}{2}\begin{bmatrix} 1+\chi^{21} & 1-\chi^{21} \\ 1-\chi^{21} & 1+\chi^{21} \end{bmatrix}. \tag{C.2}$$

with $\chi^{12} = \dfrac{k_{2x}}{k_{1x}}$, and $\chi^{21} = \dfrac{k_{1x}}{k_{2x}}$. Here, k_{1x} and k_{2x} represent the respective wavevectors of the medium 1 and medium 2 in the stacking direction along the x-axis of the 1D-PCs. In Eq. C.1, $P^1(d)$ and $P^2(d)$ represent the propagation matrices given by Eq. 2.93 and Eq. 2.94 in Chapter 2 as:

$$P^1(d) = \begin{bmatrix} e^{-ik_{1x}d} & 0 \\ 0 & e^{ik_{1x}d} \end{bmatrix} \qquad P^2(d) = \begin{bmatrix} e^{-ik_{2x}d} & 0 \\ 0 & e^{ik_{2x}d} \end{bmatrix}, \tag{C.3}$$

where d represents the distance propagated by an EM wave inside the respective medium.

Now the product of M^{12} and M^{21} would be equal to:

$$M^{12}M^{21} = \frac{1}{4}\begin{bmatrix} (1+\chi^{12})(1+\chi^{21})+(1-\chi^{12})(1-\chi^{21}) & (1+\chi^{12})(1-\chi^{21})+(1-\chi^{12})(1+\chi^{21}) \\ (1-\chi^{12})(1+\chi^{21})+(1+\chi^{12})(1-\chi^{21}) & (1-\chi^{12})(1-\chi^{21})+(1+\chi^{12})(1+\chi^{21}) \end{bmatrix}. \tag{C.4}$$

After some mathematical manipulation, the above equation yields:

$$M^{12}M^{21} = \frac{1}{4}\begin{bmatrix} 4 & 0 \\ 0 & 4 \end{bmatrix} \implies M^{12}M^{21} = 1. \tag{C.5}$$

since, $\chi^{12}\chi^{21} = \dfrac{k_{2x}}{k_{1x}}\dfrac{k_{1x}}{k_{2x}} = 1$. Same way we can show $M^{12}M^{21} = I$. That implies:

$$M^{12} = (M^{21})^{-1}, \tag{C.6}$$

which we intended to show.

Bibliography

[1] P. Yeh, *Optical waves in layered media* (Wiley-Interscience, Hoboken 2005).

D

Proof of $\det[M^u] = 1$

From Eq. 2.98 of Chapter 2, $\det[M^u]$ is expressed as:

$$\det[M^u] = \det[M^{21}P^1(d_1)M^{12}P^2(d_2)]. \tag{D.1}$$

Now from the properties of determinant of matrices, if A and B are two square matrices, then we have:

$$\det[AB] = \det[A]\det[B]. \tag{D.2}$$

With the use of the above equation, the determinant of the product $B^{-1}AB$ can be obtained as:

$$\det[B^{-1}AB] = \det[B^{-1}]\det[A]\det[B] = \det[B^{-1}]\det[B]\det[A]. \tag{D.3}$$

That implies:

$$\det[B^{-1}AB] = \det[B^{-1}B]\det[A] = \det[A]. \tag{D.4}$$

With the use of Eq. D.2, Eq. D.1 yields:

$$\det[M^u] = \det[M^{21}P^1(d_1)M^{12}P^2(d_2)] = \det\left[M^{21}P^1(d_1)M^{12}\right]\det[P^2(d_2)]. \tag{D.5}$$

Now with the use of Eq. C.6 in Appendix C, the above equation can be written as:

$$\begin{aligned}\det[M^u] &= \det\left[(M^{12})^{-1}P^1(d_1)M^{12}\right]\det[P^2(d_2)] \\ &= \det\left[(M^{12})^{-1}M^{12}\right]\det[P^1(d_1)]\det[P^2(d_2)] \\ &= \det[P^1(d_1)]\det[P^2(d_2)].\end{aligned} \tag{D.6}$$

Using Eq. 2.93 and 2.94, from Chapter 2, we can obtain $\det[P^1(d_1)]$ and $\det[P^2(d_2)]$ as:

$$\det[P^1(d_1)] = \begin{vmatrix} e^{-ik_{1x}d_1} & 0 \\ 0 & e^{ik_{1x}d_1} \end{vmatrix} = 1 \text{ and } \det[P^2(d_2)] = \begin{vmatrix} e^{-ik_{2x}d_2} & 0 \\ 0 & e^{ik_{2x}d_2} \end{vmatrix} = 1. \tag{D.7}$$

Finally, from Eqs. D.6 and D.7, we have:

$$\det[M^u] = 1, \tag{D.8}$$

which we intended to show.

E

Transfer matrix and Transmission and Reflection amplitudes

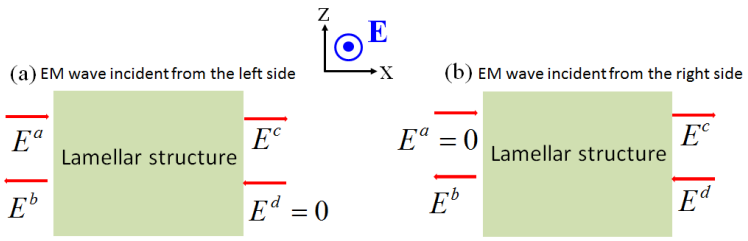

Figure E.1: (a) Schematic diagram of an EM wave incident on the lamellar structure from the left side. (b) same as (a), but for an EM wave incident on the lamellar structure from the right side. In each panel, we indicate the forward going and backward going electric field parts on both interfaces of the lamellar structure.

Let us consider a general case of a multilayer stack that consists of several material slabs that could have different thicknesses and be made from different materials. We assume that this stack is embedded in purely dielectric media from the left and the right side. Following the discussion in Section 2.3 of Chapter 2, the forward going and backward going electric field parts at the entrance of the stack can be represented as $\begin{bmatrix} E^a \\ E^b \end{bmatrix}$. Conversely, the forward going and backward going electric

field parts at the exit of the stack can be represented as $\begin{bmatrix} E^c \\ E^d \end{bmatrix}$ (see the schematics in Fig. E.1).

If we assume that a transfer matrix M^{total} correlates the electric fields at the entrance and exit of the stack, then we have [1]:

$$\begin{bmatrix} E^a \\ E^b \end{bmatrix} = \begin{bmatrix} M_{11}^{total} & M_{12}^{total} \\ M_{21}^{total} & M_{22}^{total} \end{bmatrix} \begin{bmatrix} E^c \\ E^d \end{bmatrix}. \tag{E.1}$$

If we consider that the plane EM wave is incident from the left side of the stack, then E^d will be zero, since there will be no EM wave coming in the direction opposite to the incident EM wave (see the schematics in Fig. E.1 (a)) [1] . That means:

$$\begin{bmatrix} E^a \\ E^b \end{bmatrix} = \begin{bmatrix} M_{11}^{total} & M_{12}^{total} \\ M_{21}^{total} & M_{22}^{total} \end{bmatrix} \begin{bmatrix} E^c \\ 0 \end{bmatrix}. \tag{E.2}$$

By dissolving the above matrix into equations, we get:

$$E^a = M_{11}^{total} E^c, \tag{E.3a}$$

$$E^b = M_{21}^{total} E^c. \tag{E.3b}$$

From the above equations, we can obtain the amplitude of transmission, t and reflection r as:

$$t = \frac{E^c}{E^a} = \frac{1}{M_{11}^{total}}, \tag{E.4a}$$

$$r = \frac{E^b}{E^a} = \frac{M_{21}^{total}}{M_{11}^{total}}. \tag{E.4b}$$

On the other hand, if we assume that the EM wave is incident from the right side of the stack (see the schematics in Fig. E.1 (b)), then from Eq. E.1, we can write [1]:

$$\begin{bmatrix} 0 \\ E^b \end{bmatrix} = \begin{bmatrix} M_{11}^{total} & M_{12}^{total} \\ M_{21}^{total} & M_{22}^{total} \end{bmatrix} \begin{bmatrix} E^c \\ E^d \end{bmatrix}. \tag{E.5}$$

Notice that in this case, $E^a = 0$. That implies:

$$\begin{bmatrix} E^c \\ E^d \end{bmatrix} = \frac{1}{\det[M^{total}]} \begin{bmatrix} M_{22}^{total} & -M_{12}^{total} \\ -M_{21}^{total} & M_{11}^{total} \end{bmatrix} \begin{bmatrix} 0 \\ E^b \end{bmatrix}. \tag{E.6}$$

By dissolving the above matrix in to equation, we have:

$$E^c = -\frac{1}{\det[M^{total}]} M_{12}^{total} E^b, \tag{E.7a}$$

$$E^d = \frac{1}{\det[M^{total}]} M_{11}^{total} E^b. \tag{E.7b}$$

Therefore, we can obtain the amplitude of transmission, t' and reflection r', for this right to left EM wave incidence, as:

$$t' = \frac{E^b}{E^d} = \frac{\det[M^{total}]}{M_{11}^{total}}, \tag{E.8a}$$

$$r' = \frac{E^c}{E^d} = \frac{-M_{12}^{total}}{M_{11}^{total}}. \tag{E.8b}$$

We have proved in Appendix F that $\det[M^{total}] = 1$ when both the incident and outgoing media are the same and a lossless dielectric which is the case we have here. Therefore, the expression for the amplitude of transmission t' in the above equation will become:

$$t' = \frac{1}{M_{11}^{total}} \implies t' = t. \tag{E.9}$$

Furthermore, from $\det[M^{total}] = 1$, we can write:

$$M_{11}^{total} M_{22}^{total} - M_{12}^{total} M_{21}^{total} = 1. \tag{E.10}$$

Note that for multilayer stacks that have only purely dielectric lossless constituents and are embedded in a lossless dielectric medium, the following special relation applies:

$$R + T = 1 \implies rr^* + tt^* = 1. \tag{E.11}$$

The above equation emanates from the conservation of energy [1], that is valid only for lossless lamellar structures, but not for the lossy lamellar structures. With the use of Eq. E.4, the above equation yields:

$$\frac{M_{21}^{total}}{M_{11}^{total}} \frac{M_{21}^{total*}}{M_{11}^{total*}} + \frac{1}{M_{11}^{total}} \frac{1}{M_{11}^{total*}} = 1. \tag{E.12}$$

That gives:

$$|M_{21}^{total}|^2 + 1 = |M_{11}^{total}|^2. \tag{E.13}$$

After rearranging the terms in the above equation, we get:

$$M_{11}^{total} M_{11}^{total*} - M_{21}^{total} M_{21}^{total*} = 1. \tag{E.14}$$

From Eqs. E.10 and E.14, we can obtain:

$$M_{11}^{total*} = M_{22}^{total}, \tag{E.15a}$$

$$M_{12}^{total*} = M_{21}^{total}. \tag{E.15b}$$

We will explain the consequences of the above relations in Section 2.3 of Chapter 2. In particular, we will see that as the result of the above relations the reflectance is symmetric for lossless multilayer stacks. However, for lossy multilayer stacks reflectance is asymmetric as a result of Eq. E.15(a) and Eq. E.15(b) not being valid.

Reversibility principle for lossless lamellar structures

The lossless multilayer stacks also satisfy the reversibility principle, as we will derive in the following.
With the use of Eq. E.9, Eq. E.11 yields:

$$tt'^* + rr^* = 1. \tag{E.16}$$

Furthermore, from Eq. E.8(b), we can write:

$$r'^* = \frac{-M_{12}^{total*}}{M_{11}^{total*}}. \tag{E.17}$$

After rearranging the terms, we get:

$$r'^* = \frac{-M_{12}^{total*}}{M_{11}^{total}} \frac{M_{11}^{total}}{M_{11}^{total*}}. \tag{E.18}$$

Now for the case of lossless PCs, from Eqs. E.15(b) and E.18, we can write:

$$r'^* = \frac{-M_{21}^{total}}{M_{11}^{total}} \frac{M_{11}^{total}}{M_{11}^{total*}}. \tag{E.19}$$

Finally, with the use of Eq. E.4, the above equation yields:

$$r'^* = \frac{-r}{t} t^* \implies tr'^* + rt^* = 0. \tag{E.20}$$

The Eqs. E.16 and E.20 together are referred to as the principles of reversibility [1]. Again, we stress that these are valid only for the lossless multilayer stacks, since Eq. E.15 is valid only for the lossless case [1]. From these principles of reversibility, we can infer that in the case of lossy lamellar structures, we can expect that the reflection properties will be different depending on whether the EM wave incident

on the stack from the left side or from the right side.

Bibliography

[1] P. Yeh, *Optical waves in layered media* (Wiley-Interscience, Hoboken 2005).

F

Proof of $\det[M^{total}] = 1$

From Eq. 2.118 of Chapter 2, $\det[M^{total}]$ can be expressed as:

$$\det[M^{total}] = \det\left[\left(\prod_{j=1}^{N} M^{j,j+1} P^{j+1}(d_{j+1})\right) M^{N+1,1}\right]. \tag{F.1}$$

From the properties of determinant of matrices, if A and B are two square matrices, then we have:

$$\det[AB] = \det[A]\det[B]. \tag{F.2}$$

Therefore, $\det[M^{total}]$ can be written as [1]:

$$\det[M^{total}] = \left(\prod_{j=1}^{N} \det[M^{j,j+1}]\det[P^{j+1}]\right) \det[M^{N+1,1}]. \tag{F.3}$$

Using Eq. 2.93 from Chapter 2, we can obtain $\det[P^{j+1}]$ as:

$$\det[P^{j+1}(d_{j+1})] = \begin{vmatrix} e^{-ik_{j+1x}d_{j+1}} & 0 \\ 0 & e^{ik_{j+1x}d_{j+1}} \end{vmatrix} = 1. \tag{F.4}$$

Furthermore, with the use of Eq. 2.89 from Chapter 2, $\det[M^{j,j+1}]$ can be obtained

as [1]:

$$\begin{aligned}\det[M^{j,j+1}] &= \left|\frac{1}{2}\begin{bmatrix}1+\chi_E^{j,j+1} & 1-\chi_E^{j,j+1}\\ 1-\chi_E^{j,j+1} & 1+\chi_E^{j,j+1}\end{bmatrix}\right| \\ &= \frac{1}{4}\left[(1+\chi_E^{j,j+1})^2-(1-\chi_E^{j,j+1})^2\right] \\ &= \chi_E^{j,j+1} \\ &= \frac{k_{(j+1)x}}{k_{jx}}.\end{aligned} \tag{F.5}$$

Similarly, we can determine $\det[M^{N+1,1}]$ as:

$$\det[M^{N+1,1}] = \frac{k_{1x}}{k_{(N+1)x}}. \tag{F.6}$$

Now with the use of Eqs. F.4–F.6, Eq. F.3 yields:

$$\det[M^{total}] = \left(\prod_{j=1}^{N}\frac{k_{(j+1)x}}{k_{jx}}\right)\frac{k_{1x}}{k_{(N+1)x}} = 1. \tag{F.7}$$

Note that the above relationship is valid only when the entire multilayer stack is embedded in a lossless dielectric medium.

Bibliography

[1] P. Yeh, *Optical waves in layered media* (Wiley-Interscience, Hoboken 2005).

G

Transmission and Reflection of effective homogenised PC metamaterials

With the use of the effective permittivity, ε_{eff}, we can calculate the absorptance A, of these effective media as A=1-T-R, where T and R are the respective transmittance and reflectance that can be evaluated analytically [1, 2] as below:

$$\mathrm{T} = \frac{1}{\frac{1}{4}|2\cos k_{eff}d - i(\sqrt{\varepsilon_{eff}} + \frac{1}{\sqrt{\varepsilon_{eff}}})\sin k_{eff}d|^2}, \tag{G.1}$$

$$\mathrm{R} = \frac{\frac{1}{4}|(\sqrt{\varepsilon_{eff}} - \frac{1}{\sqrt{\varepsilon_{eff}}})\sin k_{eff}d|^2}{\frac{1}{4}|2\cos k_{eff}d - i(\sqrt{\varepsilon_{eff}} + \frac{1}{\sqrt{\varepsilon_{eff}}})\sin k_{eff}d|^2}, \tag{G.2}$$

where $d = \mathrm{Na}$ is the total thickness of the effective homogeneous medium comprised of N SiC-air building blocks, with a being the lattice constant, and $k_{eff} = \sqrt{\varepsilon_{eff}}\,\omega/c$. Here, ω and c represent the angular frequency of the incident EM wave and the speed of light respectively. Note the full complex, ε_{eff} and the complex squareroot of ε_{eff} should be incorporated in Eqs. G.1 and G.2 that are consistent with the passivity requirement.

Bibliography

[1] S. Foteinopoulou, M. Kafesaki, E.N. Economou and C.M. Soukoulis, "Two-dimensional polaritonic photonic crystals as terahertz uniaxial metamaterials," Phys. Rev. B **84** 035128 (2011).

[2] P. Markos, C. M. Soukoulis, *Wave propagation from electrons to photonic crystals and left handed materials*, (Princeton University Press, Princeton, 2008).

H

Dependance of the SiC-air PC band structure properties on the PC lattice constant

In Chapter 5, we have mentioned that we can identify bandgap-like regions of lossy PCs where the spectral response of energy velocity drops almost to zero. Therefore, to understand how the bandstructure of lossy 1D-PCs changes with the PC lattice constant, we plot in Fig. H.1 (a), the energy velocity at the interface, $v_{e,int}$, of SiC-air PCs versus free space wavelength, λ_{free}, and the PC lattice constant, a. Moreover, we also plot the imaginary part of the Bloch wavevector, Im(q), of these PCs in Fig. H.1 (b). As we discussed in Chapter 2, a high imaginary part signifies band-gap like regimes in lossy PCs. We can see in Fig. H.1 that the landscapes of a low energy velocity in Fig. H.1 (a) coincide with the landscapes of a high Im(q) in H.1 (b), thus clearly identifying the bandgap-like regions of SiC 1D-PCs. Note, we represent the lattice constants of the three PCs that we investigate in Chapter 5 with the white lines in Fig. H.1. We notice from Fig. H.1 that for the five and ten-micron lattice constant PCs, we see allowed modes in most of the phonon-polariton gap regime. On the other hand, for the case of the eight-micron lattice constant PC, we see a bandgap-like regime in most of the phonon-polariton gap. We remind the reader as we saw in Fig. 5.2 that the energy velocity at the interface of the eight-micron lattice constant PC is lower than the reflectionless

energy velocity, v_{e0}, given by Eq. 5.1 throughout the spectrum. Therefore, the eight-micron lattice constant PC cannot work as a reflectionless PC, thus it is not suitable to give an enhanced absorption performance.

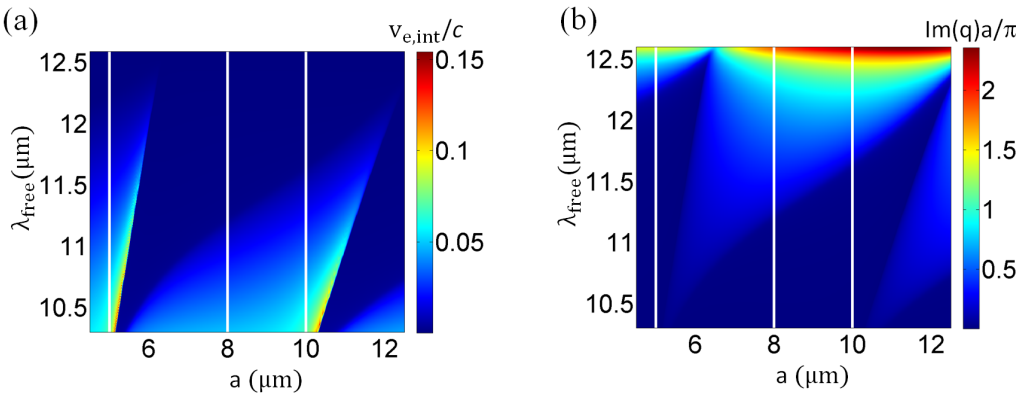

Figure H.1: (a) The energy velocity at the interface, $v_{e,int}$, of semi-infinite SiC-air PC structures, versus the free space wavelength, λ_{free}, and the lattice constant, a. The filling ratio of the PCs is f = 0.05 and we consider two-hundred unit cells in the PCs to emulate semi-infinite structures. Note, all energy velocity values are expressed in terms of the speed of light *c*. The vertical white lines at lattice constants 5 μm, 8 μm and 10 μm represent the three PCs under study in Chapter 5. (b) Same as in (a), but for the imaginary part of the Bloch wavevector, Im(q). Note, Im(q) is scaled with a/π, with a being the lattice constant of the PC.

It is important to observe that the bandgap properties do not vary monotonically with the lattice constant. We can see that for a certain frequency the PC behaviour changes from band-like to bandgap-like and again to band-like with changing lattice constant. This repetition is expected since the band properties emanate from interference effects between the backscattered beams from the PC building blocks and depend on both the sizes and optical properties of the material constituents. In other words, because of the repetitive nature of the Fabry-Perot interference effects with frequency and building block size, the band properties of PCs are not a monotonic function of the PC lattice constant. Therefore, it is not an unexpected result that while for a five- and ten- micron lattice constant the behaviour of the PC is mostly band-like in the SiC Restrahlen band regime, it is mostly bandgap-like in the same frequency region for the case of the eight-micron lattice constant PC.

I

Meaning of Bloch impedance in lossless PCs

In Section 8.2 of Chapter 8, we discussed that the approximation of the reflectivity of a PC in the limit of $N \to \infty$ seen in Eq. 8.9 is exactly valid only for the lossy PCs. However, it is natural to wonder what is the meaning of the Bloch/effective impedance for periodic finite lossless PCs. In order to understand that we evaluate the Z_{eff} from Eq. 8.13 and Z_B from Eq. 8.18, for the case of a dielectric-air PC with a lattice constant $3\,\mu$m and filling ratio 0.05. We take the permittivity of the dielectric equal to 11.56. We show the results in Fig. I.1(a), indicating Z_B and Z_{eff} with red-solid line and black-dashed line respectively. It is evident from Fig. I.1 (a) that Z_B and Z_{eff} are identical in such case as well. Note that, we should choose the correct root for the Bloch wavevector, q depending on the bandslope, as we discussed in Chapter 2, while evaluating the Z_B and Z_{eff} from the Eqs. 8.13 and 8.18 respectively.

Now with the use of this impedance, we evaluate the corresponding reflectance, R_{semi} and plot the result in Fig. I.1(b) with a black-dashed line. We compare this reflectance with the actual five and ten-unit-cell dielectric-air PC result evaluated with TMM. We designate these results with red-solid line and green-solid line respectively. It is impressive to note that still the impedance captures the average reflectance of the PC, while it ignores the fringes in the band regions. In the

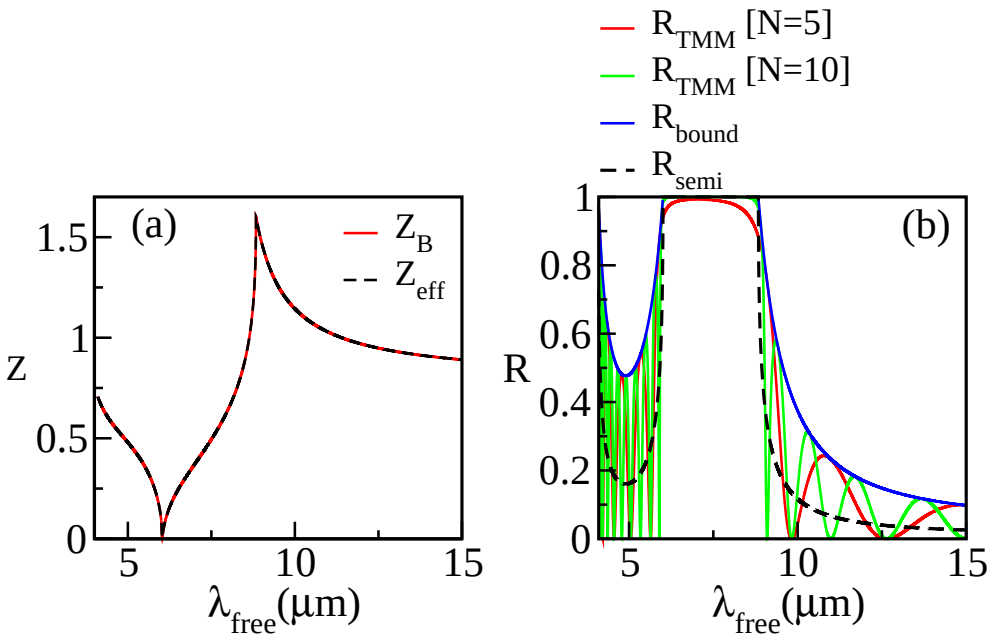

Figure I.1: (a) Bloch impedance, Z_B (red-solid line) from Eq.8.18 and effective impedance, Z_{eff} (black-dashed line) from Eq. 8.13 are plotted versus free space wavelength, λ_{free}, of a dielectric-air PC with $\varepsilon = 11.56$ and filling ratio 0.05 and lattice constant of 3 μm. (b) Reflectance versus free space wavelength, λ_{free}, of the same SiC-air PC. Black-dashed line indicates the reflectance obtained from Z_{eff}. The red-solid line and green-solid line indicate the reflectance from the actual dielectric-air PC with five and ten-unit-cells respectively, using the TMM method. The blue-solid line indicate the upper bound value of the reflectivity, that we derived (See Eq. I.2).

bandgap regions, R naturally approaches one for thick lossless PCs as we discussed in Chapter 2.

Furthermore, it would be interesting to have a check of the bounds for the oscillatory fringes in the band regions. For this purpose, we write again the reflectivity of the N unit-cell PC, given by Eq. 8.6, for the case when the incoming and outgoing media are the same as one of the constituents of the PC:

$$r(N) = \frac{M_{21}^u}{M_{11}^u - \cos(\text{qa}) + \frac{\sin(\text{qa})}{\tan(N\text{qa})}}. \tag{I.1}$$

In the above equation, it is obvious that if $\tan(N\text{qa}) \to 0$, $r(N)$ will tend to zero, thus the lower bound of reflectance, R would be zero. On the other hand, if $\tan(N\text{qa}) \to \pm\infty$, the upper bound of reflectivity is obtained as:

$$r_{bound} = \frac{M_{21}^u}{M_{11}^u - \cos(\text{qa})}. \tag{I.2}$$

We plot $R_{bound} = |r_{bound}|^2$ in Fig. I.1(b) with a blue-solid line. We can clearly see that R_{bound} captures the upper bound values of the fringes in the band regions.

J

Proof of $M^{31}M^{12} = M^{32}$

The dynamical matrix M^{31} relates the amplitude of the EM waves going from medium 3 to medium 1 [1]. Similarly, the dynamical matrix M^{12} relates the amplitude of the EM waves going from medium 1 to medium 2. From Eq. 2.88 and Eq. 2.89 of Chapter 2, we can express M^{31} and M^{12} as:

$$M^{31} = \frac{1}{2}\begin{bmatrix} 1+\chi^{31} & 1-\chi^{31} \\ 1-\chi^{31} & 1+\chi^{31} \end{bmatrix} \text{ and } M^{12} = \frac{1}{2}\begin{bmatrix} 1+\chi^{12} & 1-\chi^{12} \\ 1-\chi^{12} & 1+\chi^{12} \end{bmatrix}, \tag{J.1}$$

with $\chi^{31} = \frac{k_{1x}}{k_{3x}}$ and $\chi^{12} = \frac{k_{2x}}{k_{1x}}$, where k_{1x}, k_{2x} and k_{3x} represent the respective wavevectors of the medium 1, medium 2 and medium 3 in the stacking direction along x-axis.

Now the product of M^{31} and M^{12} would be equal to:

$$M^{31}M^{12} = \frac{1}{4}\begin{bmatrix} (1+\chi^{31})(1+\chi^{12})+(1-\chi^{31})(1-\chi^{12}) & (1+\chi^{31})(1-\chi^{12})+(1-\chi^{31})(1+\chi^{12}) \\ (1-\chi^{31})(1+\chi^{12})+(1+\chi^{31})(1-\chi^{12}) & (1-\chi^{31})(1-\chi^{12})+(1+\chi^{31})(1+\chi^{12}) \end{bmatrix}. \tag{J.2}$$

After some mathematical manipulation, we get:

$$M^{31}M^{12} = \frac{1}{2}\begin{bmatrix} 1+\chi^{31}\chi^{12} & 1-\chi^{31}\chi^{12} \\ 1-\chi^{31}\chi^{12} & 1+\chi^{31}\chi^{12} \end{bmatrix}. \tag{J.3}$$

Further, we can simplify $\chi^{31}\chi^{12}$ as:

$$\chi^{31}\chi^{12} = \frac{k_{1x}}{k_{3x}}\frac{k_{2x}}{k_{1x}} \Rightarrow \chi^{31}\chi^{12} = \frac{k_{2x}}{k_{3x}} \Rightarrow \chi^{31}\chi^{12} = \chi^{32}. \tag{J.4}$$

So:

$$M^{31}M^{12} = \begin{bmatrix} 1+\chi^{32} & 1-\chi^{32} \\ 1-\chi^{32} & 1+\chi^{32} \end{bmatrix} = M^{32}, \tag{J.5}$$

which we intended to show.

Bibliography

[1] P. Yeh, *Optical waves in layered media* (Wiley-Interscience, Hoboken 2005).